92PC92104-TPR-11

ADVANCED THERMALLY STABLE JET FUELS

Technical Progress Report
January 1995 - March 1995

H.H. Schobert, S. Eser, C. Song, P.G. Hatcher, A. Boehman, M.M. Coleman

Contributions from:

R. Arumugam, , R. Byrne, P.Chang, R.Dutta, K. Gergova, E. Kazakova,
S. Martin, M. Reddy, P. Sanghani, A.D. Schmitz, P. Vijay, E. Yoon, and J. Yu

June 1995

Prepared for U.S. Department of Energy
under
Contract No. DE-FG22-92PC92104

Table of Contents

OBJECTIVES

The Penn State program in advanced thermally stable jet fuels has five objectives: 1) development of mechanisms of degradation and solids formation; 2) quantitative measurement of growth of sub-micrometer and micrometer-sized particels suspended in fuels during thermal stressing; 3) characterization of carbonaceous deposits by various instrumental and microscopic methods; 4) elucidation of the role of additives in retarding the formation of carbonaceous solids; and 5) assessment of the potential of production of high yields of cycloalkanes and hydroaromatics by direct liquefaction of coal.

SUMMARY

Quantitative structure-property relationships have been applied to study the thermal stability of pure hydrocarbons typical of jet fuel components. A simple method of chemical structure description in terms of Benson groups was tested in searching for structure-property relationships for the hydrocarbons tested experimentally in this program. Molecular connectivity as a structure-based approach to chemical structure-property relationship analysis was also tested. Further development of both the experimental data base and computational methods will be necessary.

Thermal decomposition studies, using glass tube reactors, were extended to two additional model compounds: *n*-decane and *n*-dodecane. A comparison was made between the results from tubing bomb (i.e., stainless steel microautoclave) and glass tube reactor experiments for *n*-tetradecane. Experiments with *n*-tetradecane were carried out in tubing bomb reactors using both nitrogen and air atmospheres.

Efforts on refining the deposit growth measurement and characterization of suspended matter in stressed fuels have lead to improvements in the analysis of stressed fuels. The refinements have included detailed quantification of sources of experimental uncertainty in the analytical equipment, elimination of specific sources of measurement error, and the development of more accurate procedures for characterizing suspended matter in the stressed liquid fuel.

Further work was performed with PX-21 high surface area activated carbon. A carbonaceous overlayer formed on the surface of PX-21 after thermal stressing of model compounds can inhibit further deposition more effectively than the original PX-21. Surface oxygen complexes on the carbonaceous overlayer appear to be the active species during thermal stressing. Electron micrographs of the activated carbon show unusual carbon filaments or fibers which appear to originate from a carbonaceous overlayer formed during the first stressing. The formation of carbon filaments on activated carbon surfaces at the relatively low temperature of 425°C used in this study has not been reported in the literature previously. Extraction of PX-21 with toluene

showed the presence of some aromatic hydrocarbons which possibly diminish its activity during thermal stressing.

A literature review on the effects of carbon surfaces on organic reactions was completed.

Preliminary optimization and kinetics studies have been performed on the use of 1,2,3,4-tetrahydroquinoline as a thermal stabilizer for dodecane.

A conceptual process design scheme for a continuous flow mini-piloy plant reactor system for conversion of coal to "pre-jet fuels" and upgrading of the liquids was modified to satisfy various processing requirements. A detailed description of the modified continuous-mode process scheme has been developed.

Further results of characterization of mesoporous molecular sieve catalysts by chemical analysis, surface area measurement, thermal analysis, and solid state nuclear magnetic resonance spectroscopy have been obtained. Catalytic evaluation of these materials for hydrogenation of naphthalene and phenanthrene and alkylation of naphthalene has been performed.

The catalytic hydrogenation and dehydrogenation behavior of naphthalene, tetralin, pyrene, and hydropyrenes has been examined. The catalyst used for this work was molybdenum disulfide.

It has been confirmed that both decalin isomers can be produced in parallel during naphthalene hydrogenation over metal-loaded zeolites. The hydrogenation of $\Delta^{9,10}$-octalin and $\Delta^{1,9}$-octalin may play an important role in determining the decalin *cis/trans* configuration.

There are stong synergistic effects between water and a dispersed molybdenum sulfide catalyst for promoting liquefaction at 350° of both Wyodak subbituminous and Pittsburgh #8 bituminous coals. At 400° the promotional effects of adding water are lost, and, in the case of Wyodak, water actually inhibits the catalyst activity, resulting in a reduction in conversion. For Pittsburgh #8 coal, adding water to the catalytic reaction at 400° results in a similar conversion to that from the use of catalyst alone. There is some apparent benefit in terms of a slight improvement in product quality for the added water reaction.

Task 1. Investigation of the Quantitative Degradation Chemistry of Fuels

1. The Study of Quantitative Structure-Thermal Stability Relationships in the Pyrolysis of Hydrocarbons (Contributed by Elena Kazakova)

Introduction

This section of the report describes the application of Quantitative Structure-Property Relationships (QSPR) method in the study of thermal stability of jet fuels, particularly of pure hydrocarbons. The simplest method of chemical structure description in terms of Benson groups was performed in searching for structure-property relationship for small set of hydrocarbon compounds studied previously as part of this program. Molecular connectivity [1,2] as a structure-based approach to chemical QSPR analysis has been tested to show the necessity for further development of both experimental data base and computational methods.

The Method of Quantitative Structure-Activity or Structure-Property Relationships (QSAR/QSPR)

Molecular mechanisms involved in chemical reactions of complex organic compounds are generally too complex and not sufficiently well known to be described by a detailed model for the prediction of chemical properties of an untested molecule. Nevertheless, by means of a statistical treatment of a large set of molecules (for which the property of interest is known), structure-property relationships can be established. That means the molecular structures are characterized by various descriptors used for developing multiple regression model equations to relate the descriptor to the property. The overall approach is shown in Figure 1 [3].

The main steps involved in the computer-assisted SPR study are as follows: (1) input and storage of molecular structures with known property of interest in topological notation; (2) calculation of molecular structure descriptors for each molecule in the data set, testing the descriptors for their significance and considering only those that are not highly correlated with each other; (3) utilization of the multivariative regression analysis (both linear and nonlinear models) to obtain quantitative structure-property correlations, application of the pattern recognition methods to search for the best sets of descriptors; (4) testing the predictive ability of the obtained SP correlation.

The research implies the design, testing and application of computer software for the purpose of deriving QSPR and, thus, developing the capability to predict thermal stability for unknown compounds. The approach involves the graphical entry and storage of structures, molecular connectivity descriptor calculation and multiple linear regression analysis of available experimental data sets.

There are two general aspects that can be identified in a molecule. The first is the representation of atoms and their connections within the molecule, commonly referred as *molecular topology*. The second aspect includes dimensional information, called the *molecular topography*. Generally, molecular structure descriptor modules are developed according to the complete information provided by both aspects. Descriptor sets fall into four classes: *topological*, *geometrical*, *electronical*, and *physicochemical*. However, the followers of molecular connectivity SPR method claim that dimensional aspects of a structure are directly dependent on the molecular topology. Therefore, a descriptor module can be reduced to only one class, topological descriptor (though a few newly developed characteristics were proposed for 3D-description of a molecule in terms of graph theory [4, 5]). The latter approach works fairly well within limited classes of compounds (alkanes, cyclohexanes, benzenes, etc.) but generally fails being applied to heterogeneous data sets. Also, it performs well only for properties that have fundamental additive nature. Familiar examples are partition coefficient of alcohols and Benson group additivity method for thermodynamic property calculations. However, the molecular connectivity method has the advantage of less complexity in terms of descriptor set. Therefore, it is worthwhile to test its performance in searching for the structure-thermal stability correlations.

A chemical graph (skeleton of a molecule) can be written as a matrix called the *topological* or *adjacency matrix*. Figure 2 shows the transformation from chemical graph to topological matrix. To construct the matrix, the graph is numbered in any order. An entry T_{ij} in the matrix has the value of bond order when there is a bond (or *edge* in graph theory) between atoms (or *vertices*) i and j; otherwise it is zero.

Algebraic expression based on the topological matrix T for vertex valence may be formulated as the sum of the entries in a row as

$$\delta_i = \sum_{j=1}^{n} T_{ij} \qquad (1)$$

where n is the number of vertices and the order of T.

A number of so-called *topological indices* [6-8] has been developed on the basis of δ_i expressions. Not going deeply into the topological index classification, it is worthwhile to point out that for hydrocarbons Randic' branching index [6] and related molecular connectivity indices ${}^{m}\chi_t$ developed by Kier and Hall [1] appear appreciably better than other indices in terms of correlation coefficient and standard error.

The ${}^{m}\chi_t$ are terms defined for a subgraph of type t containing m edges, connected in T. The order of a subgraph is defined as m. Subgraphs may be classified into four types: *path, cluster path/cluster, and chain* [2,9]. Some examples of subgraphs are shown in Figure 3.

The connectivity indices ${}^{m}\chi_t$ are evaluated as a sum of terms over all distinct connected subgraphs

$$ {}^{m}\chi_t = \sum_{j=1}^{n_m} {}^{m}S_j \qquad (2) $$

where n_m is the number of type t subgraphs of order m. The subgraph term ${}^{m}S_j$ depends on the reciprocal square root of the vertex valence in a multiplicative manner

$$ {}^{m}S_j = \prod_{i=1}^{k} (\delta_i)_j^{-1/2} \qquad (3) $$

where j denotes the particular set of edges that constitute the subgraph, k is equal m+1 for all kind of subgraphs but chain, k is equal m for chain type.

In terms of multiple regression, the expression for a predicted value of property of interest $\hat{y}_i$ for i th compound is assumed to be linear dependent on the set of p indices $({}^{m}\chi_t)_i$

$$ \hat{y}_i = \alpha_0 + \alpha_1 {}^{m}\chi_{t_i}^{1} + \ldots + \alpha_p {}^{m}\chi_{t_i}^{p} \qquad (4) $$

where $\alpha_n th$ are the calculated regression coefficients. The residual e_i is defined as the difference between the observed and the predicted values

$$ e_i = \frac{y_i - \hat{y}_i}{y_i} \qquad (5) $$

The $\alpha_n th$ coefficients are obtained from minimization of Q

$$ Q = \sum_{i=1}^{n} e_i^2, \qquad (6) $$

the sum of the squared residuals.

The multiple correlation coefficient R is a measure of the adequacy of the fit defined as

$$ R^2 = 1 - \frac{\sum (y_i - \hat{y}_i)^2}{\sum (y_i - \bar{y})^2} \qquad (7) $$

where the average $\bar{y}$ value is simple arithmetic average of y_i for the set of n observations.

R has a value between 0 and 1. Value of R^2 near 1 occur when y_i and $\hat{y}_i$ are nearly identical that means the good fit of the model. Values of R^2 near zero mean that the model does not work. The overall standard deviation of the fit is given by

$$ S^2 = \frac{Q}{n - p - 1} \qquad (8) $$

Study of Structure-Thermal Stability Relationships for Hydrocarbons

The first attempt to find the QSPR correlation between structure and thermal stability was performed in the frame of group additivity description of hydrocarbons. However, the measure of the property of interest is needed to be defined as no standard definition procedure exists. The conversion in 4 hour pyrolysis of studied compounds at 450°C at high pressure conditions was chosen for the this purpose. The set of 13 hydrocarbons experimentally studied by members of the Penn State Jet Fuel Program [9-14] was used to perform linear regression analysis.

Table 1 provides the numbers for Benson's groups [15] of the hydrocarbons and their observed conversion. The numbers of aromatic and naphthenic rings are also included in the descriptor set. Figure 4 shows the comparison of the observed and calculated conversion. The obtained correlation is given by

$$C = 100 \times \left(1 + G^2\right)^{-1},$$

where

$$G = -3.3 + 0.16a_1 + 0.82a_2 - 0.23a_3 + 85.1a_4 - 82.2a_5 + 0.3a_6 + 85.1a_7 + 82.5a_8,$$

C is the conversion (%) and a_n are group coefficients as shown in Table 1.

The values of R and S are equal 0.94 and 2.74 respectively. The value of standard deviation S depends on the ratio of the number of descriptors to the number of experimental points. High value of the standard deviation indicates that, although there can be a good correlation in terms of QSPR, the number of available experimental points does not allow making final conclusion. However, the value of S can be sufficiently decreased by using smaller set of descriptors.

The two molecular-connectivity index sets

$$\left\{{}^0\chi, {}^1\chi, {}^3\chi_{cluster}, {}^6\chi_{chain}\right\} \text{ and } \left\{{}^0\chi, {}^1\chi, {}^3\chi_{cluster}, {}^5\chi_{cluster}, {}^6\chi_{chain}\right\}$$

were used in QSPR study in order to reduce the standard deviation without increasing the data set. In order to obtain the function that would range from 0 to 100 (as the experimental conversion) the multiple linear regression method was transferred to nonlinear by using function

$$f({}^m\chi_t) = 100 / \left(\varphi\left({}^m\chi_t\right)^2 + 1.\right)$$

where $\varphi\left({}^m\chi_t\right)$ is the linear expression of molecular-connectivity (MC) indices

$$\varphi\left({}^{m}\chi_t\right) = -3.12 + 1.45\ {}^{0}\chi - 1.63\ {}^{1}\chi - 1.77\ {}^{3}\chi_{cluster} + 0.87\ {}^{6}\chi_{chain}$$

for the first set of descriptors and

$$\varphi\left({}^{m}\chi_t\right) = 3.63 - 1.72\ {}^{0}\chi + 2.0\ {}^{1}\chi + 1.24\ {}^{3}\chi_{cluster} - 4.22\ {}^{5}\chi_{cluster} + 4.34\ {}^{6}\chi_{chain}$$

for the second one. The multiple correlation coefficients are 0.91 and 0.93 respectively. Standard deviations have the values of 1.14 and 1.2. The comparison of obtained results is presented in Figure 5. It is apparent that no serious improvement had been reached in sense of better correlation.

As was demonstrated, the number of available experimental points does not allow us to generate an equation with good predictive ability. However, the change of experimental data pool can be useful in that situation as can be the change of the thermal stability definition. It was proposed to use the kinetic parameters of pseudo-first-order decomposition as the other measure of thermal stability. It allows searching for the more abundant kinetic data sets aside from results of in-house experiments. The result of the literature review is shown in Tables 2–4. Table 2 gives hydrocarbon decomposition kinetic parameters that had been obtained through the last thirty years by different researchers and for sufficiently wide range of experimental conditions. Tables 3 and 4 [16] reproduce the results of experiments accomplished by the Monsanto research group [16] in the form of kinetic parameters (Table 3) and rate constants for standard conditions (Table 4). Each set of experimental data was used in QSPR analysis separately. Thus, it was demonstrated that inconsistent sets of data could not be profitable in the structure-property studies. The linear equations for kinetic parameters and the standard rate constants have been generated. Unfortunately, the results can not be compared with each other because of poor performance of the first data set (Figures 6,7) and also because of very limited information on E_{act} given by the Monsanto group. The correlations for k_0 and k_{avg} are shown in Figures 8 and 9. The correlation between $\ln(k_0)$ (for compounds studied by Fabuss and co-coworkers) and MC index set $\left\{{}^{0}\chi, {}^{1}\chi, {}^{3}\chi_{cluster}, {}^{5}\chi_{cluster}, {}^{6}\chi_{chain}\right\}$ can be displayed in the form of linear equation

$$\ln(k_0) = -291.95 + 453.8\ {}^{0}\chi - 641.2\ {}^{1}\chi - 720.2\ {}^{3}\chi_{cl} + 2783.9\ {}^{5}\chi_{cl} + 2577.0\ {}^{6}\chi_{ch}$$

with R =0.94 and S =0.03.

The similar equation for the average rate constant for decomposition of saturated cyclic hydrocarbons in terms of topological index set:

$$\left\{ {}^{0}\chi, {}^{1}\chi, {}^{3}\chi_{cluster}, {}^{5}\chi_{cluster}, {}^{5}\chi_{chain}, {}^{6}\chi_{chain} \right\}$$

can be presented as follows

$$k_{av} = -0.49 + 0.041\ {}^{0}\chi + 0.092\ {}^{1}\chi - 0.086\ {}^{3}\chi_{cl} - 0.06\ {}^{5}\chi_{cl} + 0.136\ {}^{5}\chi_{ch} - 0.876\ {}^{6}\chi_{ch}$$

with the multiple correlation coefficient 0.86 and standard deviation 1.3. There is no need to display analogous correlations for $\ln(k_0)$ and E_a because their correlation parameters sets $\{R, S\}$ are {0.37,0.29} and {0.27,0.4} respectively.

All procedures of optimization and topological index calculations have been accomplished by codes OPTIM and GRAPH available in-house .

Conclusions

It is obvious that the method of QSPR can not be used for eclectic data sets. Although the structure-property approach reveals a strong potential as a tool for chemical property prediction, however, the absence of reliable experimental data within the range of jet fuel performance conditions does not make it work properly.

The standard procedure of thermal stability measurement should be developed. Particularly, the rate of solid deposit formation under standard conditions can be used as the measure of thermal stability.

It is worthwhile to point out that the general QSPR method with a set of united quantum, experimental and topological descriptors is the most promising way for development of predictive structure-thermal stability quantitative correlation.

References

1. Kier, L.B. & Hall, L.H. *Molecular Connectivity in Chemistry and Drug Research* (Academic Press, New York, 1976).

2. Kier, L.B. & Hall, L.H.*Molecular Connectivity in Structure-Activity Analysis* (Research Studies Press LTD., Letchworth, 1986).

3. Jurs, P.C., Hasan, P.J. & Rohrbaugh, R.H. *Prediction of Physicochemical Properties of Organic Compounds from Molecular Structure* 1-209 (Springer-Verlag, Berlin, Schloss Korb, Italy, 1988).

4. Randic', M. & Razinger, R. Molecular Topographic Indices, *Journal of Chemistry Information and Computer Science*, **35**, 140 (1995).

5. Xu, L., Wang, H.-Y. & Su, Q. A Newly Proposee Molecular Topological Index for the Discrimination of Cis/Trans Isomers and for the Studies of QSAR/QSPR, *Computers and Chemistry*, **16**, 187 (1992).

6. Randic', M. On Characterization of Molecular Branching, *Journal of American Chemistry Society*, **97**, 6609 (1975).

7. Wiener, H.*Journal of American Chemical Society*, **17**, 2636 (1947).

8. Hosoya, H. . *Bull. Chem. Soc. Japan*, **44**, 2332 (1971).

9. Lai, W.-C. .*Pyrolysis of Tetradecane at Elevated Pressure for Long Duration: Product Distribution and Reaction Mechanisms* (Department of Material Science & Engineering, Pennsylvania State University, 1992).

10. Lai, W.-C. & Song, C. *Pyrolysis of Alkylcyclohexanes at 450°C and Elevated Pressure. Product Distribution and Reaction Mechanism* (Department of Material Science & Engineering, Pennsylvania State University, 1993).

11. Lai, W.-C. & Song, C..*Product Distribution of the Pyrolysis of n-Tetradecane at 400°C and 425°C* (Department of Material Science & Engineering, Pennsylvania State University, 1993).

12. Peng, Y., *Pyrolysis of Butylbenzenes: Effect of Structure of Alkyl Side Chain on the Pyrolysis of Alkylbenzenes* (Department of Material Science & Engineering, Pennsylvania State University, 1992).

13. Peng, Y.,*Pyrolisis of Octylbenzene: Effect of Structure of Alkyl Side Chain on the Pyrolysis of Alkylbenzenes* (Department of Material Science & Engineering, Pennsylvania State University, 1992).

14. Peng, Y.,*Pyrolysis of n-Alkylbenzenes* (Department of Material Science & Engineering, Pennsylvania State University, 1994).

15. Benson, S.W. ,*Thermochemical Kinetics* (John Wiley & Sons, New York, 1976).

16. Fabuss, B.N., Smith, J.O. & Satterfield, C.N. in *Advances in Petroleum Chemistry and Refining* (eds. Kobe, K.A. & McKetta, J.J.), 157 (Interscience Publishers, New York, 1964).

17. Lin, M.C. & Back, M.H., The Thermal Decomposition of Ethane. Part I. Initiation and Termination steps, *Canadian Journal of Chemistry*, **44**, 505 (1966).

18. Jezequel, J.Y., Barronet, F.& Niclause, M.,La Pyrolyse du Propane a Faible Avancement. 1-Etude Experementale et Mecanisme, *Journal of Chim. Phys.*, **80**, 455 (1983).

19. Wittig, S.L.K., Study of the Thermal Decomposition of n-Butane, *The Physics of Fluids, Suppl. 1*, **12**, 133 (1969).

20. Illes, V., The Pyrolysis of Gaseous Hydrocarbons. V. The Kinetics of the Thermal Decomposition of an Isobutane-n-Butane Mixture., *Acta Chim.(Budapest)*, **72**, 117 1972).

21. Kalinenko, R.A., *et al.* Variation of Reaction Rate Constants with Hydrocarbon Chain Length in the Pyrolysis of Paraffins and Olefins in Different Types of Reactors, *Kinetics and Catalysis*, **24**, 873 (1983).

22. Rumyantsev, A.N., Shevel'kova, L.V., Sokolova, V.M. & Nametkin, N.S. Dependence of the Decomposition Rate Constant of Higher n-Paraffins Hydrocarbons on Their Molecular Weight, *Neftehim*, **20**, 212 (1980).

23. Illes, V., Welther, K. & Pleszkats, I., Pyrolysis of Liquid Hydrocarbons, II Overall Decomposition Rates for Liquid Hydrocarbons, *Acta Chim. Acad. Sci. Hung.*, **78**, 357 (1983)

24. Müller, U.C., Peters, N. & Linan, A.. Global Kinetics for n-Heptane Ignition at High Pressures, *Symp. Int. Comb. Proc.*, **24**, 777 (1992).

25. Satanova, R.B., Kalinenko, R.A. & Nametkin, N.S., Kinetic Relationships in Pyrolysis of Dimethylcyclohexanes, *Kinetics and Catalysis*, **21**, 986 (1981).

26. Zychlinski, W., Bach, G., Glauch, B. & Zimmermann, G. Kinetische Untersuchungen zur Pyrolyse von Mono-n-Alkyl-Cyclohexanen, *J. Prakt. Chem.*, **315**, 66 (1983).

2. Thermal Decomposition of n-Alkanes in Near- and Supercritical Regions (Contributed by Jian Yu and Semih Eser)

Introduction

In previous reports we have presented experimental results from thermal decomposition of *n*-tetradecane in the near- and supercritical regions, using both the tubing bomb [1-3] and glass tube reactors [4]. It was found that the experiments with the tubing bomb reactor gave underestimated rate constants while those with glass tube reactors produced kinetic parameters which were in good agreement with the literature values for thermal decomposition of long-chain alkanes. The erroneous kinetic parameters obtained from tubing reactor data result from uncontrolled mixing in the reactor which includes a top stem with lower temperature.

In present work the thermal decomposition studies using glass tube reactors were extended to two other model compounds of petroleum-derived jet fuels: *n*-decane and *n*-dodecane. Also, a comparison was made between the results from the tubing bomb and glass tube reactor experiments for *n*-tetradecane. Since the glass tube was not completely evacuated before sealing, small amounts of oxygen remain in the sealed tube. It is desirable to know the effects of oxygen on thermal decomposition behavior. Therefore, experiments were carried out on *n*-tetradecane in ubing bomb reactors under nitrogen and air atmospheres.

Experimental

The *n*-decane, *n*-dodecane, and *n*-tetradecane, all with 99+% purity, were obtained from Aldrich and were used as received. The thermal reaction experiments of *n*-decane and *n*-dodecane were carried out using the glass tube reactors. The experimental procedures can be found in the previous report [4]. The thermal reaction experiments of *n*-tetradecane under both nitrogen and air atmospheres were carried out using the tubing bomb reactors. The experimental procedures are similar to those used before [1]. The analytical procedures have been discussed elsewhere [4].

Results and Discussion

1. Kinetics of Thermal Decomposition of *n*-Decane and *n*-Dodecane. Kinetic data were obtained from thermal decomposition of *n*-decane and *n*-dodecane at 400, 425, and 450°C for different times. The rate constants were determined by the following first-order expression

$$\ln [1 / (1 - x)] = k\,t \qquad (1)$$

where x is the fraction of the reactant converted, k is the rate constant (h^{-1}), and t is the reaction time (h). A fixed loading ratio of 0.36 was used to obtain reproducible results. The temperatures

and loading ratio were selected suct that the reactants are under supercritical conditions which are of current interest in relation to future jet fuel thermal stability problems.

For three different temperatures (400°C, 425°C, and 450°C), the first-order rate constants k's were obtained from the method of least-squares by plotting $\ln[1 / (1 - x)]$ as the function of t. Figures 10 and 11 show the relationships between $\ln[1 / (1 - x)]$ and t for the thermal decomposition of n-decane and n-dodecane respectively. The straight lines at three different temperatures in both figures indicate that thermal decomposition of n-decane and n-dodecane under supercritical conditions can be represented quite well by the first-order kinetics. From the slopes of the lines in Figures 10 and 11 the first-order rate constants can be obtained. According to these data the apparent kinetic parameters for the thermal decomposition of n-decane and n-dodecane can be calculated using the Arrhenius law as shown in eq 2

$$k = A\, e^{-Ea/RT} \qquad (2)$$

where E_a is the apparent activation energy and A is the preexponential factor. Figures 12 and 13 show the relationships between the rate constant and temperature for the thermal decomposition of n-decane and n-dodecane, respectively. The kinetic data obtained from Figures 10-13 are shown in Table 5 which also includes the kinetic parameters from thermal decomposition of n-tetradecane. The estimated activation energies for three n-alkanes are in good agreement with the value of 60±5 kcal/mol usually observed for the first-order reactions of long-chain alkane pyrolysis [5].

The rate constants shown in Table 5 can been correlated to carbon number in the n-alkane molecule. Figure 14 shows the relationship between the rate constant and carbon number, n, for three different temperatures. From the method of least-squares the following three expressions were obtained corresponding to three temperatures: 400, 425, and 450°C respectively

$$k = 0.00685n - 0.0343\ h^{-1} \qquad (3)$$

$$k = 0.042925n - 0.259\ h^{-1} \qquad (4)$$

$$k = 0.23727n - 1.6201\ h^{-1} \qquad (5)$$

There are two correlations available in the literature for the relationship between the rate constant and carbon number. Tilicheev [6] gave the following correlation for the thermal decomposition of C_{11}-C_{32} hydrocarbons at 425°C and 150 atm. pressure

$$k = (2.3n - 15.6) \times 10^{-5}\ s^{-1} \qquad (6)$$

Voge and Good [7] presented the following expression for the thermal decomposition of *n*-alkanes from C_4 to C_{16} at 500°C and atmospheric pressure

$$k = (n - 1)\,(1.57n - 3.9) \times 10^{-5}\ s^{-1} \qquad (7)$$

Figure 15 shows the relationship between the rate constant and carbon number at 425°C, calculated by eqs 4, 6, and 7. The units of the rate constant from eqs 6 and 7 were converted to h^{-1}. For Voge and Good's correlation, the rate constants at 425°C were calculated using an activation energy of 60 kcal/mol. From Figure 15 one can find that the first-order rate constants calculated by presented correlation fall in the middle between those predicted by Tilicheev and those by Voge and Good. The differences between the rate constants calculated by three methods may be due to the differences in pressure. The pressures used in present work are in the range 50–100 atmospheres which are between the pressure ranges used by Tilicheev and by Voge and Good. It seems that in the pressure range presented here (atmospheric to 150 atm. pressure) the first-order rate constants increase as pressure increases. This is not always the case, as presented below.

2. Effects of Pressure on Conversion. The effects of pressure on conversion were studied in the near- and supercritical regions. The different loading ratios were used to obtain different initial pressures. The experiments were carried out at 425°C for 15 min. For *n*-dodecane the experiments were also carried out at 400°C for 60 min. The last three data points at higher pressure for 15 min run in Figure 17 in the *previous* quarterly report and the experiments with *n*-tetradecane at 425°C for 15 min were repeated. All the experiments with the same compound at the same temperature and run length were finished on the same day to minimize the experimental uncertainty. The flow rate of air in the sand bath was always kept constant and the glass tube reactor was always plunged into the same position in the sand bath. It was expected that the glass tube reached to desired temperature in less than two minutes. (Measurements showed that it took about one minute for a thermal couple probe with a sheath, which has an equivalent volume to the reactor set, to reach 425°C. It was found that the temperature of the bath was very uniform and was always within ±1°C of the desired temperature during the stressing experiments.

Figures 16-19 show the changes in conversion with initial reduced pressure from thermal decomposition of *n*-decane, *n*-dodecane, and *n*-tetradecane under the conditions indicated. The reduced pressure ($P_r = P/P_c$) was calculated at given temperature and loading ratio using Soave-Redlich-Kwong equation of state [8]. The critical temperature and pressure for three compounds are [9]: T_c = 344.6, 385.3, and 419.2°C; P_c = 2.099, 1.810, and 1.573 MPa for *n*-decane, *n*-dodecane, and *n*-tetradecane respectively. It can be seen that pressure has a significant effect on conversion in the near-critical region. For example, for the thermal decomposition of *n*-dodecane at

400°C ($T_r = T/T_c = 1.022$) for 60 min, an increase in P_r from 1 to 1.5 results in a decrease in conversion from ≈5% to ≈3.5%. It seems that the significant changes in conversion fall in the near-critical region and do not extend to farther supercritical region. This can be seen from Figures 16-19 which show that at $P_r > 1.5$ the rate constants only exhibit slight decrease with increased pressure. For *n*-decane there is no large decrease in the rate constant with increased pressure from Pr = 1–1.5 since the reaction temperature is much higher than the critical temperature ($T_r = 1.130$).

There are some literature data about the effects of pressure on the first-order rate constant. Voge and Good [7] observed that the first-order rate constant for the thermal decomposition of *n*-hexadecane at 500°C increased from ≈10 h^{-1} at 1 atm. to ≈28 h^{-1} at 21 atm. Appleby et al. [10] reported that the first-order rate constants for *n*-heptane pyrolysis at 580°C were essentially the same at 1 and 8.71 atm. Fabuss et al. [11] studied the thermal cracking of *n*-hexadecane at temperature range of 1100–1300°F (593–704°C) and found no pressure dependence of the rate constant in the pressure range from 200–1000 psig (13.6–68 atm.). Fabuss et al. [5] reviewed the literature and concluded that for the thermal decomposition of alkanes, the first-order rate constant increases with increased pressure between 1 atm. and about 100–300 atm. pressure. In the low-pressure range the rate constant may double as pressure is increased for about 35–40 atm. It should be mentioned that the above conclusions came from limited literature data and are not necessarily applicable to the other alkanes. For example, the rate constant for the thermal cracking of 2,4,8-trimethylnonane at 371°C decreases from 0.0226 h^{-1} at 17.3 atm. to 0.0150 h^{-1} at 23.0 atm. [5].

From above discussion it can be concluded that the effects of pressure on the first-order rate constant for the thermal decomposition of alkanes are not only related to the structure of compound itself but also dependent upon the temperature and pressure ranges studied. The different or even inverse pressure dependence of the rate constant may be a result for different compound and/or different temperature or pressure range. Figure 19 clearly shows that while the rate constants for thermal decomposition of *n*-tetradecane under supercritical conditions decrease with increased pressure, the contrary may be correct under subcritical conditions.

3. Comparison of the Results Obtained from Glass Tube Reactors and from Tubing Bomb Reactor. In a previous study we have observed that the conversions from tubing bomb reactor experiments are lower than those from glass tube experiments [4]. In this work we conducted comparative experiments using the glass tube reactor and tubing bomb reactor under otherwise consistent conditions. Figure 20 shows the change in conversion with reaction time for these two different reactors. It can be seen that the reaction rates obtained from the glass tube reactor are much larger than those from the tubing bomb reactor. It is felt that the lower reaction rates in the tubing reactor experiments result from uncontrolled mixing in the tubing bomb reactor which includes a top stem with a lower temperature. It is clear that the average temperature of the sample stressed will be lower than the sand-bath temperature and underestimated rate constants will be

obtained from thermal reactions conducted in the tubing bomb reactor with longer top stem. Since it is difficult to correct for the effect of the top stem, the resulting kinetic parameters may be misleading.

Figures 21 and 22 show the changes in n-alkane and 1-alkene composition with carbon number from the glass tube and tubing bomb experiments. Both experiments have similar loading ratio (≈0.36) and similar conversion as shown in the figures. It can be seen that the changes in product distributions with carbon number are sharper from the tubing bomb reactor than from the glass tube reactor. The *n*-C_9 to *n*-C_{13} mole yields are higher and the mole yields of *n*-alkane with carbon number below 8 are lower in the glass tube reactor than the corresponding values in the tubing bomb reactor. The mole yields of all 1-alkene components are lower in the glass tube reactor than in the tubing bomb reactor. These results can also be explained by the lower temperature in the top stem of the tubing bomb reactor. The lower temperature in the top stem results in lower pressure in the tubing bomb reactor than in the glass tube reactor under otherwise comparable conditions. Since the higher pressure favors bimolecular hydrogen abstraction reactions and radical addition reactions, which enhance the yields of *n*-alkanes and correspondingly depress the yields of 1-alkenes, the higher long-chain *n*-alkane yields and the lower 1-alkene yields are observed in the glass tube reactor. The sharper product distribution vs carbon number curves in the tubing bomb reactor can also be attributed to the existence of the low-temperature region in the top stem which results in non uniform distributions of the primary products, and to the significant secondary reactions at higher conversions (≈25%). During the reaction the light primary product will stay longer in the low-temperature region in the top stem and thus undergo fewer secondary reactions while the heavier primary products will mainly stay in the high-temperature region in the bottom reactor body and thus undergo significant secondary reactions. This, of course, will result in the sharper changes in product distribution vs carbon number curves.

4. Effect of Oxygen on Thermal Decomposition. In the glass tube reactor experiments no specific technique was used for complete removal of air in the tube. It is important to know the effect of oxygen on thermal decomposition. In this work the parallel experiments were conducted in tubing bombs under nitrogen and air. The *n*-tetradecane was used as the reactant. Figures 23 and 24 show the product distributions from the thermal reaction of *n*-tetradecane at 425°C for 60 min under both nitrogen and air atmospheres. The figures also show the conversion values. It can be seen that there is no significant difference between nitrogen and air atmospheres in terms of conversion and main product distributions. It should be mentioned that the above conclusion can not be extended to the deposit formation. In fact, the liquid products from different atmospheres exhibit quite different appearances. While the liquid product from nitrogen atmosphere was almost colorless, the liquid from air atmosphere exhibited obvious yellow color with small amount of suspended gum. The presencee of oxygen is expected to enhance the deposit formation [12].

References

1. Schobert, H. H.; Eser, S.; Song, C.; Hatcher, P. G.; Walsh, P. M.; Coleman, M. M. *Advanced Thermally Stable Jet Fuels*. Technical Progress Report (October 1993 - December 1993), January **1994**, The Pennsylvania State University.
2. Schobert, H. H.; Eser, S.; Song, C.; Hatcher, P. G.; Walsh, P. M.; Coleman, M. M. *Advanced Thermally Stable Jet Fuels*. Technical Progress Report (January 1994 - March 1994), May **1994**, The Pennsylvania State University.
3. Schobert, H. H.; Eser, S.; Song, C.; Hatcher, P. G.; Walsh, P. M.; Coleman, M. M. *Advanced Thermally Stable Jet Fuels*. Technical Progress Report (April 1994 - June 1994), July **1994**, The Pennsylvania State University.
4. Schobert, H. H.; Eser, S.; Song, C.; Hatcher, P. G.; Boehman, A.; Coleman, M. M. *Advanced Thermally Stable Jet Fuels*. Technical Progress Report (July 1994 - September 1994), October **1994**, The Pennsylvania State University.
5. Fabuss, B. M.; Smith; J. O.; Satterfield, C. N. *Adv. Pet. Chem. Refin.* **1964**, *9*, 157.
6. Tilicheev, M. D. *Foreign Petro. Technol.* **1939**, *7*, 209.
7. Voge, H. H.; Good, G. M. *J. Am. Chem. Soc.* **1949**, *71*, 593.
8. Soave, G. *Chem. Eng. Sci.* **1972**, *27*, 1197.
9. Teja, A. S.; Lee, R. J.; Rosenthal, D.;Anselme, M. *Fluid Phase Equil.* **1990**, *56*, 153.
10. Appleby, W. G.; Avery, W. H.; Meerbott, W. K. *J. Am. Chem. Soc.* **1947**, *69*, 2279.
11. Fabuss, B. M.; Smith, J. O.; Lait, R. I.; Borsanyi, A. S.; Satterfield, C. N. *Ind. Eng. Chem. Process Des. Dev.* **1962**, *1*, 293.
12. Taylor, W. F. I*nd. Eng. Chem. Prod. Res. Dev.* **1974**, *13*, 133.

Task 2. **Investigation of Incipient Deposition**

Uncertainty Analysis on Growth and Deposition of Particles During Heating of Coal-Derived Aviation Gas Turbine Fuels (Contributed by Prashant C. Sanghani and Andre Boehman)

In the previous report we described the uncertainty analysis for measurements of the kinetics of deposit and particle formation [1]. Measurement of deposit growth and development of a kinetic model to predict the onset of carbon deposition and particle formation will continue. Efforts on refining the deposit growth measurement and characterization of suspended matter in stressed fuels have lead to improvements in the analysis of stressed fuels. The refinements have included: detailed quantification of sources of experimental uncertainty in the analytical equipment; elimination of specific sources of measurement error; and development of more accurate procedures for characterizing suspended matter in the stressed liquid fuel.

The amount of suspended matter in the stressed fuel was measured by a solubility method. Stressed fuel was first mixed with about 10 parts toluene and was allowed to stand in the dark for 10–12 hours and then filtered through 0.1μ filter paper. The amount of toluene insoluble (T.I.) deposit that remained on the filter was obtained by drying the filter paper in a vacuum for 6–8 hours and then reweighing the filter paper and measuring the weight change of filter paper after drying. Toluene was then separated from the filtrate (i.e. mixture of toluene and stressed fuel) by roto-evaporator. The filtrate after toluene removal was mixed with about 100 parts pentane and was allowed to stand in the dark for 8–10 hours. Pentane was used in large amount to ensure that sufficient pentane is always present in the sample in spite of its evaporation. Pentane-insoluble (P.I.) and toluene-soluble solids will precipitate and will settle at the bottom of the container.

The toluene-insoluble (T.I.) part of suspended matter was found to be negligible. However, the toluene-soluble and pentane-insoluble fraction of suspended matter was found to be small but measurable. The graph of total solid formed on the wall and pentane insoluble - toluene soluble (P.I. - T.S.) suspended in the stress fuel versus time is shown in Figure 25. The pentane insoluble - toluene soluble portion is small compared to the total solid formed on the wall. The plot shows that under an ultra high purity N_2 environment deposit formation in the bulk is negligible. As soon as a reactive precursor forms it goes to the wall and reacts immediately with deposit layer there. Since the mass of P.I.-T.S. is very small and the rate of formation and disappearance of P.I.-T.S. is equal, PSSA (pseudo steady state approximation) can be applied [2]. Since deposit formation in the bulk is negligible, the particle size distribution measurement will not be significant in this case. These results are very different from that obtained at Wright Laboratory [3]. However, stressing carried out in pressurized air will form significant particles in the bulk which will be comparable to deposit on the wall [4].

The improved measurement and analysis procedures will be applied to neat jet fuels and mixtures of model compounds with jet fuels both in pyrolizing and oxidizing environments. Enhanced laboratory analysis will provide the basis for a more sophisticated model for fuel decomposition than the simple model previously postulated. The analyses will apply GC/MS measurements of stressed fuel composition using an "internal standard" to quantify species concentration. Statistical analyses will be applied to the chromatographic results to correlate species concentration with deposit formation and growth in the tubing bomb reactor. As much as possible, compounds will be grouped in terms of their degree of correlation with deposit growth. By grouping species in terms of their degree of correlation with deposit formation, the description of the complex fuel chemistry can be simplified to yield a tractable kinetic model which describes the essential features of the deposition process. These features are the induction period where no deposit forms, followed by a steady increase in the rate of deposition for several hours.

The problem with grouping the species is that model parameters will become very sensitive to the type of reactor and the type of fuel. Thus a more general kinetic model should include reaction pathways in terms of several species which can represent the behavior of the fuel rather than lumping the fuel in to several groups. The effects of increasing or decreasing the number of species on the accuracy of the kinetic model needs further investigation.

References

1. Schobert H. H. et al Advanced Thermally Stable Jetfuel, Technical Progress Report, October 1994 - January 1995, 92PC92104-TPR10.
2. S. Eser,*Private Communication* 1995.
3. W. N. Roquemor,*Private Communication* Wright Laboratory, Dayton Ohio, 1995
4. C. Song, S. Eser, H.H. Schobert, Hatcher P. G., Energy & Fuels 1993, **7**, 234-243.

Task 3. Characterization of Solid Gums, Sediments, and Carbonaceous Deposits

1. Effects of Surface Changes and Toluene Extraction of PX-21 Carbon on Thermal Stressing of Model Compounds (contributed by Katia Gergova, Rathnamala Arumugam, and Semih Eser)

Introduction

In our first report on effects of surface chemistry of PX-21 activated carbon we discussed the important role that the surface complexes play during thermal degradation of jet fuel and model compounds. We concluded that the activity of a carbon surface is dependent not only on its surface area but also on the nature of the surface [1]. The outgassing of carbon at high temperatures leads to the removal of chemisorbed oxygen and creates active sites for free radical reactions.

In this report, we present additional data on the effects of carbon surfaces on degradation reactions of model compounds. It is expected that the carbonaceous solid deposited on the surface of activated carbon during thermal stressing will also affect the degradation reactions. Carbonaceous overlayers have always been associated with catalytic poisoning but it seems that, in some cases, they can have catalytic activity. There is some evidence reported in the literature that carbon deposited on a catalyst surface is also catalytically active [2]. For example, some hydrogenation reactions are catalyzed by carbon overlayers [3].

It is possible that the small amounts of aromatic and/or PAH contaminants in the activated carbons are released from the activated carbon structure into the jet fuel mixture during thermal stressing. When activated carbons were extracted with benzene and the PAH were separated with chromatographic methods, it was confirmed that fluoranthene and benzofluoranthene were present in small quantities [4].

In this study we investigate the effect of carbonaceous deposit overlayer on PX-21 surfaces and the removal of aromatic and PAH contaminants from PX-21 carbon on the thermal degradation of model compounds dodecane and decalin.

Experimental

Thermal stressing experiments were carried out on 10 mL dodecane mixed with 5% decalin and 100 mg PX-21 at 425°C. The outgassed and original PX-21 carbon were used for this set of experiments and were, as a preliminary step, stressed with dodecane + 5% decalin at 450°C. The second set of experiments were carried out on 10 mL dodecane + 5% decalin and 100 mg PX-21 extracted with toluene for 24 h. In all experiments the 10 mL dodecane +5% decalin alone were stressed for comparison.

The *n*-dodecane and *cis/trans* decalin used as a model compounds were purchased from Aldrich Chemical Company and PX-21 was obtained from Amoco Carbon Company.

Gas chromatography (GC) of liquid products obtained after stressing experiments was conducted on a Perkin-Elmer 8500 GC with DB-17 fused silica capillary column. Relative percentages of the components were calculated. The liquid products were qualitatively analyzed using Hewlett Packard GC with mass detector.

The thermogravimetric analysis (TGA) were done on a Mettler TA 4000 system using 200 ml/min N_2 flow. The temperature in TGA experiments was increased from 30 to 1000°C at 10°C/min. The microstructure of the PX-21 carbon after stressing with dodecane +5% decalin was analyzed using a polarized-light microscope (Nixon-Microphot-FXA) and a scanning electron microscope (SEM) ISI model SX-40A.

The extraction of PX-21 carbon was carried out in Soxhlet apparatus using 300 mL toluene and 5 g sample. Spectrochemical determination of Ni and V in PX-21 activated carbon was conducted using Atomic Emission.

Results and Discussion

Study of solid deposit produced from thermal stressing of model compounds at high temperature (500°C) A mixture of 10 mL dodecane + 5% decalin was stressed at 500°C for 1h with and without PX-21 in order to study the deposit formation at this high treatment temperature. Samples of original PX-21 and PX-21 outgassed at 900°C for 2h in N_2 were used.

Figure 26a,b shows the polarized-light micrographs of PX-21 stressed with dodecane + 5% decalin at 500°C for 1h. Figure 26 suggests that the deposit formed with PX-21 particles was produced by liquid phase carbonization after initial nucleation in fluid phase. The microscopic examinations of PX-21 surfaces showed that there is considerably higher amount carbonaceous solid deposited with the original PX-21 (Fig.26a) than with the outgassed PX-21 (Fig. 26b), which is in agreement with our previous results [1]. The high-magnification micrograph shown in Figure 26c shows the microstructure the deposit formed on the reactor walls during thermal stressing of dodecane and 5% decalin at 500°C for 1h, with similar structural features as those of the solids found with activated carbon particles.

Effect of carbonaceous overlayer on the degradation reactions of model compounds. Dodecane + 5% decalin with and without 100 mg PX-21 were stressed at 425°C for 1h. We used the color of the stressed liquids to compare the degrees of degradation of dodecane in different experiments. The samples stressed with PX-21 are lighter in color than the sample stressed without PX-21, and the liquids stressed with outgassed carbons are lighter compared to the liquids stressed with original PX-21.

GC and GC/MS analysis of the liquids showed that the concentration of all compounds identified vary insignificantly for all the liquids analyzed except for the concentration of dodecane, hexane, and naphthalene. Figure 27 shows the concentration of dodecane after thermal stressing experiments. One can see that dodecane concentration is lowest for the liquid stressed without carbon and highest for the liquid stressed with used PX-21. The presence of outgassed PX-21 leads to higher concentration of dodecane than the original PX-21. However, the outgassed used PX-21 did not show better activity than outgassed PX-21. From Figure 27, the effectiveness of PX-21 to suppress thermal degradation of dodecane + decalin can be classified in order:

1. used PX-21 (stressed previously with dodecane+5%decalin)
2. outgassed PX-21
3. original and outgassed used PX-21 have almost the same concentration of dodecane.

Figure 28 shows the concentration of hexane in the same liquids. It should be noted that hexane concentration decreases when original PX-21, used PX-21, and outgassed PX-21 are present. However, there is a sharp increase of hexane concentration in the liquid obtained from stressing of dodecane + decalin + 10 mg outgassed used PX-21.

Figure 29 shows the concentration of naphthalene in the analyzed liquids. One can clearly see that the addition of used PX-21, original and outgassed, leads to considerable decrease in the naphthalene concentration. In our previous work, the liquid obtained from stressing with outgassed carbon showed lower naphthalene concentration than the liquid obtained in the presence of original carbon. The liquid obtained from thermal stressing of dodecane + 5% decalin has lower naphthalene concentration than the liquid stressed with original PX-21 because of the active sites of PX-21 carbon which contribute to the H transfer from decalin to naphthalene. The *cis*- and *trans*-decalin area percent of all five samples are listed in Table 6. The liquids obtained from stressing of outgassed and outgassed used PX-21 have very close decalin concentration, as well as the liquids obtained from original used PX-21. The only noticeable difference in the decalin concentration is between the liquid stressed without PX-21 and the liquid stressed with original PX-21, probably because of the active surfaces of PX-21 as we mentioned above.

These results suggest that important changes take place on the surface of outgassed and used PX-21 compared to the original PX-21 during thermal stressing. The increase of the surface activity of the outgassed samples introduced by higher dodecane concentration in the stressed liquid was attributed to higher number of active sites which were not available before outgassing the carbon [1].

In our present study, we determined that the concentration of dodecane in the liquid obtained after thermal stressing of dodecane + decalin + used PX-21 is higher than in the liquid obtained from stressing with outgassed PX-21. It was shown [5] that if there is some oxygen in the system it could react with the carbonaceous overlayer to form quinone-like structures that

appear to be the active species. This was confirmed by studies over carbon and charcoal catalysts [6,7]. In the absence of gas-phase oxygen, reaction proceeds until surface oxygen groups were removed. It would be of considerable interest to relate overlayer activity with specific surface groups. However, the difficulty of analyzing surface groups make the correlation also difficult.

The SEM micrographs of original PX-21 and outgassed PX-21 after thermal stressing with dodecane + decalin showed that there is no carbonaceous deposit on the surface of outgassed sample. After the outgassed PX-21 was once used during thermal stressing, its activity decreases because the amount adsorbed liquid from dodecane + decalin mixture blocks its active centers.

The naphthalene concentrations of the liquids obtained after thermal stressing of dodecane + decalin in the presence of used PX-21 and outgassed used PX-21 are very low (0.6%, Figure 28). This is an indication that there are no active sites on the used carbon surfaces similar to these on the original carbon surfaces to promote H transfer reactions. Most probably they are blocked either by oxygen surface groups or adsorbed hydrocarbons compounds produced during thermal degradation of dodecane.

Figure 30 shows the TGA of used PX-21 after thermal stressing with dodecane + 5% decalin at 425°C for 5h (Fig.30a) and PX-21 outgassed used after thermal stressing with dodecane + 5% decalin at the same heating conditions (Fig. 30b). Figure 30 shows that used carbon adsorbed less liquid (< 20%) during thermal stressing compared to the original PX-21 and outgassed PX-21 (< 32%) (Figure 41a,b from previous report). This is to be expected because the active centers have been blocked during first thermal stressing of the carbon as we mentioned above. Figure 30 also showed that used PX-21 adsorbed 7% more liquids during thermal stressing than the outgassed and used sample (Fig.30b). This can be explained by the release of the oxygen functional groups from the carbonaceous overlayer during heating up to 1000°C in N_2.

Microstructure of the used PX-21 after thermal stressing with dodecane + 5% decalin at 425°C for 5h. Figure 31a,b shows the scanning electron micrographs of used PX-21 (Fig. 31a) and outgassed used PX-21 (Fig. 31b) after thermal stressing with dodecane + decalin at 425°C for 5h. The features of the carbonaceous deposit on the PX-21 surface can not be clearly seen because of low magnification. However, the microstructure in micrograph 31a is somehow smoother and small needle-like particles can be observed. On the other hand, the microstructures in micrograph 31b are much rougher and the characteristic features of PX-21 carbon can be clearly distinguished. These micrographs suggest the coverage of the surface of used PX-21 carbon by carbonaceous deposit together with separate, large carbonaceous particles which were not observed on the surface of the used outgassed PX-21 carbon.

The higher magnification micrographs on Figure 32a,b show the microstructures on PX-21 surfaces more clearly. The micrograph 32a, which represents the used PX-21 is characterized by small round grains which are located under thin carbonaceous film. The most striking feature,

however, is the presence of carbon filaments or fibers (seen as needles in Figure 31a) which appear to originate from the thin film deposited on the activated carbon. These vapor-grown filaments are usually formed on metal substrates at substantially higher temperatures (8,9). The structure and composition of these filaments, and whether their formation is associated with trace metals (Ni and V) present in the activated carbon, will be investigated. Figure 32b shows the same protuberances on the carbon surfaces these in Figure 32a but they are not covered with a carbonaceous overlayer.

The higher magnification micrographs on Figure 33a,b of the PX-21 carbons show the same visual characteristics as these on Figure 31a,b and 32a,b. It is interesting that the overlayer which covers the used PX-21 surface have porous structure (Fig. 33a). The long tubular carbonaceous solid is situated on this overlayer and obviously was formed during the second thermal stressing of the used carbon. The used and outgassed PX-21 has a rough structure and the individual features are very small. No carbonaceous deposit can be seen on the surface of the used and outgassed PX-21 after thermal stressing with dodecane + decalin at 425°C for 5h (Fig. 33b).

Effects of extracted PX-21 on thermal stressing of model compounds at 450°C. In order to improve the activity of PX-21 and investigate the effect of trace metals, such as Ni and V in the carbon during thermal stressing, the PX-21 was analyzed spectrochemically. The amount of Ni determined was 0.02% and the amount of V was even smaller < 0.01% which indicates that probability of metal catalysis of degradation reactions is low. Furthermore, we conducted toluene extraction of 5g PX-21 for 24h. The extract was condensed and analyzed using GC and GC/MS. The following aromatic compounds were determined in the toluene extract: C_3-benzene, benzaldehyde, C_4-benzene, indene, tetralin, naphthalene and C_2- biphenyl. All the compounds identified were found in very low concentrations. We stressed model compounds dodecane + 5% decalin at high temperature (450°C) with original and extracted PX-21 in order to determine the effect of the aromatic compounds identified in the extract on the carbon activity.

Figures 34, 35, and 36 show the concentration of *n*-alkanes from C_4 to C_{11} identified in the liquids obtained from thermal stressing of dodecane + 5% decalin with original and extracted carbon at 450°C for 0.5h, 1h, and 2h, respectively. The area percent of dodecane in the analyzed liquids after thermal stressing is also listed in the right corner of the Figures. There is a striking difference in the concentration of dodecane in the liquids obtained from thermal stressing of dodecane + 5% decalin +100 mg original PX-21 and dodecane + 5% decalin + 100 mg extracted PX-21 at 450°C for 0.5 and 1h. This difference is 10% for 0.5h and 19% for 1h in the benefit of the liquids obtained from stressing in the presence of extracted PX-21. There is also a considerable difference in the concentration of *n*-alkanes from C_4 to C_{11} formed as a result of thermal decomposition of dodecane during stressing experiments. The liquid obtained from stressing of dodecane + decalin in the presence of original PX-21 have higher concentrations of the above-

mentioned alkanes. However, Figure 36 shows that these differences decline with the increasing stressing time to 2h and there is only 2% difference in dodecane concentration; the concentrations of alkanes are very similar, except for pentane which has 1.5% higher concentration in the liquid obtained from stressing with original PX-21. We conducted the same thermal stressing experiments for 3 and 5h but there was no difference in the concentrations of alkanes, i.e. the effect of toluene extraction to suppress thermal degradation processes diminished with the increasing thermal stressing time. These data suggest that the aromatic contaminants in PX-21 , even in these small concentrations, play an important role during thermal stressing at high temperatures at the beginning of the thermal stressing experiments. Although the high surface area of PX-21 carbon and its high activity in preventing solid deposition was proved, the aromatic contaminants most probably initiate decomposition reactions. These data can explain the contrary effects of the presence of PX-21 during thermal stressing which were observed in some of our previous studies.

Figure 37 shows the TGA of extracted PX-21 (Fig. 37a) compared to the TGA thermogram of original PX-21 (Fig.37b). The weight loss for both samples is 33% during heating up to 1000°C. After the initial weight loss up to 100°C for the original carbon which is due to the water weight loss (Fig. 37a), there is a continuous weight loss up to 1000°C. The sharp weight loss (15%) of the extracted sample (Fig. 37b) up to 300°C is probably due to the toluene adsorbed during extraction. Obviously, the different activity that original and extracted PX-21 showed during thermal stressing at 450°C is not a result of different amount oxygen functional groups on the carbon surfaces as we observed for the original and outgassed samples.

Figure 38a,b shows the TGA curves for the original and extracted PX-21 after thermal stressing with dodecane + 5% decalin at 450°C for 2h. The weight loss for both samples is 19%. The curves practically coincides which is an indication that the samples adsorbed equal amount of liquids during thermal stressing. Therefore, their different performance is due to the removal of the organic contaminants from the extracted PX-21 carbon.

The microstructure of the original and extracted PX-21 after thermal stressing with dodecane + decalin at 450°C was examined by polarized-light microscopy. Figure 39a,b shows the polarized-light micrographs of original PX-21 (Fig. 39a) and extracted PX-21 (Fig. 39b) after thermal stressing. Long and thin flakes can be clearly seen in the micrograph are formed during thermal stressing and the carbonaceous deposit was produced in the gas phase. It looks like they are not formed on the carbon surfaces but somehow associated with the activated carbon particles. The micrograph of the extracted PX-21 after thermal stressing (Fig. 39b) does not show any carbonaceous deposit. The higher magnification micrographs of the same carbons (Figure 40a,b) shows individual small deposit particles (Fig. 40b) mixed with extracted PX-21. However, the comparison of the micrographs 40a and 40b is a clear indication that considerably smaller amounts

of carbonaceous deposit have been formed during thermal stressing of dodecane + decalin in the presence of extracted PX-21, compared to the original PX-21. No carbonaceous deposit was found on the reactor walls after stressing experiments in the presence of original or extracted carbon. The difference is in the amount solid deposition associated with PX-21 carbon particles.

Conclusions

The optical microscopy showed that considerably higher amounts carbonaceous solid are associated with the original PX-21 than with outgassed PX-21 after thermal stressing at 500°C for 1h.

There is some evidence that the carbonaceous overlayer formed on the PX-21 surface after thermal stressing of model compounds dodecane + decalin can inhibit further deposition more effectively than the original PX-21. Surface oxygen complexes, formed on the carbonaceous overlayer appear to be the active species during thermal stressing. Unlike the case of oxygen functional groups on the surface of original activated carbon, the deposit overlayer renewed the activity of the carbon. The TGA experiments show that the used activated carbon appears to adsorb less liquid during thermal stressing than the original PX-21. This is a very important feature of the used carbon if it is applied to prevent solid deposition and stabilize jet fuel during thermal stressing.

SEM micrographs of the activated carbon stressed subsequently with dodecane and decalin mixtures show unusual carbon filaments (or fibers) which appear to originate from a carbonaceous overlayer formed during the first stressing. The formation of carbon filaments on activated carbon surfaces at relatively low temperatures used in this study (425°C) has not been reported in the literature.

It was found that the PX-21 carbon contains of Ni and V as trace metals (0.02% and 0.01%, respectively) which are not expected to exhibit strong catalytic effects during thermal stressing. However, the extraction of PX-21 with toluene proved the presence of some aromatic hydrocarbons which possibly diminish the activity of PX-21 during thermal stressing. The comparison of the alkane concentration in the liquids obtained from thermal stressing of dodecane + decalin in the presence of extracted and original PX-21 showed that dodecane concentration of the liquid produced after thermal stressing at 450°C for 0.5 and 1h in the presence of extracted PX-21 is considerably higher than that obtained with the original PX-21. The concentration of short-chain alkanes is also lower in the liquid obtained after thermal stressing in the presence of the extracted carbon. This differences diminished when longer stressing time was applied. The optical microscopy showed more carbon deposition in the presence of the original PX-21 compared to that produced with the extracted PX-21.

References:

1. H. H. Schobert, S. Eser, C. Song, P. G. Hatcher, A. Boehman, M. M. Coleman, Advanced Thermally Stressed Jet Fuels, Technical Progress Report, 92PC92104-TPR-6, October-December 1994.

2. D. L. Trimm, Catal. Rev. Sci. Eng. **16**, 155, 1977.

3. M. C. Gardner and R. S. Hansen, J. Phys. Chem. **74**, 3298, 1970.

4. J. Borneff, Activated Carbon Adsorption of Organics from the Aqueous Phase, Vol 1, edited by J. H. Suffet and M. J. McGuire, Ann Arbor Science Publishers, Inc., Ann Arbor, MI 1980.

5. T. G. Alkhazov and A. G. Lisovskii, Kinet. Catal. **17**, 375, 1976.

6. A. E. Lisovskii, A. L. Kozharov, Yu. A. Ismailov, and T. G. Alkhazov, Kinet. Catal. **19**, 76, 1978.

7. T. G. Alkhazov, A. E. Lisovskii, and T. K. H. Gulakhmedova, React. Kinet. Catal. Lett., **2**, 189, 1979.

8. T. Koyama, Carbon **10**, 757, 1972.

9. G. G. Tibbetts, Appl. Phys. Lett. **42**, 666, 1983.

2. Catalytic Effects of Carbon Surfaces in Organic Reactions-A Literature Review(Contributed by Philip H. Chang)

Introduction

Apart from being known as adsorbents and catalyst supports, solid carbons have been known to catalyze many reactions (e.g., decomposition of hydrogen peroxide and oxidation of oxalic acid) for a rather long time [1,2]. However, less known are the catalytic effects in some organic reactions such as substitution and isomerization. In this section of the report I have attempted to summarize the literature on known organic reactions that are catalyzed by various carbons, and compare the catalytic activities of carbons with those of other catalysts. There is a large volume of literature on inorganic reactions catalyzed by solid carbons [3-5]. However, this literature will not be included in this review.

Since the reactions that are catalyzed by carbon are mainly heterogeneous reactions, heterogeneous catalysis and catalysts are discussed briefly in the introduction section.

Catalytic Action.

Catalysis is a kinetic phenomenon; a catalyst acts by providing an alternative reaction path with a lower activation energy. It only affects the rate at which equilibrium is attained, not the thermodynamically determined equilibrium composition of the system. A catalyst must not be consumed in the catalytic process. A catalytic reaction on the surface of a catalyst occurs repeatedly in a sequence of elementary reactions which includes adsorption, surface diffusion, chemical rearrangement of the adsorbed reaction intermediates, and desorption of the products. Chemisorption is a form of adsorption which involves the formation of chemical bonds between reactants and surface atoms. A good catalyst should form chemical bonds of intermediate strength. These bonds should be strong enough to induce bond dissociation in the reactant molecules, but weak enough to allow short residence times for surface intermediates and rapid desorption of the products.

Metal Catalysis.

In metal catalysis, *d*-electrons dominantly contribute to the bonding between atoms and molecules at surfaces. Transition metals are especially good catalysts for reactions involving hydrogen and hydrocarbons. One of the important functions of transition metals in catalytic reactions is the dissociation of diatomic molecules to produce atoms which react with other molecules or reaction intermediates. For hydrogenolysis, the volcano-shaped plot of catalytic activity shows that the catalytic reaction rates peak at the group VIII metals in the periodic table. Studies indicate that large changes in the local density of electronic states at the surface defect sites

correlate with changes in catalytic activity-increasing reaction rates at the steps and kinks [6]. During hydrocarbon reactions, a carbonaceous overlayer with a composition of (H/C)~1 covers the surface of the active metal catalyst. In some cases, this carbonaceous overlayer provides the true active sites for some catalytic reactions (discussed in more detail later).

Acid-Base Catalysis.

Most surface reactions and the formation of surface intermediates involve charge transfer—either an electron or proton. It is common to refer to an oxide catalyst as acidic or basic according to its ability to donate or accept electrons or protons. The electron and proton transfer capability of a catalyst is expressed according to the Lewis and Brønsted definitions. Solid carbon is a great catalyst for redox reactions because of its electron-transfer ability on the surface. Many oxides are excellent oxidation catalysts because they interact with oxygen and other molecules. Oxygen functional groups on the carbon surface also play an important role in many catalytic reactions. Aluminosilicates are solid acids. Most organic molecules are electron donors. Thus, hydrocarbons may be viewed as weak bases that can be protonated by strong acids to form carbenium ions. Tertiary carbenium ions are more stable than secondary ions, which are more stable than primary ions. Therefore, hydrocarbon conversion reactions (isomerization, cracking and alkylation) occur on acids via formation of stable carbenium ions.

Classification of Heterogeneous Catalysts and Carbon Catalyst.

Catalysts are classified by their electroconductivity (see Table 7). It seems difficult to classify solid carbons in a single category included in Table 7. As shown later, carbon behaves not only like metal catalysts but also like oxides and acid catalysts. Even though there is no unique reaction that only carbon can catalyze, it seems that carbon possesses a wide variety of catalytic properties which result from its unique structural and chemical properties. The catalytic reaction mechanisms in the presence of a carbon catalyst are not very different from those associated with a conventional catalyst; either ionic or radical.

Some Organic Reactions Catalyzed by Carbons

Redox Reactions. Since this section only deals with organic reactions, the definition of an organic redox reaction should be made clear. Unlike the definition of reduction and oxidation in inorganic reactions, which is the gain or loss of electrons by atoms respectively, it is often difficult to decide whether atoms gain or lose electrons in an organic reaction. For the purpose of this review, an organic reduction is a reaction that either adds hydrogen or removes an electronegative element (oxygen, nitrogen, or halogen). Conversely, an organic oxidation is a reaction that either adds electronegative elements or removes hydrogen [8].

Hydrogenation-Dehydrogenation: The decomposition of secondary alcohols (propan-2-ol and butan-2-ol) was carried out in the presence of oxidized activated carbon by Szymanski *et al.* [9,10]. Dehydrogenation as well as dehydration occurred under the conditions applied. The products are *cis*- and *trans*-isomers of butene-2 and methylethyl ketone from butan-2-ol decomposition, and di-2-propyl ether, propene and acetone from propan-2-ol decomposition. The authors concluded that the dehydrogenation activity results from the simultaneous presence of Lewis acid and base sites on the carbon, which is very similar to metal oxides in dehydrogenation reactions. The formation of a surface alkoxide is suspected to be the intermediate step for the catalytic dehydrogenation. The introduction of Zn^{2+} or Ni^{2+} ions results in increasing the dehydrogenation activity and selectivity. Figure 41 shows a possible mechanism for dehydrogenation of an alcohol.

Malhotra *et al.* [11] reported catalytic activity of C_{60} in dehydrogenation, bond-cleavage and coupling reactions. They demonstrated the catalytic properties of fullerenes in coal liquefaction and pyrolysis reactions. Their experiments were performed with 1,2'-dinaphthylmethane in aromatic/hydroaromatic solvents at 400°C. For bond cleavage reactions, the addition of C_{60} increased the rate constant from $4.4E^{-6}$ to $10.8E^{-6}$ s^{-1}, and the aromatic to hydroaromatic ratio at the end of the experiment changed from 1.3 to 33 when fullerene was added. The above results represent the catalytic activity of C_{60} in dehydrogenation of hydroaromatics. Thus, the ability of fullerene to shuttle hydrogen atoms in alkylaromatics causes bond cleavage and coupling as well as dehydrogenation. Hydrogen transfer reactions are very important in petroleum refining. Thus, a potential for the use of fullerenes as a catalyst has been demonstrated.

Oxidative dehydrogenation: Carbon molecular sieves (CMS) have also been shown to be very effective catalysts in the oxidative dehydrogenation and dehydration of a variety of substrates due to their novel capability of hydride and hydrogen atom abstractions [12,13]. Oxidative dehydrogenation is superior to direct dehydrogenation because the overall reaction is exothermic due to the formation of H_2O as a byproduct. By using CMS, Grunewald and Drago achieved 80% conversion with over 90% selectivity to styrene from ethylbenzene in a single pass at 350°C. This result is superior to that of an inorganic oxide catalyst (Al_2O_3) and pyrolyzed polyacrylonitrile (PPAN) (see Table 8) [12]. It is evident from this study that the surface area of the PPAN is a very important parameter for catalyst activity; the conversion percentage increased from 11.6 to 22.4 while the surface area of PPAN increased from 8 to 50 m^2g^{-1}. Although activated carbon has a higher surface area than PPAN, its catalytic activity is not superior to PPAN. All the samples studied catalyze via a hydrogen abstraction mechanism. In an inert atmosphere, very little conversion is observed, and after 5 hours there was no formation of products. This is because the catalytic surface is fully hydrogenated and hence no more hydrogen abstraction can occur. The authors concluded that this high catalytic activity results from the ultrahigh surface area,

extraordinary adsorption capability, and 6% oxygen content which is probably similar to the quinone-type moieties likely present in the carbonaceous overlayers on an inorganic oxide catalyst.

The oxidative dehydrogenation and dehydration of alcohol was performed using a CMS catalyst [13]. The activity of CMS for the oxidative dehydrogenation and dehydration of alcohol is shown in Table 9. The mechanisms of both reactions on the inorganic oxide is such that the catalyst either abstracts a hydride via a Lewis site or protonates the alcohol OH via a Brønsted site to produce a carbocation or a protonated alcohol followed by loss of a proton from the former moiety to generate the aldehydes or loss of water and a proton to generate the alkenes. The products indicate that a typical Lewis acid catalysis mechanism via the formation of a carbocation species is involved

There is evidence in some cases that the carbonaceous overlayers on the inorganic and metal oxide catalysts are the true active sites for the catalytic reactions [14-16]. Carbonaceous materials are deposited on the surface of a catalyst during the catalytic reactions. Some deposits deactivate the catalyst whereas others promote the chemical reaction. The conversion of ethylbenzene to styrene in the presence of alumina (a typical dehydrogenation reaction by inorganic oxide catalysts) is an example of a reaction catalyzed by the active coke layer on the oxide catalyst [14,15]. This catalyst system has an induction period for forming a thin uniform layer of carbon provided by acid-base properties of the oxide catalyst, and the coke deposited has a high content of oxygen, suggesting that the presence of electronegative groups (quinoid type oxygen) is important. Thus, the reaction might occur by means of a redox-type mechanism. In metal catalysts, this overlayer may play a role in restructuring the surface to create new active sites and in altering the bonding of reactants, intermediates, and products [6]. Galuszka *et al.* [17] identified at least five different forms of carbonaceous materials (aliphatic, aromatic, oxygenated, carbidic, amorphous) on the surface of the oxide-supported iron catalyst.

Hydrodehydroxylation and Hydrodehalogenation: Farcasiu *et al.* [18] performed hydrodehydroxylation and hydrodehalogenation of substituted polycyclic aromatics. In this work, carbon black was found to catalyze dehydroxylation and dehalogenation reactions of aromatic compounds only in the presence of a hydrogen donor, the reactions being initiated by hydrogenation through hydrogen transfer from a donor solvent, which is the first step for both reactions. The degree of dehalogenation and dehydroxylation in various substituted aromatic compounds is increased with an increase in the size of the aromatic system and depends upon the nature of the substituent (see Table 10). For example, the bromo-derivatives are more reactive than the chloro-derivatives in the same aromatic system. Figure 43 depicts the results of catalytic conversion when carbon black was used as a catalyst.

Oxidation: Various kinds of organic chemicals from hydrocarbons to acids can be oxidized in the presence of solid carbons. The oxidation of cyclohexene in the presence of activated carbons

and carbon blacks was performed by Tomita *et al.* [19]. Cyclohexenone and cyclohexenol were the main products. At an early stage in the reaction, surface free radicals, C•, were the active sites for oxidation, and the free radical on the carbon surface was also involved at the stationary stage. This radical mechanism is very similar to the action of metal ion catalyst for the oxidation of hydrocarbons. The authors also found that basic oxides are associated with catalytic activity.

The catalytic oxidation of mercaptans to disulfides by activated carbon in aqueous suspensions has been reported [20]. The catalytic activity is reduced drastically by outgassing. Two possible mechanisms were proposed: participation of quinone groups and/or metal ions on the surface of carbon. The quinone group mechanism illustrated the disulfide formation via a redox reaction involving the formation of thiol radicals and semiquinone anions. Other metal ion mechanisms are well known for oxidation of hydrocarbons. The authors finally concluded that both quinone group and metal are involved in the catalytic activity of carbon for oxidation of mercaptan.

The oxidation of methanol was carried out in the presence of activated carbon by Stohr and Boehm [21]. The product was formaldehyde. An adsorbed molecule, O_2, can be activated by electron transfer from the carbon surface:

$$O_2 + e^- \text{ Æ } O_2^-, \quad O_2^- + e^- \text{ Æ } 2O^-$$

Then, atomic oxygen attacks the alcohol to produce formaldehyde.

Rideal and Wright showed that an aqueous suspension of sugar charcoal catalyzed the oxidation of oxalic acid [2]. They also studied the influence of nitrogen and iron on carbon's catalytic activity for the oxidation of oxalic acid. When both iron and nitrogen were incorporated into the carbon, the iron-carbon-nitrogen complex enhanced the catalytic activity 800 times that of the original carbon. The mechanism for the oxidation of oxalic acid by chromene-like structure on the carbon surface was proposed. Oxalic acid was also oxidized catalytically in the presence of activated carbon to produce CO_2 [22]. Heat treatment of the carbon enhanced the catalytic activity, whereas the presence of organic molecules like phenol slowed the catalytic oxidation reaction. The authors concluded that the anionic reducing species were adsorbed by basic surface oxides and then oxidation occurred with the adsorbed oxygen.

Substitution Reactions. *Halogenation:* Puri and Bansal studied the chlorination of toluene in the presence of sugar and coconut charcoals [23]. In the presence of the charcoals, toluene was chlorinated to benzyl chloride and benzoyl chloride. It was found that the catalytic activity of charcoals correlated with the hydrogen content of the carbons. It was suggested that the chemisorbed hydrogen atoms in the charcoal react with a molecule of chlorine, producing atomic chlorine, which then attacks the hydrocarbons.

Hydrolysis: The alkaline hydrolysis of benzyl acetate was carried out by Spiro [24].

$PhCH_2OOCCH_3 + OH^- Æ PhCH_2OH + CH_3COO^-$

Various carbons were added to reaction mixtures. Carboliac 1 carbon black increased the rate six-fold, whereas addition of graphitised Black Pearls carbon decreased the hydrolysis rate. These different results originate from the different structures and specific surface areas, the presence of quinonoid and other functional groups and the ability of carbons to adsorb hydroxide ions as well as aromatic molecules.

Solvolysis: Carbon black catalyzed solvolysis of a phosphate ester was performed by Hayano and Pincock [25].When methyl phosphate ester is present with monoethylether, diethylene glycol and a variety of different carbons, a loss of optical activity increased ten-fold due to solvolysis. The product of solvolysis of ester is 1,1'-bi-2-naphthol. The heterogeneous reaction of the suspended carbon particles is involved in the more rapid loss of ester. The deactivation also showed up due to the fact that some active sites on carbon might be covered up and inactivated by transfer of the phosphate group from naphthyl to the carbon surface. Unlike the catalytic effect of carbon in the racemization of 1,1'-binaphthyl, which was inhibited by naphthalene due to covering up of the graphitic basal plane, the catalysis by carbon of this phosphate ester solvolysis is not inhibited by naphthalene. The authors concluded that the acceleration of rate of solvolysis of the phosphate ester is due to acidic and/or basic nucleophilic functional groups on the carbon surface.

Addition-Elimination Reactions. *Dehydration:* The catalytic dehydration of alcohol promoted by oxidized activated carbon was reported by Szymanski *et al.* [9,10]. The treatment of carbon with $NaHCO_3$ made the dehydration activity of the oxidized carbon disappear. It was concluded that the dehydration activity results from the presence of carboxyl groups of various strengths on the surface. It is also suspected that the reaction occurs via carbenium ion intermediates. The treatment of metal ions with carbon changes the dehydration activity caused by the ion exchange of hydrogen ions with metal cations. It is suggested that the oxidized carbon behaves as a strong solid acid because the only products from the dehydration of butan-2-ol are cis- and trans- isomers of butene-2. A possible mechanism of alkene and ether formation from the dehydration of propan-2-ol is shown in Figure 43.

The dehydration of alcohol by CMS was also reported [13]. Dehydration as well as dehydrogenation occurred in the presence of ultra high surface area CMS. The mechanism for both reactions is similar to that of inorganic oxide catalysts.

Polymerization: Catalytic polymerization of alkenes (2-methylpropene and 2-methyl-2-butene) was reported, following the same carbocation mechanism that was responsible for the isomerization reaction as well [26]. The oligomer mixture was obtained after a while, and chromatographic analysis showed that dimeric oligomers predominate in the mixture. The cationic mechanism for the dimerisation of 2-methylpropene is given in Fig. 44.

The polymerization of N-vinylcarbazole in the presence of carbon black was also reported [27]. Solvents with higher dielectric constants increased the degree of conversion, and the cationic mechanism may be responsible for polymerization by carbon black surface. The addition of 2,2-diphenyl-1-picrylhdrazyl (DPPH) to the reaction mixture showed an inhibition since DPPH abstracts hydrogen atoms from phenolic hydroxyl groups. The authors concluded that the cationic mechanism of polymerization of N-vinylcarbazole was initiated by the phenolic hydroxyl groups on the surface of carbon black.

Hydrogen halide elimination: Boehm and coworkers reported the dehydrohalogenation of alkyl halide by using various carbons, especially activated carbon [21,28,29]. Treatment of carbon with ammonia or incorporation of nitrogen increased the catalytic activity drastically. The substitution of carbon by nitrogen atoms at the edges of the carbon sheets was also proposed. An explanation would be that the extra electrons go to the conduction band and make transfer to the adsorbed species easier. Not only the presence of alkenes, but the fact that the dimerization product of the alkyl radicals was found in the products supported the radical mechanism:

$$R\text{–}X + e^- \text{ Æ } X^- + R\bullet \;;\quad R\bullet \text{ Æ } R'\text{–}CH{=}CH_2 + H^+ + e^-$$

Treatment with ammonia and nitrogen induced the formation of amino groups and pyridine-like groups which are basic, and these basic surface groups might play a substantial role. Thus, a base-catalyzed mechanism was also considered.

Molecular Rearrangement. *Racemization:* Hutchins and Pincock demonstrated the heterogeneous catalytic racemization of 1,1'-binaphthyl and 4,4'-disubstituted 1,1'-binaphthyl by carbon blacks and active carbons, respectively [30,31]. Increasing the number of functional groups on the surface did not affect the rate of racemization. They also found that the bromination and chlorination of a carbon increased catalytic activity, and all substituted molecules are less sensitive to catalysis due to a steric effect. Activity of carbons in the catalyzed racemization reaction increases with the surface area of carbons (relative catalytic order is Acetylene Black < Spheron 6 < Norit < Carbolic 1). There is no relationship between catalytic activity and the surface pH value of carbons.

The catalytic activity of carbon can be inhibited or poisoned by unsubstituted aromatics. The inhibition effect increases with the size of aromatics (benzene << naphthalene < anthracene < pyrene < perylene). High concentrations of 1,1'-binaphthyl itself could be an inhibitor in the catalytic racemization.

The authors assumed that the transition state of rotation was planar electron-accepting molecules loosely bound on electron-donor sites of the graphitic planes of the carbon. The inhibition effect of large aromatics can be explained by the fact that all graphite-like surfaces are occupied by aromatics due to adsorption. In addition, racemization might be promoted by electron transfer to binaphthyl since carbon blacks can act as reducing agents as well as oxidizing agents.

Isomerization: Catalytic isomerization of alkenes by carbon has also been reported [26,32,33]. Isomerization of C_4, C_5, and C_6 alkenes and a-olefins by carbon black was performed [33]. Lower carbonization temperatures increased the content of oxygen on the surface of carbon and oxidation of the blacks caused an increase in the acidity, thereby the catalytic activity increased. The pre-exponential factor and activation energy for isomerization were changed extensively upon oxidation of carbon blacks. In the runs 2 and 5 in Table 11, which had the same duration of oxidation with different oxidation temperatures, indicated an increase in the rate constant and a decrease in activation energy for the carbon blacks oxidized at lower temperatures. Runs 3,4, and 5 in Table 11, which had the same oxidation temperature with different oxidation times, suggested that the sites of greatest activity are being removed or converted to less active sites while the number of sites are being created, indicated by a concurrent increase in pre-exponential factors (see Table 11). Thus, not all acidic surface groups are active for isomerization; only a small fraction of acidic groups can promote the reaction. An ionic mechanism in which alkene isomerization occurs over common acidic catalysts like silica-alumina was proposed. It was concluded, in general, that protonation of the alkene by an acidic group of the carbon surface formed an adsorbed saturated alkyl carbenium ion.

Other Reactions. The decomposition of benzoyl peroxide in organic solvents is catalyzed by carbon blacks [34]. Benzoyl peroxide breaks into two radicals first, then these radicals abstract hydrogen from the solvents to produce benzoic acid. Other radicals on the surface break down into CO_2. The extent of decomposition is proportional to the surface area of the carbon blacks, but independent of the nature of the surface in this case.

The decomposition of 4-(1-naphthylmethyl)bibenzyl using carbon blacks was carried out by Farcasiu and Smith [35]. A high surface area carbon black (Black Pearls 2000) was most effective in terms of catalytic activity and selectivity. It was found that the surface of carbon black became positively charged at 320°C where catalytic decomposition started without thermal reaction (see Table 12). Therefore, they concluded that the mechanism involved a cation radical species that gave up an electron to the positively charged carbon black surface because the removal of an electron from the molecule to form a cation radical species accelerates the bond cleavage.

The conversion of methane to other hydrocarbons is also catalyzed by carbon [36]. Decomposition of methane on the carbon film produced forty times more ethane and ethylene than when this process was carried out on the quartz surface. It was suggested that the catalytic dissociation of methane on the carbon increased the rate. A free radical mechanism was proposed for the formation of ethane and other hydrocarbons by adsorbed methyl radicals reacting on the carbon film surface or desorbed methyl radicals reacting in gas phase. The mechanism for the formation of ethane may be written as follows:

$$CH_4 + 2C(s) \text{ Æ } CH_3\text{–}C(s) + H\text{–}C(s)$$

CH_3–C(s) Æ CH_3 + C(s)

H–C(s) Æ H + C(s)

CH_4 + M Æ CH_3 + H + M

H + CH_4 Æ H_2 + CH_3

2CH_3 Æ C_2H_6

H + C_2H_6 Æ H_2 + C_2H_5

C_2H_5 Æ C_2H_4 + H

The production of dichloromethane from phosgene and formaldehyde was carried out in the presence of the activated carbon by Ryan and Stacey [37]. The reaction mechanism involves the intermediate, chloromethyl chloroformate, which is normally present in small amounts and strongly adsorbed on the carbon. The rate-determining step is the formation of this ester. The following sequence is therefore proposed for the main process:

$CH_2O(g)$ <--> $CH_2O(a)$

$COCl_2(g)$ <--> $COCl_2(a)$

$CH_2ClO{\cdot}OCOCl(g)$ <--> $CH_2Cl{\cdot}O{\cdot}COCl(a)$

CH_2Cl_2 <--> $CH_2Cl_2(a)$

and the surface reactions are:

$CH_2O(a) + COCl_2(a)$ <--> $CH_2Cl{\cdot}O{\cdot}COCl(a)$ (RDS)

$CH_2Cl{\cdot}O{\cdot}COCl(a)$ --> $CO_2(g) + CH_2Cl_2(a)$

The catalytic activity proposed involved several types of polar surface groups with acid-base properties.

Summary of Reactions.

As shown above, carbon clearly demonstrates the ability to promote a variety of catalytic reactions. Table 13 is a summary of reactions where carbon is employed as a catalyst and also shows the responsible sites on the carbon surface and the proposed mechanism for the corresponding reactions. Carbon catalysts behave either like metal catalysts[19,20] or acid catalysts[11,26,32,33]. The responsible sites and capabilities can be categorized into several areas independent of carbon type: surface functional groups such as oxygen functional groups, electron donor sites, carbocation mechanism, etc. Sometimes the same reaction can be explained by a different mechanism. For example, oxidation of cycloalkene and mercaptan can be explained by a free radical mechanism [19,20] whereas oxidation of alcohol proceeds via an ionic mechanism [21]. Different active sites were responsible for the same reaction with different reactants[12,13,19,20]. The ionic mechanism is dominant for both polymerization and isomerization[26,27,32,33] whereas decomposition reactions occur via the radical mechanism

[34,35,36] Thus, miscellaneous mechanisms and active sites are dependent upon not only different reactions but also different reactants within the same reaction.

Discussion

All the catalytic activities of various carbons are the result of the physical and chemical properties of carbon. High surface area and large pore size provide significant adsorption ability and selective catalytic activity. Their catalytic activity is also characterized by electron transfer from the edges of the carbon sheets-graphitic lattice. Heteroatoms such as sulfur and nitrogen in the graphitic lattice change the catalytic activity of the graphitic structure by altering its electron cloud. The presence of acidic and basic surface oxide complexes also influence the catalytic activity. Therefore, the key physical and chemical properties of solid carbons which affect the catalytic properties of solid carbons will be discussed.

Surface Chemistry of Carbon. Even in a well ordered material, there are many exposed defects, dislocations, and discontinuities in and at the edge of layer planes. Carbon atoms near such defects tend to chemisorb atoms and molecules in order to complete their valence requirements. The chemisorption of oxygen, hydrogen, halogens, etc., is well established. Many of the properties of carbons (including catalytic activities) are found to be related to the presence of the surface complexes. Due to the degree of importance of oxygen and nitrogen surface groups for catalytic activity, only oxygen and nitrogen surface groups will be discussed in this section. Other surface complexes like hydrogen and halogen surface complexes also affect the catalytic activity of carbon [23,30,31].

Oxygen surface groups are the most important surface groups as far as physicochemical properties are concerned. Since catalytic reactions take place at the surface of the catalyst, oxygen complexes play significant roles in several reactions catalyzed by solid carbons. Oxygen surface complexes are formed either in oxidizing gases (O_2, N_2O, CO_2, H_2O, etc.) or oxidizing solutions ($KMnO_4$, HNO_3, $KClO_3$, etc.). A schematic drawing of various oxygen functional groups on the carbon surface is presented in Fig. 45.

Three kinds of surface oxides (acidic, basic, and neutral) are proposed. Carboxylic, lactone and phenolic groups have been suggested as the major acidic surface groups whereas chromene-like (benzopyran) structure and pyrone-like structure are suggested as the major sites for the basic properties (see Figure 45). The chromene and pyrone-like structures are a conjugated structure with aromatic carbons in the layer planes. The pyran structure also associated with an activated $>CH_2$ or >CHR group (R = alkyl group). These oxygen surface groups are suspected of being responsible for many catalytic reactions mentioned earlier. Different acidic functional groups are responsible for different reactions, in other words, the activity among the acidic surface groups varies from reaction to reaction.

The percentage of nitrogen surface groups is not significant in the as-received carbon, usually below 0.5% by weight. The carbon-nitrogen complexes were found to be highly stable. Nitrogen is fixed not only in a heterocyclic ring structure (see Fig. 46), but also present in the form of a nitrile group. When carbon is treated with ammonia or diethylamine the fixation of nitrogen occurs, causing a significant increase in catalytic activity [39].

Electronic Properties. Of particular importance to catalytic activity are the electronic properties of carbon. The strong anisotropic conductance exhibited as well as the thermal and mechanical behavior results from the structure and bonding in graphite. The low resistivity parallel to the layer planes of graphite is comparable to the resistivity range found for common metals: 10^{-4} ohm-cm for the resistivity parallel to the layer planes whereas 1 ohm-cm for the resistivity perpendicular to the hexagonal networks for single crystals of natural graphite and pyrolytic graphite at room temperature[40]. The conduction in the hexagonal layer planes of graphite is facilitated primarily by π-electrons, while in the perpendicular direction conduction occurs by positive holes. Figure 47 depicts the variations in electronic properties with heat-treatment temperature.

Thus, the degree of carbonization and graphitization of any given carbon is dependent upon both heat-treatment temperatures and the nature of precursors. Well-ordered carbons whose electronic properties approach that of a metal, as well as some highly disordered carbon with electronic behavior similar to an insulator may exist within a typical carbon sample. The electron transfer ability of carbon is very important for the catalytic redox reaction for both organic and inorganic reactions Austin *et al.*[42] listed nineteen inorganic redox reactions and proposed a mechanism for the catalysis by carbons. The carbon reacts with adsorbates to form surface donor complexes which influence the electronic properties. For example, activated carbon has similar behavior to inorganic semiconductor catalysts.

Pore Structure. Pores are generated naturally as empty spaces between crystallites or produced deliberately in carbon by activating with oxidizing gas. The presence of pores should be accessible to the molecular species when a carbon is employed as a catalyst. These pores can be enlarged by activation or contracted by heat treatment. Some catalytic reactions occur mainly on the outer surface while some reactions take place inside pores depending upon whether the molecules can reach the inside of pores or not. Unfortunately, there is no study about the significance of the porous structure for the catalytic activity of solid carbon. However, it is not difficult to look at the role of porous structure of carbon from the studies of solid carbons used as catalyst supports for shape-selective reactions. For example, the study of hydrogenation of olefins on the CMS containing 1% Pt revealed that only the straight chain alkene, 1-butene, is effectively hydrogenated to *n*-butane whereas the branched alkene, 3-methyl-1-butene, is inadequately hydrogenated [43]. In another study, addition of acetic acid to acetylene on the impregnated active carbons,

demonstrated that a better catalytic activity of a catalyst results from: i) a higher number of pores and their smaller average length, ii) a larger volume as well as surface area of mesopores and a larger radius of macropores [44]. Thus, the porous structure of carbons especially the pore size distribution affects the catalytic activity of carbons with respect to the selectivity of catalytic reactions.

Crystal Structure. Unlike the three-dimensional lattice of diamond in which carbon atoms are joined by covalent sp^3 bonds, the graphite is layered material. Within these layers the carbon atoms are bonded by sp^2 covalent bonds while the layers are held together by weak van der waals forces [45]. Only microcrystalline (amorphous) carbons are considered as catalyst material; they are activated carbon, carbon blacks, coke, etc. The microcrystalline carbon has a similar layered structure of graphite, but the thickness of those stacking layers is about 10 to 100 Å and the stacked sequence of layers is greatly disordered. Carbons with their graphitic surface structure often adsorb aromatic compounds well and thereby affect their catalytic reaction rates. Racemization and other reactions involving reactants with aromatic compounds are often catalyzed by solid carbons due to increases in adsorption rate of aromatic compounds on the carbon surface [18,30,31,35].

The graphitic layer planes possess the various defects such as holes, steps, and chemical impurities within the layers. Impurities, defects and dislocations are obviously several of the factors necessary to determine the activity of carbon. These are heavily dependent on the nature of the raw material and the process for preparing the carbon. Dislocations are the sites for collecting impurities, and those impurities alter greatly the catalytic activity. Sometimes impurities like alkaline metals are deliberately added to improve the catalytic activity of carbons. The alkylation of imidazole with different alkylating agents was performed in the presence of activated carbon with/without addition of alkaline metals [46]. In this study, the authors achieved 90% conversion with sodium/activated carbon whereas pure activated carbon only had 20% conversion for alkylation of imidazole with 1-bromo-butane.

Conclusion

Carbon possesses the properties to catalyze many organic reactions from dehydrogenation to polymerization as demonstrated in many citations earlier. It is somewhat surprising that carbon exhibits varieties of catalytic activities throughout the categories in Table 7; solid carbons catalyze reactions mainly catalyzed by metal to acid catalysts. The responsible sites and mechanisms for the reactions vary from one reaction another. In the case of one reaction (e.g., oxidation and dehydrogenation), use of different reactants will change the active site of catalysis. The selectivity as well as catalytic activity is influenced by the chemical and physical properties of the carbon.

Pore size distribution in solid carbon affects the shape selectivity of the catalytic reaction. Surface functional groups and impurities incorporated directly influence the catalytic activity.

Based on the information provided in this section, one can predict other reactions in which ordinary catalysts can be replaced by carbon. Since solid carbons possess properties of metals, metal oxides, and acidic catalysts, all other heterogeneous catalytic reactions in Table 7 besides the reactions mentioned in this text could be catalyzed by carbon. However, the feasibility of carbon acting as a catalyst for a certain reaction is heavily dependent upon the reactants involved.

Even though electronic properties are not the only factors used to determine the catalytic activity of carbon, other factors such as surface complexes work independently as an active site for catalytic reactions, it is interesting to look at the catalytic activity of carbon from the viewpoint of the electrical conductivity. As mentioned earlier, solid carbons may possess electronic properties ranging from conductor to insulator depending upon the method of preparation and treatment. Different electronic properties may exist in a single microcrystalline carbon sample. Hence, proper treatment of carbon catalysts alters their electronic properties; further, it also alters their catalytic activity and selectivity for a particular reaction. For example, heat treatment and graphitization of carbon would lead to metallic property, and oxidation and the formation of oxide would lead to more semiconductivity. Manufacturing of highly disordered carbon might result in an insulator type of carbon.

Since solid carbons have a high adsorption capability, considerable amounts of products and/or reactants are adsorbed during the reactions. This often leads to the false kinetic conclusion especially the reaction in solution. Hence, kinetic studies of catalytic reactions with carbon should be carefully studied in order to avoid the false kinetic conclusions. There are also some disadvantages to use of solid carbons as catalysts. First, though solid carbons are inert material for the wide range of temperatures, they are easily oxidized to form unwanted surface functional groups creating problems like difficulty in tailoring of surface groups. Second, if solid carbons are used for certain reactions in the industry, regeneration of carbon catalysts might be a problem since metal ions during reaction often become incorporated within the carbon structure during the regeneration process; consequently, the regenerated carbons can differ from the original carbon catalyst.

Future research must be focused on the clear identification of the active sites for a given reaction, and tailoring the carbon surface for specific reactions.

References

1. E. C. Larson and J. H. Walton, *J. Phys. Chem.* **44**, 70-85 (1940)

2. E. K. Rideal and W. M. Wright, *J. Chem. Soc.* **128**, 1813-1821(1926)

3. L. Singoredjo, F. Kapteijn, J. A. Mouijin, Jose-Miguel, Martin-Martinez and H-P. Boehm, *Carbon* **31**, 213-222 (1993)

4. J. K. Lee, D. J. Suh, S. Park and D. Park, *Fuel* **72**, 935-939 (1993)

5. J. J. Choi, M. Hirai and M. Shoda, *Applied Catalysis A: general* **79**, 241-248 (1991)

6. G. A. Somorjai, *Introduction to Surface Chemistry and Catalysis*, John Wiley and Sons, Inc. (1994)

7. G. C. Bond, *Heterogeneous Catalysis: Principles and Application*, Oxford Science Publications (1987)

8. J. McMurry, *Organic Chemistry*, Brooks/Cole Publishing Company (1984)

9. G. S. Szymanski and G. Rychlicki, *Carbon* **29**, 489-498 (1991)

10. G. S. Szymanski and G. Rychlicki, *Carbon* **31**, 247-257 (1993)

11. R. Malhotra, D. McMillen, D. Tse, D. Lorents, R. S. Ruoff and D. Keegan, *Energy & Fuels* **7**, 685-686 (1993)

12. G. C. Grunewald and R. S. Drago, *Journal of Molecular Catalysis* **58**, 227-233 (1990)

13. G. C. Grunewald and R. S. Drago, *J. Am. Chem. Soc.* **113**, 1636-1639 (1991)

14. L. E. Cadus, L. A. Arrua, O. F. Gorriz and J. B. Rivarola, *Ind. Eng. Chem. Res.* **27**, 2241-2246 (1988)

15. G. E. Vrieland and P. G. Menon, *Applied Catalysis* **77**, 1-8 (1991)

16. P. G. Menon, *Journal of Molecular Catalysis* **59**, 207-220 (1990)

17. J. Galuszka, T. Sano and J. A. Sawicki, *Extended Abstracts of '91 Int. Carbon Conf.* 92-93

18. M. Farcasiu, S. C. Petrosius and E. P. Ladner, Preprint for publishing (1993)

19. A. Tomita, S. Mori and Y. Tamai, *Carbon* **9**, 224-225 (1971)

20. C. Ishizaki and J. T. Cookson, *Influence of Surface Oxides on Adsorption and Catalysis with Activated Carbon* in *Chemistry of Water Supply Treatment and Distribution* edited by A. J. Rubin, Ann Arbor Science Publishers, Inc. (1974)

21. T. Stohr and H. P. Boehm, *Extended Abstracts of '86 Int. Carbon Conf. Baden-Baden* 354-356

22. R. Kurth, B. Tereczki and H. P. Boehm, *Extended Abstracts of '81 15th. Bienn. Int. Carbon Conf. Philadelphia* 224

23. B. R. Puri and R. C. Bansal, *Indian J. of Chem.* **5**, 381-390 (1967)

24. M. Spiro and Mills, Unpublished work.

25. Y. Y. Hoyano and R. E. Pincock, *Can. J. Chem* **58**, 134-137 (1980)

26. P. H. Given and L. W. Hill, *Carbon* **6**, 525-535 (1968)

27. K. Ohkita, M. Uchiyama and H. Nishioka, *Carbon* **16**, 195-198 (1978)

28. H. P. Boehm, G. Mair, T. Stoehr, A. R. de Rincon and B. Tereczki, *Fuel* **63**, 1061-1063 (1984)

29. F. A. Gupta, G. Lange and H. P. Boehm, *Extended Abstracts of '93 Int. Carbon Conf.* 428-429

30. R. E. Pincock, W. M. Johnson and J. Haywood-Farmer, *Can. J. Chem.* **54**, 548-553 (1976)

31. L. G. Hutchins and R. E. Pincock, *J. Org. Chem.* **45**, 2414-2418 (1980)

32. J. A. Meier and L. W. Hill, *Journal of Catalysis* **32**, 80-87 (1974)

33. L. W. Hill, V. K. Acharya and W. E. Wallace, Jr., *Carbon* **9**, 222-223 (1971)

34. B. R. Puri, V. K. Sud and K. C. Karla, *Indian Journal of Chemistry* **9**, 966-969 (1971)

35. M. Farcasiu and C. Smith, *Energy & Fuels* **5**, 83-87 (1991)

36. M. H. Back, R. Venkateswaran and G. Scacchi, *Extended Abstracts of '93 Int. Carbon Conf.* 537-538

37. T. A. Ryan and M. H. Stacey, *Fuel* **63**, 1101-1106 (1984)

38. K. Kinoshita, *Carbon, Electrochemical and Physicochemical properties*, A Wiley-Interscience Publication (1988)

39. B. Stohr and H. P. Boehm, *Carbon* **29**, 707-720 (1991)

40. R. W. Coughlin, *Ind. Eng. Chem., Prod. Res. and Develop.* **8**, 12-23 (1969)

41. B. D. McMichael, E. A. Kmetko and S. Mrozowski, *J. Opt. Soc.* **44**, 26 (1954)

42. J. M. Austin, T. Groenewald and M. Spiro, *J. C. S. Dalton* 854-859(1980)

43. J. L. Schmitt, Jr. and P. L. Walker, Jr., *Carbon* **10**, 87(1972)

44. J. Kloubek and J. Medek, *Carbon* **24**, 501-508(1986)

45. I. A. S. Edwards, *Ch.1: Structure in Carbons and Carbon Forms* in *Introduction to Carbon Science* edited by H. Marsh, Butterworths & Co. Ltd. (1989)

46. R. M. Martin-Aranda, M. L. Rojas-Cervantes, L. de D. Lopez-Gonzalez and A. J. Lopez-Peinado, *Extended Abstracts of '93 Carbon Conf.* 565-566

$$\ln\left(\frac{C_A}{C_{A_0}}\right) = -kt \qquad (2)$$

Plots of $\ln C_A$ versus time should be linear with a slope equal to (–k) and an intercept equal to $\ln C_{A_0}$ [2]. Values of $9.4*10^{-7}$, $7.2*10^{-6}$ and $4.6*10^{-5}$ sec^{-1} were obtained for temperatures of 400, 425 and 450°C, respectively. Note that as the temperature increases from 400 to 450°C the rate constant k increases significantly. Further experiments at different temperatures and different THQ concentrations are in progress and it is our intention to determine activation energies from these data. Similar experiments are planned for benzyl alcohol. We are particularly interested in the relative stability of THQ *vis-a-vis* benzyl alcohol in hydrocarbons at temperatures in the range of 400–500°C.

References

1. Yoon, E.M.; Coleman, M.M.; *Advanced Thermally Stable Jet Fuels*, Technical Progress Report, 92PC92104-TPR-10, February 1995.

2. Hill Jr., C.G. An Introduction of Chemical Engineering Kinetics & Reactor Design, John Wiley & Sons, New York, 1977.

Task 5. Exploratory Studies on the Direct Conversion of Coal to High-Quality Jet Fuels.

1. Design, Assembly, and Operation of a Batch Mode and a Continuous Mode Three-Phase Reactor Systems for the Liquefaction of Coal and Upgrading of Coal Liquids. (Contributed by P. Vijay and Chunshan Song)

Introduction

In the previous jet fuels report [1], the following topics were discussed in detail:

- Design of a batch-mode mini-pilot plant scale reactor system, for the liquefaction of coal.
- Brief overview of existing coal liquefaction and coal liquids upgrading units (Advanced Coal Liquefaction Facility at Wilsonville, AL; Unit of the Hydrocarbon Research Institute (HRI), Inc. NJ; and the PETC Coal Liquefaction Process, Pittsburgh, PA).
- Conceptual design of a continuous-mode mini-pilot plant scale reactor scheme for liquefaction of coal and upgrading of coal liquids.

Topics Presented in this Report

The assembly, operation, and an overview of the design of experiments, and analysis of gases, liquids, and solid products to be performed in the batch-mode mini-pilot plant scale reactor system will be discussed.

The conceptual process design scheme for the continuous flow mini-pilot plant reactor system for the liquefaction of coal and upgrading of the coal liquids that was developed earlier, was modified as deemed necessary to satisfy our requirements. Detailed description of this modified continuous-mode process scheme, along with the cost analysis of the various equipments and accessories, will be presented later in this report.

Batch-Mode Mini-Pilot Plant Scale Reactor System for Coal Liquefaction Process

The design of the batch-mode mechanically agitated slurry reactor system for the liquefaction of coal was discussed in the previous jet fuels report [1]. The assembly of this mini-pilot plant scale process system was accomplished. A few initial trial runs were performed to better understand the behavior of this slurry phase process.

Based on experiments conducted earlier in the 25 mL tubing bomb microautoclave reactor [2,3], a series of experiments were designed to be conducted in the batch-mode agitated reactor system. The experiments cover a wide range of variables that include:

- Raw Coal or Vacuum-dried Coal
- Single-Stage Liquefaction (SSL)
- Temperature-Programmed Liquefaction (TPL)
- With and Without the Addition of Catalyst (Molyvan L)
- With and Without the Addition of Water
- Using H_2 or Syngas (H_2 + CO) in the SSL and in the 1st Stage of TPL
- Temperature Range: 350–450 °C
- Duration of Experimental Run: 30–60 min.

Details of the Experimental Design.

Coal Samples: DECS-8 Wyodak Subbituminous Coal

1) Raw Coal: as-received coal from coal sample bank

2) Vacuum-dried Coal: coal dried in a flask, covered with Al foil with very small holes drilled, in a vacuum oven at 100 °C for 2 hrs. before use

Charge into 300 mL Reactor:

Coal: 40 g on a dry basis

Solvent: 60 g Wilsonville Middle Distillates (WI-MD) from Run 259

Solvent/Coal: Mass ratio close to 1.5, on the dry coal basis

Catalyst: Molyvan L, 0.5 wt. % Mo based on dmmf coal (Molyvan L contains 8.1 wt. % Mo (metal basis) dissolved in oils)

H_2 gas: 1000 psi initial pressure (cold)

Liquefaction Conditions:

1. SSL Raw Coal + WI-MD 350 °C–30 min
2. SSL Raw Coal + WI-MD 400 °C–30 min
3. SSL Raw Coal + WI-MD + Molyvan L 350 °C–30 min
4. SSL Raw Coal + WI-MD + Molyvan L 400 °C–30 min
5. SSL Vacuum-dried Coal + WI-MD + Molyvan L 350 °C–30 min
6. SSL Vacuum-dried Coal + WI-MD + Molyvan L 400 °C–30 min
7. SSL Vacuum-dried Coal + WI-MD + Molyvan L 350 °C–30 min + added Water (Equivalent to Original Moisture) [4]
8. SSL Vacuum-dried Coal + WI-MD + Molyvan L 400 °C–30 min + added Water (Equivalent to Original Moisture)

9. SSL Vacuum-dried Coal + WI-MD + Molyvan L 400 °C–60 min
10. SSL Vacuum-dried Coal + WI-MD + Molyvan L 425 °C–60 min
11. TPL Raw Coal + WI-MD + Molyvan L 1st Stage - 350 °C –30 min., Cool r eactor to 200 °C followed by venting gas to simulate Inter-stage Separator, re-pressurization and heat to 2nd Stage - 400 °C–30 min. (H_2 in both stages)
12. TPL Raw Coal + WI-MD + Molyvan L 1st Stage - 350 °– 30 min., Cool reactor to 200 °C followed by venting gas to simulate Inter-stage Separator, re-pressurization and heat to 2nd Stage - 425 °C–30 min. (H_2 in both stages)
13. TPL Raw Coal + WI-MD + Molyvan L 1st Stage - 375 °C–30 min., Cool r eactor to 200 °C followed by venting gas to simulate Inter-stage Separator, re-pressurization and heat to 2nd Stage - 400 °C–30 min. (H_2 in both stages)
14. TPL Raw Coal + WI-MD + Molyvan L 1st Stage - 375 °C–30 min., Cool reactor to 200 °C followed by venting gas to simulate Inter-stage Separator, re-pressurization and heat to 2nd Stage - 425 °C - 30 min. (H_2 in both stages)
15. SSL Vacuum-dried Coal + WI-MD + Molyvan L 350 °C–30 min Syngas - H_2/CO - 25/75
16. SSL Vacuum-dried Coal + WI-MD + Molyvan L 400 °C–30 min Syngas - H_2/CO - 25/75
17. SSL Raw Coal + WI-MD + Molyvan L 350 °C–30 min Syngas - H_2/CO - 25/75
18. SSL Raw Coal + WI-MD + Molyvan L 400 °C–30 min Syngas - H_2/CO - 25/75
19. TPL Raw Coal + WI-MD + Molyvan L 1st Stage - 350 °C–30 min., Cool reactor to 200 °C followed by venting gas to simulate Inter-stage Separator, re-pressurization and heat to 2nd Stage - 400 °C –30 min. (Syngas - H_2/CO - 25/75 in 1st Stage; H_2 in 2nd Stage)
20. TPL Raw Coal + WI-MD + Molyvan L 1st Stage - 350 °C–30 min., Cool reactor to 200 °C followed by venting gas to simulate Inter-stage Separator, re-pressurization and heat to 2nd Stage - 425 °C–30 min. (Syngas - H_2/CO - 25/75 in 1st Stage; H_2 in 2nd Stage)
21. TPL Raw Coal + WI-MD + Molyvan L 1st Stage - 375 °C–30 min., Cool reactor to 200 °C followed by venting gas to simulate Inter-stage Separator, re-pressurization and heat to 2nd Stage - 425 °C–30 min. (Syngas - H_2/CO - 25/75 in 1st Stage; H_2 in 2nd Stage)
22. TPL Vacuum-dried Coal + WI-MD + Molyvan L 1st Stage - 350 °C–30 min., Cool reactor to 200 °C followed by venting gas to simulate Inter-stage Separator, re-

pressurization and heat to 2nd Stage - 400 °C - 30 min. (Syngas - H_2/CO - 25/75 in 1st Stage; H_2 in 2nd Stage)

23.	SSL	Raw Coal + WI-MD + Molyvan L	325 °C–30 min
24.	SSL	Raw Coal + WI-MD + Molyvan L	375 °C–30 min
25.	SSL	Raw Coal + WI-MD + Molyvan L	425 °C–30 min
26.	SSL	Raw Coal + WI-MD + Molyvan L	450 °C–30 min
27.	SSL	Vacuum-dried Coal + WI-MD + Molyvan L	325 °C–30 min
28.	SSL	Vacuum-dried Coal + WI-MD + Molyvan L	375 °C–30 min
29.	SSL	Vacuum-dried Coal + WI-MD + Molyvan L	425 °C–30 min
30.	SSL	Vacuum-dried Coal + WI-MD + Molyvan L	450 °C–30 min
31.	SSL	Vacuum-dried Coal + WI-MD + Molyvan L	400 °C–60 min
32.	SSL	Vacuum-dried Coal + WI-MD + Molyvan L	425 °C–60 min
33.	SSL	Vacuum-dried Coal + WI-MD + Molyvan L	450 °C–60 min
34.	SSL	Raw Coal + WI-MD	325 °C–30 min
35.	SSL	Raw Coal + WI-MD	350 °C–30 min (2nd run)
36.	SSL	Raw Coal + WI-MD	375 °C–30 min
37.	SSL	Raw Coal + WI-MD	400 °C–30 min (2nd run)
38.	SSL	Raw Coal + WI-MD	425 °C–30 min
39.	SSL	Raw Coal + WI-MD	450 °C–30 min

Experimental studies based on this design have commenced.

Analysis of Products.

Gases: After the mechanically agitated slurry reactor (300 cc) has cooled down, some amount of gases are collected in a sampling bag, and analyzed using both TCD (H_2, CH_4, CO, and CO_2) and FID (C_1-C_4 hydrocarbon gases) detectors.

Liquid and Solid products: The traditional Soxhlet extraction procedure is suitable mainly for products from the microautoclave (25 mL reactors) tests, since the quantity of product samples involved is very small [5]. In order to analyze the products obtained from the agitated slurry

3. Most liquids from flask Ia is poured through a filter into another clean 500-mL flask (IIa). The THF from this flask IIa is evaporated with the aid of a rotary evaporator. About 70-90 mL of the flask contents is left remaining in it.
4. An additional 150 ml of fresh THF is added to flask Ia, stirred for 30 min., and allowed the solids to settle for 10 min.
5. Operation 3 and 4 repeated, followed by a repeat of Operation 3.
6. The solids in flask Ia is collected after filtration, dried in a vacuum-oven at 105-110°C for 6-8 hrs., and weighed after vacuum-drying. The product from this step is THF-insoluble residue, whose weight is used for calculation of coal conversion.
7. About 800 ml hexane is transferred into a 1-L beaker (IIIa), and stirred with a magnetic stirrer.
8. The liquids from flask IIa is emptied slowly into the beaker IIIa, with vigorous stirring. The contents of the beaker IIIa is stirred for an additional 30 min. and allowed to settle for an hour.
9. The mixture in IIIa is filtered and the liquids and filter cake are separately collected.
10. The clear liquids from the above filtration is collected in a clean 500-mL flask, and the hexane is evaporated off in a rotary evaporator. The final product from this step is the remaining reaction solvent and hexane-soluble products from coal, defined as oil.
11. The filter cake collected from Operation 9 is dried in a vacuum-oven at 105-110° C C for 6-8 hrs, and weighed after drying. This fraction is hexane-insoluble but THF-soluble products, and consists of asphaltene and preasphaltene.

This procedure for gas, liquid, and solid analysis is performed at the end of each experimental run, to determine the conversion of H_2, composition of product gases, quantity of oil produced, amount of asphaltene and preasphaltene formed, and the conversion of coal.

Modified Process Design of the Continuous-Mode Reactor Scheme for Coal Liquefaction and Upgrading of Coal Liquids

The process design scheme proposed in the earlier report [1] for the continuous-mode mini-pilot plant scale reactor configuration, for liquefaction of coal and upgrading of coal liquids was modified accordingly to suit our process/budgetary limitations. Comparing the process design schemes shown in Figures 1 and 2, with the figures presented in the earlier report, the following modifications are noted:

1. Although it is necessary to recycle H_2 gas in an industrial-scale process, we have eliminated all recycle gas streams and the compressors in these lines, mainly due to budget and space limitations. In Figure 51, this includes the recycle gas streams exiting from the 1st stage reactor to the inlet of thepreheater, interstage separator to the inlet of 2nd stage reactor, and the vapor-liquid separator to the inlet of 2nd stage reactor. In Figure 52, this includes the recycle gas stream from the vapor-liquid separator to the inlet of the preheater.

2. In Figure 51, the gas outlet/recycle stream from the 1st stage reactor along with the accessories in the line that includes, a condenser, liquid collection bomb, and a back pressure regulator for this recycle stream, has been entirely eliminated. Thus, the gas along with the slurry would flow into the interstage separator, where the separation of gas/slurry would occur.

3. In Figure 51, a condenser has been added to the process stream exiting the vapor-liquid separator and flowing through the BOM Valve into the atmospheric flash tank. This would help in reducing the temperature and pressure of the stream exiting the V/L separator, and assist in the condensation of the desired product vapors.

4. In Figure 51, at the exit of the atmospheric flash tank a filter bag is placed in the process stream. This would aid in the separation of liquids from the solids in the slurry stream. The liquids are collected in the coal liquids collector tank, that also acts as the feed tank for the upgrading section of the mini-pilot plant reactor scheme.

Several of the major process equipments (slurry pump, water pump, pneumatic compressor, compressed gas cylinders for storage, liquid collection bombs, etc.) were ordered to be delivered from the manufacturers, and a few of them have been received. The other equipments and accessories will also be ordered from the manufacturers soon. Depending on budgetary constraints, the continuous-mode mini-pilot plant scheme will either have only manual controls, or have computer controls for selected equipments, or will be an entirely computerized state-of-the-art system.

Based on the modified process design scheme, an abstract entitled, "Process Design of a Novel Continuous-Mode Mini-Pilot Plant for Direct Liquefaction of Coal and Upgrading of Coal Liquids", authored by P. Vijay, Chunshan Song, and Harold H. Schobert, has been submitted to be considered for presentation in the Symposium on "Direct Coal Liquefaction", at the ACS National Meeting in Chicago, August 20-25, 1995.

Future Plans

Coal liquefaction research studies in the batch-mode mini-pilot plant reactor system will continue to be performed, according to the experimental design and method of analysis of products, mentioned earlier. Regarding the continuous-mode mini-pilot plant process scheme, a

few of the equipments and accessories have been ordered to be delivered from the manufacturers and the rest of the equipments will be ordered soon. Whenever the equipments are received from the vendors, the assembly of this mini-pilot plant will commence immediately.

References

1. Schobert, H.H., Eser, S., Song, C., Hatcher, P.G., Boehman, A., and Coleman, M.M.; *Jet Fuels Technical Progress Report - October 1994 - December 1994*, Prepared for the U.S. Department of Energy under Contract No. DE-FG22-92PC92104, February, 1995.

2. Song, C., Parfitt, D. S., and Schobert, H. H.; *Energy & Fuels*, Vol. **8**, No. 2, 313-319, 1994.

3. Song, C. and Saini, A. K.; *Preprints of Papers presented at the 208th ACS National Meeting*, Washington, D.C., August 20-25, 1994, 1103-1107.

4. Song, C. and Saini, A. K.; *Energy & Fuels*, Vol. **9**, No. 1, 188-189, 1995.

5. Song, C. and Saini, A. K. and Schobert, H. H.; *Energy & Fuels*, Vol. **8**, 301, 1994.

2. Exploratory Studies on Coal liquids Upgrading using Mesoporous Molecular Sieve Catalysts (Contributed by Madhusudan Reddy Kondam and Chunshan Song)

Introduction

In the previous report we have reported the successful synthesis of phase-pure mesoporous molecular sieves, Al-MCM-41, with varying Si/Al ratios and using different aluminum sources [1]. Preliminary results based on X-ray diffraction showed that type of aluminum source and Si/Al ratio have significant influence in the synthesis and their physico-chemical characteristics of these mesoporous molecular sieves. For example, aluminum isopropoxide and aluminum sulfate were found to be better sources for complete aluminum incorporation in the framework as compared to Catapal B alumina source. It was also observed that the higher the Si/Al ratio, the better the crystallinity of the solid obtained. In order to further confirm earlier results, in this report we present more results of characterization by chemical analysis, surface are measurement, thermal analysis and solid state NMR spectroscopy techniques. Some catalytic evaluation results of these materials in the reactions of hydrogenation of naphthalene and phenanthrene and alkylation of naphthalene are also reported before they can be tested for upgrading the coal liquids.

Experimental

Chemical analyses of calcined MCM-41 samples were obtained from Penn State's Materials Characterization Laboratory in order to know the Si/Al ratios of the resulting solid products (mesoporous molecular sieves) of the synthesis. Calcined forms of MCM-41 molecular sieves were characterized by nitrogen adsorption at 77 K using a Quantachrome automated adsorption apparatus (Autosorb 1-Model ASIT) and the BET surface areas were calculated.

The ^{29}Si and ^{27}Al MAS NMR spectra were of as-synthesized MCM-41 samples recorded on a CMX 300 Chemagnetic solid state NMR spectrometer. All spectra were recorded at room temperature and chemical shifts were measured with respect to TMS for ^{29}Si and $Al(H_2O)_6^{3+}$ for ^{27}Al.

Thermal analysis was performed on a Mettler TG50 thermobalance. All the samples prepared using different aluminum sources are examined at regular calcination conditions (temperature from room temperature to 823 K at rate of 5 K/min and first 3 hours in 200 cc/min nitrogen flow then later 5 hours in 200 cc/min air flow) reported in the last report [1]. The MCM-41 sample prepared with Al isopropoxide was also examined at different conditions of air and nitrogen flows and at different temperature programming rates in order to establish better calcination conditions.

Characterization of acidity of MCM-41 molecular sieves was done by a thermal study of *n*-butylamine adsorbed samples. In the preparation of *n*-butylamine adsorbed samples, prior to

adsorption, samples (protonic forms) were degassed under vacuum at 723 K for 2 hours then the *n*-butylamine vapor was passed through the sample with flow rate of about 100 cc/min. using nitrogen as a carrier at room temperature for about 1 hour. The base-covered samples were then transferred to a thermal analyzer. Nitrogen was used as purge gas and was maintained (60 cc/min) at room temperature for 30 min. before thermal analysis was started. TGA and DTG data were obtained from 303 K to 973 K at the rate of 10 K/min.

Prior to catalytic runs, MCM-41 samples were converted into protonic form and then Pt was loaded by wet impregnation. First as-synthesized samples were calcined according to procedure described in pervious report [1]. These calcined samples were exchanged with excess NH_4NO_3 solution and calcined again at 723 K for 3 hours in order obtain samples of protonic form. Finally 3 wt% Pt was loaded by taking required amount of hexachloro- platinic acid (Aldrich) solution and MCM-41 sample in a beaker and evaporated the water while stirring it overnight. The Pt-loaded samples were then calcined in air at 737 K for 3 hours.

Catalytic tests (hydrogenation of naphthalene and phenanthrene and propylation of naphthalene) and product analyses were done according to the procedure identical to those reported earlier [2,3]. All the reactions were carried out in horizontal tubing-bomb reactors (with vertical shaking, 200 cycles per minute) with 0.1 g of catalyst, 1.0 g of reactant and *n*-nonane as internal standard. 4.0 g of n-tridecane was used as a solvent for hydrogenation reactions and no solvent was used for alkylation reaction. The propylation of naphthalene was performed under 150 psi initial propylene pressure and at 473 K for 2 hours. The hydrogenation of naphthalene was done under 1000 psi initial hydrogen pressure and at 473 K for 1 hour. Finally the hydrogenation of phenanthrene was carried out under 1500 psi and at 573 K for 2 hours. Products were analyzed by Gas Chromatography (Perkin-Elmer 8500) using DB-17 fused silica capillary column.

Results and Discussion

The SiO_2/Al_2O_3 molar ratios of calcined MCM-41 samples from the chemical analyses are presented in Table 14. Initial molar ratios taken while synthesizing samples (input) and the ratios obtained from the crystalline solid products (output) are compared. Results show that input ratios are higher than output ratios which is a common observation in the synthesis of high-silica molecular sieves. Because zeolites normally incorporate all of the aluminum present in the reaction mixture leaving varying amounts of silica or silicate in solution according to other factors such as the hydroxide concentration and the presence of various inorganic and organic cations in the reaction mixture [4]. Exceptionally, the samples prepared with aluminum sulfate produced molecular sieves with high SiO_2/Al_2O_3 ratios. The reason is not clear, but may be due to the different nature of hydrolysis for aluminum sulfate.

Figure 53 shows one of the nitrogen adsorption isotherms of MCM-41 samples at 77K. Typically all the calcined MCM-41 samples irrespective of source of aluminum used to synthesize showed similar isotherms. These isotherms are characteristic of mesoporous materials with uniform pore size [5-7] with an inflection characteristic of capillary condensation within the pores. The relative pressure at which this inflection occurs increases with the diameter of the pores [7]. In our case, it occurred at p/p^0 in between 0.20 to 0.40. The average pore diameters calculated using the BJH model [8] are given in Table 14. BET surface areas (Table 14) also clearly confirm our earlier results of crystallinity comparison. MCM-41 sample prepared with Catapal B has high BET surface area means high crystallinity and the one prepared with aluminum sulfate has low BET surface area confirming poor crystallinity.

TGA curves (Figure 54) clearly show that samples are thermally stable at least at our calcination conditions. The organic template is decomposed below 823 K leaving well crystalline mesoporous materials. The weight loss is about 60 wt% which indicates that as-synthesized samples contain large amounts of organic templates because of the presence of mesopores with large void volume. The weight loss for the sample prepared using Al isopropoxide was noticed to be slightly less, this could probably due to excess removal of organic template while filtering and washing after the crystallization. Figure 55 shows the TGA of the same sample obtained at different calcination conditions; only at nitrogen or air flow and at different programming rates. All the curves are basically same except that when the nitrogen was used as carrier, organic template seems to be decomposed at two different stages. There is a slight shift in the curves obtained at different programming rates, this may be due to that fact that degradation of organic template may not be as faster as the temperature raise.

Thermal analysis of *n*-butylamine pre adsorbed MCM-41 samples are shown in Figure 56. It is observed from the TGA curves that most of n-butylamine is desorbing below 473 K. From the weight losses due to n-butylamine desorption (presuming n-butylamine adsorption was done at completely dry conditions), it is also clear that MCM-41 samples prepared with aluminum isopropoxide and aluminum sulfate adsorbed more *n*-butylamine (about 18 wt%) whereas the sample prepared with Catapal B alumina source adsorbed less *n*-Butylamine (about 10 wt%). These results indicate that first two samples are more acidic than the last one, which again confirms our earlier results that aluminum incorporation is better for first two samples hence they are more acidic.

Figures 57-59 illustrate the ^{29}Si and ^{27}Al MAS NMR spectra of as-synthesized mesoporous molecular sieves, MCM-41.It is clearly seen that samples prepared with aluminum isopropoxide and aluminum sulfate exhibit mainly a single peak at around 50 ppm (Figure 57). No peak, or a negligible peak at 0 ppm, corresponding to octahedral Al species is detected in these samples, confirming that all the Al atoms in the as-synthesized MCM-41 materials are present in a

tetrahedral environment [8]. This peak was found to be somewhat broader when compared with the ^{27}Al MAS NMR spectrum of ZSM-5 zeolite. The broadening of the peak may be an indication of the presence of some of the Al species in distorted tetrahedral environments. The ^{27}Al MAS NMR spectrum of MCM-41 sample prepared using Catapal B alumina as Al source shows mainly a peak at 0 ppm corresponds to octahedral Al species with a small peak at around 50 ppm corresponds to tetrahedral Al species. Similar results were observed by Devis *et al* [8] for their samples prepared with Catapal B as Al source These results clearly indicate that Catapal B is not a good source to incorporate the Al in the framework (tetrahedral Al species). Aluminum sulfate and aluminum isopropoxide are better sources for maximum incorporation of aluminum in the framework. Figure 58 represents the ^{27}Al MAS NMR spectra for the samples prepared with the same source, aluminum isopropoxide, with two different Si/Al ratios. It shows that decreasing the Si/Al ratio from 50 to 25 did not change the Al symmetry much, which indicates that it is possible to incorporate most of the aluminum even with increasing Al contents. Recently Borade *et al* synthesized MCM-41 molecular sieves with Si/Al ratios as low as 2 without observing the presence of octahedral Al using sodium aluminate as aluminum source [9]. Figure 59 illustrates the ^{29}Si MAS NMR of the samples prepared with three different sources. All the samples showed almost similar spectra with two broad peaks at around 99 and 108 ppm. The spectra did not give any apparent information in terms of its aluminum environment. These results indicate that these spectra closely resemble those of amorphous silica [10] suggesting a broad range of Si-O-Si bond angles in these materials. Similar results were observed by all earlier authors [5,8].

Catalytic test results for the reactions of hydrogenation of naphthalene and phenanthrene and propylation of naphthalene are presented in Tables 15-17. The first observation is that they are all active in these reactions with good conversion. However, reactions went non-selectively as expected, because of the non-shape-selective nature of mesoporous materials with wide pores.

In the case of hydrogenation of naphthalene, conversion was almost hundred percent with all the catalysts. There is large amount of unconverted tetralin observed for the MCM-41 catalysts prepared with Catapal B alumina whereas for other MCM-41 catalysts, the conversion of tetralin to decalin was almost complete. The *t*-decalin/*c*-decalin ratios for all the MCM-41 catalysts are smaller and in case of the MCM-41 catalyst prepared with Catapal B the ratio is even more smaller compared to the earlier results reported on mordenite [1,2]. These results indicate that in this reaction, the isomerization of *c*-decalin to *t*-decalin takes place probably on acid sites. If that is the case, MCM-41 samples are less acidic as compared to Mordenite hence the *t*-decalin/*c*-decalin ratio is low for these materials. Moreover this ratio is even smaller for the MCM-41 catalyst prepared with Catapal B because of the poor incorporation of aluminum in the framework and hence the poor acidity.

Table 16 shows the product analyses in hydrogenation of phenanthrene over three different MCM-41 catalysts.They are all active but product selectivities are different compared to earlier results reported [11]. Especially sym-octahydroanthracene is less, which is a isomerized product from sym-octahydrophenanthrene. This isomerization is believed to be occurring on acid sites. Hence MCM-41 catalysts are not as acidic as other zeolites, especially the MCM-41 catalyst prepared with Catapal B alumina.

The product analyses of propylation of naphthalene reaction are presented in Table 17. The alkylation over zeolites is known to occur on acid sites. The MCM-41 catalyst prepared with Catapal B is not as active as other two MCM-41 catalysts. Hence the catalyst prepared with Catapal B is less acidic, which again confirms the poor incorporation of aluminum in the framework compared to other two catalysts. From the product analyses it is clear that tri- and tetraisopropylnaphthalene are formed in large quantities, which is clear indication of the non-selective nature of these mesoporous materials compared other zeolites [12, 13].

In conclusion, all the results presented in this section confirm our earlier results regarding mesoporous molecular sieves (MCM-41) synthesis and their physico-chemical properties. Our results and findings can be summarized as follows: 1) Al-MCM-41 mesoporous molecular sieves can be synthesized using different aluminum sources; 2) among three different sources (aluminum isopropoxide, aluminum sulfate and Catapal B) the first two are good for better aluminum incorporation resulting good acidity. These results are confirmed by XRD, NMR, TGA of *n*-butylamine desorption and catalytic tests.

References

1. H. H. Schobert, S. Eser, C. Song, P. G. Hatcher, A. Boehman and M. M. Coleman, *Advanced Tjermally Stable Jet Fuels*, 92PC92104-TPR-10, p. 90.

2. H. H. Schobert, S. Eser, C. Song, P. G. Hatcher, A. Boehman and M. M. Coleman, *Advanced Thermally Stable Jet Fuels*, 92PC92104-TPR-9, p. 37.

3. E. Schmidt, S. Kirby, C. Song and H. H. Schobert, *Novel bimetallic dispersed catalyts or temperature programmed coal liquifaction*, DE AC22-92PC92122-TPR-5.

4. P. A. Jacobs and J. A. Martens, *Synthesis of high silica aluminosilicate zeolites*, Elsevier, 1987.

5. C. T. Kresge, M. E. Leonowicz, W. J. Roth, J. C. Vartuli and J. S. Beck, *Nature*, 1992, 359, 710.

6. J. S. Beck, J. C. Vartuli, W. J. Roth, M. E. Leonowicz, C. T. Kresge, K. D. Schmitt, C. T. W. Chu, D. H. Olson, E. W. Sheppard, S. B. McCullen, J. B. Higgins and J. C. Schlenker, *J. Am. Chem. Soc.*, 1992, 114, 10834.

7. P. J. Branton, P. G. Hall and K. S. W. Sing, *J. C. S., Chem. Commun.*, 1993, 1257.

8. C.-Y. Chen, H.-X Li and M. Davis, *Microporous Mater.*, 1993, 2, 27.

9. R. B. Borade and A. Clearfield, *Catalysis Letters*, 1995, 31, 267.

10. G. E. Maciel and D. W. Sindorf, *J. Am. Chem. Soc.*, 1980, 102, 7606.

11. C. Song and K. Moffatt, *Mictoporous Mater.*, 1994, 2(5), 459.

12. C. Song and S. Kirby, *Mictoporous Mater.*, 1994, 2(5), 467.

13. A. D. Schmitz and C. Song, *Preprints of ACS Symp.*, Washington D. C., 1994, p.986.

3. Hydrogenation/dehydrogenation of polycyclic compounds using MoS_2 as catalyst (contributed by Richard Dutta)

Introduction

Coal liquefaction can be considered a viable alternative for production of advanced fuels if the coal macromolecule can be broken up into low molecular weight fragments and hydrogenated to decrease the concentration of aromatics in the final product. Previous studies have shown that the initial breakdown of coal can be achieved using various catalysts and various conditions. However, if the final product is to be a very high quality distillate, the coal liquids still need further hydrotreatment if they are to be satisfactory. One way to improve the quality is to add another step to the liquefaction process. This would employ a very active catalyst to hydrogenate the products from the first liquefaction stage. However, if operating costs are to be kept to a minimum, it would be advantageous to hydrogenate the coal fragments as they are being released during the first stage of liquefaction. This would decrease the cost of the second stage because the amount of hydrogen needed would be less. Burgess has shown that ammonium tetrathiomolybdate can be used as a catalyst precursor for coal liquefaction to produce a "pre-jet fuel" [1]. Coal conversion up to 95% were observed but the products were aromatic and contained some phenols.

Various temperature strategies have been formulated for coal liquefaction. The majority of these strategies are concerned with the depolymerisation of coal and the avoiding of retrogressive reactions. Another important aspect of temperature strategies is the thermodynamic behavior of released coal fragments. With careful "fine tuning" of the reaction conditions, it could be possible to have advantageous thermodynamics in the system along with reasonably fast kinetics of depolymerisation of the coal macromolecule. Basically, a trade-off between kinetics and thermodynamics is possible.

Model compound studies can be used to understand the fundamental behavior of coal fragments during coal liquefaction and coal liquids upgrading. The literature on hydrogenation of model compounds is vast and has been recently reviewed by Girgis [2].

The objective of the work reported in this section is to analyse the hydrogenation/dehydrogenation behavior of 2, 3, 4 and 5-ring compounds. Kinetic and thermodynamic parameters will be calculated from product distribution trends. From these parameters it should be possible to outline a possible reaction strategy that allows all these compounds to remain in their hydroaromatic states during a coal liquefaction operation. What will be important is once we have hydrogen in the system, what conditions will allow the hydrogen to remain there and which conditions will favor the dehydrogenation reactions?

Experimental

All reactions were carried out in 25mL microautoclave reactors (made of type 316 stainless steel). In all runs, 3±0.01g naphthalene or pyrene (Aldrich, 99%, used as received) and 0.075±0.005g ammonium tetrathiomolybdate (Aldrich, used as received) were weighed into the reactor. The reactor was then evacuated and pressurized with hydrogen to 7MPa. Heating was accomplished by lowering the reactor into a fluidized sand bath preheated to the desired temperature. After a measured reaction time, the reactor was quenched to room temperature by immersing it in a cold water bath. The products from the reaction were removed from the reactor using THF. The THF was removed by rotary evaporation and the product was weighed. It was found that in all cases the weight of the products equaled the weight of the original pyrene before reaction. The products were dissolved in acetone and analysed using a Perkin-Elmer 8500GC. As all of the compounds in the products were detected, and the responses of these compounds are similar, peak areas gave mass fractions directly. This was confirmed by injecting standard mixtures of naphthalene and tetralin.

In order to determine the dehydrogenation behavior of the hydrogenated pyrenes, the products from pyrene hydrogenated at 350°C and 60 minutes, 400°C and 80 minutes, and 450°C and 40 minutes, were catalytically dehydrogenated under N_2. This was accomplished using the same reactors as in the hydrogenation step. The products from the three hydrogenations listed above were weighed into the reactor along with a 1wt% (metal) loading of ATTM. The reactor was pressurised with approx. 3MPa N_2 and immersed in a sand bath at the desired temperature and for the desired reaction time. After this time, the reactor was quenched as before, and the products were removed using THF. The THF was rotary evaporated leaving the product behind. The products were analysed using GC as before. The dehydrogenation behavior of tetralin was investigated in a similar way to the hydrogenated pyrenes.

Results and discussion

1. Naphthalene

Thermodynamics. Figure 60 shows the product distributions of naphthalene hydrogenation at 350, 400 and 450°C for various reaction times up to 3hrs. In all cases only tetralin was detected as a hydrogenation product of naphthalene. No decalin was observed. Cracking/isomerisation products of tetralin were observed at 450°C, but total concentration did not exceed 5wt%. At 450°C, conversion of naphthalene to tetralin reaches a maximum at 51%. At 400°C, conversion is 62% and at 350°C the reaction does not reach equilibrium, but after 3hrs conversion is 72% (to calculate K_p for 350°C reaction, extrapolation used to assume 95% conversion). From these equilibrium compositions, K_p values were calculated as below:

$$K_p = \frac{[\text{tetralin}]_{eq.}}{}$$

$$[\text{naphthalene}]_{eq}.[H_2 \text{ pressure}]^2$$

Table 18 reports the Kp values for naphthalene hydrogenation. As expected, Kp decreases with increasing temperature. This is because thermodynamics controls the extent of the reaction as the temperature increases. This can be confirmed by looking at the expression $\Delta G=\Delta H-T\Delta S$, but written in the form $-\Delta G/T=-\Delta H/T+\Delta S$. When the reaction is exothermic (hydrogenation reactions are exothermic), $-\Delta H/T$ represents a positive change in the entropy of the surroundings, and this is a driving force for the reaction going from left to right. But if the temperature is raised, $-\Delta H/T$ gets smaller, and so the increasing entropy of the surroundings is a less potent driving force, and the equilibrium lies less far to the right.

The variation in Kp with temperature can be used to find the enthalpy of the reaction. This is done using the van't Hoff isochore equation:

$$\frac{d \ln Kp}{dT} = \Delta H/RT^2 \qquad 1$$

This can be changed to:

$$\frac{d \ln Kp}{d(1/T)} = -\Delta H/R \qquad 2$$

Figure 61 shows the van't Hoff plot of naphthalene hydrogenation. The plot shows two lines, one includes the value at 450°C, the other does not. The reason for plotting two lines is because in practice the van't Hoff equation is inaccurate, especially at the higher temperatures. Therefore a range of values for ΔH is reported. The values of –25.5–39.5 kcal/mol are comparable to values given in the literature (–29–32 kcal/mol) [3, 4].

Kinetics. A simple pseudo-first order reaction is proposed for the hydrogenation of naphthalene to tetralin:

$$\text{Naphthalene} + 2H_2 \text{ -------> Tetralin}$$

$$\frac{d[\text{naphthalene}]}{dt} = -k\,[H2]\,[\text{naphthalene}] = -k'[\text{naphthalene}]$$

$$-\frac{d[\text{naphthalene}]}{[\text{naphthalene}]} = k'\,dt$$

$$\ln \frac{[\text{naphthalene}]_t}{[\text{naphthalene}]_0} = -kt \qquad 3$$

Figure 62 shows a plot of equation 3 vs time for the three temperatures employed in this investigation. If all the data for each time are plotted, deviations from the straight line are observed. This is due to several reasons including heat-up effects, change in overall pressure as hydrogenation proceeds and thermodynamics "pulling" the reaction away from first-order

behavior. Therefore only the data points that lead up to these effects are plotted. It can be seen that the reaction at 450°C is affected sooner than at 400°C, and 400°C is affected earlier than the reaction at 350°C. This trend suggests that thermodynamics are affecting the reaction as time and temperature increase. The slopes of the lines give the rate constant.. It can be seen that as temperature increases, the rate constant increases.

Figure 63 shows an Arrhenius plot of naphthalene hydrogenation. An activation energy of 12.6 kcal/mol is calculated from this plot.

Kinetics vs Thermodynamics. If hydroaromatics are to be produced from aromatics, two factors have to be considered.

1. Conversion.
2. Length of time to get to the desired conversion level.

As can be seen from the data, conversion decreases with increasing temperature, but the kinetics of the reaction are slower at lower temperatures. From the data, it can be concluded that high temperatures are desirable for the first 40 minutes of reaction, but after this time thermodynamics limit the conversion. At this point, it is then advisable to drop the temperature to below 400°C, and continue to convert naphthalene to tetralin as seen in the 350°C reaction. To hydrogenate only at 350°C would take too long to achieve respectable conversions, i.e. conversion at 350°C and 120 minutes is the same as 450°C and 60 minutes. Therefore in hydrogenating naphthalene to tetralin a reverse temperature stage reaction is proposed.

Stage 1. 400°C and 40 minutes reaction time.

Stage 2. 350°C and 60 minutes reaction time.

Dehydrogenation reactions of tetralin

Figure 64 shows the product distribution of tetralin dehydrogenation at 350, 400, and 450°C for various reaction times up to 30 minutes. Figure 65 shows the kinetics of dehydrogenation of tetralin using a similar model as the hydrogenation reaction. As temperature increases, the rate of dehydrogenation increases, and the conversion of tetralin to naphthalene also increases . At 350 and 400°C, conversion to naphthalene does not exceed 13%, but at 450°C conversion is 42%. This explains the rapid approach to equilibrium seen in the hydrogenating reactions and the relatively low conversions seen at the high temperature of 450°C.

2. Pyrene

Thermodynamics. Product distribution of pyrene, dihydropyrene, tetrahydropyrene and hexahydropyrene are shown in Figures 66, 67 and 68. From these product distributions it can be seen that temperature is affecting the conversion of pyrene to hydrogenated pyrenes. At 450°C, equilibrium is reached after 20 minutes, with 28% conversion of pyrene. At 400°C, equilibrium is reached after 80 minutes, with 45% conversion of pyrene. At 350°C, equilibrium is not observed, even after 120 minutes of reaction. Conversion at this point is 55% pyrene to hydrogenated

pyrenes. These product distribution trends are similar to that observed for napthalene hydrogenation in that as temperature increases, conversion decreases but the rate of reaction to equilibrium increases. Kp values are reported in Table 19. Kp decreases with increasing temperature. These values can be used to determine the enthalpy of reaction as described earlier. A value of –6.4 kcal/mol is obtained from Figure 10. This value is a reasonable comparison to the value obtained by Johnston (–10 kcal/mol)[5].

Kinetics. Figure 70 shows a first order kinetic plot of pyrene hydrogenation. As temperature increases, the rate constant increases from 0.0088 min^{-1} (350°C) to 0.014 min^{-1} (400°C) and 0.019 min^{-1} (450°C). Figure 71 ahows an Arrhenius plot for pyrene hydrogenation and an activation energy of 6.88 kcal/mol is calculated from the slope of the plot.

Kinetics vs thermodynamics. The same arguments apply for pyrene as they did for naphthalene. A reverse temperature stage reaction is proposed for pyrene hydrogenation:
Stage 1. 400°C and 20 minutes reaction time
Stage 2. 350°C and reaction time set for the desired conversion.

Dehydrogenation of hydropyrenes.

Figures 72, 73 and 74 show the dehydrogenation product distributions of dihydropyrene, tetrahydropyrene and hexahydropyrene. Figures 75, 76 and 77 show the kinetics of dehydrogenation of the three hydropyrenes. It can be seen that dehydrogenation is rapid and complete at 450°C. At the lower temperatures, dehydrogenation is slower and complete dehydrogenation to pyrene is not seen in the 30 minutes reaction used in this study. The rate constants calculated from the first-order kinetic plots are reported in Table 20. It can be seen that the dehydrogenation rate constants are similar for the three hydropyrenes.

Comparisons between naphthalene and pyrene

Table 21 shows a comparison of the parameters for the two compounds. It can be seen that as ring size increases, enthalpy of reaction decreases and activation energy decreases. Figure 78 shows a plot of dehydrogenation rate/hydrogenation rate vs temperature. This graph represents the sucseptibility of compounds to dehydrogenation. As can be seen pyrene is more readily dehydrogenated than naphthalene, and the effect of increasing temperature is more prominent as ring size increases.

Future Work

The work will be expanded to inlude 3-ring systems and other 4-ring compounds. When the parameters are calculated for these compounds and plotted vs ring size, molecular weight etc., it should be possible to make predictions as to how other compounds behave under

hydrogenating/dehydrogenating conditions. Ideal temperature strategies will be estimated from the product distribution curves and compared for the different compounds.

References

1. Burgess, C. PhD, 1994, Pennsylvania State University.
2. Girgis, M. J. and Gates, B. C. *Ind. Eng. Chem. Res.* 1991, ***30***, 2021.
3. Frye, C. G. *J. Chem. Eng. Data.* 1962, ***7***, 592.
4. Frye, C. G. and Weitkamp, A. W. *J. Chem. Eng. Data.* 1969, ***14***, 372.
5. Johnston, K. P. *Fuel* ,1984, ***63***, 463.

4. Shape-Selective Naphthalene Hydrogenation for Production of Thermally Stable Jet Fuels. (Contributed by Andrew D. Schmitz and Chunshan Song)

Introduction

Per-hydrogenation of naphthalene (Nap) results in two decalin (DeHN) isomers, *cis-* (c) and *trans-* (t). We previously reported that compared with Pd/zeolite catalysts, Pt/zeolite catalysts show lower initial t-DeHN selectivities and lower isomerization rates [1-2]. In the extreme case, Pt/HY gives a decalin trans/cis ratio of 0.2-0.4 which does not change with time.

Huang and Kang have reported the pathway shown in Scheme 1 for Nap hydrogenation over Pt/Al_2O_3 at 200-260 °C [3]. It was assumed that dehydrogenation of DeHN could be neglected because the temperature was low and hydrogen is in large excess. The isomerization of c-DeHN was also treated as irreversible. As shown in Scheme 1 for reaction at 200 °C, $k'_2/k'_3 = 2.39$; whereas, at 260 °C, $k'_2/k'_3 = 3.62$. Clearly, Pt/Al_2O_3 is selective for c-DeHN at 200 °C and above. Isomerization of c-DeHN k'_4 is slower than hydrogenation of TeHN to t-DeHN. Therefore, t-DeHN is predominantly formed by direct hydrogenation rather than by c-DeHN isomerization. This is even more true at lower reaction temperatures where k'_4 is comparatively very small. Temperature dependencies of the rate constants show that below 135 °C, k'_3 exceeds k'_2., so Pt/Al_2O_3 should be selective for t-DeHN at low temperatures.

Review of the data reported by Huang and Kang revealed that the activation energies cited in the paper are really E_a/R, where R is the gas constant (1.987 cal/mol·K). The activation energies cited in Scheme 1 were corrected by multiplying the reported values by R.

Herein we report experiments designed to determine if both decalins are formed in parallel, or if t-DeHN is formed primarily by isomerization of c-DeHN, on metal-loaded zeolites. Our approach was to test the previously reported [1-2] metal-loaded zeolite catalysts under conditions that disfavor c-DeHN isomerization, and to examine the differences in the decalin product distributions. First, a series of tests was done where the catalyst charge in the reactor was decreased from 0.40 to 0.10 g. A second series of tests was done again with 0.10 g catalyst, but at 100, rather than 200 °C. According to Arrhenius equation and the corrected activation energies for Pt/Al_2O_3 from above, lowering the reaction temperature increases the ratio k'_3/k'_4 by a factor of 70 (Scheme 2). Likewise, k'_2/k'_4 is 16 times greater at 100 °C. Therefore, isomerization of c-DeHN at 100 °C on Pt/Al_2O_3 is comparatively very slow. It is plausible that the same trend should hold for noble-metal/zeolite catalysts.

Experimental

The methods used here are similar to those reported earlier [1]. Reactions were run in tubing-bomb reactors charged with 0.10 g catalyst (instead of 0.40 g), 1.0 g (7.8 mmol) Nap, 4.0 g *n*-tridecane reaction solvent, and 0.35 g *n*-nonane internal standard. Reaction temperatures

were either 100 or 200 °C. Four catalysts were reexamined under the new decreased catalyst charge, decreased temperature conditions: Pd/HY(GB), Pt/HY(GB), Pd/HM38(AS) and Pt/HM38(AS). Conventions for catalyst nomenclature were introduced in ref. 2. The letter designations refer to catalysts prepared by G. Bowers or the two catalysts prepared by A. Schmitz which replaced the HM38-supported catalysts prepared by G. Bowers that had been used up.

Results and Discussion

The currently accepted mechanism for Nap hydrogenation, as detailed by Weitkamp [4], will first be examined to better understand the experimental data. This mechanism makes clear accounts of the modes of formation of both decalin isomers based on the results of a large number of independent experiments.

Mechanism of Naphthalene Hydrogenation [4]. TeHN is almost always observed in the hydrogenation of Nap and is assumed to be the predominant intermediate. Other partially hydrogenated forms of Nap are also observed at very low concentrations. Of particular importance are the alkenes shown in Scheme 3, $\Delta^{9,10}$-octahydronaphthalene 1 ($\Delta^{9,10}$-octalin) and $\Delta^{1,9}$-octalin 2. The other partially hydrogenated products do not play a direct role in determining DeHN *cis/trans* configuration.

Since the isomer-configuration determining step in Nap hydrogenation probably involves a cyclic alkene, it is helpful to review some concepts concerning the coordination and reaction of alkenes on organometallic metal-hydride complexes [5]. The proposed intermediates are either isolable, have been spectroscopically observed, or at least, directly implied by reaction stoichiometry, stereochemistry, isotope tracer studies, etc. Any mechanisms proposed for reactions on heterogeneous metal particles should follow the principles gleaned from reactions observed for molecular organometallic species in solution.

Hydrogen addition to a cyclic alkene may occur with or without prior coordination of the alkene, although only prior coordination is considered here. Regardless, hydrogen addition is always *cis*. For example, Muetterties et al. used η^3-$C_3H_5Co[P(OCH_3)_3]_3$ precatalyst for Nap hydrogenation to obtain complete Nap conversion to 99% cis-DeHN and 1% TeHN [6]. The first step in this reaction is believed to be generation of a coordinatively unsaturated complex by η^3 6 η^1 conversion, followed by oxidative addition of hydrogen as shown in Scheme 4. Thus, alkene hydrogenation involves oxidative addition (dissociative adsorption) of molecular hydrogen to make metal-hydride species. The metal M has a certain coordination sphere of ligands L which are generally neighboring metal atoms for heterogeneous catalysts. Surface metal atoms in microcrystalline particles are coordinatively unsaturated; whereas, for molecular compounds, oxidative addition of hydrogen requires a prior ligand dissociation or reductive elimination (see below) to make a coordinatively unsaturated species. Hydrogen adsorption on Pt and Pd

heterogeneous catalysts is dissociative with a 1:1 stoichiometry between M and hydrogen atoms (Scheme 5).

In Scheme 6, it is shown that alkene coordination to a metal complex is possible when there is an open coordination site. The second step of this scheme, migratory insertion of the cyclic alkene into the M-H bond, can be viewed as a *cis*-addition of M-H across the double bond. However, if R_1 and R_2 are not the same, it is often not easy to predict whether M-H addition will occur Markovnikov or not. Reductive elimination, the last step of Scheme 6, completes the cycle, and gives a net cis addition of H_2.

Now, it will be demonstrated how these principles apply to the alkenes 1 and 2 which are known to play a critical roles in determining DeHN configuration. Coordination of 1 to a metal atom with subsequent hydrogen addition by the steps outlined above, and no alkene isomerization, can only result in the formation of c-DeHN [4]. If fact, Weitkamp showed by deuterogenation of 1 and 2 over heterogeneous Pt catalysts that dideuterium addition across the $\Delta^{9,10}$-alkene only occurs cis [4]. Any t-DeHN formed from 1 had deuterium incorporation d_3 (not just d_2) due to prior isomerization of 1 to 2 as shown in Scheme 7. The second step in Scheme 7, abstraction of a ß-hydrogen, results in coordinated $\Delta^{1,9}$-octalin 2. This coordinated olefin may remain adsorbed and undergo deuterogenation, forming c-DeHN-d_3. Or, it may dissociate from the metal (i.e., desorb from the catalyst surface). Readsorption of 2 can occur in two ways: deuterium down or deuterium up. Deuterogenation then gives either c-DeHN-d_3, or t-DeHN-d_3, respectively. Platinum, rhodium, iridium and especially ruthenium favor cis-adsorption of 2 (metal and bridgehead deuterium on the same face as shown in Scheme 7) and produce mostly c-DeHN. Other metals, especially palladium, favor trans-adsorption leading to t-DeHN.

Naphthalene Experimental Data. Data for the 16 new experiments reported here are compared with the related test data using 0.40 g catalyst at 200 °C from previous work in Tables 22-25. Except for Pt/HY, nearly 100% Nap conversion is obtained even with the lower catalyst charge and lower reaction temperature. Pt/HY is quite inactive at 100 °C. Tables 22 and 24 show that at 100 °C, Pd is highly selective for stopping the hydrogenation at TeHN as has been previously reported [4]. Both Pd and Pt will preferentially hydrogenate alkenes in alkene/arene mixtures. Other metals, such as Ru, Rh and Ir, are more selective for arene hydrogenation. Reasons for these differences are certainly tied to the interaction strength between the unsaturated ligand and the metal. If the bonding is too weak, the unsaturated ligand will react sluggishly. Whereas, formation of very robust unsaturate-metal complexes prevents desorption and poisons the catalyst.

Of particular importance to the focus of this report are the columns labeled t-DeHN selectivity (percent t-DeHN in the DeHN products) in Tables 22-25. If both decalin isomers are produced in parallel, this ratio should remain constant over time, barring significant contribution

from c-DeHN isomerization. As the concentrations of partially saturated intermediates diminish, more active sites will be made available to promote c-DeHN isomerization. When all of the Nap and TeHN have been saturated, the main catalytic reaction becomes isomerization.

HM38-supported catalysts (Tables 24 and 25) have high c-DeHN isomerization activity. None of the parallel experiments show t-DeHN selectivity constant over time, rather t-DeHN selectivity increases over time due to c-DeHN isomerization. All runs at 200 °C give complete Nap saturation in a very short time, so isomerization of c-DeHN is the main reaction. It is difficult to judge whether there are truly parallel paths to *cis*- and *trans*-DeHN from these data alone. Comparing the same catalysts at 100 °C, only partial Nap saturation occurs in 30 and 60 min. Still, isomerization of c-DeHN occurs, to a larger extent on Pd/HM38 (18% increases in t-DeHN selectivity) compared to Pt/HM38 (10% increase).

Quite on the contrary, Tables 22 and 23 show that t-DeHN selectivity is quite constant within parallel tests for M/HY. For Pd/HY at 200 °C, isomerization of c-DeHN seems to occur slowly even though complete Nap saturation occurs at an early stage. Within experimental error, t-DeHN selectivity is constant for the two runs at 100 °C on Pd/HY. Isomerization is insignificant, yet the DeHN *trans/cis* ratio is approximately 1. This is, then, direct evidence for parallel formation of the two DeHN isomers. On Pt/HY, the t-DeHN selectivity is constant at 200 °C. c-DeHN isomerization is insignificant and this is another example of parallel DeHN isomer formation. (We have already discussed the possible sources of experimental error that cause small variations in the DeHN trans/cis ratios for Pt/HY [2].) Strangely, there is 30% increase in t-DeHN selectivity between 30 and 60 min at 100 °C (Table 2). The Nap conversions are very low, so it is possible that experimental error has caused a discrepancy.

Implications on the Mechanism. Although we have a plausible mechanism for Nap hydrogenation, where the hydrogenation of 1 and 2 ultimately determine DeHN configuration, it is still not clear why some catalysts make more t-DeHN than others, and why Pt/HY makes so little t-DeHN and does not promote c-DeHN isomerization. The most important factors seem to be the relative concentrations of 1 and 2 together with the relative ease of desorption of 2 from the catalyst. The Dewar, Chatt Duncanson model [5] for alkene coordination to a metal is shown in Scheme 8. Alkenes can function both as σ-donors (electron density transfer from the filled alkene π-orbital to empty σ-symmetry metal orbital) and π-acceptors (electron density transfer a filled metal d orbital of π-symmetry to a non-bonding π^*-alkene orbital). Alkene σ-donation is most significant when the metal bears a positive charge; on the other hand, alkene ligands are primarily π-acceptors when the metal retains more electron density [5, 7]. Similar models are proposed for arene coordination to a metal, but the ligand molecular orbitals are more complicated.

Group VIII metals on acidic zeolites, especially on HY, are known to be electron deficient [7]. Consequently, alkene or arene adsorption results in a net electron density transfer from the

alkene or arene to the metal (σ-donation) More electron-rich ligands bond more strongly to the metal and give higher heats of adsorption. Thus, toluene is adsorbed more strongly than benzene and is hydrogenated at a slower rate than benzene [7].

Compared to Pd on the same zeolite, Pt always gives a higher initial c-DeHN selectivity, Pt isomerizes c-DeHN more slowly, and Pt has lower activity (compare Nap conversions at 100 °C in Tables 1 and 2). These differences may tied to the metal-$\Delta^{1,9}$-octalin bond strengths. Formation of t-DeHN requires that 2 desorb from the surface of the catalyst, rotate, and undergo *trans* adsorption. If this key octalin intermediate is strongly bound on electron deficient Pt, its desorption prior to hydrogenation is unlikely. Its most probable course of reaction is hydrogenation to c-DeHN, but since it is strongly bound, even hydrogenation occurs slowly. It follows that k'_2/k'_3 will be larger for Pt/zeolite, and since 2 is also an intermediate in c-DeHN isomerization, k'_4 will be smaller for Pt/zeolite. In the extreme case, Pt/HY has very low activity and has high selectivity for c-DeHN with little or no isomerization. If the alkene-metal bond strength argument applies, Pt on HY is extremely electron deficient.

Is it a coincidence that Pt/HY has the largest metal particle size (1700 Å average diameter) of all the catalysts examined by XRD line-broadening [1]? Metal-support interactions are generally unimportant for large particles; significant effects on metal particle shape and electronic properties are generally only noted for very small metal particles (i.e., < 50 Å diameter). It may be that c-DeHN is produced on highly dispersed Pt that is XRD transparent and located in the confines of the HY major pore structure. Large-particle Pt has proportionately much lower surface area and probably resides on the external surfaces of the catalyst. Nap and its hydrogenated products, however, are concentrated in the catalyst particle's interior. Only a small fraction of molecules would diffuse to the external surface and react on the large metal particles. A second possibility with large Pt particles on the external surface of the catalyst is partial channel-opening blockage which could give rise to shape-selectivity.

Further study is clearly necessary to deepen our understanding of the mechanisms involved. Electron microscopy and hydrogen chemisorption could be used to reevaluate metal particle dispersion. A simple test run could be done with Pt foil as the catalyst. If the locus of activity on Pt/HY is really the large Pt particles that interact very little with the support, Pt foil should give a similar product distribution.

Conclusions

By adjusting the reaction conditions, it has been confirmed that both decalin isomers can be produced in parallel during Nap hydrogenation over metal-loaded zeolites. Reaction kinetics for Nap hydrogenation over Pt/Al_2O_3 were discussed. Particular attention was paid to the effects of temperature on the relative magnitudes of the rate constants. In accord with previously reported

mechanisms, we have shown that hydrogenation of $\Delta^{9,10}$-octalin and $\Delta^{1,9}$-octalin may play an important role in determining the DeHN *cis/trans* configuration. It has been proposed that Pt on acidic zeolites is electron deficient, and that strong bonding between the octalins and electron deficient Pt retards the rate of the alkene desorption step necessary for production of t-DeHN. Alternative suggestions were made to explain the uniquely high c-DeHN selectivity of Pt/HY: a bidisperse metal phase, or a special shape selectivity that arises from partial channel blockage by large Pt particles.

References

1. Schmitz, A.D.; Bowers, G.; Song, C. *Advanced Thermally Stable Jet Fuels*, Technical Progress Report, 92PC92104-TPR-9, p 37.
2. Schmitz, A.D.; Song, C. *Advanced Thermally Stable Jet Fuels*, Technical Progress Report, 92PC92104-TPR-10, p 66.
3. Huang, T.-C.; Kang, B.-C., "Kinetic Study of Naphthalene Hydrogenation over Pt/Al_2O_3," *Ind. Eng. Chem. Res.* ***1995***, 34, 1140.
4. Weitkamp, A.W. "Stereochemistry and Mechanism of Hydrogenation of Naphthalenes on Transition Metal Catalysts and Conformational Analysis of the Products," *Adv. Catal.* **1968**, *18*, 1.
5. Collman, J.P.; Hegedus, L.S.; Norton, J.R.; Finke, R.G. *Principles and Applications of Organotransition Metal Chemistry*; University Science Books: Mill Valley, CA, 1987.
6. Stuhl, L.S.; Rakowski DuBois, M.; Hirsekorn, F.J.; Bleeke, J.R.; Stevens, A.E.; Muetterties, E.L., "Catalytic Homogeneous Hydrogenation of Arenes. 6. Reaction Scope for η^3-$C_3H_5Co[P(OCH_3)_3]_3$ Catalyst," *J. Am. Chem. Soc.* **1978**, *100*(8), 2405.
7. Stanislaus, A.; Cooper, B.H., "Aromatic Hydrogenation Catalysis: A Review," *Catal. Rev.-Sci. Eng.* **1994**, *36*(1), 75.

5. Novel Approaches to Low-Severity Coal Liquefaction and Coal/Resid Co-processing using Water and Dispersed Catalysts.
(Contribution by Russell Byrne and Chunshan Song).

Introduction

As outlined in our previous introductory report, work in our laboratory has demonstrated a remarkable synergism between water and a dispersed molybdenum sulfide catalyst for promoting liquefaction of Wyodak subbituminous coal at low severity (350-375°C). These results appear to be contrary to conventional wisdom regarding the detrimental effects of water during the catalytic hydroliquefaction of coal [1-4]. Our findings, to date, indicate that both reaction temperature range and water/coal ratio are key factors in determining the net influence of water upon the catalytic liquefaction of this particular coal [5-9]. Significantly, we have observed the same promotional trends arising from the co-use of water and dispersed molybdenum sulfide catalyst both in solvent-free experiments, and in liquefaction experiments performed in the presence of either a non-donor (1-methylnaphthalene), or an H-donor (tetralin) [6,9]. Indeed, for experiments performed using water and Mo catalyst at 350°C, the presence of either tetralin or 1-methylnaphthalene had no positive impact on conversion compared to that achieved in the solvent-free reactions. In contrast, however, for catalytic runs at 400°C, using ATTM without added water always gives the highest conversion, either with or without an organic solvent [6,9]. These interesting results have demonstrated unequivocally that at a relatively low temperature, and in the correct proportion, water can have a dramatic promoting effect on the catalytic liquefaction of Wyodak subbituminous coal.

Our findings with Wyodak coal have provided the impetus behind an ongoing fundamental and exploratory study on the promotional effects of water on catalytic coal liquefaction. Although the synergistic enhancement in conversion through co-use of water and dispersed Mo sulfide catalyst has been amply demonstrated for Wyodak subbituminous coal, one of our primary interests is to determine whether this interesting and potentially significant phenomenon is observable with other coals, particularly coals of differing rank. In this section, preliminary results from recent work using Pittsburgh #8 high-volatile bituminous coal are presented which indicate a similar dramatic improvement in coal conversion upon addition of a small amount of water in the presence of dispersed molybdenum sulfide catalyst. Reactions performed at two different temperatures (350 and 400°C) are discussed and compared to those for Wyodak coal.

Experimental

Materials. The coals used were Wyodak subbituminous coal and Pittsburgh #8 high-volatile bituminous coal. These are Department of Energy Coal Samples (DECS-8 and DECS-12, respectively) maintained in the DOE/Penn State Coal Sample Bank, ground to < 60 mesh, and stored under argon atmosphere in heat sealed, argon-filled laminated foil bags consisting of three layers. Wyodak subbituminous coal contains 28.4% moisture, 32.4% volatile matter, 29.3% fixed carbon and 9.9% ash, on as-received basis; 75.8% C, 5.2% H, 1.0% N, 0.5% S, and 17.5% O, on dmmf basis. Pittsburgh #8 high-volatile bituminous coal contains 2.4% moisture, 35.2% volatile matter, 52.4% fixed carbon and 10.0% ash, on as-received basis; 84.8% C, 5.7% H, 1.4% N, 0.8% S, and 7.4% O, on dmmf basis.

Drying Treatment. Both fresh raw coals, and coals pre-dried in a vacuum oven (vd) were used. Vacuum drying was performed by placing a flask containing around 10-15 g of the coal into an oven which was then evacuated at room temperature and gradually heated up within 1 h to 100°C, followed by isothermal holding for 2 h and subsequent cooling down to room temperature under vacuum. Fresh as-received coal, with minimum possible exposure to air, was used as the raw coal.

Catalyst Impregnation. Reagent grade ammonium tetrathiomolybdate (ATTM, obtained from Aldrich with 99.97% purity) was employed as the dispersed catalyst precursor. The water-soluble inorganic salt ATTM is expected to generate molybdenum sulfide particles on the coal surface upon thermal decomposition at > 325°C. ATTM was dispersed onto either the raw coal or vacuum-dried coal samples by incipient wetness impregnation from its aqueous solution. The metal loading was kept constant at 1 wt% Mo on dmmf coal basis, unless otherwise specified. The general procedure employed involved dissolving the required mass of ATTM in the minimum amount of water necessary to effect solubilization. The ATTM solution was then slowly added dropwise to the coal with stirring. For vacuum-dried Wyodak coal, typically around 0.5 g H_2O/g coal was needed to reach the point of incipient wetness. For raw Wyodak coal, correspondingly less water was required. In the case of Pittsburgh #8 coal, however, the minimum amount of water needed for complete solubilization of ATTM was found to exceed the point of incipient wetness, and after catalyst addition, the coal had almost a slurry-like appearance. Following impregnation, the coal samples were dried in a vacuum oven at 100°C for 2h prior to use.

Liquefaction and Product Work-up. Liquefaction experiments were carried out in 25 mL tubing bomb reactors with around 4 g of coal at 350 or 400°C for 30 min (plus an additional 3 min for reactor heat-up time). For both thermal and catalytic experiments with added water, the weight ratio of water to dmmf coal was kept at around 0.46. All reactions described in this section were performed in the absence of any organic solvent. The reactors were purged several times with H_2 and finally pressurized with 6.9 MPa H_2 (cold). A fluidized

sandbath maintained at the desired temperature was used as the heater. After the desired reaction time, the reactors were removed from the sandbath and quenched in a cold water bath to rapidly bring down the temperature < 150°C, then were allowed to cool down to ambient temperature in air. The reactors were vented and the mass of product gases (including residual H_2) determined. Gaseous products were analyzed by GC, with the aid of gas standards for quantitative calibration of GC responses of CO_2, CO, H_2 and C_1–C_4 hydrocarbon gases. H_2 consumption was determined by subtracting the mass of residual H_2 found in the product gases (determined by GC) from the mass of H_2 initially charged. The total yield of coal-derived product gases was also determined by the mass difference between (charged reactor + reactants) and the (vented reactor + products). The liquid and solid products were carefully recovered from the reactor and transferred to an extraction thimble. For the solvent-free experiments performed with added water, it was found necessary to grind up the recovered product solids prior to transferring them to the extraction thimble. The coal solids from these reactions were hard granules and had an entirely different physical appearance than those from comparable anhydrous experiments (which generally remained as fine particles). As will be described later, a considerable difference was observed, in terms of product extractability, between duplicate experiments where the coal solids were extracted "as-recovered", compared to where the coal solids were first ground up prior to extraction. In the former case, the heavier asphaltene and preasphaltene molecules were found to be retained within the granules, resulting in a significant under-estimation of conversion. The products were subsequently separated by sequential Soxhlet extraction into oil (hexane solubles), asphaltene (toluene soluble but hexane insoluble), preasphaltene (THF soluble but toluene insoluble), and residue (THF insoluble). After removing the bulk of the solvent on a rotary evaporator, the asphaltenes and preasphaltenes were dried under vacuum at 110°C for > 10 h. The THF-insoluble residues were rinsed through, first with acetone, then with pentane, in order to remove all the THF, followed by drying at 110°C for > 10 h under vacuum. The overall conversion of coal into soluble products was determined on the basis of the mass of recovered vacuum-dried THF-insoluble residues. It is noteworthy that the THF-insoluble residues from Pittsburgh #8 coal were found to apparently require longer drying times than those from Wyodak coal, and were typically dried at 110°C > 24 h under vacuum. Frequently, for this coal, the yields of isolated products (ie, oils + asphaltenes + preasphaltenes + gas) were greater (by a few percent) than indicated from the overall conversion based on the mass of vacuum-dried THF-insoluble residue. The exact reason for this observation remains to be clarified. The data presented for Wyodak coal experiments have been at least duplicated and generally represents the average of two or more reactions. For Pittsburgh #8 coal, the data presented here are preliminary and duplicate experiments are presently ongoing. Duplicate reactions which have been performed

show good reproducibility, the deviation in conversions and product yields are generally within ±2 wt%.

Results and Discussion

Experimental results for the catalytic and non-catalytic solvent-free reactions of Pittsburgh #8 coal, performed in both the presence and absence of added water, are summarized in Table 26. These results are also illustrated in Figure 79 (350°C) and Figure 80 (400°C). For ease of comparison in the following discussion, equivalent data for Wyodak coal is also given in Figure 3 (350°C) and Figure 4 (400°C), respectively.

Positive Effect of Added Water in Catalytic Liquefaction at 350°C. Referring to Figure 79 for the runs of Pittsburgh #8 coal at 350°C, it can be seen that compared to the non-catalytic run of vacuum-dried coal, adding water increased coal conversion from 21.9 to 33.6 wt% (dmmf). Surprisingly, using ATTM at 350°C had no apparent benefit on conversion for this coal, giving a conversion of only 24.7 wt%. This is in stark contrast to the results for Wyodak subbituminous coal. Adding water to the catalytic run, however, dramatically increased conversion of Pittsburgh #8 coal to 51.0 wt%, representing a 106% increase from the catalytic run without water, and a 133% increase from the non-catalytic run without water. Clearly, as previously seen for Wyodak coal, there is an apparent synergistic enhancement in conversion at 350°C for Pittsburgh #8 coal resulting from co-use of water and dispersed Mo sulfide catalyst. These interesting findings reveal that dispersed Mo sulfide catalyst and added water can act in concert to promote coal liquefaction at relatively low temperature. Considering product quality, it is noteworthy that Pittsburgh #8 high-volatile bituminous coal is converted largely to preasphaltenes (ie, THF-soluble but toluene-insoluble) at 350°C. The enhancement in conversion through co-use of water and catalyst is also manifest primarily as an increase in preasphaltene yields. As one might expect, gas yields from Pittsburgh #8 coal (particularly CO_2) are significantly lower than from Wyodak subbituminous coal. Interestingly, however, as can be discerned from perusal of the data in Table 26, CO_2 yields are doubled or even tripled for all reactions with added water. Similar observations have also been made for the hydrous experiments with Wyodak coal [7]. This suggests that water is interacting with certain coal functionalities, ultimately resulting in the evolution of CO_2 through oxidative processes and/or enhanced decarboxylation.

Comparing the conversion data for Pittsburgh #8 (Figure 79) at 350°C to that for Wyodak coal (Figure 81), it is interesting to note that for the non-catalytic reactions, the high-volatile bituminous coal is apparently more reactive than the lower-rank subbituminous coal, both in the absence and presence of water (ie. 21.9 wt% vs 14.5 wt%) and (33.6 wt% vs 22.5 wt%), respectively. In contrast, however, for the catalytic reactions, Wyodak coal always

gives higher conversion than Pittsburgh #8 (ie. 29.8 wt% vs 24.7 wt% for anhydrous experiments) and (66.5 wt% vs 51.0 wt% for hydrous experiments). These results clearly demonstrate that in the presence of an effective dispersed catalyst, lower-rank subbituminous coals are more reactive than first thought [10], and may in fact be more amenable feedstocks for direct liquefaction than bituminous coals (similar trends are also apparent for the reactions of these coals at 400°C).

As discussed in the Experimental section, there was a distinct difference in physical appearance between the hard granular solid products recovered from the solvent-free liquefaction experiments performed with added water, and those from comparable anhydrous experiments (which generally remained as fine particles). We adopted the practice of grinding up the granular solids from the runs with added water, prior to sequential Soxhlet extraction. A considerable difference was observed, in terms of product extractability, between duplicate experiments, one where the recovered solids were extracted "as-recovered", compared to one where the recovered coal solids were ground-up with a ground-glass stopper prior to extraction. This is illustrated for Pittsburgh #8 coal in Table 26. Experiments 14 and 15 were duplicate runs, in run 14 the product solids were extracted 'as-recovered' and an apparent conversion of 38.5 wt% was observed. In run 15, however, the product solids were ground prior to Soxhlet extraction and a conversion of 51.0 wt% was observed. In the former case, it became obvious that the heavier preasphaltene molecules were being retained within the granules, resulting in a significant under-estimation of conversion.

Effect of Temperature on Coal Conversion with H_2O and ATTM. For Wyodak coal runs at 400°C (Figure 82), using ATTM without water always gave the highest conversions. The use of ATTM alone at 400°C afforded a very high conversion for this coal (85.4 wt% (dmmf)), and a high oil yield (45.8 wt%), illustrating that, at this temperature, dispersed Mo sulfide catalyst is highly effective at promoting the hydroliquefaction of Wyodak subbituminous coal. However, addition of water to the catalytic run decreased coal conversion (to 62.1 wt%) and oil yield (to 28.2 wt%). An important implication from Figure 82 is that the presence of water at 400°C apparently decreased the effectiveness (or activity) of the dispersed catalyst. This is in distinct contrast to the strong promotional trends observed in the corresponding runs at 350°C.

Considering now the runs at 400°C for Pittsburgh #8 high-volatile bituminous coal (Figure 80), it can be seen that the addition of water to the non-catalytic run of vacuum-dried coal resulted in an increase in conversion from 36.3 wt% to 45.8 wt%. The use of ATTM alone resulted in only a modest increase in conversion (to 54.6 wt%). Adding water to the catalytic run gave a similar conversion (55.4 wt%), though interestingly, did not result in a reduction in conversion as was seen for the catalytic run of Wyodak coal at this temperature.

Indeed, addition of water to the catalytic run of Pittsburgh #8 appeared to have some benefit, in terms of product quality, in that there was a notable shift from exclusively preasphaltenes, to an increased yield of asphaltenes isolated in the added water reaction. As was the case for Wyodak coal, however, it is apparent that the strong synergistic enhancement in conversion observed through co-use of water and dispersed catalyst at 350°C, is lost at higher temperature (400°C). As was seen at 350°C, it is interesting to note that in the absence of catalyst at 400°C, Pittsburgh #8 is apparently more reactive than Wyodak coal. In the catalytic reactions, however, Wyodak coal always gives the highest conversion. The dispersed Mo sulfide catalyst generated from ATTM does not appear to be a very effective catalyst for promoting the hydroliquefaction of the higher-rank coal. For example, the conversion of Pittsburgh #8 coal achieved in the catalytic run with added water at 350°C (51.0 wt%), is similar to that observed in the catalytic run at 400°C (54.6 wt%).

Summary

We have found that there are strong synergistic effects between water and a dispersed molybdenum sulfide catalyst for promoting the low temperature (350°C) liquefaction of both Wyodak subbituminous and Pittsburgh #8 bituminous coals. Relative to the catalytic runs of the dried coals, the co-use of catalyst and water (at water/dmmf coal = 0.46) can double the coal conversion at 350°C for 30 min, from 29.8 wt% to 66.5 wt% for Wyodak coal, and from 24.7 wt% to 51.0 wt% for Pittsburgh #8. At higher temperature (400°C) the promotional effects of adding water are lost and, in the case of Wyodak coal, actually inhibits catalyst activity resulting in a reduction in conversion. For Pittsburgh #8 coal, adding water to the catalytic run at 400°C results in a similar conversion to that from the use of catalyst alone. There is, however, some apparent benefit in terms of a slight improvement in product quality for the added water reaction. We plan to perform a more thorough study of the effects of reaction temperature (ie. 325–425°C) on the water-promoted catalytic liquefaction of Pittsburgh #8 coal in order to construct a temperature vs conversion profile, as we have already done for Wyodak coal [5,9]. In this way, we hope to identify the optimum temperature window in which water-dispersed catalyst synergistic interaction is maximized for conversion of Pittsburgh #8 coal.

In the present study, the water/dmmf coal ratio employed was kept constant at around 0.46. This ratio was selected for this preliminary series of reactions with Pittsburgh #8 as it was previously found to be the optimum ratio for Wyodak coal experiments. Clearly, however, it may not necessarily be the most suitable for Pittsburgh #8, we therefore intend to perform a series of catalytic runs at various H_2O/coal ratios in order to determine the optimum ratio for maximizing conversion of this particular coal.

References:

1. Bockrath, B.C.; Finseth, D.H.; Illig, E.G. *Fuel Process. Technol.* **1986**, 12, 175.

2. Ruether, J.A.; Mima, J.A.; Kornosky, R.M.; Ha, B.C. *Energy & Fuels.* **1987**, 1, 198.

3. Kamiya, Y.; Nobusawa, T.; Futamura, S. *Fuel Process. Technol.* **1988**, 18, 1.

4. Weller, S. *Energy & Fuels*, **1994**, 8, 415.

5. Song, C.; Saini, A.K. *Energy & Fuels*, **1995**, 9, 188.

6. Song, C.; Schobert, H.H.; Saini, A.K. *Am. Chem. Soc. Div. Fuel Chem. Prepr.* **1993**, 38, 1031.

7. Song, C.; Schobert, H.H.; Saini, A.K. *Energy & Fuels.* **1994**, 8, 301.

8. Song, C.; Saini, A.K. *Am. Chem. Soc. Div. Fuel Chem. Prepr.* **1994**, 39, 1103.

9. Song, C.; Saini, A.K.; Mc Connie, J. *Proc. of 8th Int. Conf. Coal Science,* Oviedo, Spain, Sept 10-15, **1995**, in press.

10. DOE COLIRN Panel. *"Coal Liquefaction"*, Final Report, DOE-ER-0400, **1989**, Vol. I and II.

6. Exploratory Studies on the Possibility of Non-Radical Hydrogen Transfer under Low Temperature Liquefaction Conditions. (contributed by Shona Martin)

Introduction

It has been observed that gaseous hydrogen reacts with coals under low temperature conditions in preference to hydrogen from donor solvents like tetralin. Indeed, in the presence of a catalyst in a hydrogen atmosphere, there are two possible pathways for hydrogen transfer. Firstly, hydrogen can directly hydrogenate the sample using a catalyst; alternatively, hydrogenation of an aromatic solvent into a donor species may occur, which then hydrogenates the samples. It has not yet been proven which pathway is followed. To date, one problem has been that when sample, hydrogen and catalyst are present, which is the main pathway of hydrogen transfer; from donor or from gaseous hydrogen? And why does preferential donation from gaseous hydrogen occur in some cases?

Previous studies have indicated that this phenomenon may depend upon the catalyst activity and type of donor or sample. The liquefaction of coals by direct hydrogenation from gaseous hydrogen with an active hydrogenation catalyst such as stabilized nickel, even in the presence of a donor solvent such as tetralin, has been reported [1,2]. Conversely, when the catalyst activity was reduced, hydrogen transfer from the donor became important [3]. Similar findings have been observed that in the presence of both active dispersed and supported catalysts, consumption of gas-phase H_2 is the dominant pathway rather than via the H-donor solvent [4,5].

Hydrogen transfer mechanisms have been studied by means of tritium tracers [6], where it was proposed that radicals produced in polycondensed aromatic hydrocarbons can behave as catalyst for the dissociation of hydrogen molecules. The observation that hydrogen exchange between gas phase and coal components proceeds before hydrogen migration among the system components takes place, points toward the possibility that the hydrogen atoms in large coal molecules (having the structure of polycondensed aromatics) are highly exchangeable with gaseous hydrogen, even without catalyst. However, due to the complex nature of the coal structure, it is more appropriate to use model compounds to obtain a transfer mechanism.

In one such study [7], dibenzyl and benzyl phenyl ether were reacted in decalin, tetralin and naphthalene using stabilized nickel catalyst under hydrogen or nitrogen atmospheres. The hydrogenation pathway of dibenzyl was mainly by direct hydrogenation by gaseous hydrogen on the catalyst surface. Benzyl phenyl ether was hydrogenated at 250 °C in a similar fashion.

These observations have all been based upon experiments conducted in the presence of catalysts under the premise that the initial steps for coal hydrogenation have occurred via radical hydrogen transfer. Recently, however, the existence of non-radical pathways for hydrogen incorporation has been proposed. Reactions of coals are not necessarily limited to free radical processes. Generally, radical reactions are dominant at temperatures ≥ 350 °C and if non-radical reaction pathways exist, this may explain a higher gas-phase H_2 consumption observed in comparative non-catalytic runs with raw and dried coals at 350 °C [8]. Indeed, the polar functionalities in coals make it likely that reactions involving charge separation, i.e. ionic reactions, might play a key role in coal conversion processes. As many of the oxygen-containing constituents of coal liquids are phenolic, possible structures that could participate in non-radical pathways include β-naphthols and 1,3- and 1,4-dihydroxy aromatics. These kinds of structures may be able to add H_2 through a concerted pathway, forming enols which then convert to ketones.

Preliminary Approaches. To test the hypothesis of non-radical hydrogen transfer in coal liquefaction, DECS-8 Wyodak coal, which is relatively rich in phenolic structures, was reacted at low temperature (350 °C) without the presence of catalyst to observe any increase in carbonyl content. The FT-IR difference spectrum between the whole product and the vacuum dried but unreacted coal indicates that the reaction involved the loss of hydroxyl groups (3300-3600 cm^{-1}) and increase of aliphatic C-H groups (2920 and 2850 cm^{-1}). However, the anticipated increase in carbonyl groups (1600, 1700 cm^{-1}), according to the possible conversion of some phenolics into their corresponding ketones, was not observed. This was proposed to be due, in part, to decarbonylation at 350 °C, because the formation of CO was detected.

In light of these preliminary results, further experiments were conducted under a nitrogen atmosphere to examine whether the results with hydrogen were due to hydrogenation or thermal reactions. N_2 gas (1000 psi, cold) rather than H_2 was employed, under otherwise identical conditions. The yields of CO, CO_2 and hydrocarbon gases produced from the thermal runs under H_2 and N_2 pressure were almost identical. Figure 83 compares the FT-IR spectrum from both experiments completed under H_2 and N_2 atmospheres. Therefore, the gas formation in both runs may be attributable to thermally driven reactions alone. Consequently, the aforementioned CO formation in the run conducted under H_2 at 350 °C does not appear to be the result of decarbonylation of newly formed ketones.

Therefore, in summary, these preliminary data largely rule out the possibility that, under the conditions employed, there is significant ketone formation which would be the

product of non-radical incorporation of molecular H_2 into coal. To examine the possibility that the reaction of H_2 may be a mineral matter catalysed reaction, tests will be conducted on (i) demineralised coal samples, and (ii) representative model compounds.

Theoretically, the objective of demineralization is to isolate the kerogen (the insoluble organic matter) by making the mineral matter phase soluble, whilst keeping modifications in the chemical composition of the organic matter as small as possible. In most cases, good recovery of the organic matter is achieved, which is little altered except for recent organic matter (recent sediments, soil, peat etc.). The methods now used are based upon the dissolution of carbonates, sulphides, oxides and hydroxides by HCl and the subsequent dissolution of silicates by HF [9]. The most frequent of these residual minerals is pyrite (FeS_2), followed by rare earth ions. Heavy oxides and sulfates and some silicates are also found. Demineralization is commonly carried out at a temperature which is sufficient to dissolve all the carbonates but not too high to prevent possible oxidation of the organic matter, i.e. ≈60 °C.

Model compounds, such as 2-naphthol and 1,3-dihydroxynaphthalene would also be suitable candidates for testing the hypothesis. The reactive network of 1-naphthol with hydrogen at 200 °C and 35 atm, in the presence of a sulfided Ni-Moly-alumina catalyst, has been studied [10,11]. 1-Tetralone, naphthalene and 5,6,7,8-tetrahydro-1-naphthol were observed to be the primary products; *cis*- and *trans*-decalin were minor products. Each reaction was approximated as first order in the organic reagent. The proposed reaction network is outlined in Figure 84.

Preliminary reactions have been conducted with 2-naphthol under non-catalytic conditions; temperatures ranging from 300-400 °C, 1000 psi H_2 pressure (cold), reaction time 30 minutes. Reaction products identified by GC-MS included naphthalene, 3,4-dihydro-2-naphthalenone and 5,6,7,8-tetrahydro-2-naphthol. This suggests that under the conditions tested, 2-naphthol may follow a similar reaction pathway. However, % conversion of 2-naphthol to products was low as no catalyst was present; *ca* 10% for the experiments completed to date. As yet, no definitive product distributions have been evaluated to determine a quantitative model of the reaction network.

Investigation of these approaches, demineralized coal and model compound studies, will provide valuable mechanistic information concerning the possibility of non-radical hydrogen transfer in coal liquefaction.

References

1. S. Ohe, H. Itoh, M. Makabe and K. Ouchi Fuel **64**, 901 (1985)
2. S. Ohe, H. Itoh, M. Makabe and K. Ouchi Fuel **64**, 1108 (1985)

3. M. Makabe, S. Ohe, H. Itoh and K. Ouchi Fuel **65**, 296 (1986)
4. C. Song, H.H. Schobert
Am. Chem. Soc., Div. Fuel Chem, Prep. **37**(2), 976 (1992)
5. L. Artok, H.H. Schobert, O. Erbaut Fuel Proc. Tech. **37**, 211 (1994)
6. K. Yamamoto, K. Kimura, K. Ueda, T. Horimatsu, O. Nitoh and T. Kabe
Coal Sci. Tech. (Proc. 1987 ICCS), 211 (1987)
7. K. Ouchi and M. Makabe Fuel **67**, 1536 (1988)
8. C. Song, A.K. Saini and H.H. Schobert Energy and Fuels **8**, 301 (1994)
9. B. Durand and C. Nicaise "Kerogen, Insoluble Organic Matter from Sedimentary Rocks" Editor B. Durand, Editions Technip Paris p35 (1980)
10. C.L. Li, Z.R. Xu, Z.A. Cao and B.C. Gates AIChE, J **31**(1), 170 (1985)
11. C.L. Li and B.C. Gates Ind. Eng. Chem. Proc. Des. Dev. **24**, 92 (1985)

APPENDIX I

Tables

Table 1. Benson's groups and the observed conversion of hydrocarbon compounds.

compound	c-(c)(c)(h)(h) a_1	c-(h)(h)(h) a_2	cb-(h) a_3	c-(c)(cb)(h)(h) a_4	cb-(c) a_5	c-(c)(c)(c)(h) a_6	c-(c)(c)(cb)(h) a_7	c-(c)(c)(c)(cb) a_8	conversion % at 723 K, high pressure at 4 hrs of pyrolysis
benzene, butyl	2	1	5	1	1	0	0	0	97.05
benzene, 1-methylpropyl	1	2	5	0	1	0	1	0	92.08
benzene, 2-methylpropyl	0	2	5	1	1	1	0	0	86.42
tert-butylbenzene	0	3	5	0	1	0	0	1	25.47
benzene, octyl	6	1	5	1	1	0	0	0	99.4
cyclohexane	6	0	0	0	0	0	0	0	5.03
methylcyclohexane	5	1	0	0	0	1	0	0	11.88
ethylcyclohexane	6	1	0	0	0	1	0	0	33.74
n-propylcyclohexane	7	1	0	0	0	1	0	0	64.78
n-butylcyclohexane	8	1	0	0	0	1	0	0	74.44
n-teteradecane	12	2	0	0	0	0	0	0	97.08
tetralin	2	0	4	2	2	0	0	0	19.92
decalin	8	0	0	0	0	2	0	0	25.58

Table 2. First-order decomposition rate constants for various compounds obtained from literature.

compound	$\ln(k_0)$	E_a/R	Conditions	Reference
ethane	37.35	39049.0	P = 0.05–0.8 atm, T = 823–893 K	[18]
propane	38.45	42.724	P = 0.13 atm, T = 748–778 K	[19]
butane	21.89	20984.0	P = 10 atm, T = 900–1500 K	[20]
i-butane	34.63	33641.0	P = 1 atm, T = 913–1063 K	[21]
n-pentane	33.62	31752.0	P = 1 atm, T = 973–1123 K	[22]
n-hexane	31.13	30213.0	P = 1 atm, T = 883–993 K	[23]
pentane, 2-methyl	32.26	29907.0	P = 1 atm, T = 853–1053 K	[24]
butane, 2,2-dimethyl	31.45	30189.0	P = 1 atm, T = 898–1053 K	[24]
n-heptane	23.03	21650.0	P = 40 atm, T = 600–1420 K	[25]
pentane 2,4-dimethyl	33.74	31225.0	P = 1 atm, T = 873–1073 K	[24]
n-octane	27.67	26334.0	P = 1 atm, T = 873–1073 K	[24]
heptane, 2-methyl	30.35	28141.0	P = 1 atm, T = 873–1046 K	[24]
n-decane	33.02	31271.0	P = 1 atm, T = 918–958 K	[23]
n-dodecane	32.12	30213.0	P = 1 atm, T = 873–953 K	[23]
n-tetradecane	43.205	33865.0	high pressure, T = 675–750 K	[12]

Table 2 (continued).

compound	$\ln(k_0)$	E_a/R	Conditions	Reference
n-hexadecane	33.97	29775.0	P = 35 atm	[17]
n-amylbenzene	18.672	19280.0	high pressure, T = 675--750 K	[15]
n-hexylbenzene	15.943	16908.0	high pressure, T = 675--750 K	[15]
n-octylbenzene	23.20	21866.0	high pressure, T = 675--750 K	[15]
cyclohexane	43.63	44737.0	P = 1 atm, T = 993--1103 K	[26]
methylcyclohexane	39.33	38127	P = 1 atm, T = 993--1083 K	[27]
ethylcyclohexane	32.19	31993.0	P = 1 atm, T = 953--1083 K	[27]
n-propylcyclohexane	29.8	28986.0	P = 1 atm, T = 953--1073 K	[27]
n-butylcyclohexane	29.63	28625.0	P = 1 atm, T = 923--1023 K	[27]

Table 3. First-order decomposition rate constant kinetic parameter for n-paraffins, decalin, and cyclohexane.

compound	$\ln(k_o)$	E_a/R	note
n-butane	28.6	30108	high pressure T=673-923K
n-pentane	30.09	30108	same
n-hexane	30.48	30108	same
n-heptane	31.23	30108	same
n-octane	32.115	30108	same
n-nonane	32.14	30108	same
n-decane	32.475	30108	same
n-dodecane	32.483	30108	same
n-tetradecane	32.78	30108	same
n-hexadecane	33.08	30108	same
n-hexadecane(other)	33.97	29775	P=35 atm T=773-873K
n-octadecane	33.752	30108	high pressure T=673-923K
n-$C_{20}H_{42}$	33.862	30108	same
cyclohexane	31.86	28108	P=130 atm T=700-800 K
decalin	36.12	30120	P=30-40 atm T=700-870K

Table 4. First-order decomposition rate constants for saturated cyclic hydrocarbons (Static tests, 700 K, high pressure).

compound	First-Order decomposition rate constants, (static test, 427°C), hr^{-1}
cyclohexane	0.00944
cyclohexane, methyl-	0.0138
cyclohexane, ethyl-	0.0558
cyclohexane, n-propyl-	0.0844
cyclohexane, n-butyl-	0.126
cyclohexane, iso-propyl-	0.129
cyclohexane, tert-butyl-	0.127
cyclohexane, 1,4-ethyl-methyl-	0.0668
cyclohexane, diethyl-	0.135
cyclohexane, 1,3,5-trimethyl	0.0312
cyclohexane, 1,2,4,5-tetramethyl-	0.0772
decalin	0.0431
decalin, dimethyl-	0.0582
decalin, 1-ethyl-	0.146
decalin, isopropyl-	0.161
decalin, 1-tert-butyl-	0.139
cyclopentane, n-propyl-	0.104
cyclopentane, n-butyl-	0.132
bicyclopentyl	0.0768
bicyclohexyl	0.171
bicyclohexyl, iso-propyl	0.401
methane, dicyclohexyl-	0.26
butane, 1,3-dicyclohexyl-	0.644

Table 5. Kinetic Parameters for Thermal Cracking of n-Alkanes.

reactant	rate constant, h^{-1}			E_a, kcal/mol	A, h^{-1}
	400°C	425°C	450°C		
n-C_{10}	0.0346	0.1760	0.7590	59.76	8.78×10^{17}
n-C_{12}	0.0471	0.2446	1.2144	62.87	1.20×10^{19}
n-C_{14}	0.0620	0.3477	1.7081	64.15	4.18×10^{19}

Table 6. Weight percent of *Cis* and *Trans* Decalin Indentified in the Liquids Obtained after Stressing of Dodecane + 5% Decalin at 425°C for 1h.

Components	Without PX-21, wt%	PX-21, wt%	PX-21 used, wt%	PX-21 outgassed, wt%	PX-21used and outgassed, wt%
cis decalin	3.14	2.24	2.49	2.94	3.14
trans decalin	3.83	3.03	2.69	3.86	3.44

Table 7. A Classification of Heterogeneous Catalysts [7].

Class	Conductivity	Functions	Examples
Metals	conductors	hydrogenation dehydrogenation hydrogenolysis (oxidation)	Fe, Ni, Pt, Pd, Cu, Ag
Metal oxides & sulfides	semiconductors	oxidation reduction dehydrogenation cyclization desulphurization (hydrogenation)	NiO, ZnO, CuO, Cr_2O_3, WS_2
Metal oxides	insulators	dehydration isomerization	Al_2O_3, SiO_2, MgO
Acids		polymerization isomerization cracking alkylation halogenation hydrogen transfer	SiO_2-Al_2O_3, zeolites

Table 8. Results of the Dehydrogenation of Ethylbenzene over Various Catalyst Samples [12].

Sample	Surface area ($m^2 g^{-1}$)	Styrene (%)	Benzene (%)	Toluene (%)	CO_x (%)	Conversion (%)	Selectivity (%)
Al_2O_3	360	1.0	0.1	0.05	0.8	0.8	50.0
PPAN 1	8	10.5	0.3	0.01	0.7	11.6	90.5
PPAN 2	50	20.5	0.7	0.01	1.1	22.4	91.5
PPAN 3	10	11.1	1.6	0.2	1.3	14.6	76.0
A.C.	800	21.9	2.0	0.4	2.5	26.8	81.7
AX21	3000[b]	72.1	2.2	1.1	4.0	80.0	90.1
PPAN 2(N_2)[a]		2.0	0.4	0.1	0	2.5	80.0
AX21 (N_2)[a]		2.1	2.0	0.8	0	5.2	40.4

(a) N_2 carrier flow used; reaction time 4 h; (b) This surface area measurement is known to be high. See [15].

Table 9. Reactivity of C_3 Oxygenated Substrates over CMS Catalyst [13].

substrate	products	selectivity[b] (%)	conversion[c] (%)
1-propanol	propene	63	40
	propanol	13	
2-propanol	propene	70	46
	acetone	20	
propanal	acetaldehyde	69	48
	ethanol	10	
	ethylene	8	
acetone			<1

[a]Conditions: reaction temperature, 230 °C; carrier flow, 5 mL/min; substrate flow, 0.2 mL/h. [b]Percentage of stated product among all products. [c]Other products include small amounts of ethers and esters.

Table 10 Hydrodehydroxylation and Hydrodehalogenation of Ar-X [18].

Ar	X	No.	Catalyst, Conversion None	BP2000
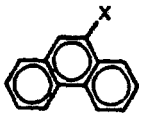	OH	I	20	46
	Br	II	20	95
	Cl	III	13	39
	Br	IV	17	64
	OH	V	12	50
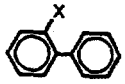	OH	VI	0	< 1
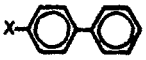	OH	VII	4	4
	Cl	VIII	2	5

[a] All Reactions at 410 °C, 4:1:0.1 weight ratio solvent to Ar-X to catalyst

Table 11. Effect of Oxidation in an O_2 Stream on Catalytic Activity of Spheron 6 [33].

Run	Oxidation temperature (°C)	Oxidation duration (hr.)	Forward* rate constant (hr^{-1})	Activation* energy (kcal/mole)	Preexponential*
1	unoxidized		No detectable activity		
2	310	36	0·44	13·6	$5·9 \times 10^8$
3	335	12	0·29	12·0	$4·5 \times 10^7$
4	335	24	0·15	14·8	$1·1 \times 10^9$
5	335	36	0·083	17·3	$4·5 \times 10^{10}$

*For the conversion of 2-methyl-1-pentene to 2-methyl-2-pentene at 52·5°C using 0·021 g black/ml olefin.

Table 12. Influence of Temperature on Overall Conversion of 4-(1-Naphthylmethyl)bibenzyl [35].

	conversion at X% catalyst			
temp, °C	0	2	5	10
320	0	0.8		3.9
375	0	9.1	16.2	27.0
400	3.0	17.6	33.6	43.6
429	28.7	53.8	75.9	87.2

*Reaction conditions: sealed tube; 1 h; weight ratio 9,10-DHP:I 4:1; catalyst weight based on I.

Table 13. The List of the Responsible Sites and Mechanisms for the Carbon Catalyzed Reactions.

Carbons/Reactions	Responsible sites of carbon/mechanisms	Ref.#
Activated carbon		
Dehydrogenation of alcohol	Lewis acid and base which is similar to metal oxides	9, 10
Dehydration of alcohol	Carboxyl groups/Carbenium ion intermediates	9, 10
Hydrogen halide elimination of alkyl halide	Amino and pyridine-like group /Radical mechanism	21, 28, 29
Racemization of binaphthyl	Electron-donor sites of the graphitic planes	30, 31
Oxidation of cycloalkene	Free radicals mechanism similar to metal ion catalyst/Basic oxide on surface	19
Oxidation of mercaptan	Quinone group/Metal ion mechanism like oxidation of hydrocarbon	20
Oxidation of alcohol	Electron transfer to O_2, then atomic oxygen O^- attack alcohol	21
Oxidation of oxalic acid	Anionic reducing species adsorbed by basic surface oxides	22
Formation of dichloromethane	Polar surface groups/Mechanism involved chloromethyl chloroformate intermediate	37
Charcoals		
Oxidation of oxalic acid	Basic surface oxides/Chromene-like structure	2
Halogenation of toluene	Chemisorbed hydrogen atom react with Cl_2 to produce atomic chlorine	23
Active coke layer on metal/inorganic catalyst		
Dehydrogenation of ethylbenzene	Electronegative groups (quinoid type group) /Redox-type mechanism	14, 15
C.M.S		
Oxidative dehydrogenation /dehydration of ethylbenzene	Quinone-type moieties suggested in carbonaceous overlayers on inorganic oxide catalyst/Hydrogen abstraction mechanism	12
Oxidative dehydrogenation /dehydration of alcohol	Lewis acid catalysis mechanism via a carbocation	13
Carbon Black		
Hydrodehydroxylation	Hydrogen transfer as a first step	18
Hydrodehalogenation	Hydrogen transfer as a first step	18

Solvolysis of ester	Acidic and/or basic nucleophilic group	25
Hydrolysis of benzyl acetate	Quinonoid and other groups /Adsorbed hydroxide ions and aromatics	24
Polymerization of olefins	Carbocation mechanism	26
Polymerization of n-vinylcarbazole	Phenolic hydroxyl group/Cationic mechanism	27
Racemization of binaphthyl	Electron-donor sites of the graphitic planes	30, 31
Isomerization of olefins	Acidic groups/Ionic mechanism in acidic catalysts	26, 32, 33
Decomposition of benzoyl peroxide	Independent from surface groups /Radical mechanism	34
Decomposition of 4-(1-Naphthylmethyl)bibenzyl	Positively charged carbon surface/Cation radical mechanism	35
Carbon Film		
Conversion of CH_4 to hydrocarbon	Fast dissociation on the surface /Radical mechanism	36
Fullerene		
Dehydrogenation /bond-cleavage and coupling of 1,2'-Dinaphthylmethane	Hydrogen transfer ability	11

Table 14. Some characteristics of mesoporous molecular sieves

Sample	Source of Al	SiO_2/Al_2O_3 (mole ratio)		BET surface Area (m^2/g)	Pore Size from sorption (Å)
		Input	Output		
MRK9a	Al isopropoxide	100	88.4	1147	27.67
MRK9b	Al isopropoxide	50	53.8	1206	28.02
MRK10a	Catapal B	100	95.5	1010	21.92
MRK10b	Catapal B	50	44.3	----	-----
MRK11a	Al sulfate	100	164.6	834	25.38
MRK11b	Al sulfate	50	87.4	----	-----

Table 15. Naphthalene hydrogenation over Pt/MCM-41 catalysts

Catalyst	naphthalene conv. (%)	Product distribution (wt%)				*t-/c-* decalins
		tetralin	*t*-decalin	*c*-decalin	total decalins	
MRK9b	100.0	0.18	33.15	66.67	99.82	0.497
MRK10b	99.7	25.43	17.96	56.31	74.57	0.319
MRK11b	100.0	0.00	32.25	67.75	100.00	0.476

Table 16. Hydrogenation of phenanthrene over Pt/MCM-41 catalysts

	Product distribution (wt%)		
	MRK9b	MRK10b	MRK11b
Phenanthrene	20.39	12.00	33.37
1,2,3,4 tetrahydrophenanthrene (THP)	6.08	6.02	9.79
9,10 dihydro phenanthrene (DHP)	33.11	40.02	36.16
sym-octahydrophenanthrene (sym-OHP)	11.80	27.50	8.83
sym-octahydroanthracene (sym-OHA)	13.30	1.24	5.14
unsym-octahydrophenanthrene (unsym-OHP)	12.16	11.43	6.34
tetradecahydrophenanthrenes (TDHP)	3.14	1.79	----
sym-OHA/sym-OHP	1.13	0.06	0.60

Table 17. Isopropylation of naphthalene over Pt/MCM-41 catalysts

	Product distribution (wt%)		
	MRK9b	MRK10b	MRK11b
naphthalene	3.38	62.59	9.75
2 isopropyl naphthalene	8.82	9.20	10.44
1 isopropyl naphthalene	9.55	21.00	18.27
di isopropyl naphthalenes	37.92	6.14	38.08
tri isopropyl naphthalenes	33.10	0.94	20.17
tetraisopropyl naphthalens	7.21	0.11	3.28
2,6 di isopropyl naphthalenes	4.71	0.30	1.89
2,7 di isopropyl naphthalenes	3.70	0.29	2.33
% Conversion	96.22	37.41	90.25
% of tetraisopropyl naphthalens	7.49	0.30	3.63

Table 18. Kp values of naphthalene hydrogenation at various temperatures

Temperature/°C	Kp	ln Kp
350	0.0045	-5.4
400	0.00037	-7.9
450	0.00027	-8.25

Table 19. Kp values of pyrene hydrogenation at various temperatures

Temperature/°C	Kp	ln Kp
350	0.0078	-4.85
400	0.0058	-5.14
450	0.0038	-5.58

Table 20. Dehydrogenation rate constants for hydropyrenes

	Dihydropyrene	Tetrahydropyrene	Hexahydropyrene
350C	0.027 min^{-1}	0.033 min^{-1}	0.029 min^{-1}
400C	0.046 min^{-1}	0.075 min^{-1}	0.065 min^{-1}
450C	0.166 min^{-1}	0.209 min^{-1}	0.213 min^{-1}

Table 21. Comparison of calculated parameters for hydrogenation of naphthalene and pyrene

	Naphthalene	Pyrene
Kp 350C	0.0045	0.0078
Kp 400C	0.00037	0.0058
Kp 450C	0.00027	0.0038
k 350C/min-1	0.0059	0.0088
k 400C/min-1	0.0150	0.0139
k 450C/min-1	0.0301	0.0187
ΔH/kcal/mol	-32	-6.4
Ea/kcal/mol	12.6	6.9

Table 22. Hydrogenation of Naphthalene Over Pd/HY(GB) Catalyst
Effects of Catalyst Charge and Temperature

run no.	time, min	temp, °C	catalyst charge, g	%Nap conv.	Product Distribution (mole %) TeHN	trans-DeHN	cis-DeHN	% trans-DeHN selectivity	trans/cis DeHN
188	6	200	0.40	100.00	0.00	62.94	37.06	62.94	1.70
189	15	200	0.40	99.97	0.05	64.70	35.25	64.73	1.84
190	30	200	0.40	100.00	0.00	68.94	31.06	68.94	2.22
171	60	200	0.40	100.00	0.00	72.94	27.06	72.94	2.69
210	30	200	0.10	100.00	0.04	64.90	35.06	64.93	1.85
208	60	200	0.10	100.00	0.04	69.27	30.69	69.29	2.26
214	30	100	0.10	99.31	95.17	2.42	2.41	50.16	1.01
212	60	100	0.10	99.00	93.69	3.30	3.01	52.30	1.10

Table 23. Hydrogenation of Naphthalene Over Pt.HY(GB) Catalyst
Effects of Catalyst Charge and Temperature

run no.	time, min	temp, °C	catalyst charge, g	%Nap conv.	Product Distribution (mole %) TeHN	trans-DeHN	cis-DeHN	% trans-DeHN selectivity	trans/cis DeHN
184	6	200	0.40	99.89	48.42	9.97	41.61	19.32	0.24
185	15	200	0.40	100.00	0.29	20.35	79.36	20.41	0.26
186	15	200	0.40	100.00	2.29	19.10	78.62	19.54	0.24
187	30	200	0.40	100.00	0.04	20.51	79.46	20.51	0.26
166	60	200	0.40	99.94	2.58	15.12	82.30	15.52	0.18
209	30	200	0.10	100.00	14.66	20.40	64.94	23.90	0.31
207	60	200	0.10	99.94	0.62	23.54	75.84	23.68	0.31
213	30	100	0.10	3.88	91.07	1.80	7.14	20.10	0.25
211	60	100	0.10	5.64	87.53	3.28	9.19	26.29	0.36

Table 24. Hydrogenation of Naphthalene Over Pd/M38(AS) Catalyst
Effects of Catalyst Charge and Temperature

run no.	time, min	temp, °C	catalyst charge, g	%Nap conv.	Product Distribution (mole %) TeHN	trans-DeHN	cis-DeHN	% trans-DeHN selectivity	trans/cis DeHN
195	6	200	0.40	100.00	0.00	78.86	21.14	78.86	3.73
196	15	200	0.40	100.00	0.00	88.92	11.08	88.92	8.03
197	30	200	0.40	100.00	0.00	92.46	7.54	92.46	12.27
198	60	200	0.40	100.00	0.00	93.08	6.92	93.08	13.46
202	30	200	0.10	100.00	0.00	78.60	21.40	78.60	3.67
200	60	200	0.10	100.00	0.00	88.28	11.72	88.28	7.53
206	30	100	0.10	94.86	94.88	2.35	2.77	45.86	0.85
204	60	100	0.10	99.98	92.69	3.96	3.36	54.10	1.18

Table 25. Hydrogenation of Naphthalene Over Pt/HM38(AS) Catalysts
Effects of Catalyst Charge and Temperature

run no.	time, min	temp, °C	catalyst charge, g	%Nap conv.	Product Distribution (mole %) TeHN	trans-DeHN	cis-DeHN	% trans-DeHN selectivity	trans/cis DeHN
191	6	200	0.40	100.00	0.00	53.86	46.14	53.86	1.17
192	15	200	0.40	100.00	0.00	71.15	28.85	71.15	2.47
193	30	200	0.40	100.00	0.00	84.75	15.25	84.75	5.56
194	60	200	0.40	100.00	0.00	92.50	7.50	92.50	12.33
201	30	200	0.10	100.00	0.00	61.97	38.03	61.97	1.63
199	60	200	0.10	100.00	0.00	71.69	28.31	71.69	2.53
205	30	100	0.10	99.60	79.49	5.22	15.29	25.44	0.34
203	60	100	0.10	100.00	15.70	23.66	60.63	28.07	0.39

Expt No.	20	19	16	14	15		22	23	18	17
DECS-No.	12	12	12	12	12		12	12	12	12
raw or v-dried	vd	vd	raw	raw	raw		vd	vd	raw	raw
coal feed	4.356	4.48	4.207vd	4.275vd	4.517vd		4.329	4.786	4.422vd	3.963vd
dmmf coal (g)	3.839	3.948	3.707	3.767	3.98		3.815	4.217	3.897	3.492
H2O (g) added	none	1.815	none	1.705	1.722		none	1.75	none	1.668
Cat (ATTM)	none	none	ATTM	ATTM	ATTM		none	none	ATTM	ATTM
H2O/dmmf coal,wt		0.46		0.45	0.43			0.41		0.48
Mo/dmmf coal,wt%			1	1	1				1	1
Rxn Temp, °C	350	350	350	350	350		400	400	400	400
Rxn time, min	30	30	30	30	30		30	30	30	30
THF-I residue (g)	3.516	3.154	3.293	2.824	2.489		2.943	2.853	2.293	2.027
conversion (g)	0.84	1.326	0.914	1.451	2.028		1.386	1.933	2.129	1.936
THF-Sol Preasp (g)	0.793	1.209	0.82	1.511	1.921		1.193	1.783	1.592	1.084
Tol-Sol Asp (g)	0.033	0.104	0.084	0.066	0.085		0.13	0.079	0.118	497
Hex-Sol Oil (g)	0.028	0.056	0.056	0.063	0.071		0.084	0.172	0.125	0.223
Gas by Rtor wt diff.	0.014	0.016	0.021		0.023		0.04	0.08	0.07	0.08
Gas prod - H2(GC)	0.01	0.02	0.01		0.02		0.03	0.05	0.05	0.08
dmmf %Coal Conv a	21.88	33.59	24.66	38.52 c	50.95		36.33	45.84	54.63	55.44
b	[22.51]	[35.18]	[26.17]	[44.76]	[52.69]		[37.67]	[49.42]		
%Y of Preasph,dmmf	20.66	30.62	22.12	40.11	48.27		31.27	42.28	40.85	31.04
%Y of Asph,dmmf	0.86	2.63	2.27	1.75	2.14		3.41	1.87	3.03	14.23
%Y Oil (isol), dmmf	0.73	1.42	1.5	1.67	1.78		2.2	4.08	3.21	6.39
%Y Oil (diff), dmmf									9.47	7.88
%Y Gas (GC), dmmf	0.26	0.51	0.27		0.5		0.79	1.19	1.28	2.29
%Y Gas (diff), dmmf	0.36	0.41	0.57		0.58		1.05	1.9	1.8	2.29
Gas Comp, dmmf										
CO	0.03	0.02	0.04		0.01		0.06	0.04	0.05	0.01
CO2	0.12	0.41	0.1		0.32		0.33	0.63	0.31	1
CH4	0.03	0.05	0.04		0.05		0.25	0.28	0.43	0.51
C2-C4	0.03	0.03	0.06		0.1		0.14	0.23	0.48	0.76
%H2 Consump, dmmf	<0.2	0.51	<0.3		0.5		0.52	0.71	0.77	2

a	Conversion based on recovered THF-insoluble residue
b	Conversion based on isolated products
c	Coal solids not ground prior to Soxhlet extraction

Table 26 Reaction Data for Pittsburgh #8 (DECS-12) Coal.

APPENDIX II

Figures

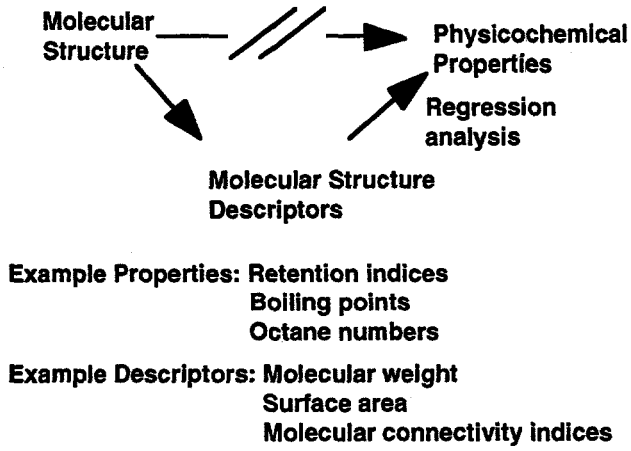

Figure 1. Schematic diagram of structure-property relationship study.

decalin

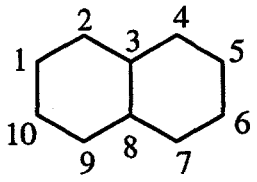

$$\begin{pmatrix} 0 & 1 & 0 & 0 & 0 & 0 & 0 & 0 & 0 & 1 \\ 1 & 0 & 1 & 0 & 0 & 0 & 0 & 0 & 0 & 0 \\ 0 & 1 & 0 & 1 & 0 & 0 & 0 & 1 & 0 & 0 \\ 0 & 0 & 1 & 0 & 1 & 0 & 0 & 0 & 0 & 0 \\ 0 & 0 & 0 & 1 & 0 & 1 & 0 & 0 & 0 & 0 \\ 0 & 0 & 0 & 0 & 1 & 0 & 1 & 0 & 0 & 0 \\ 0 & 0 & 0 & 0 & 0 & 1 & 0 & 1 & 0 & 0 \\ 0 & 0 & 1 & 0 & 0 & 0 & 1 & 0 & 1 & 0 \\ 0 & 0 & 0 & 0 & 0 & 0 & 0 & 1 & 0 & 1 \\ 1 & 0 & 0 & 0 & 0 & 0 & 0 & 0 & 1 & 0 \end{pmatrix}$$

Figure 2. Representation of a chemical structure as a graph and a matrix.

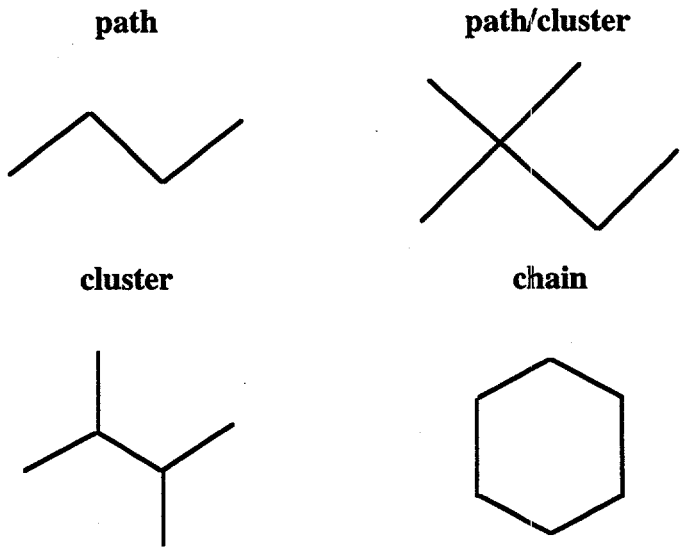

Figure 3. Examples of subgraph types in chemical structures.

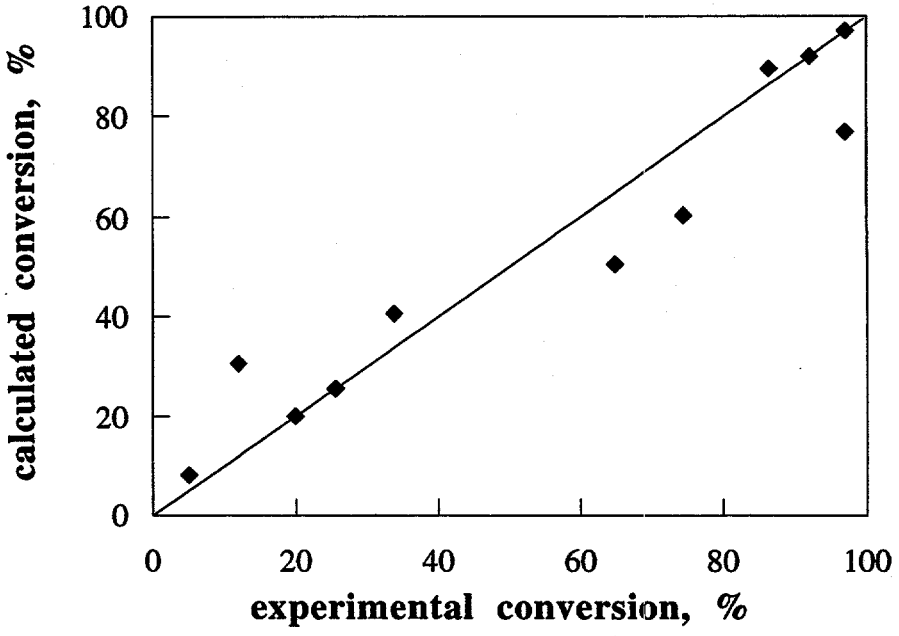

Figure 4. Plot of observed vs. calculated conversion using Benson's group descriptors.

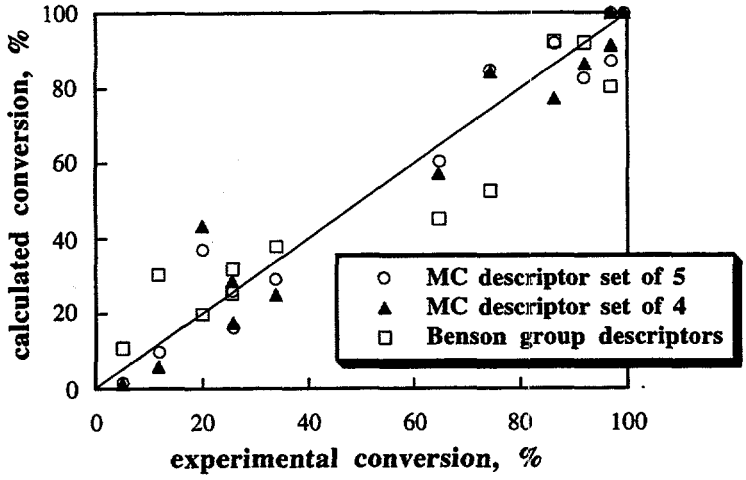

Figure 5. Comparison of the calculated vs. the experimental conversion (with $\left\{{}^{0}\chi, {}^{1}\chi, {}^{3}\chi_{cluster}, {}^{6}\chi_{chain}\right\}$, $\left\{{}^{0}\chi, {}^{1}\chi, {}^{3}\chi_{cluster}, {}^{5}\chi_{cluster}, {}^{6}\chi_{chain}\right\}$, and Benson's descriptor sets)

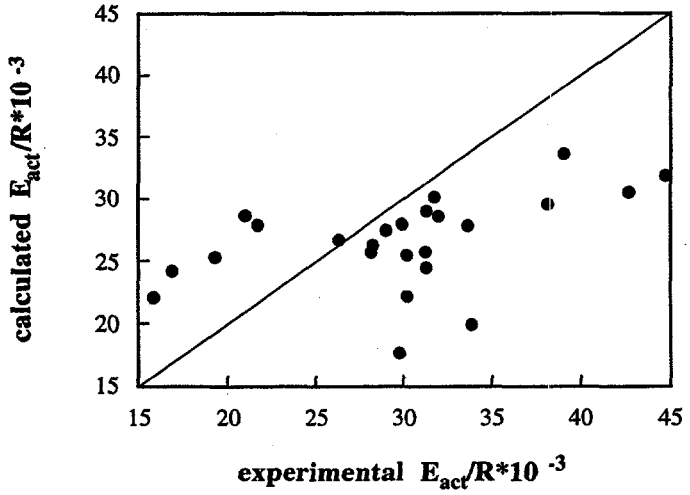

Figure 6. Plot of the observed vs. calculated activation energy for pseudo-first-order decomposition constant for various compounds.

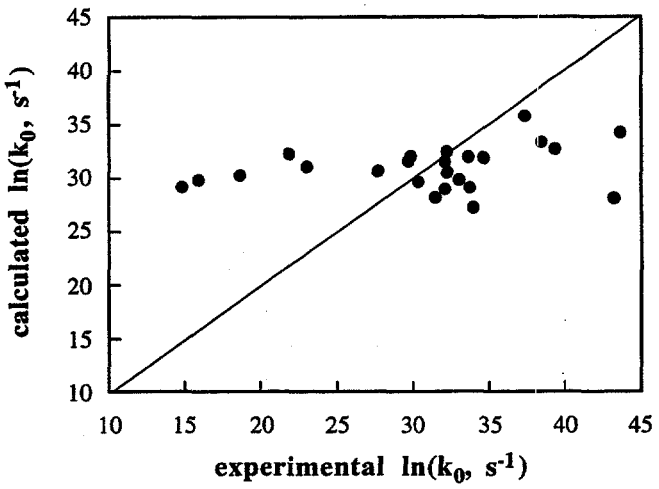

Figure 7. Plot of the observed vs. calculated predexponential factor for pseudo-first-order decomposition constant for various compounds.

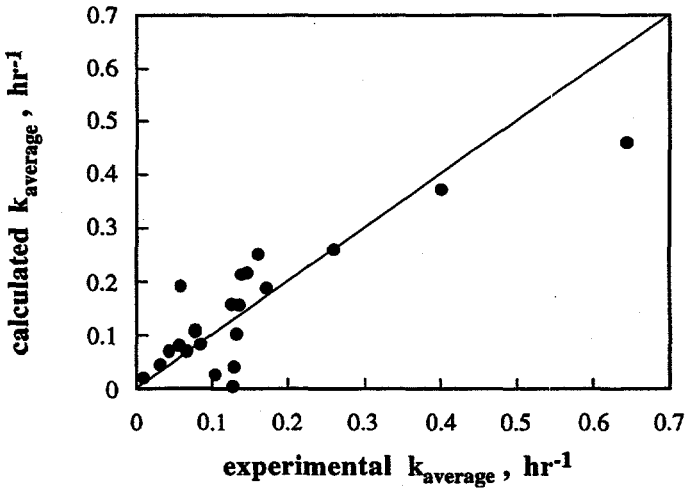

Figure 8. Plot of the observed vs. calculated pseudo-first-order rate constants for saturated cyclic hydrocarbons (static tests, 700 K, high pressure).

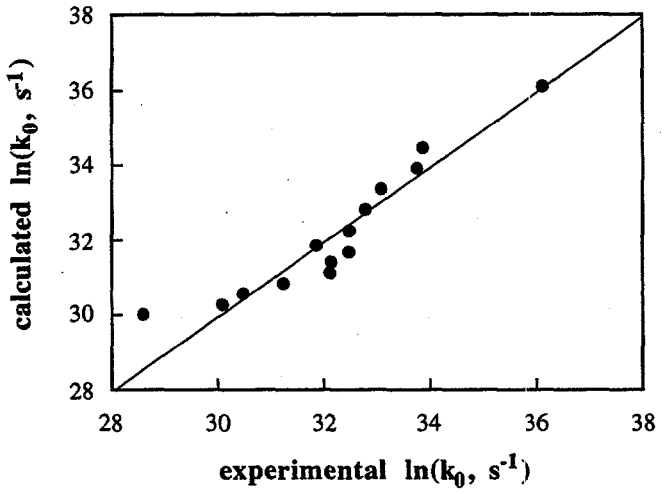

Figure 9. Plot of the observed vs. calculated predexponential factor for pseudo-first-order decomposition constant for n-paraffins, decalin and cyclohexane.

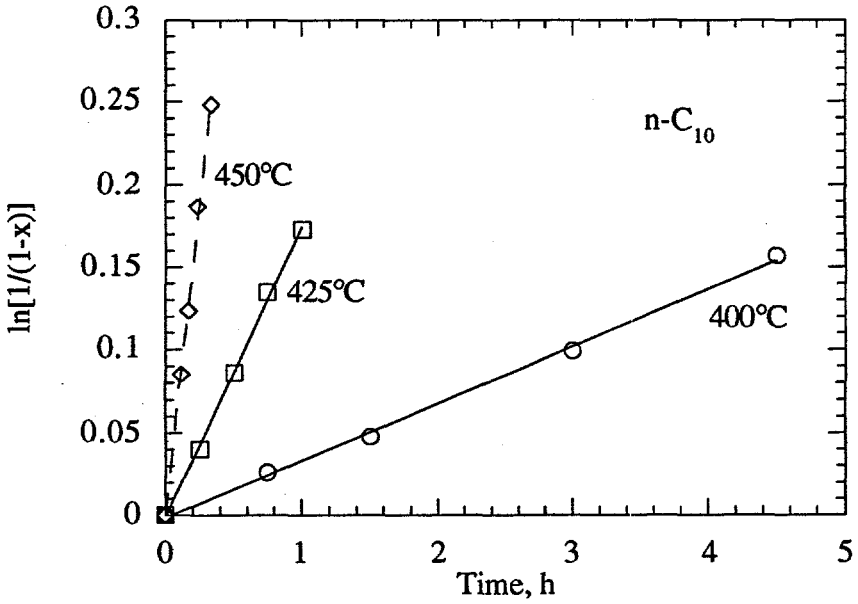

Figure 10. Relationship between ln[1/(1-x)] and Time for n-Decane Pyrolysis.

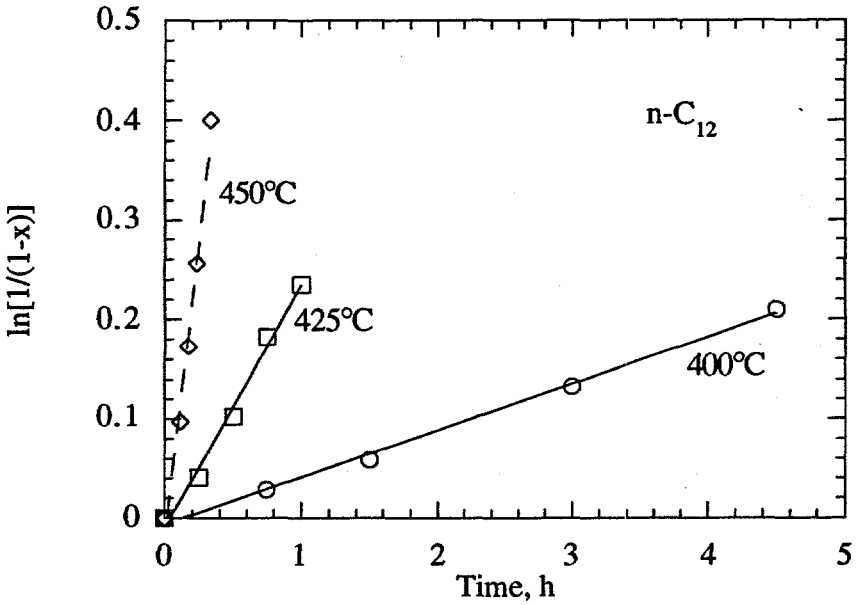

Figure 11. Relationship between ln[1/(1-x)] and Time for n-Dodecane Pyrolysis.

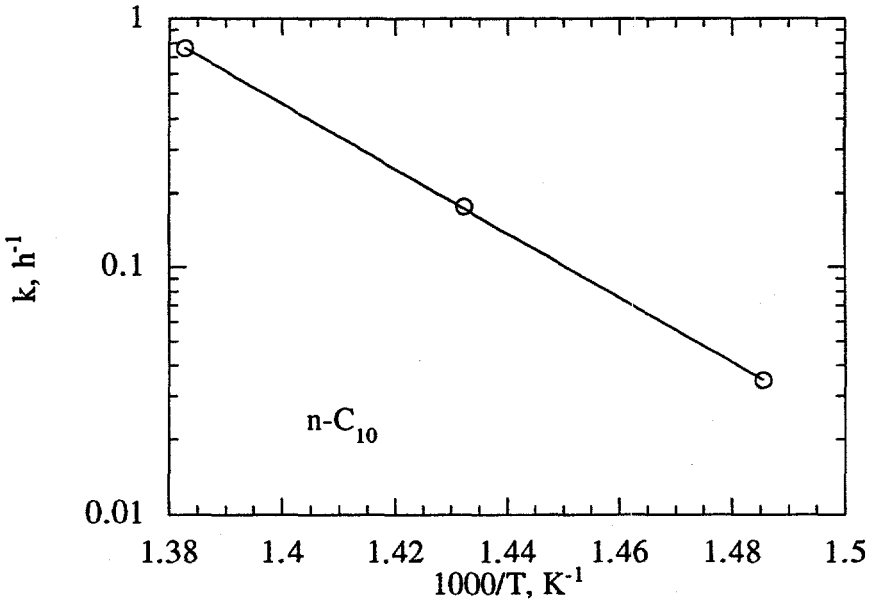

Figure 12. Relationship between Rate Constant and Temperature for n-Decane Pyrolysis.

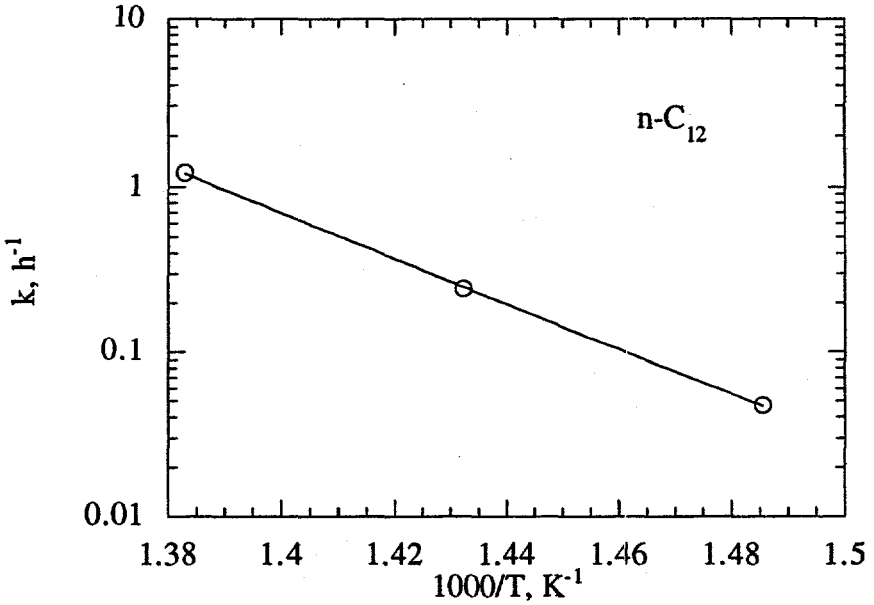

Figure 13. Relationship between Rate Constant and Temperature for n-Dodecane Pyrolysis.

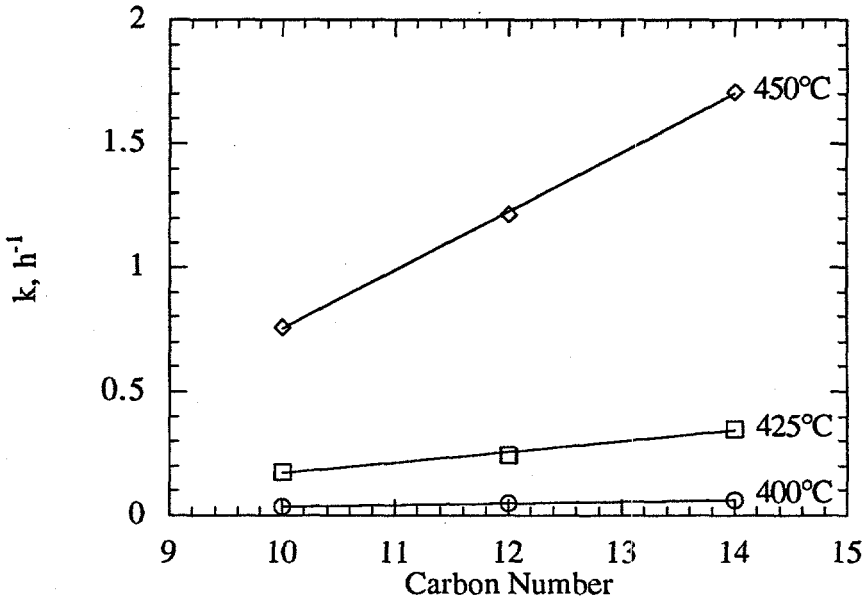

Figure 14. Relationship between Rate Constant and Carbon Number for Three Temperatures.

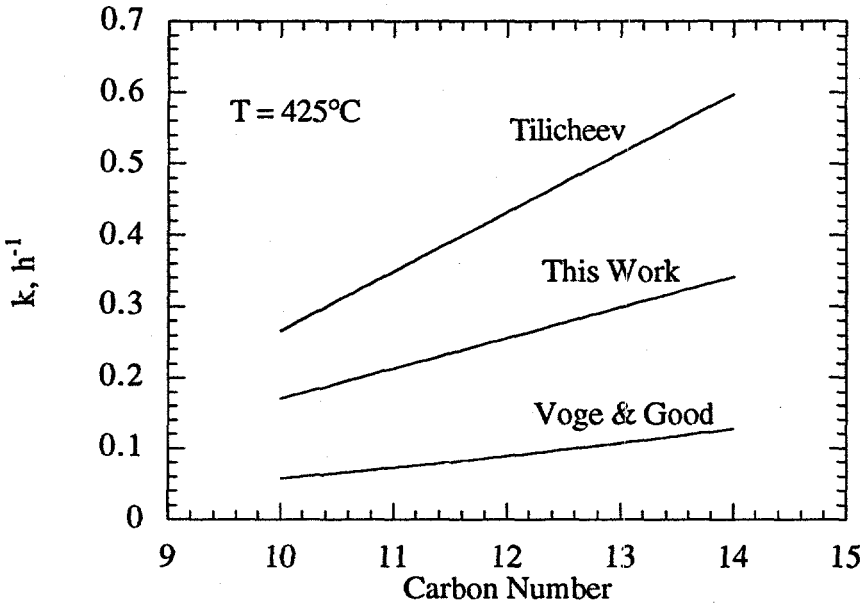

Figure 15. Relationship between Rate Constant and Carbon Number at 425°C.

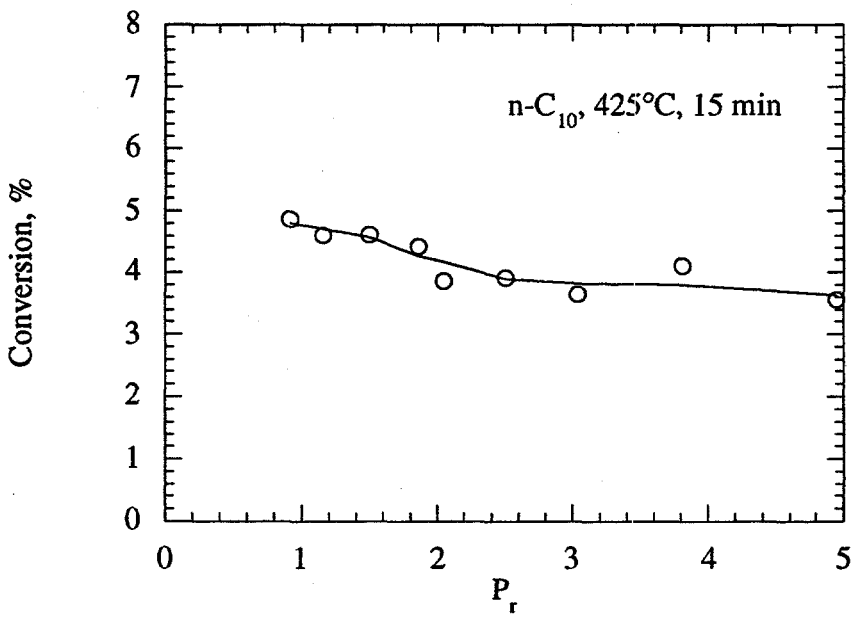

Figure 16. Change in Conversion of n-Decane with Initial Reduced Pressure at 425°C for 15 min.

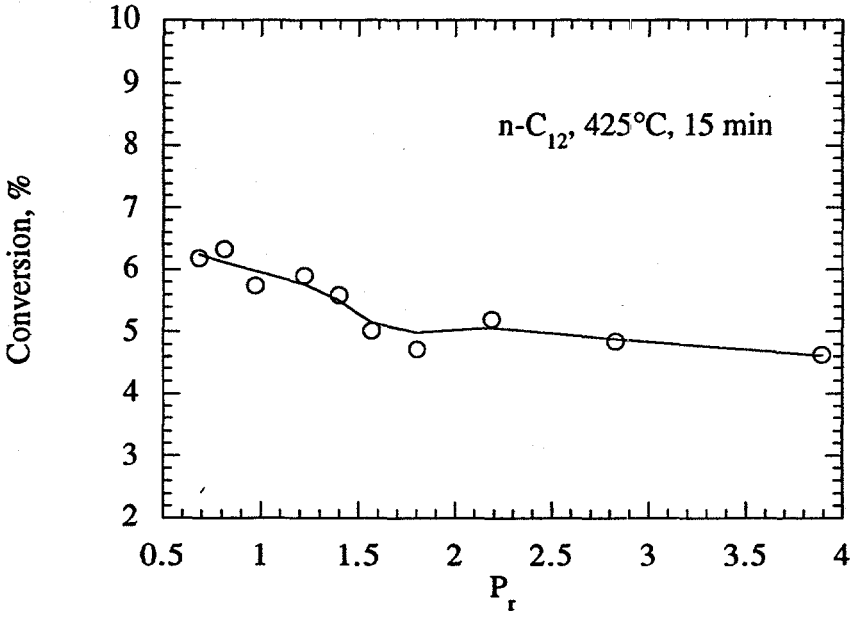

Figure 17. Change in Conversion of n-Dodecane with Initial Reduced Pressure at 425°C for 15 min.

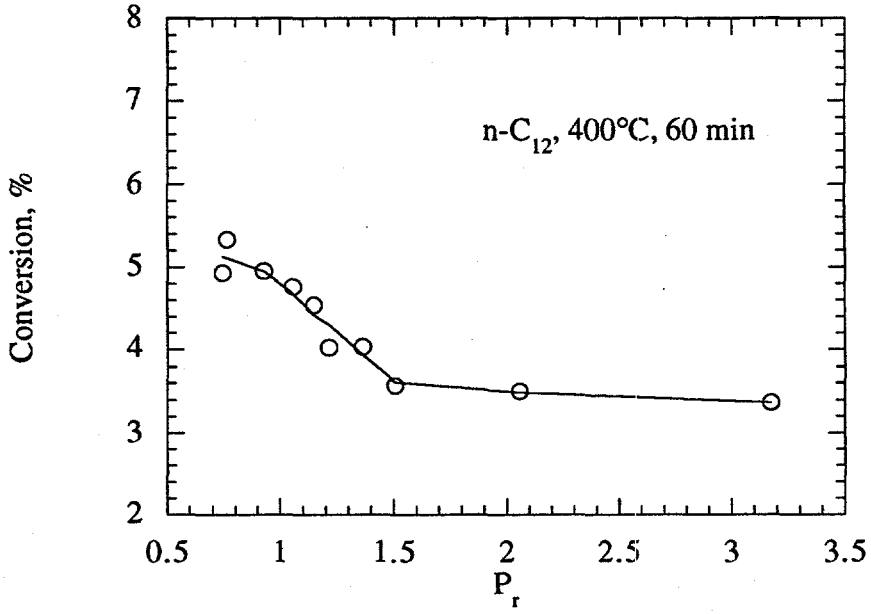

Figure 18. Change in Conversion of n-Dodecane with Initial Reduced Pressure at 400°C for 60 min.

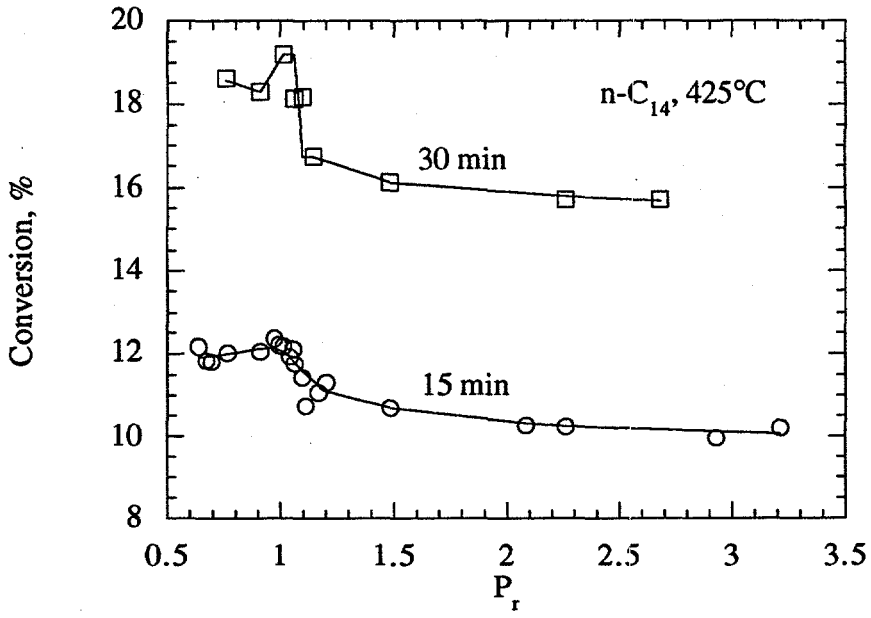

Figure 19. Change in Conversion of n-Tetradecane with Initial Reduced Pressure at 425°C for 15 and 30 min.

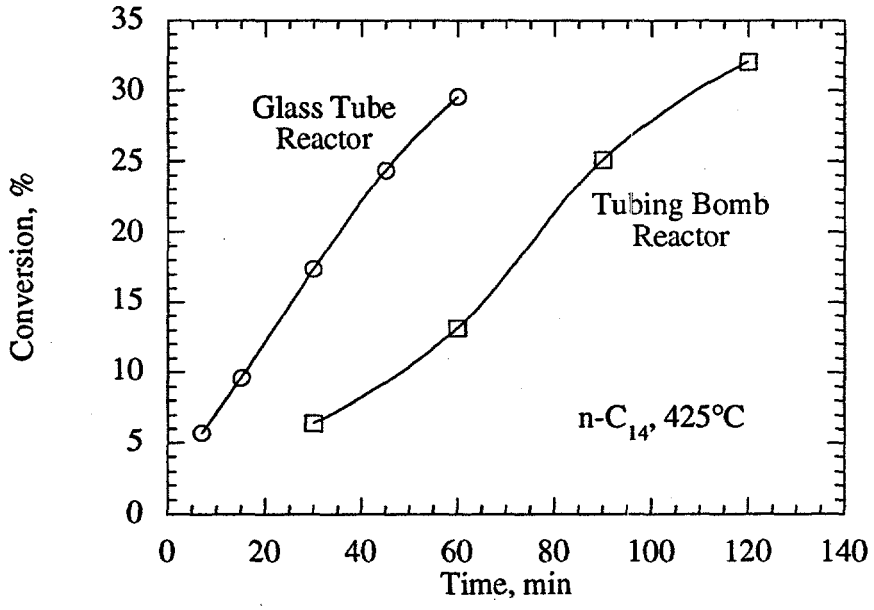

Figure 20. Change in Conversion of n-Tetradecane with Reaction Time at 425°C for Two Different Reactors.

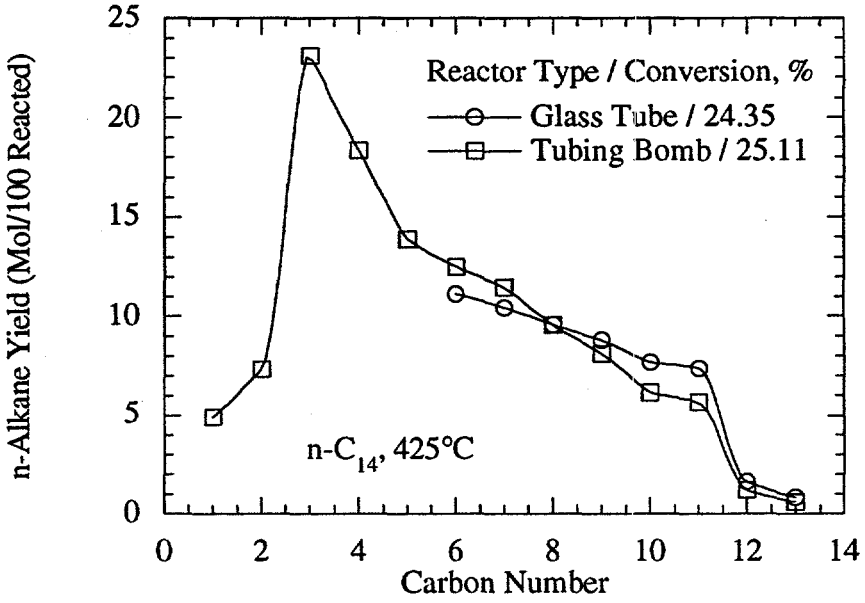

Figure 21. Relationship between n-Alkane Yield and Carbon Number for n-Tetradecane Pyrolysis at 425°C in Two Different Reactors.

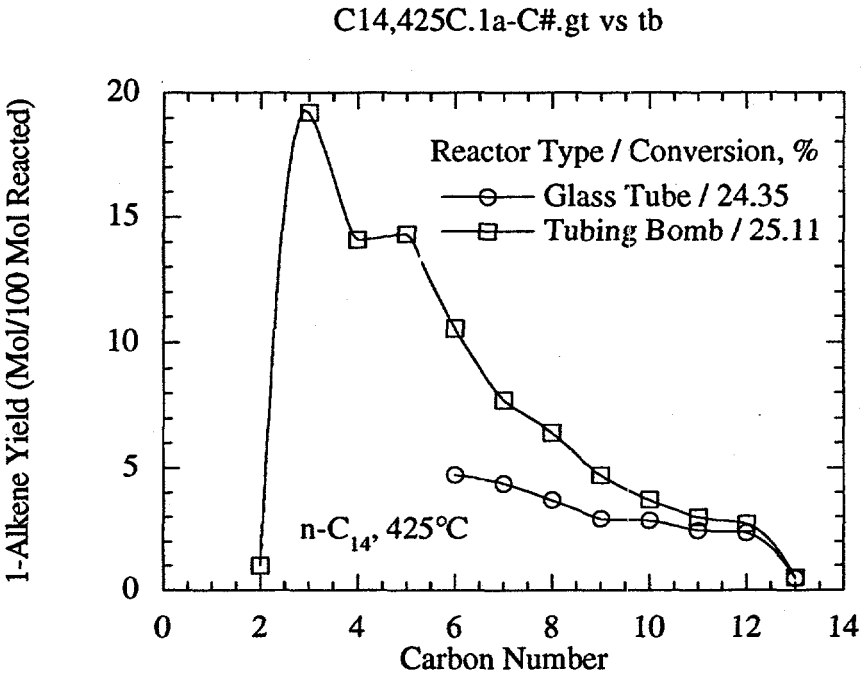

Figure 22. Relationship between 1-Alkene Yield and Carbon Number for n-Tetradecane Pyrolysis at 425°C in Two Different Reactors.

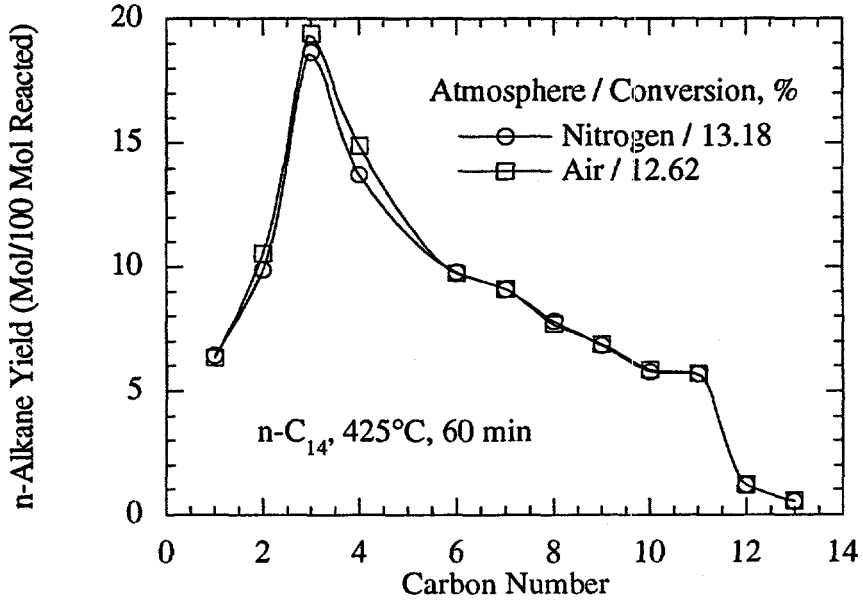

Figure 23. Relationship between n-Alkane Yield and Carbon Number for n-Tetradecane Pyrolysis under Two Different Atmospheres: Nitrogen and Air.

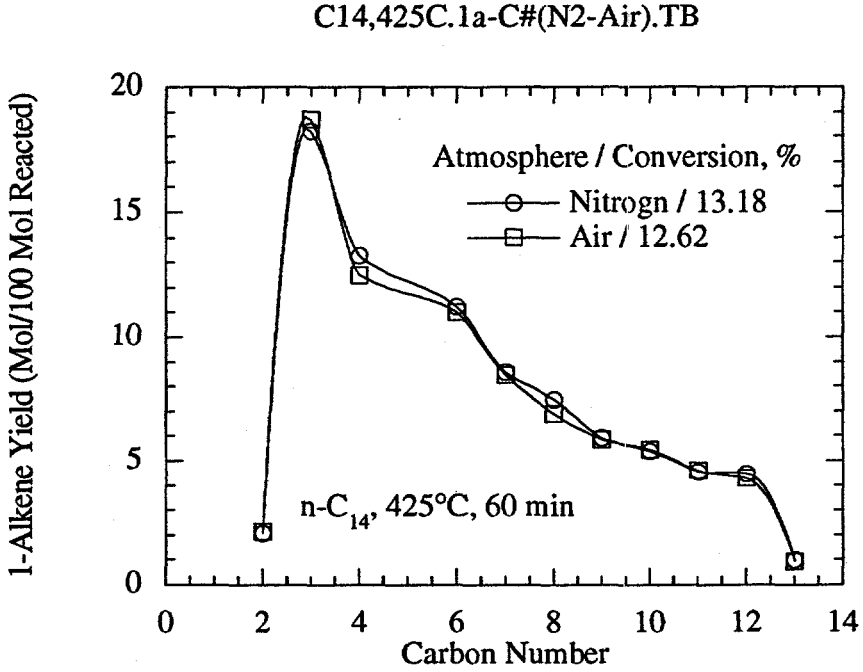

Figure 24. Relationship between 1-Alkene Yield and Carbon Number for n-Tetradecane Pyrolysis under Two Different Atmospheres: Nitrogen and Air.

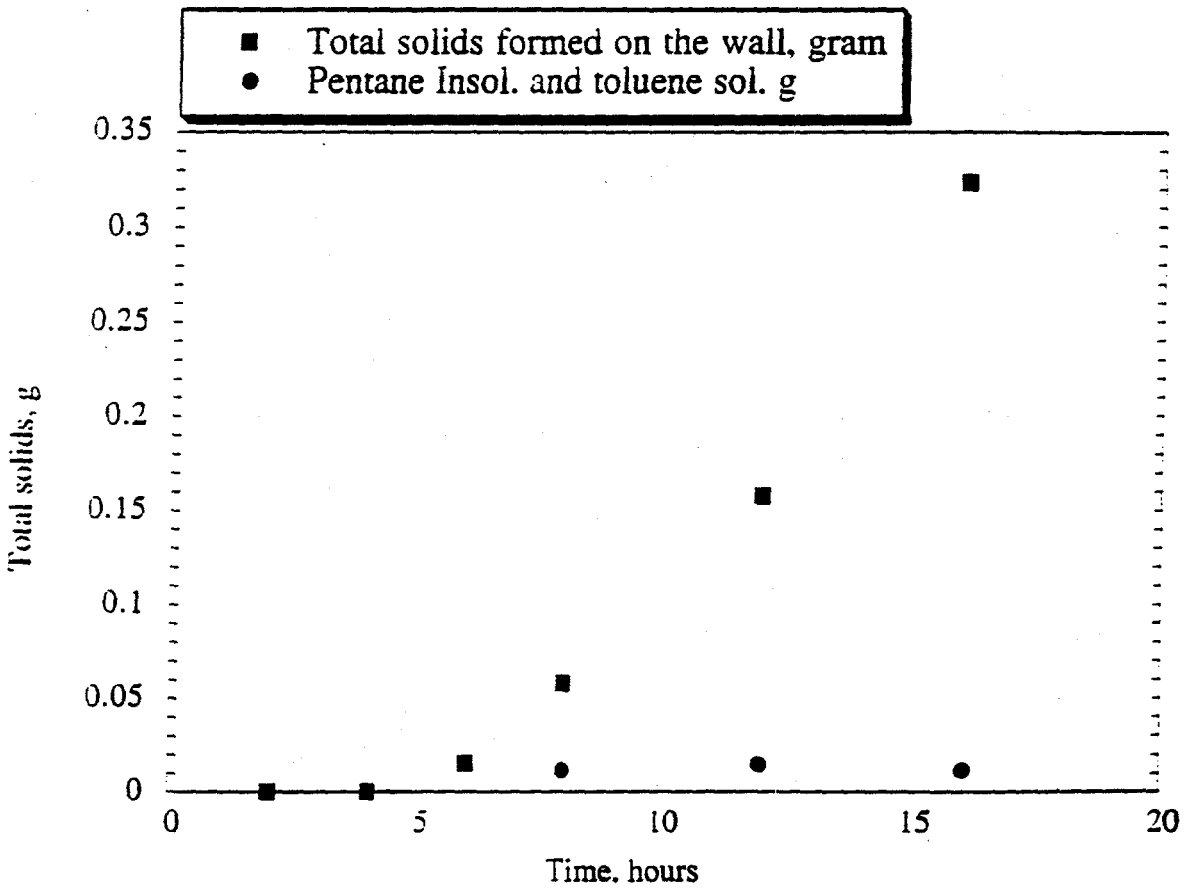

Figure 25. Weight of total Deposit formed on the wall and suspended particle

400 μm

a

b

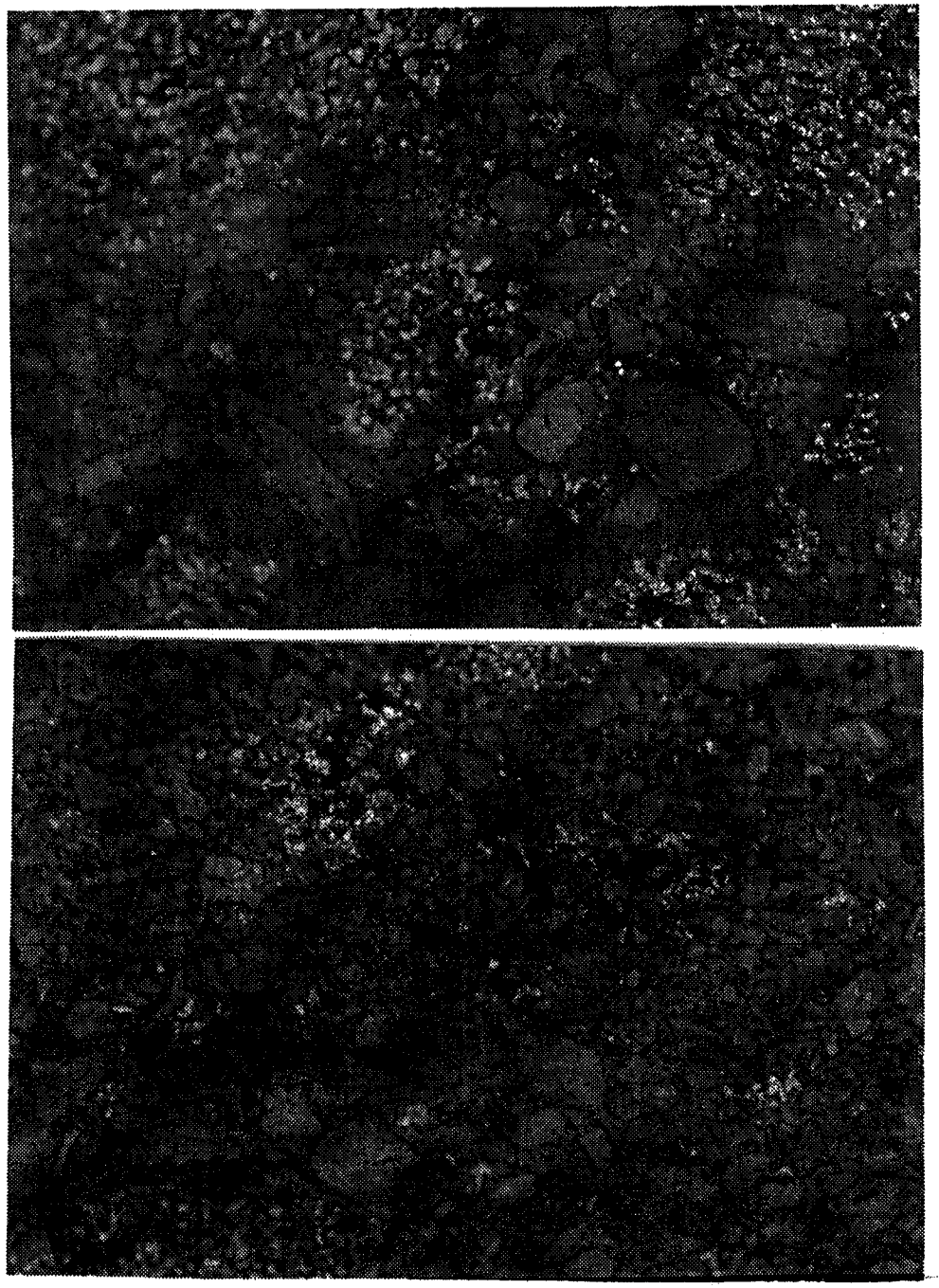

Figure 26 a,b. Polarized-Light Micrographs of (a) PX-21; (b) Outgassed Stressed with Dodecane + 5% Decalin at 500°C, 1h.

c

200 μm

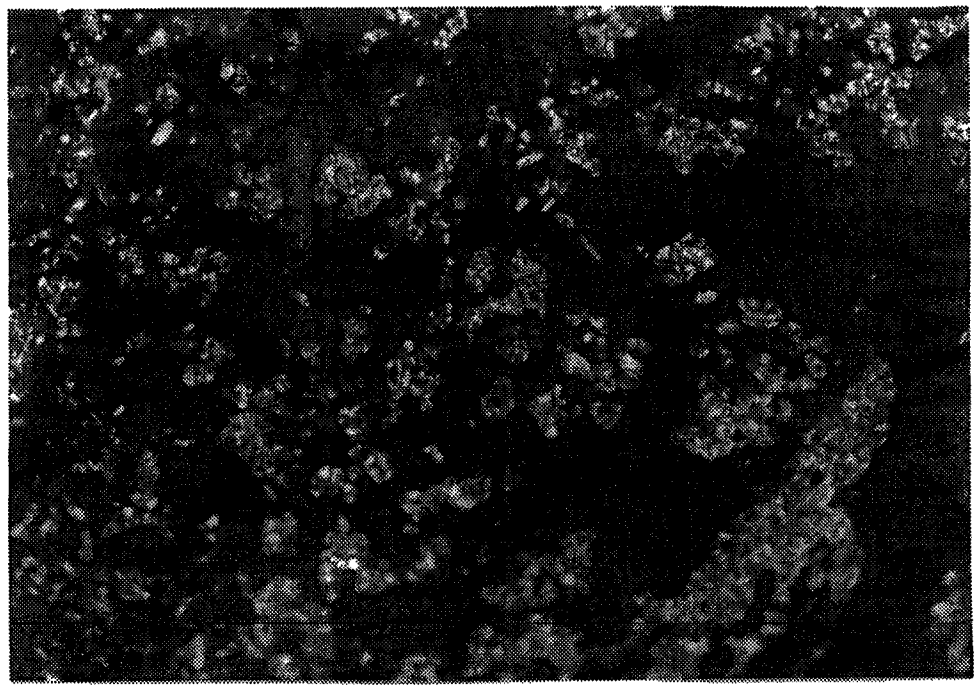

Figure 26 c. Solid Deposit Obtained from Thermal Stressing of Dodecane +5% Decalin at 500°C for 1 h.

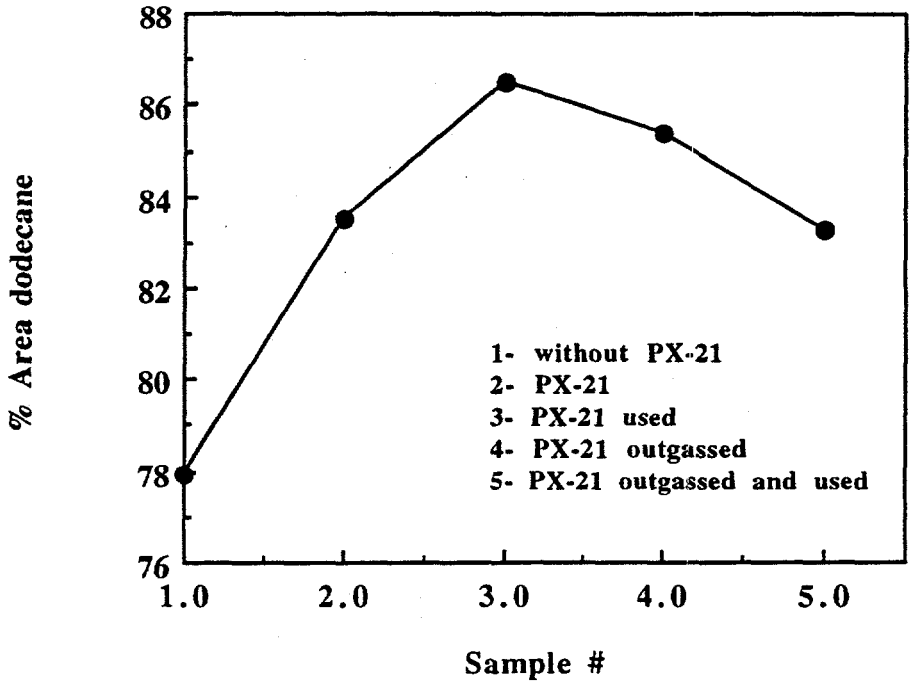

Figure 27. The Percent Area of Dodecane in the Liquid obtained after Thermal Stressing of Dodecane + 5% Decalin + 100 mg PX-21 at 425°C for 5h.

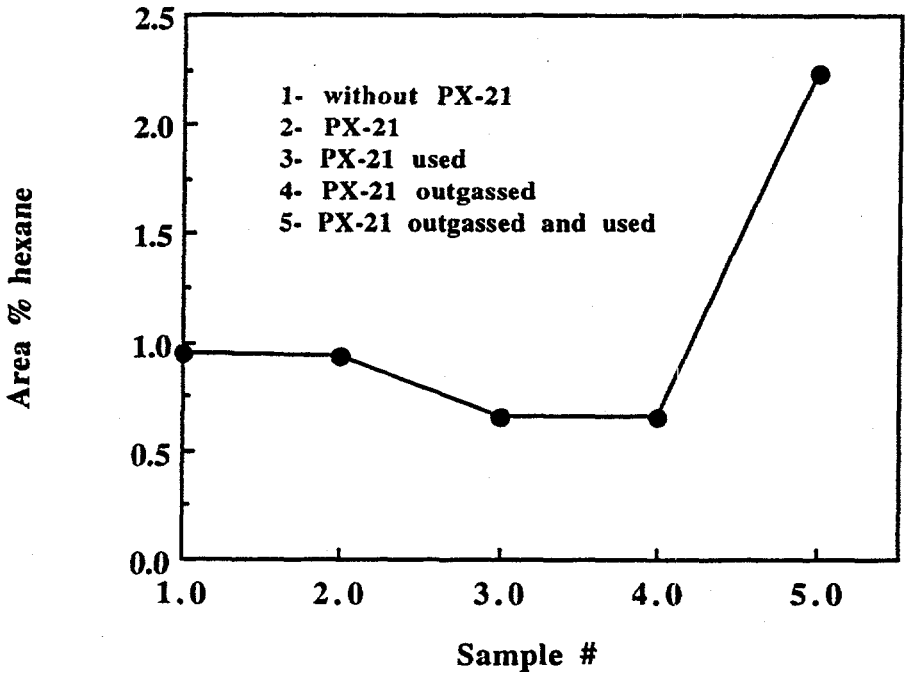

Figure 28. The Percent Area of Hexane in the Liquid obtained after Thermal Stressing of Dodecane + 5% Decalin + 100 mg PX-21 at 425°C for 5h.

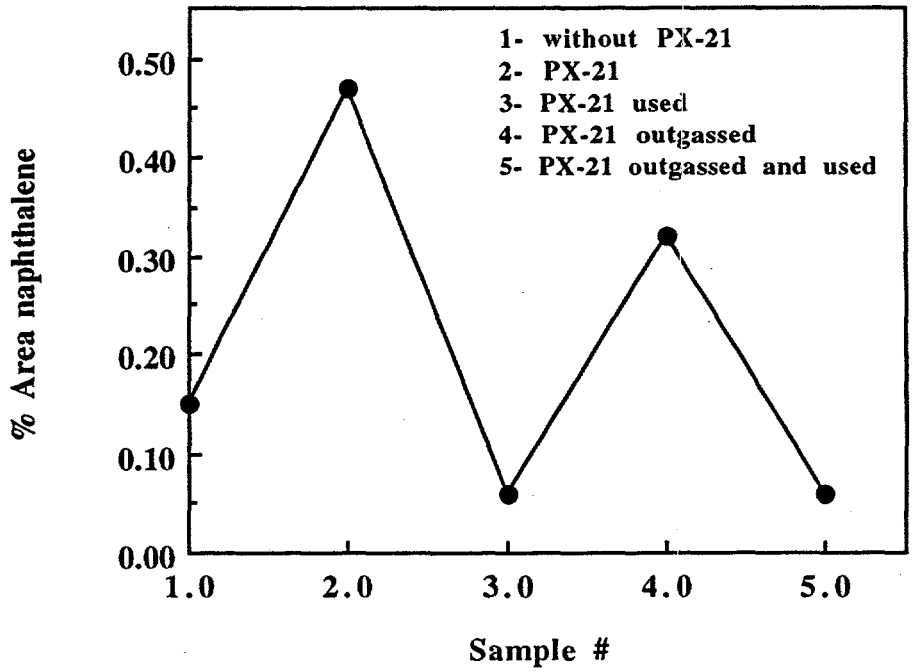

Figure 29 The Percent Area of Naphthalene in the Liquid obtained after Thermal Stressing of Dodecane + 5% Decalin + 100 mg PX-21 at 425°C for 5h.

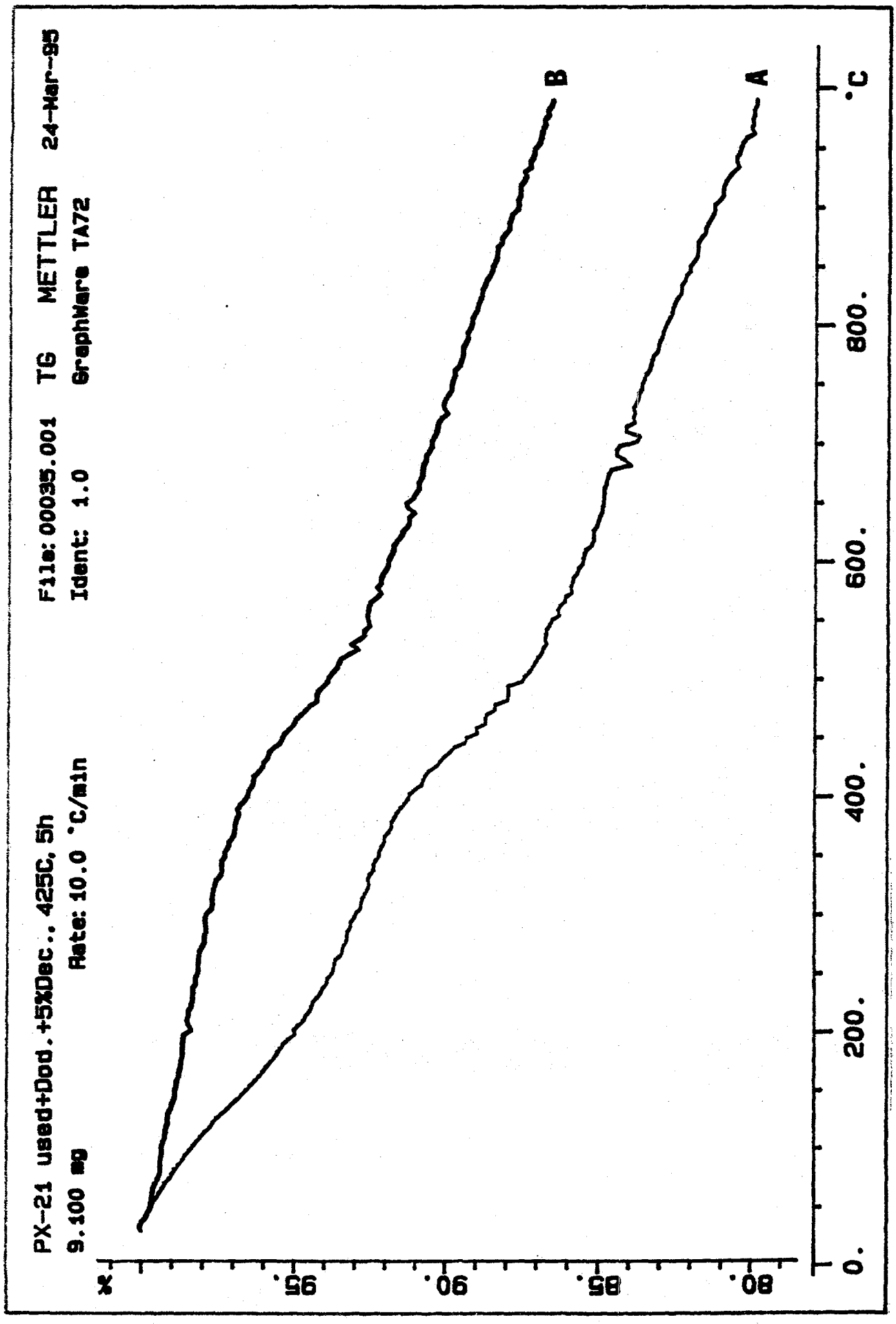

Figure 30. Thermogravimetric Analysis of (A) PX-21 Used (B) PX-21 Outgassed Used Stressed with dodecane + 5% Decalin at 425 °C for 5h.

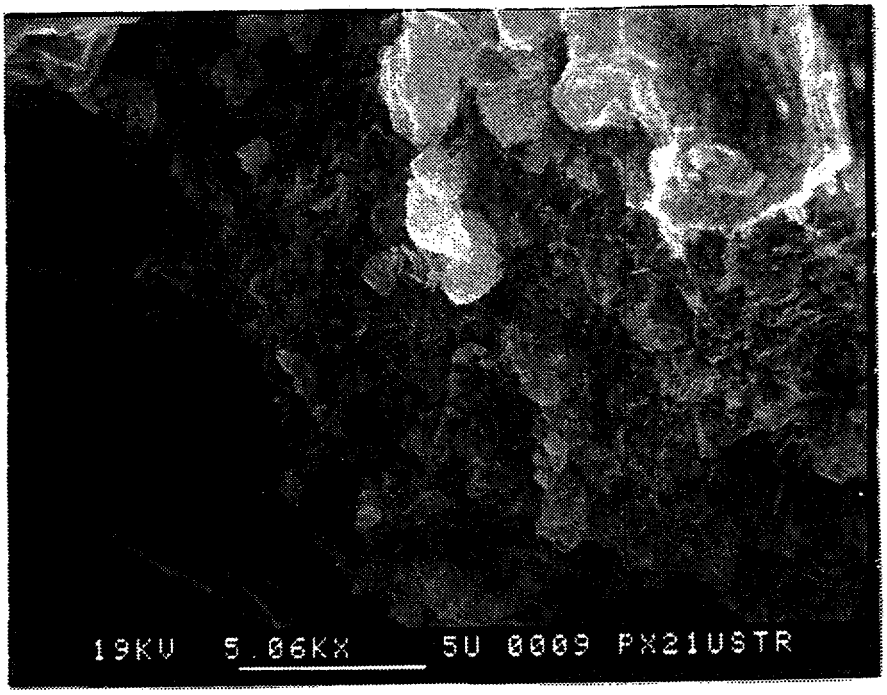

a

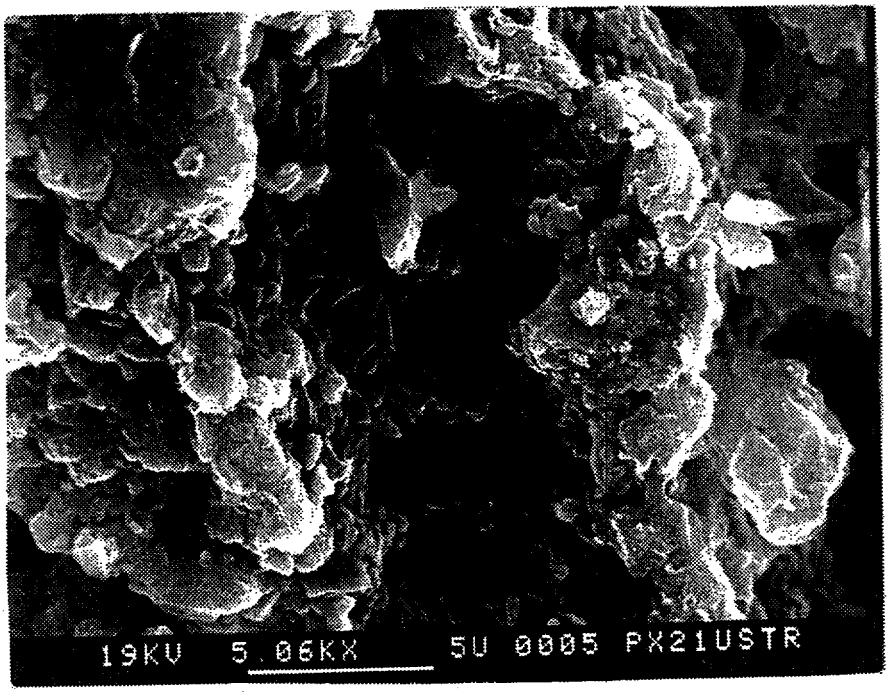

b

Figure 31. Scanning Electron Micrographs of (a) PX-21 Used; (b) PX-21 Used Outgassed Stressed with Dodecane + 5% Decalin at 425°C for 5h.

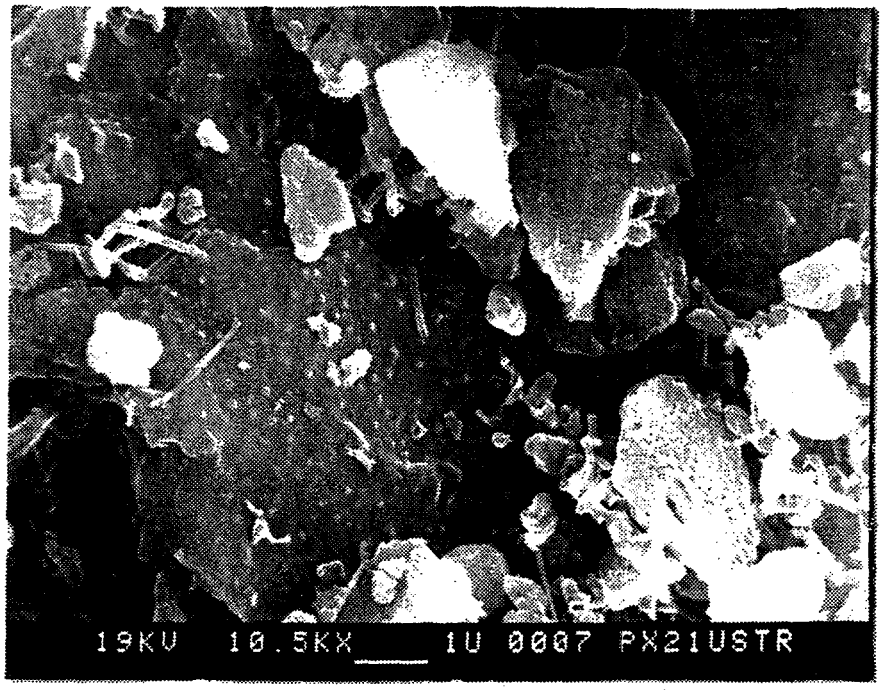

a

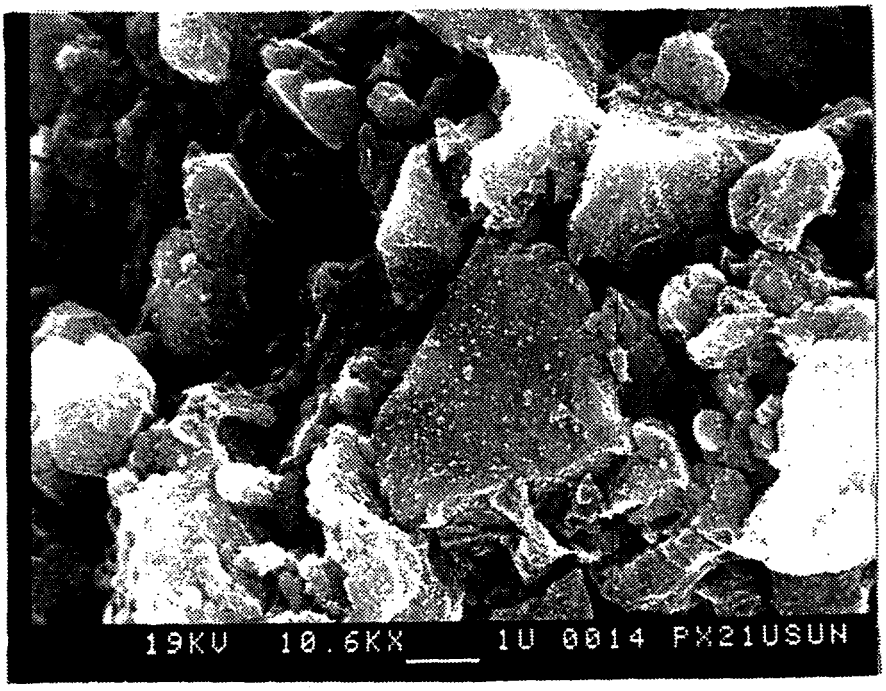

b

Figure 32. Scanning Electron Micrographs of (a) PX-21 Used; (b) PX-21 Used Outgassed Stressed with Dodecane + 5% Decalin at 425 °C for 5h.

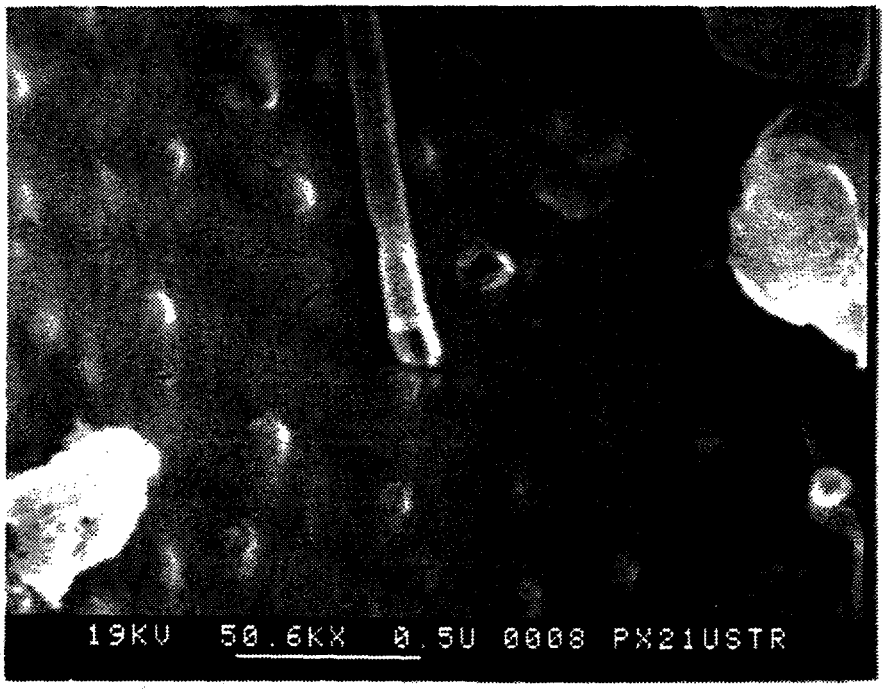

a

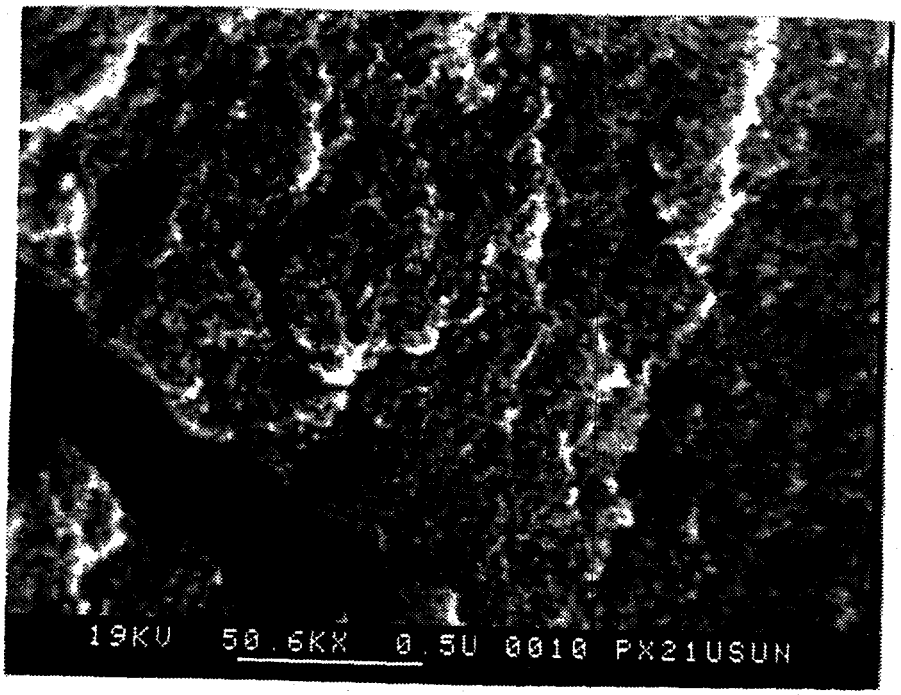

b

Figure 33. Scanning Electron Micrographs of (a) PX-21 used; (b) Used Outgassed Stressed with Dodecane + Decalin at 425°C for 5h.

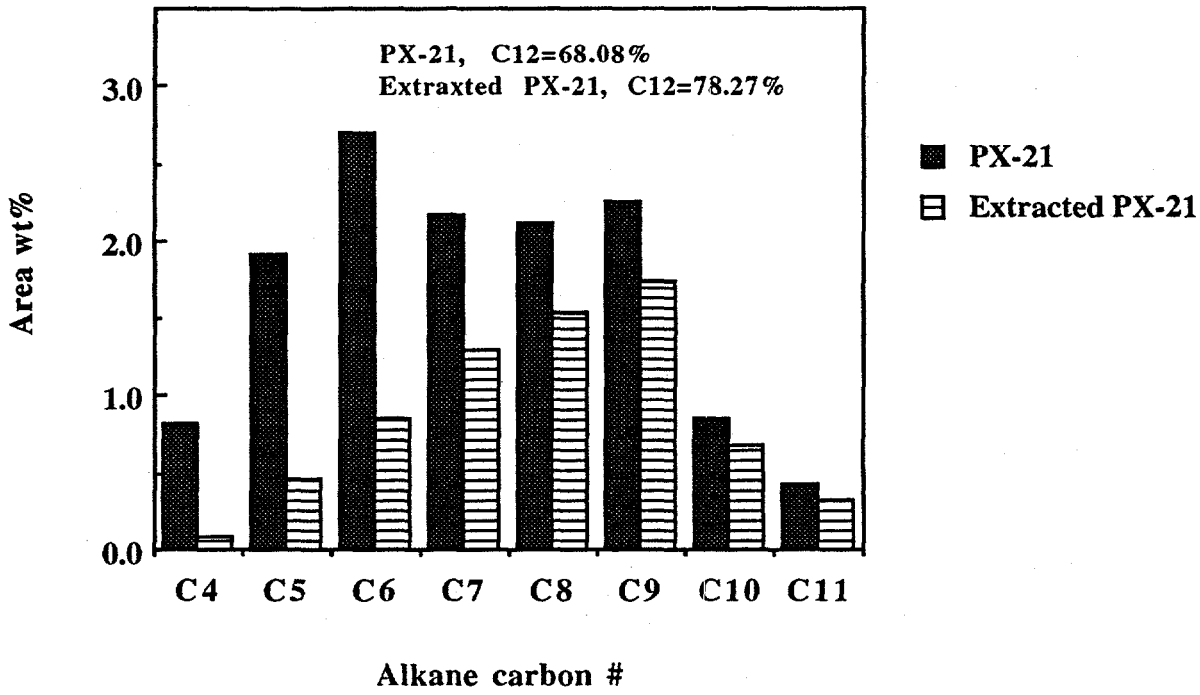

Figure 34. The Area Percent of Alkanes in the Liquids Obtained after Thermal Stressing of Dodecane + 5% Decalin + 100 mg Original and Extracted PX-21 at 450°C, 0.5h.

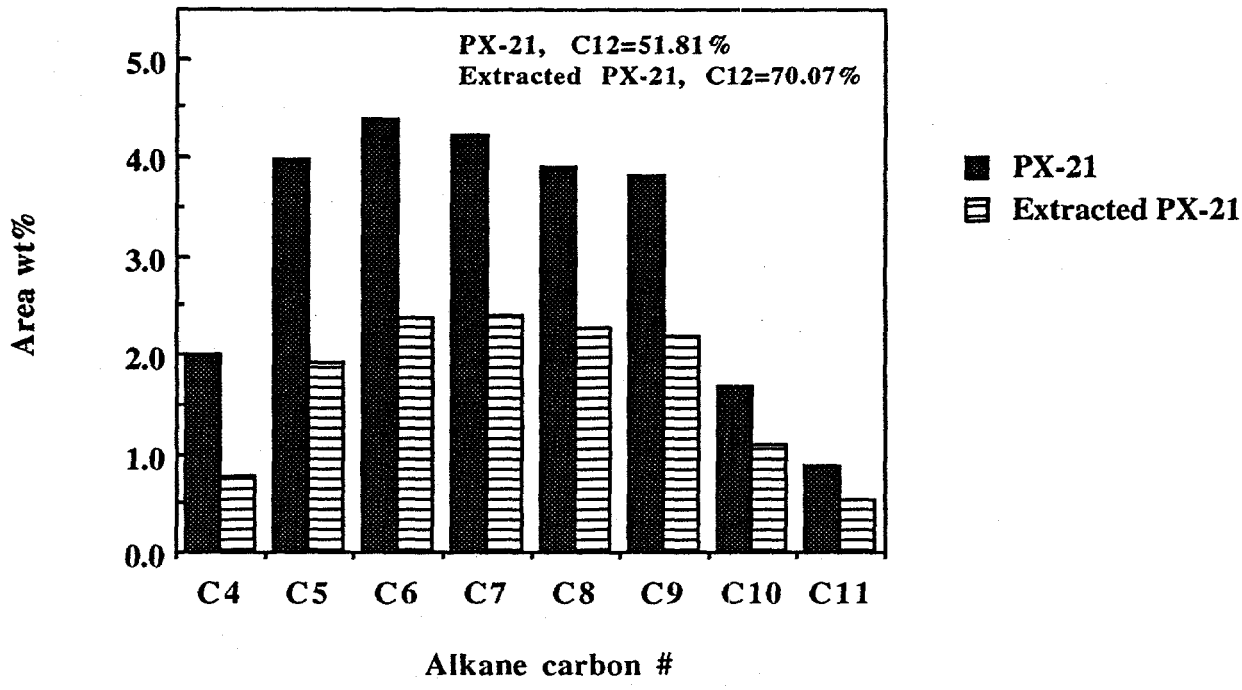

Figure 35. The Area Percent of Alkanes in the Liquids Obtained after Thermal Stressing of Dodecane + 5% Decalin + 100 mg Original and Extracted PX-21 at 450°C, 1h.

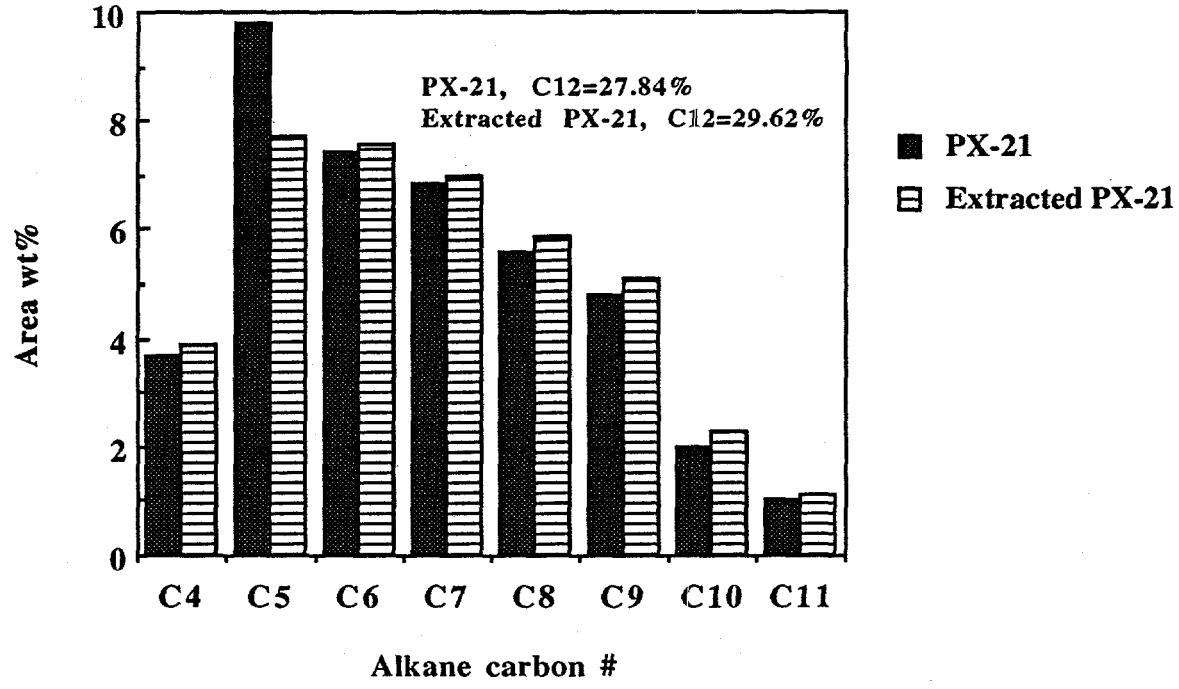

Figure 36. The Area Percent of Alkanes in the Liquids Obtained after Thermal Stressing of Dodecane + 5% Decalin + 100 mg Original and Extracted PX-21 at 450°C, 2h.

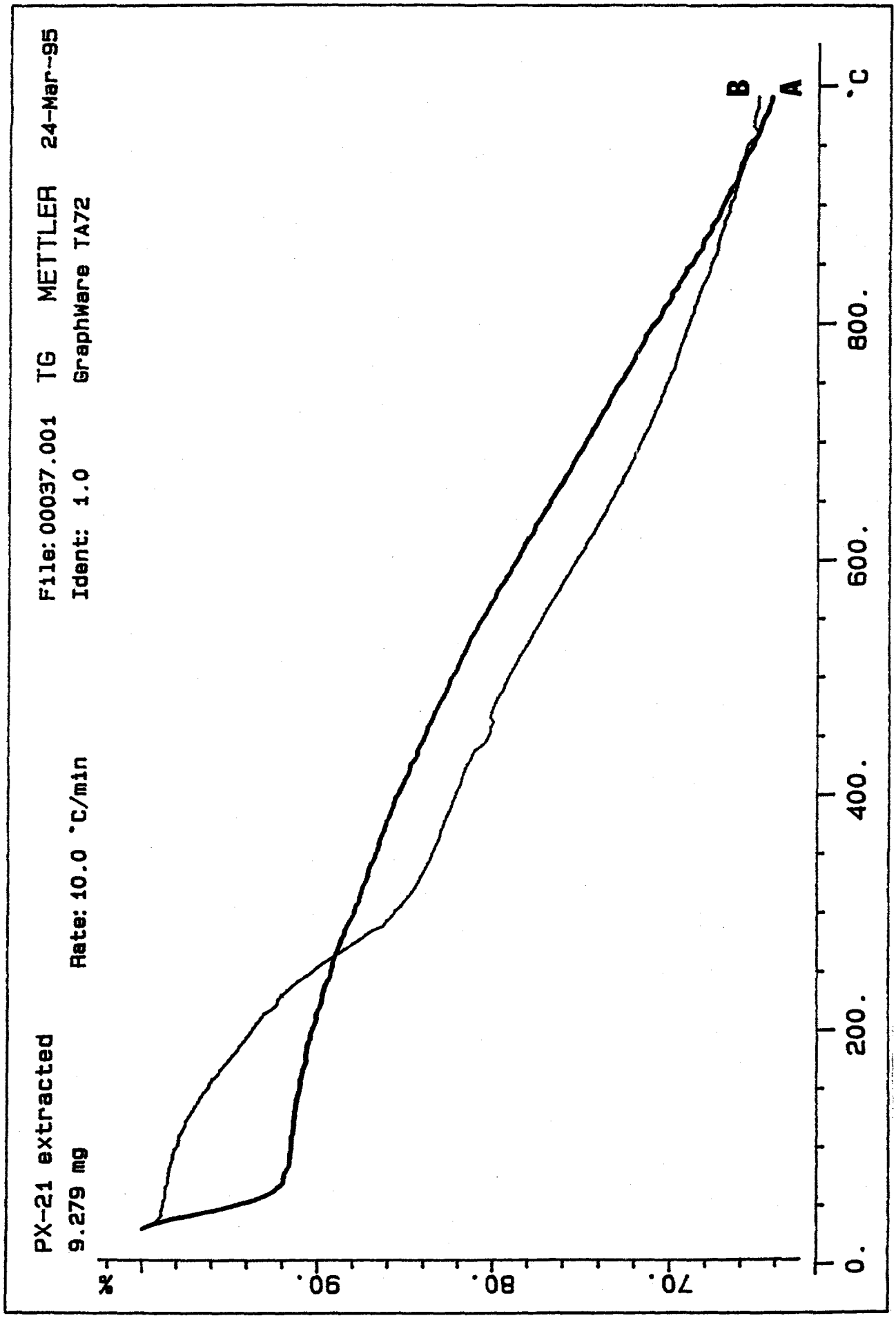

Figure 37. Thermogravimetric analysis of (A) PX-21 (B) PX-21 Extracted with Touene for 24h.

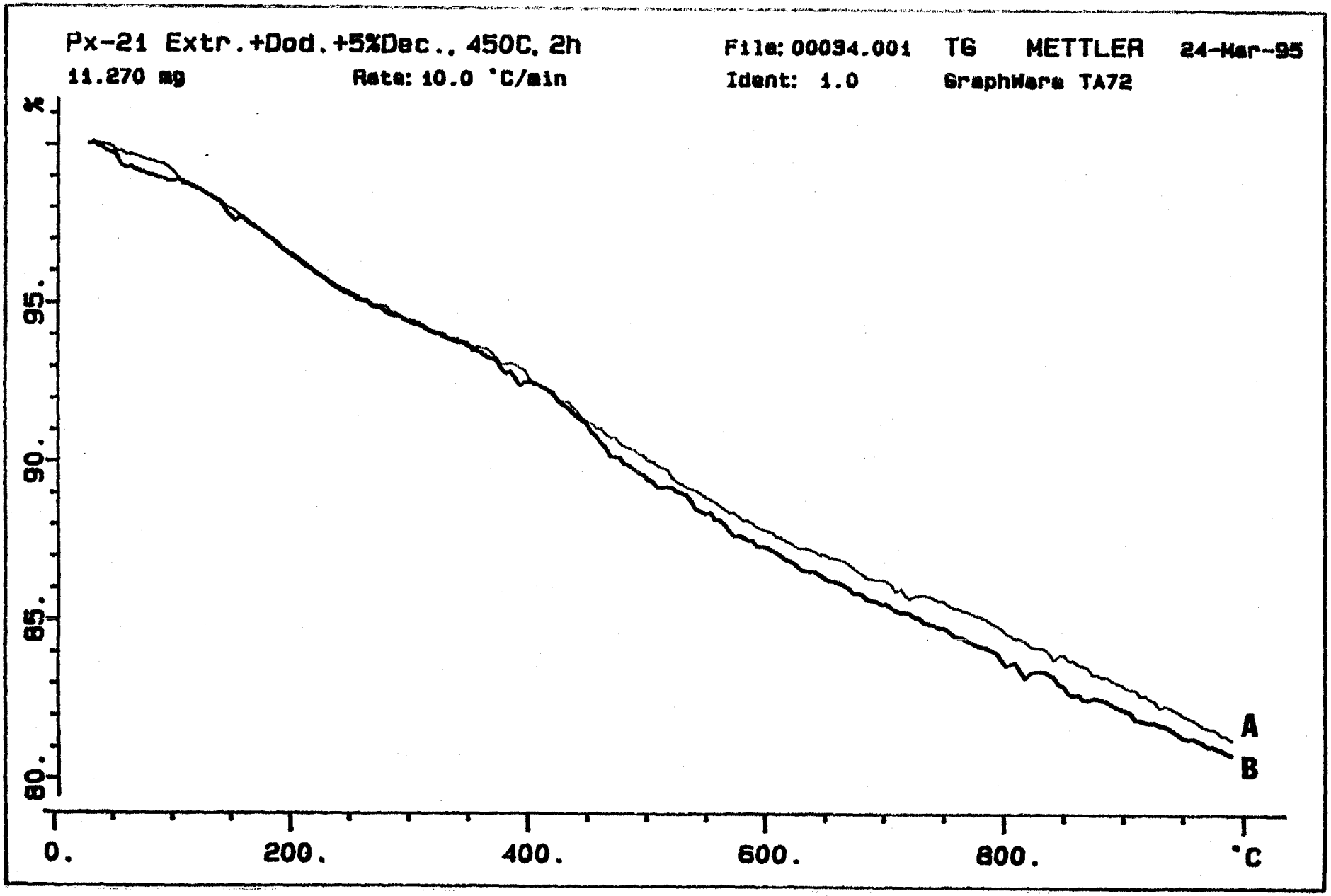

Figure 38. Thermogravimetric analysis of (A) PX-21 (B) PX-21 Extracted Stressed with Dodecane + 5% decalin 450°C for 2h.

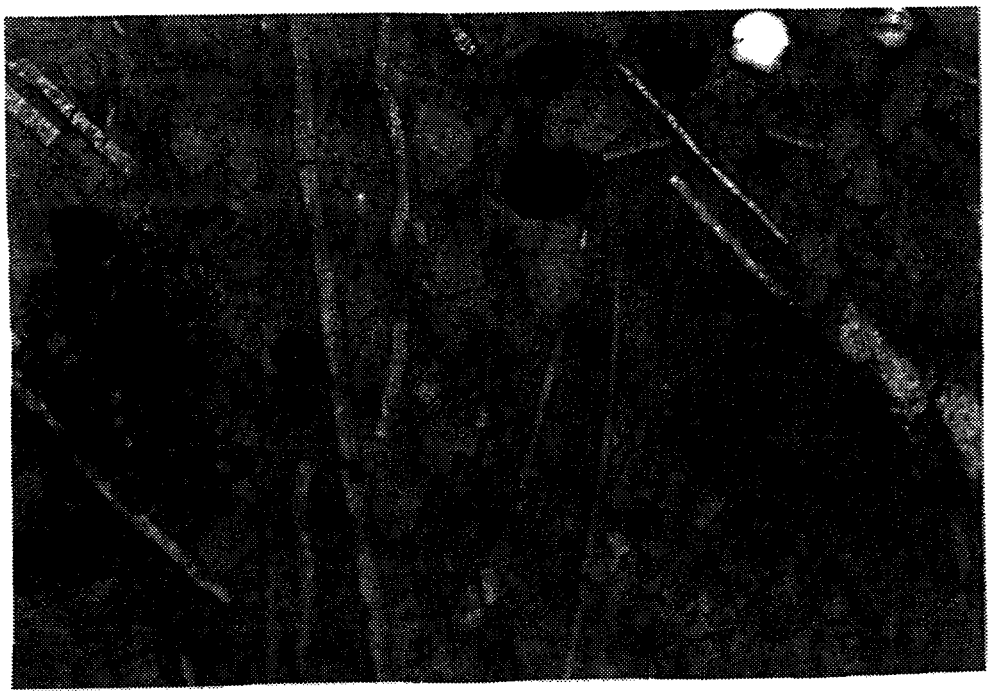

a

400 μm

b

Figure 39. Polarized-Light Micrographs of (a) PX-21; (b) PX-21 Used Extracted Stressed with Dodecane + 5% Decalin at 450°C for 1h.

a

200 μm

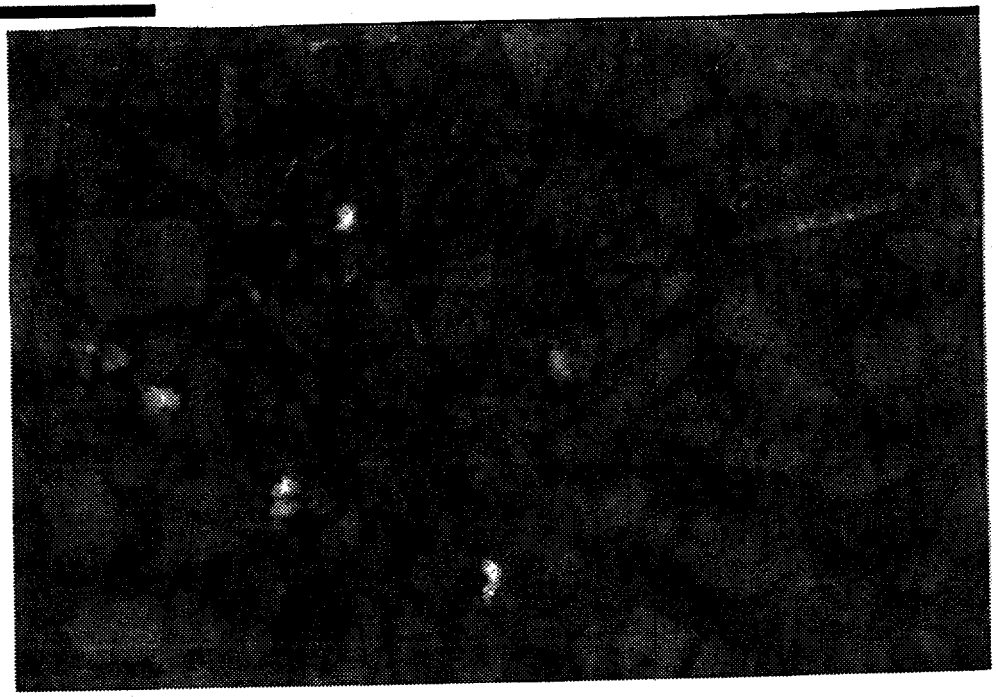

b

Figure 40. Polarized-Light Micrographs of (a) PX-21; (b) PX-21 Extracted Stressed with Dodecane +5% Decalin at 450°C for 1h.

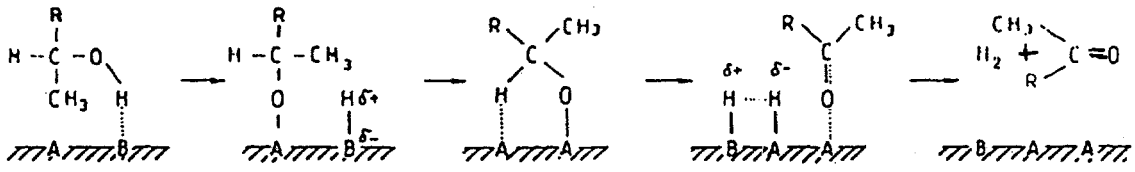

Figure 41. Dehydrogenation Mechanism [10].

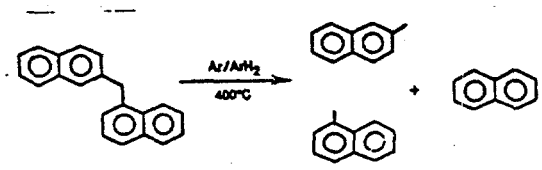

Figure 42. Decomposition of 1,2'-Dinaphthylmethane in Aromatic/Hydroaromatic Solvents [11]

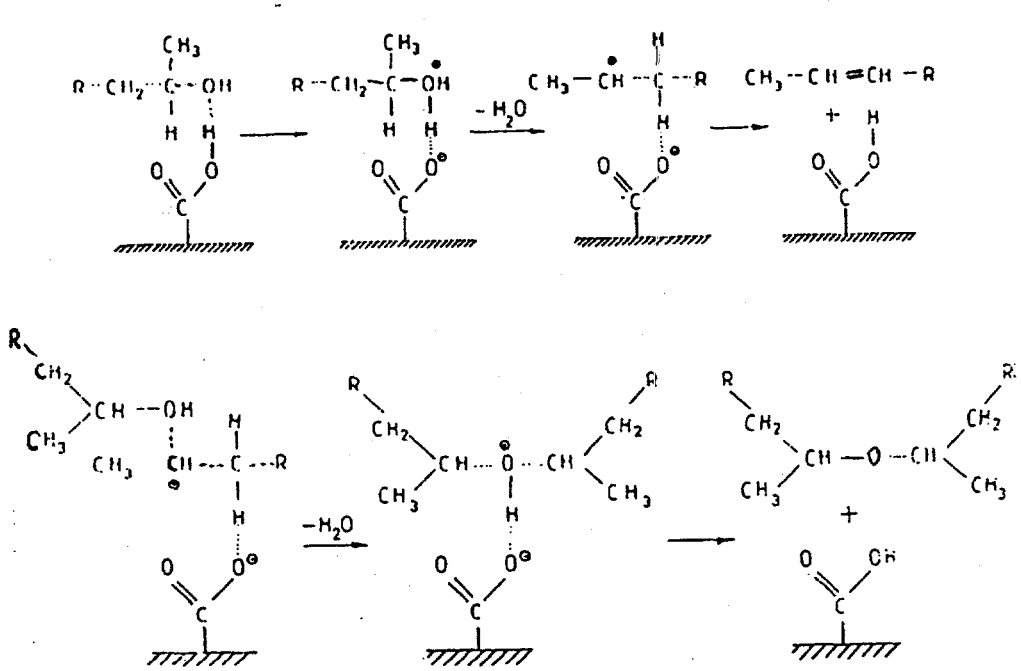

Figure 43. Dehydration of Alcohol [10].

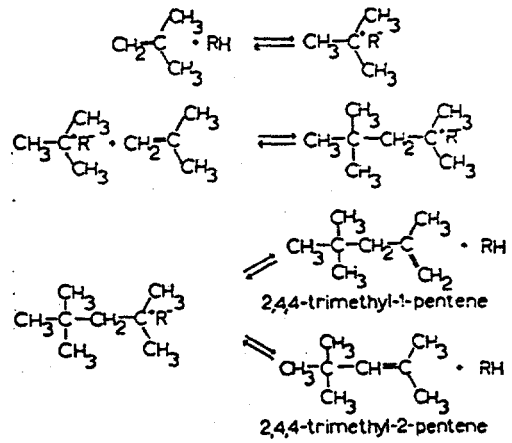

Figure 44. Proposed Cationic Mechanism for the Dimerisation of Methylpropene [26].

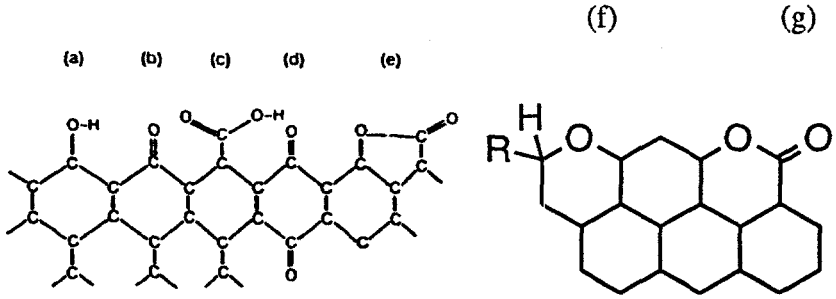

Figure 45. Various Oxygen Functional Groups on the Surface of Carbon[38] (a) phenol; (b) carbonyl; (c) carboxyl; (d) quinone; (e) lactone; (f) pyran; (g) pyrone

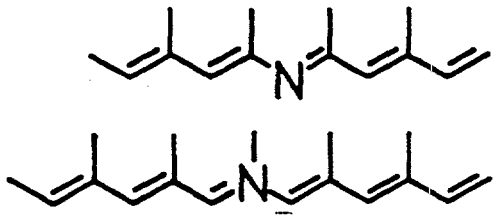

Figure 46 The Substitution of Carbon by Nitrogen Atoms at the Edges of the Carbon Sheets[28].

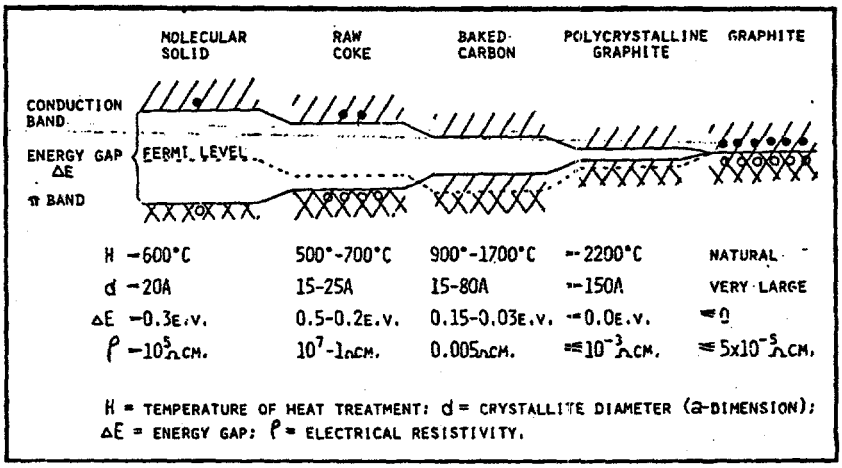

Figure 47. Band Model of Electronic Structure of Different Carbons [41].

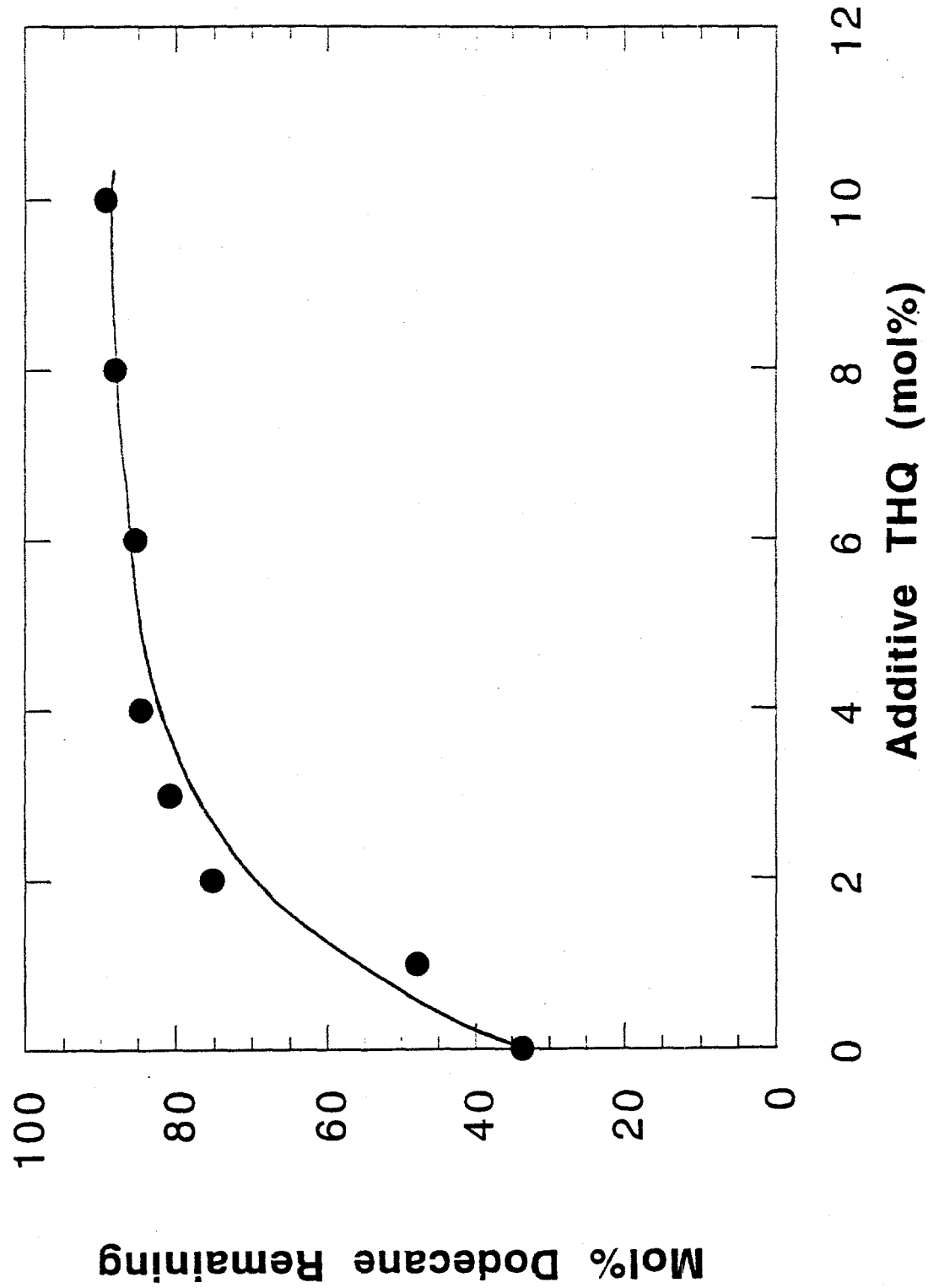

Figure 48. Mol% Dodecane Remaining as a function of Concentration of THQ at 425°C for 6h under Initian N_2 Pressure of 0.69 MPa.

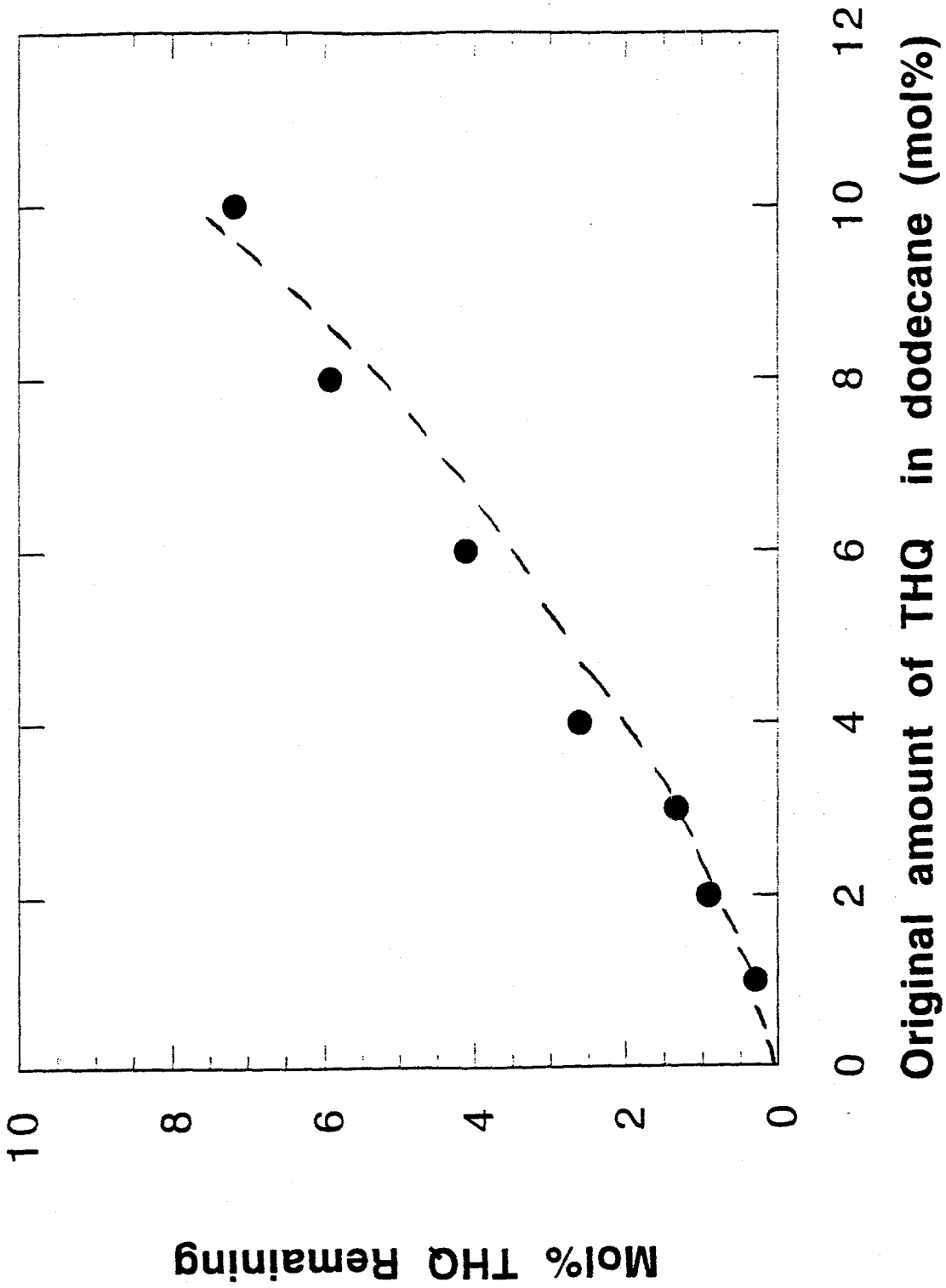

Figure 49. Mol% THQ Remaining in Dodecane after 6h at 425°C under Initial N_2 Pressure of 0.69 MPa.

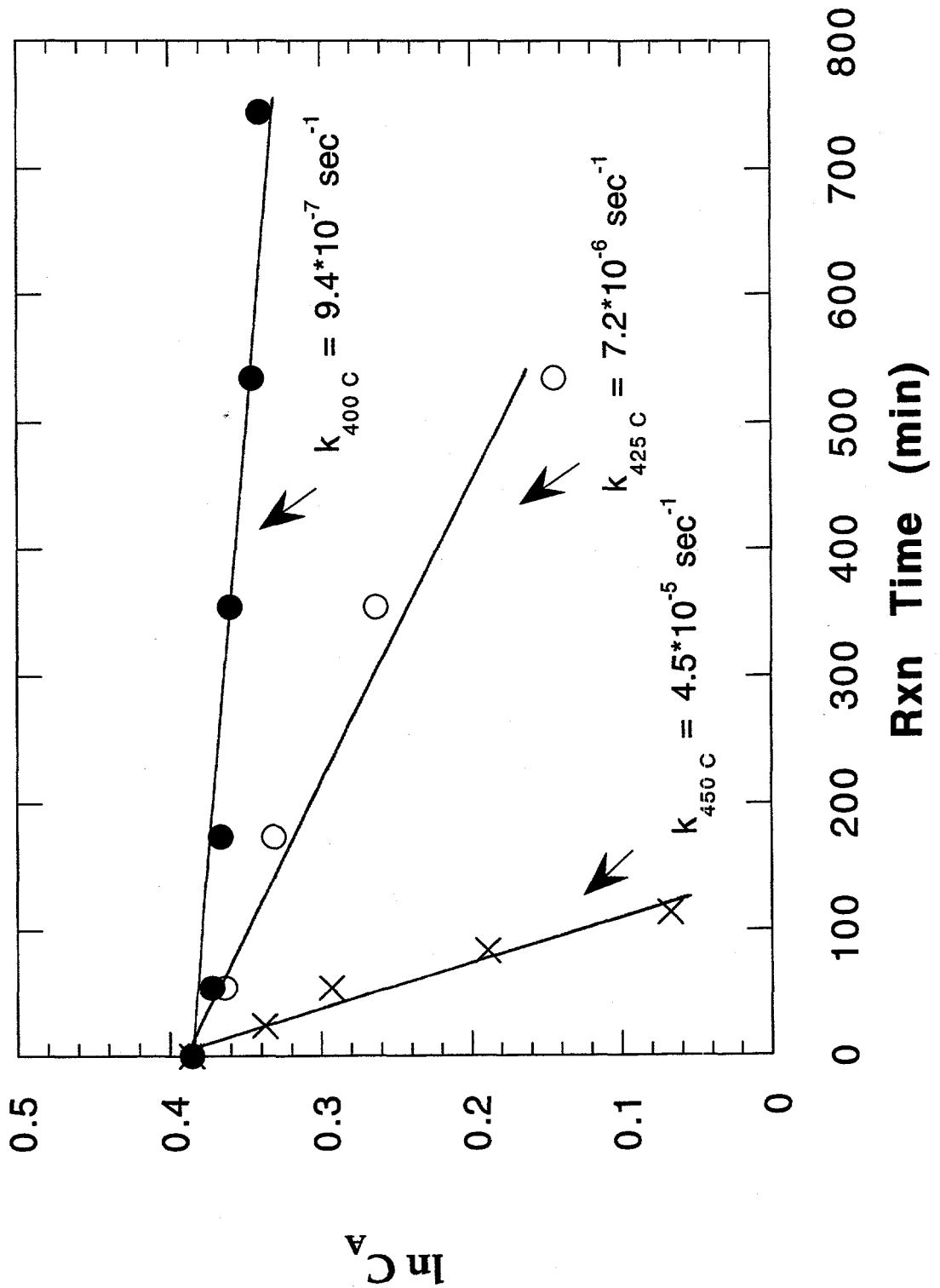

Figure 50. Plot of In C_A versus time to determine rate constant k of dodecane in the presence of THQ at 400, 425, and 450°C.

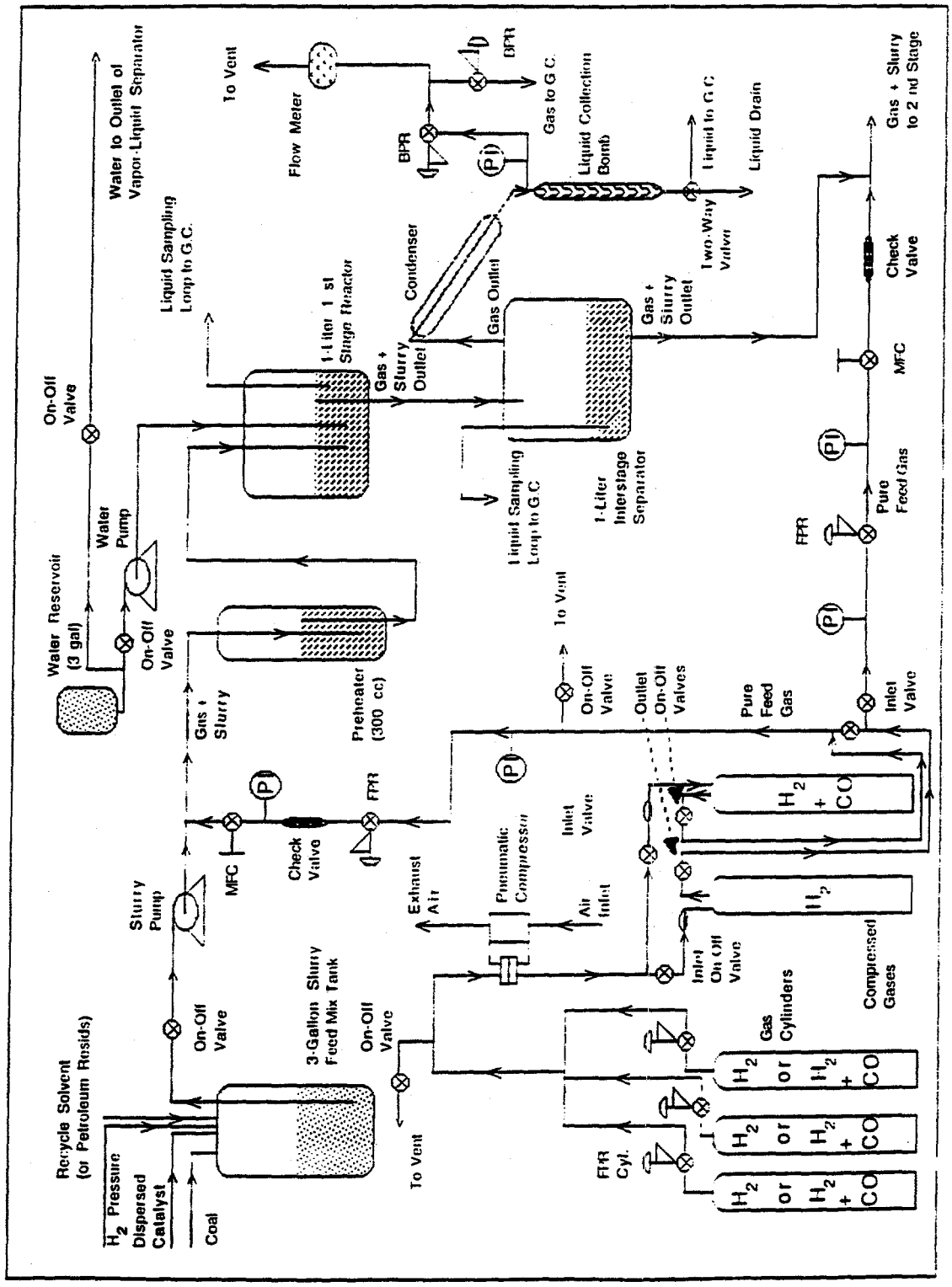

Figure 51. Process Flow Diagram of the Mini-Pilot Plant for Liquefaction of Coal in a Continuous Mode.

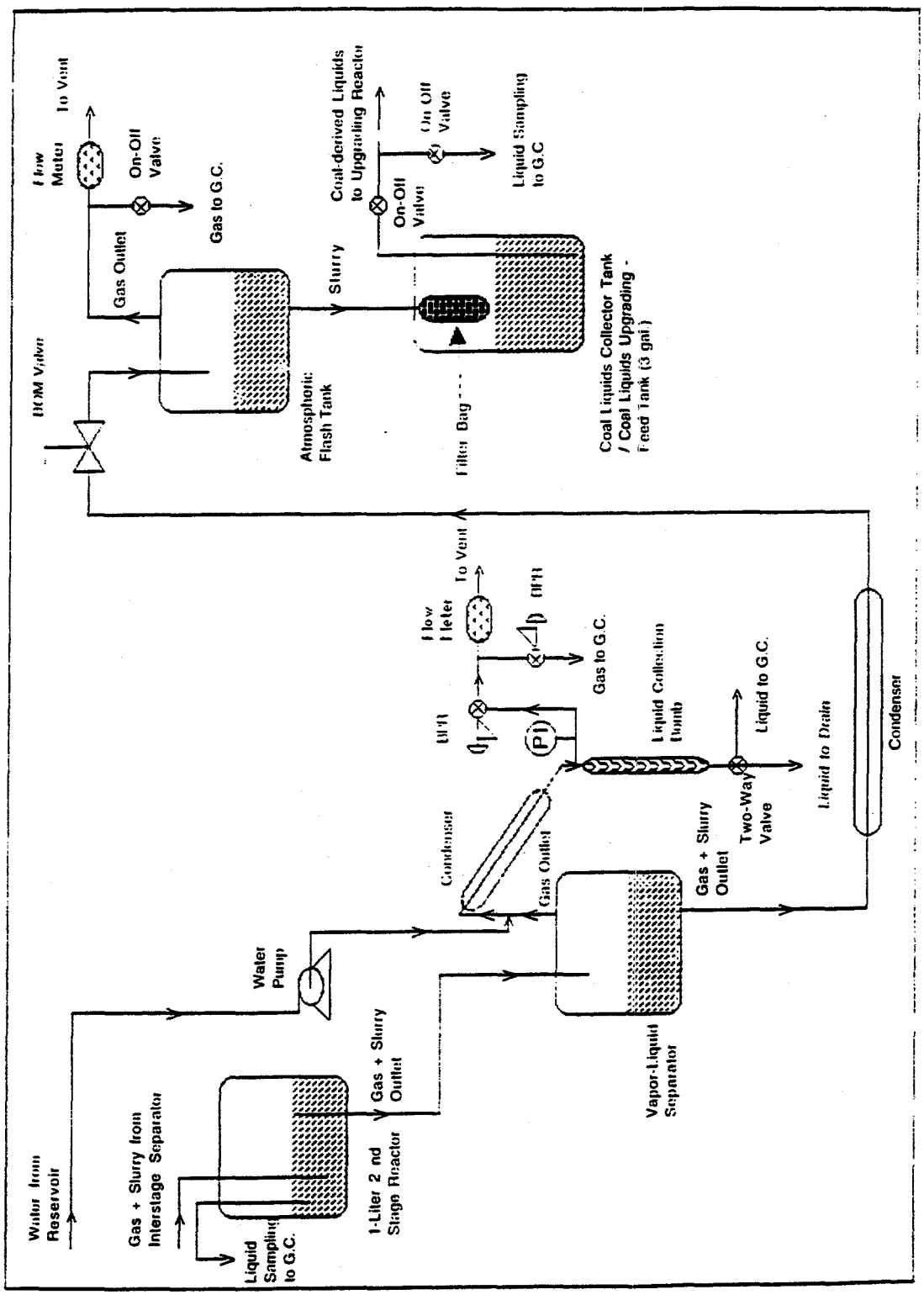

Figure 51 (contd.). Process flow Diagram of the Mini-Pilot Plant for Liquefaction of Coal in a Continuous Mode

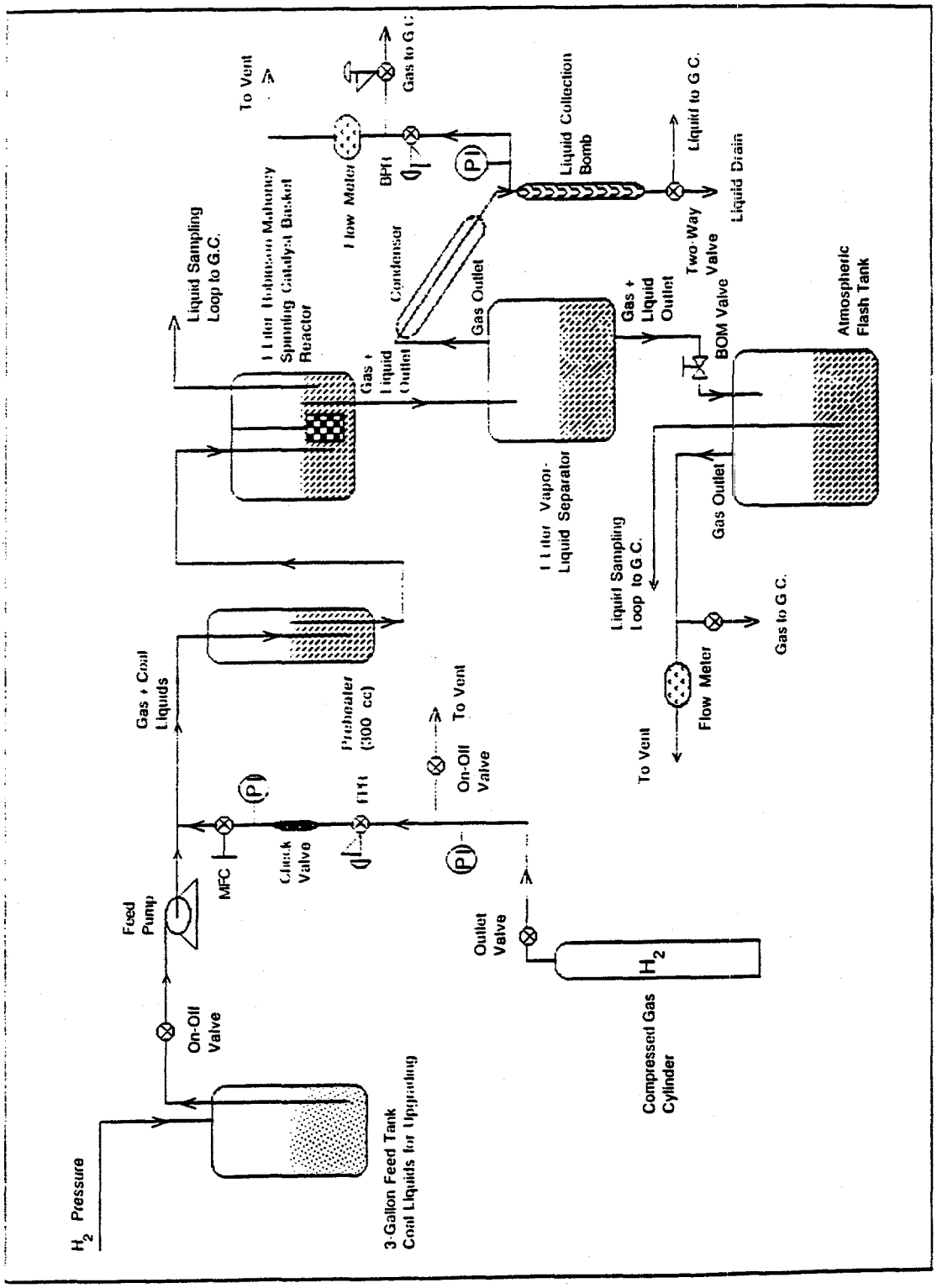

Figure 52. Process flow Diagram of the Mini-Pilot Plant for Upgrading of Coal Liquyids in a Continuous Mode.

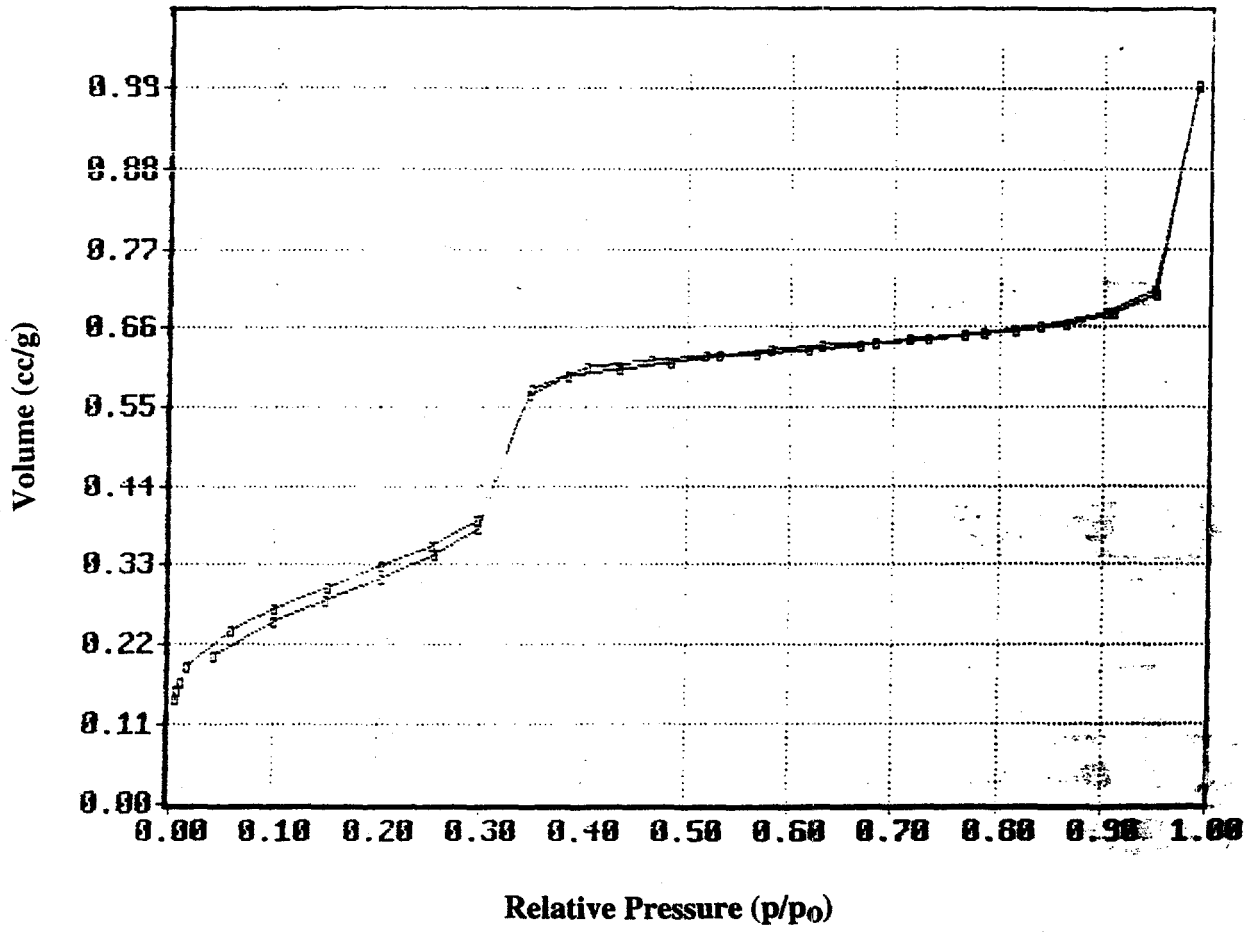

Figure 53. Typical nitrogen adsorption isotherm of mesoporous molecular sieves at 77K.

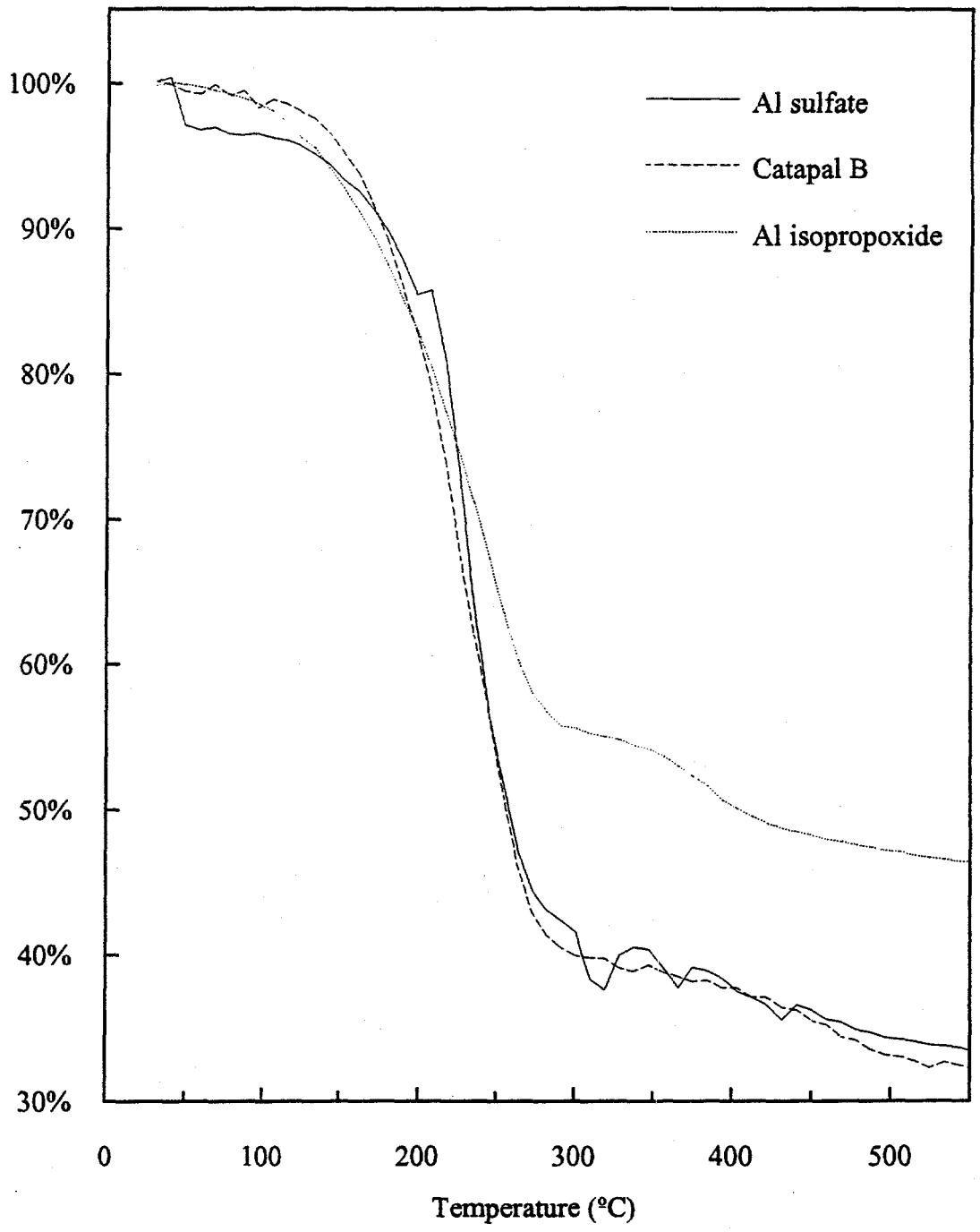

Figure 54. TGA of as-synthesized mesoporous molecular sieves prepared using different Al sources.

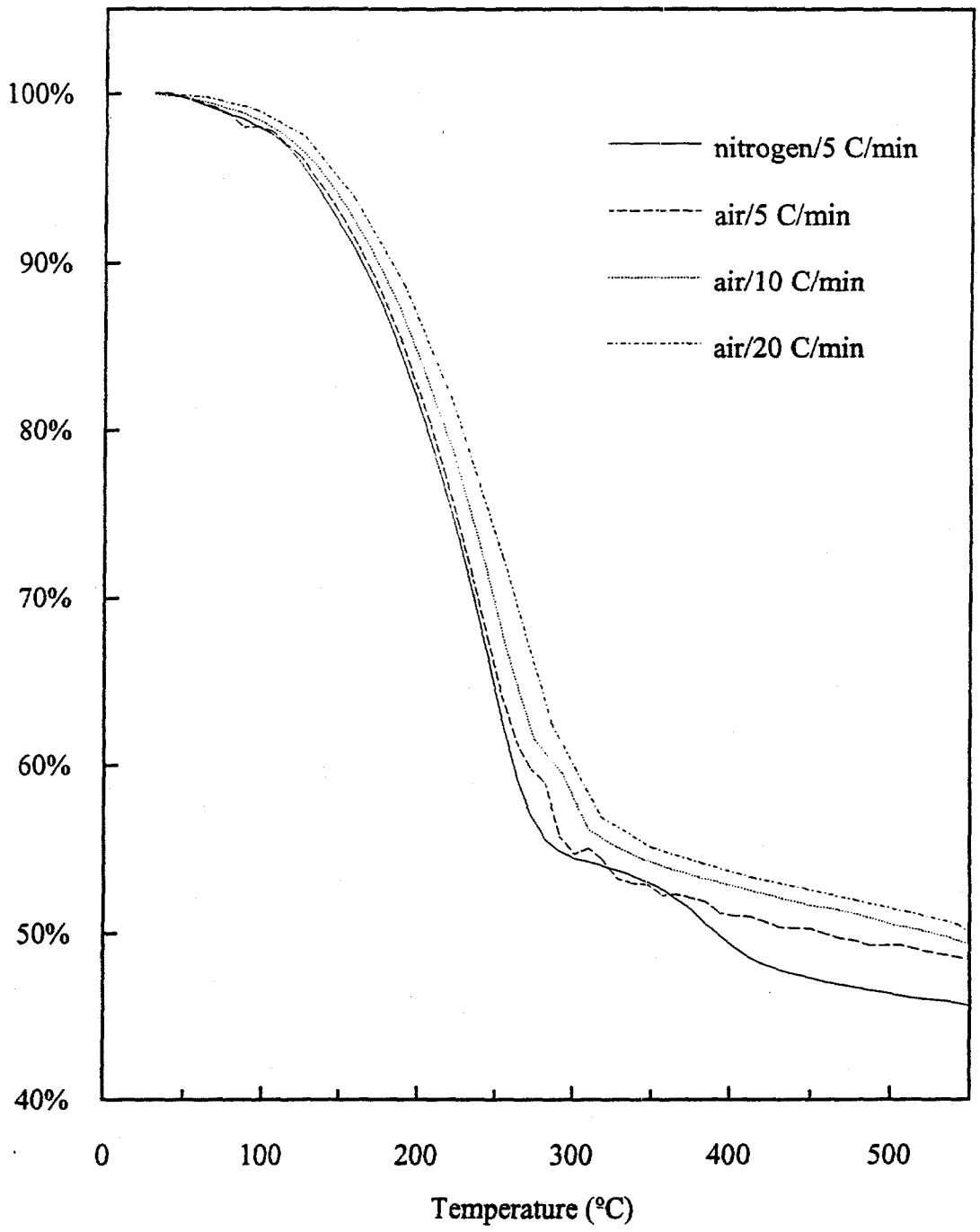

Figure 55. TGA of mesoporous molecular sieves at different conditions.

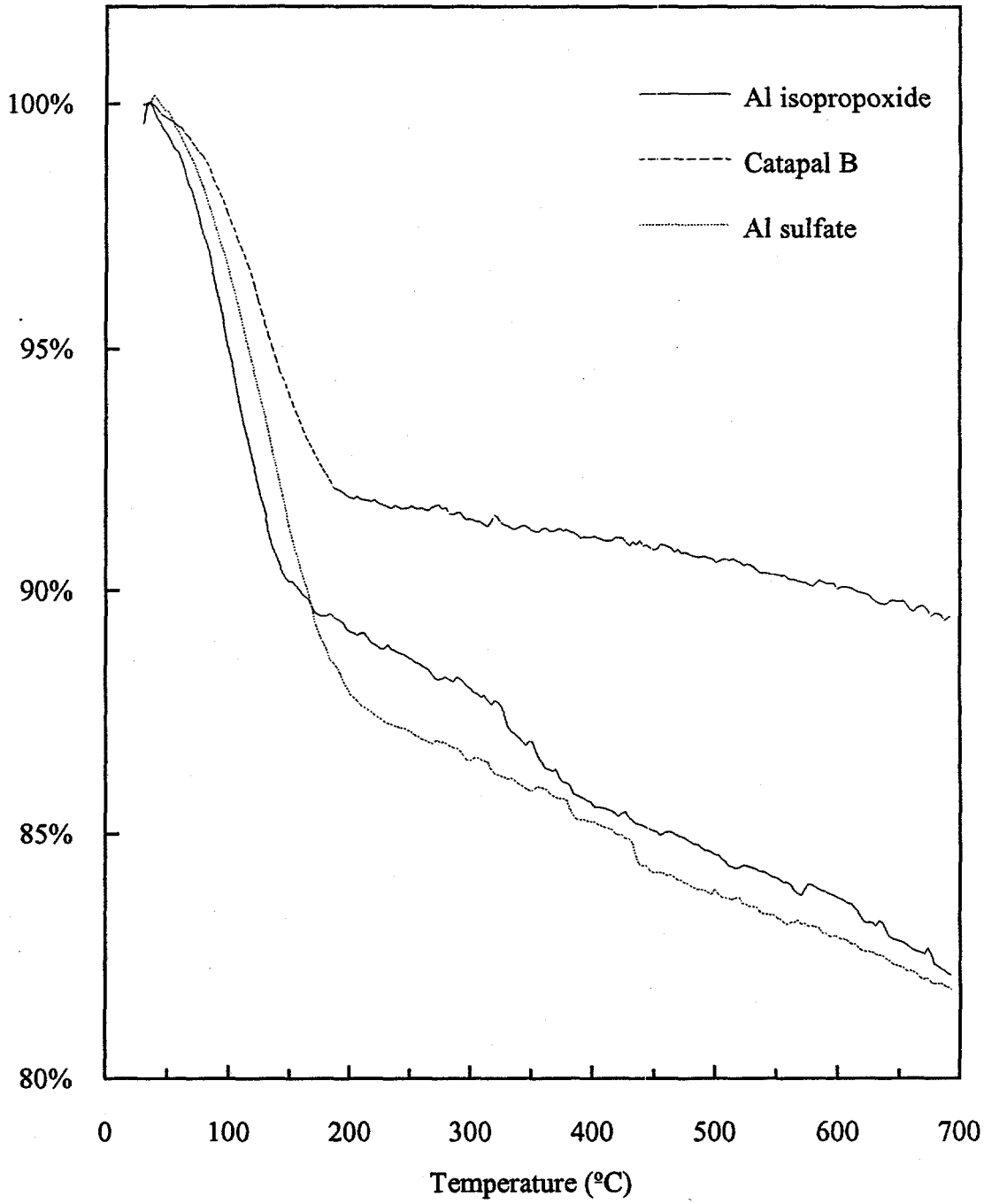

Figure 56. TGA of n-butylamine desorption from mesoporous molecular sieves prepared using different Al sources.

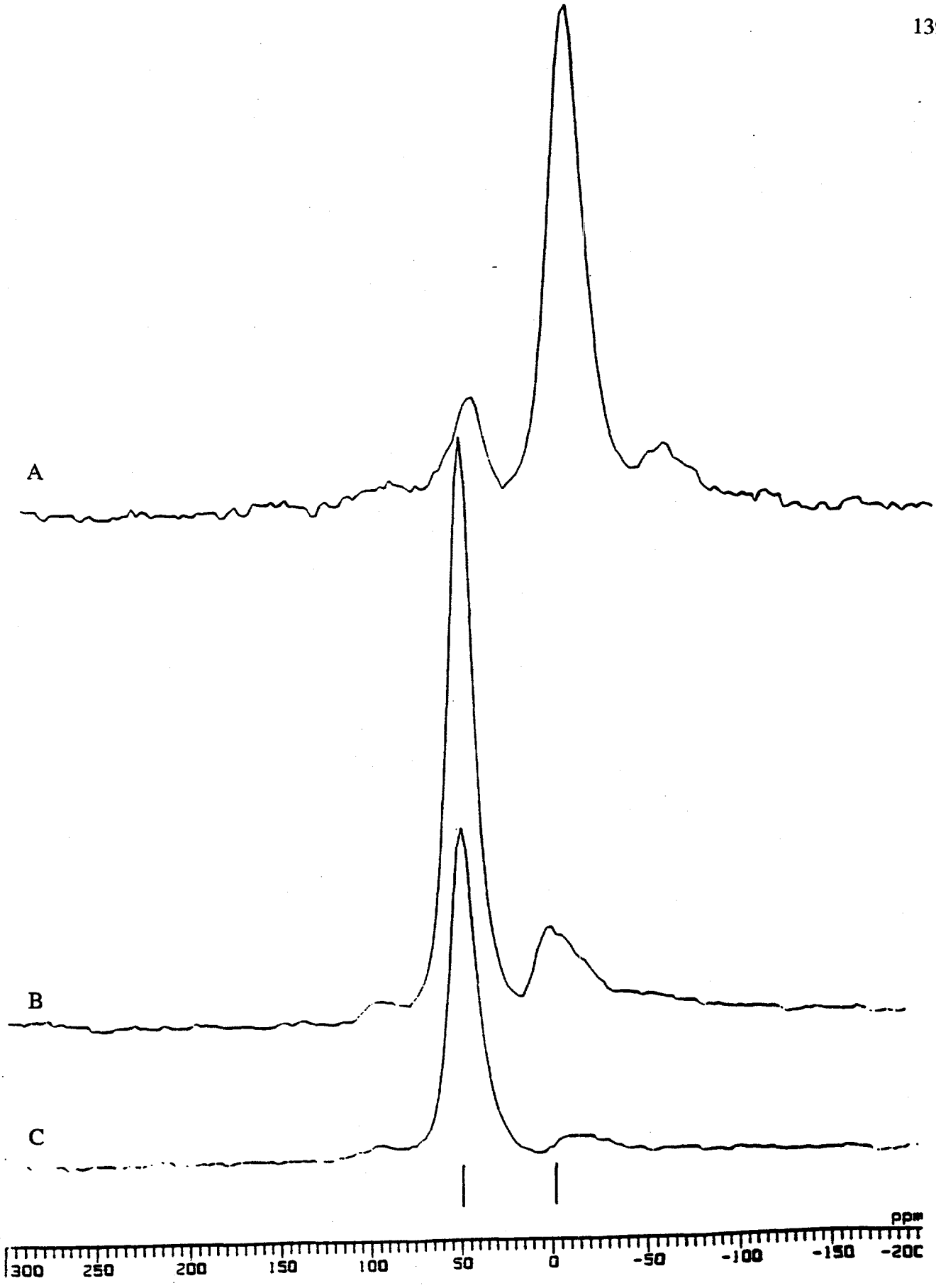

Figure 57. ^{27}Al MAS NMR spectra of mesoporous molecular sieves prepared using A) Catapal B, B) Aluminum Ispropoxide and, C) Aluminum Sulfate.

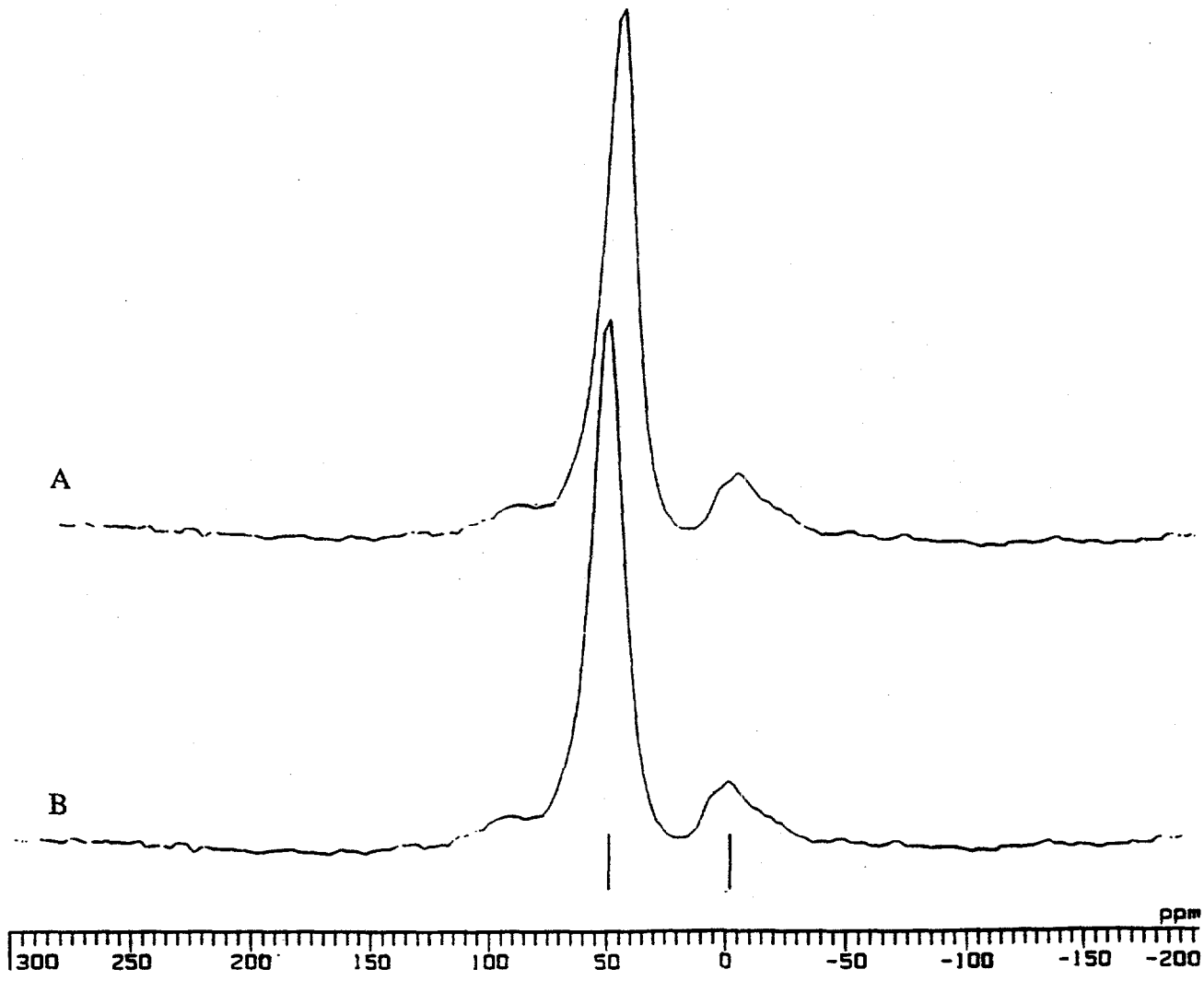

Figure 58. ^{27}Al MAS NMR spectra of mesoporous molecular sieves prepared using aluminum Ispropoxide and with SiO_2/Al_2O_3 A) 50 and B) 100.

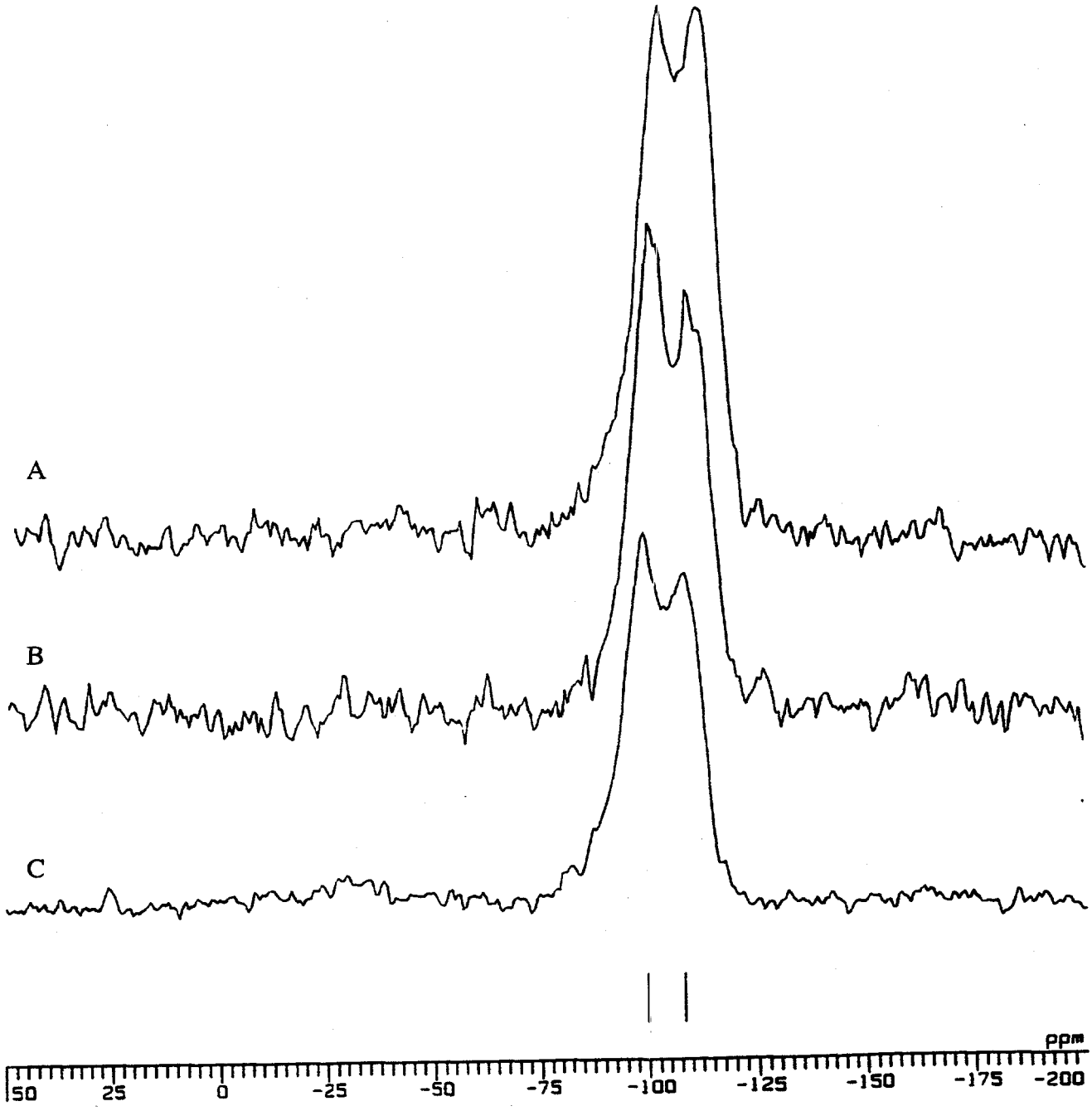

Figure 59. ^{29}Si MAS NMR spectra of mesoporous molecular sieves prepared using A) Aluminum Sulfate, B) Catapal B and, C) Aluminum Ispropoxide

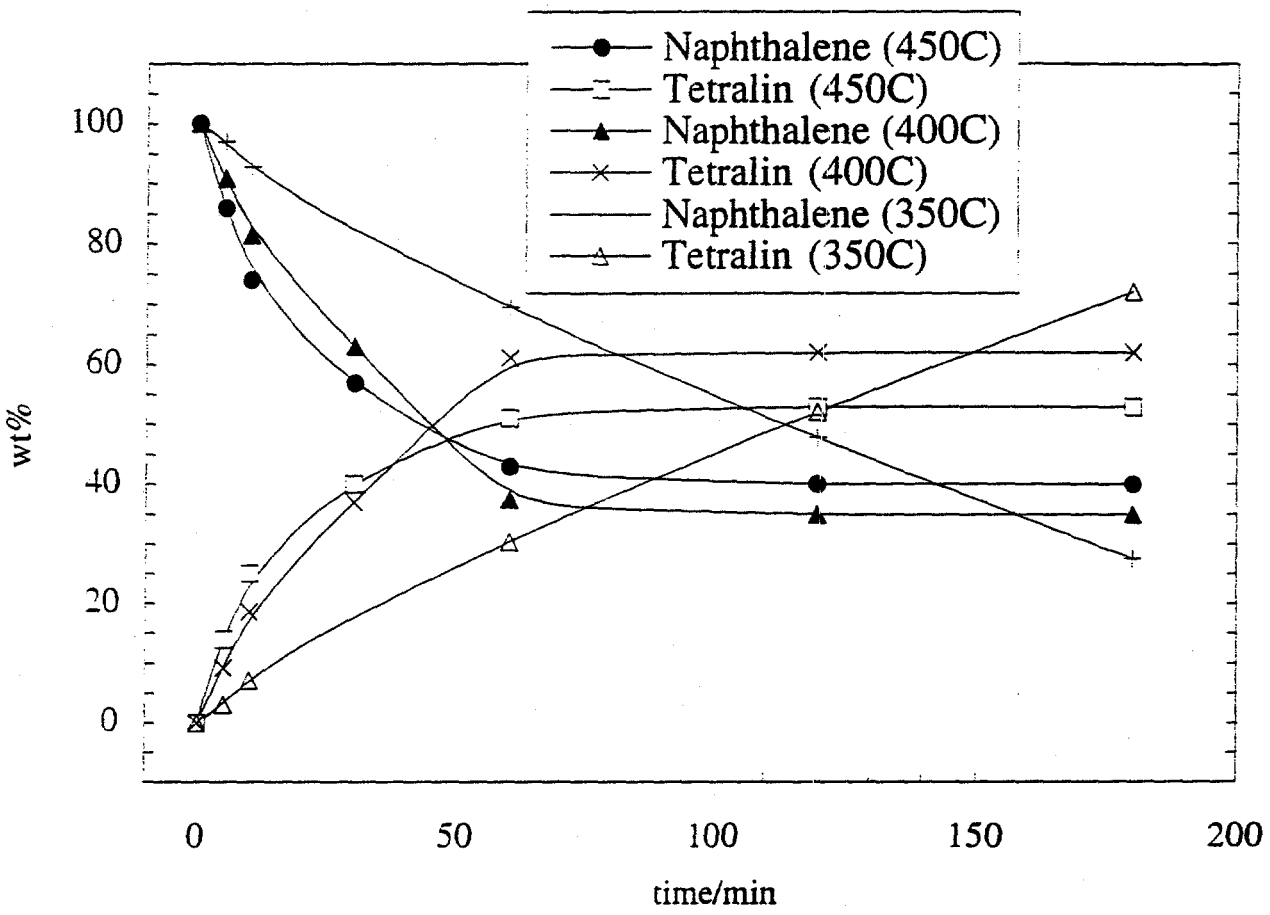

Figure 60. Product distribution of naphthalene hydrogenation.

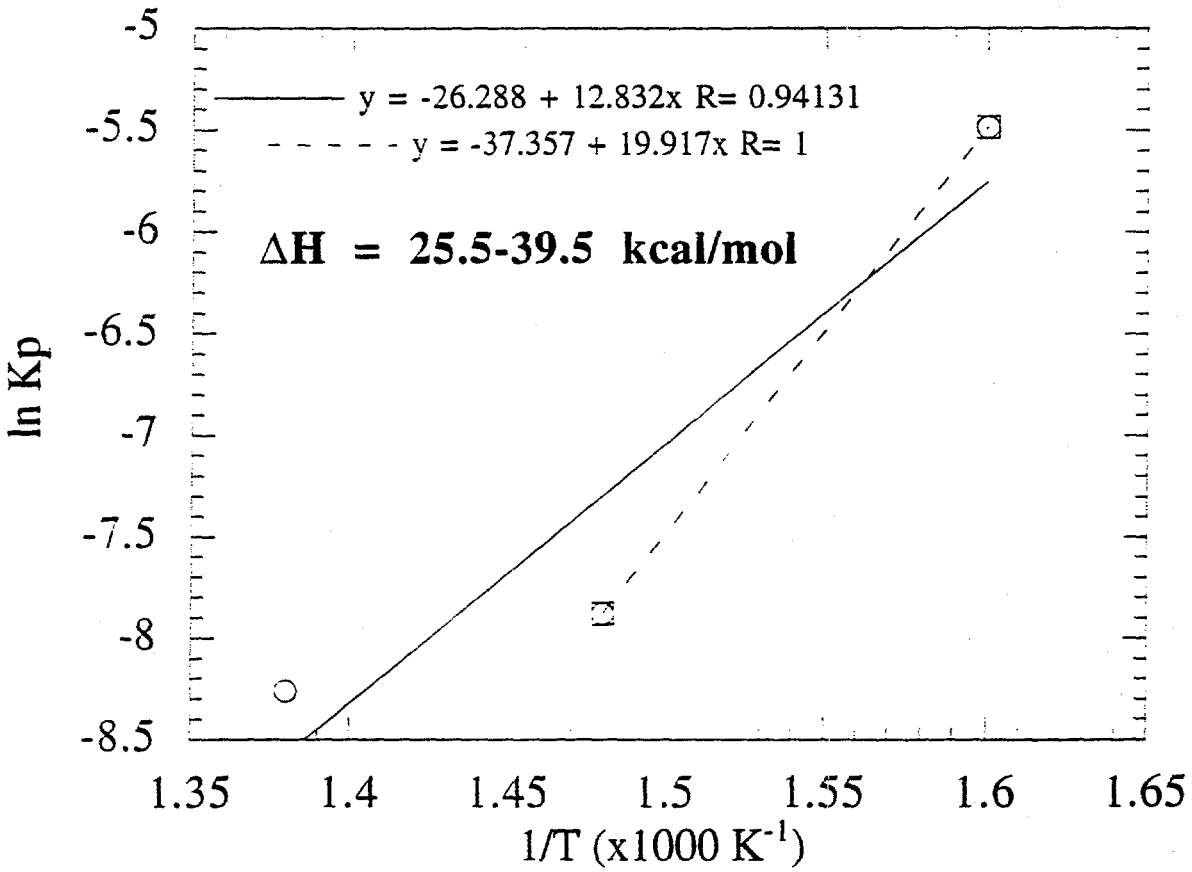

Figure 61. Van't Hoff plot - naphthalene hydrogenation.

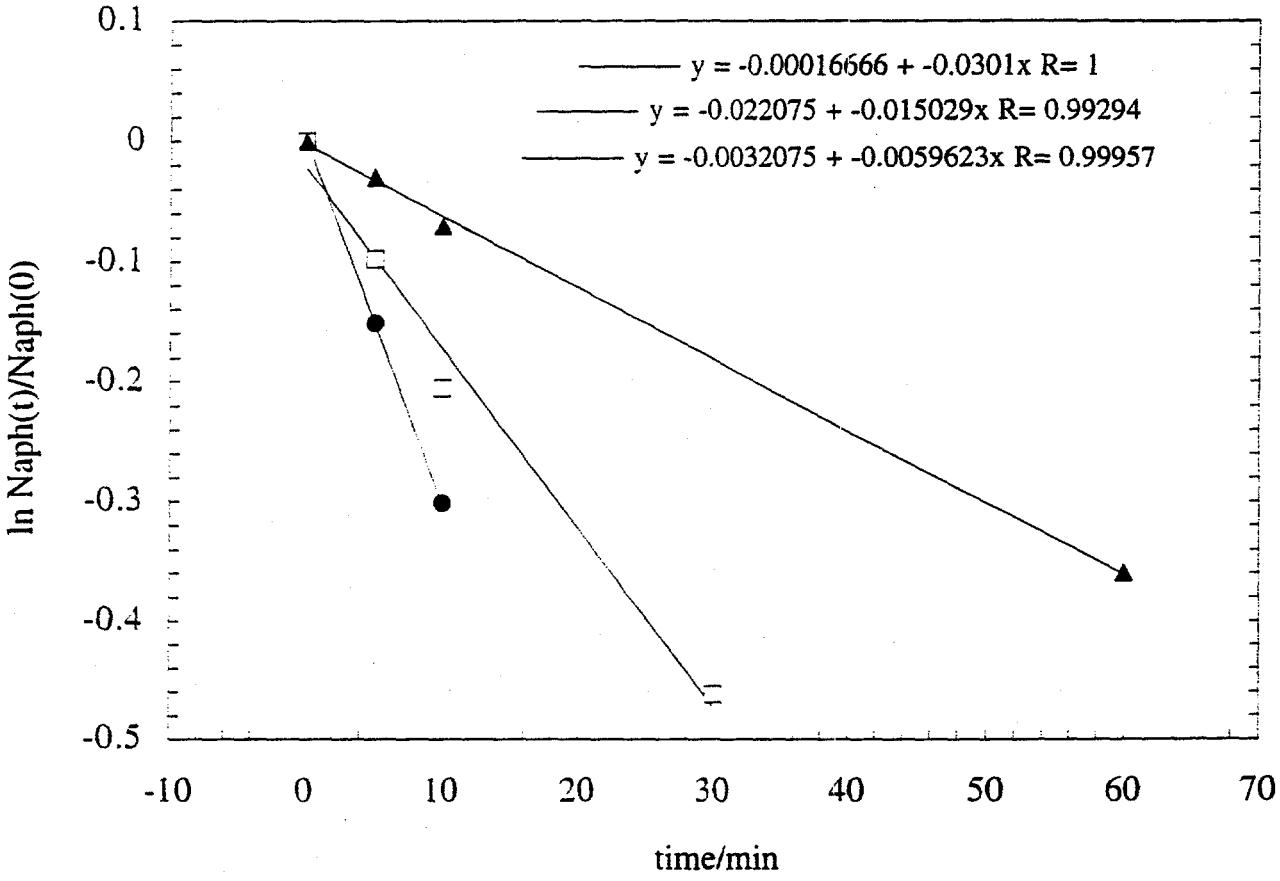

Figure 62. Pseudo first order kinetic plot - naphthalene hydrogenation.

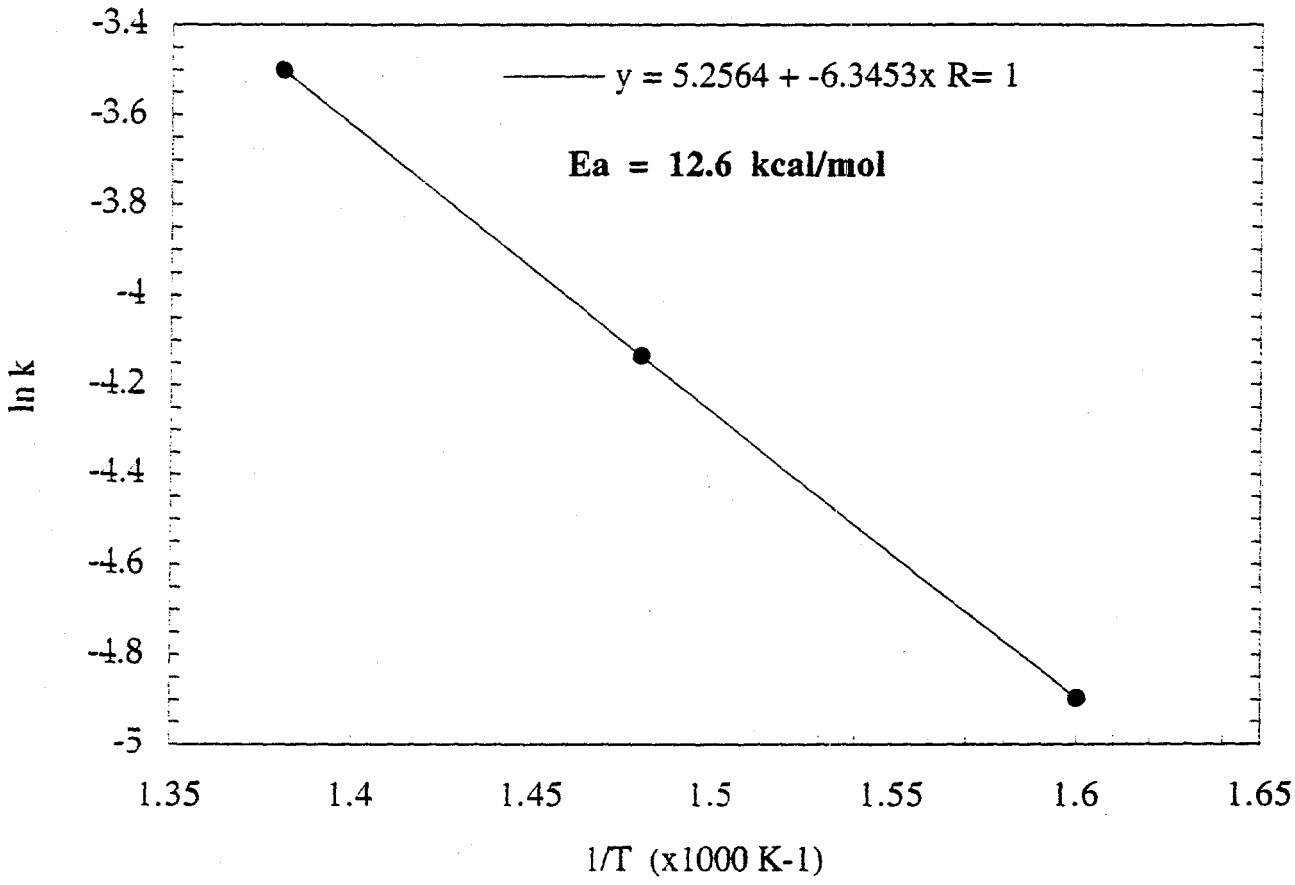

Figure 63. Arrhenius plot - naphthalene hydrogenation.

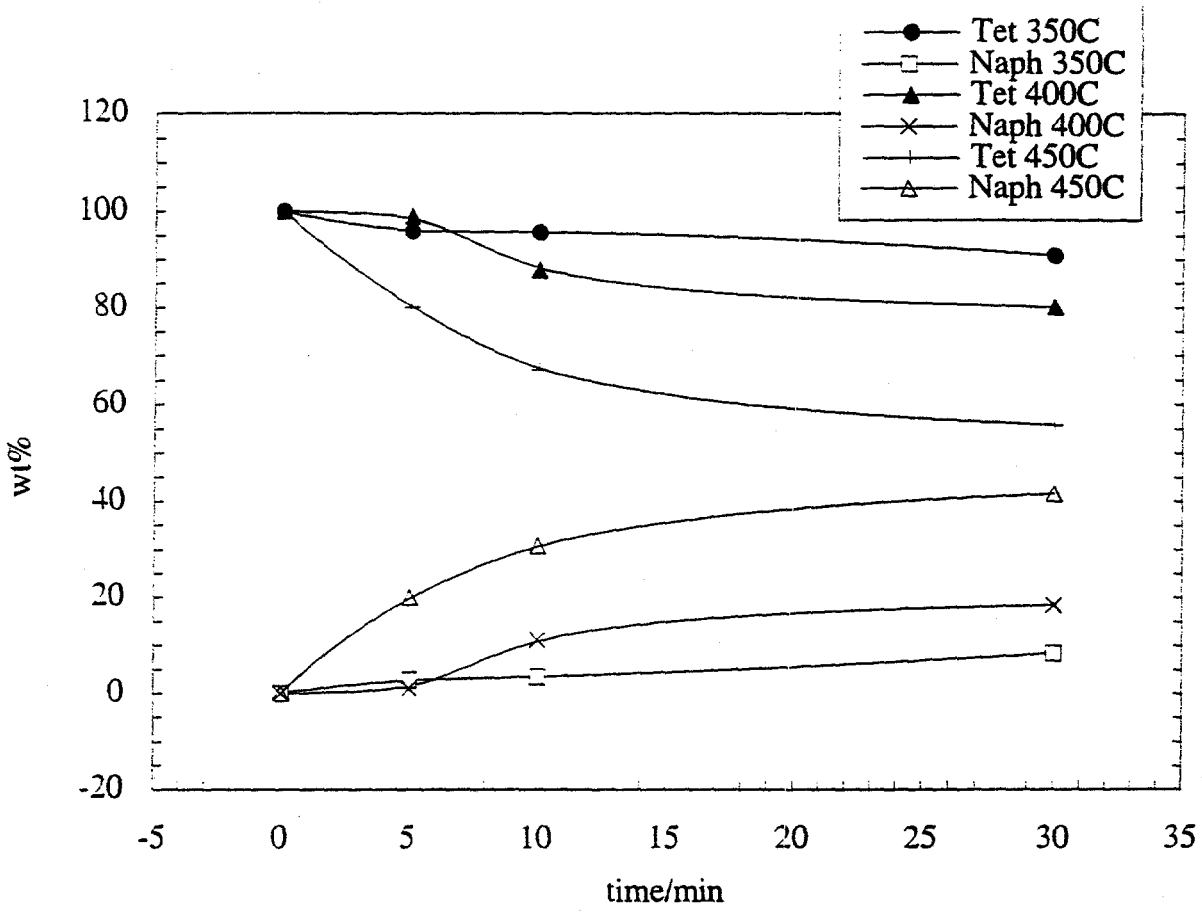

Figure 64. Product distribution of tetralin dehydrogenation.

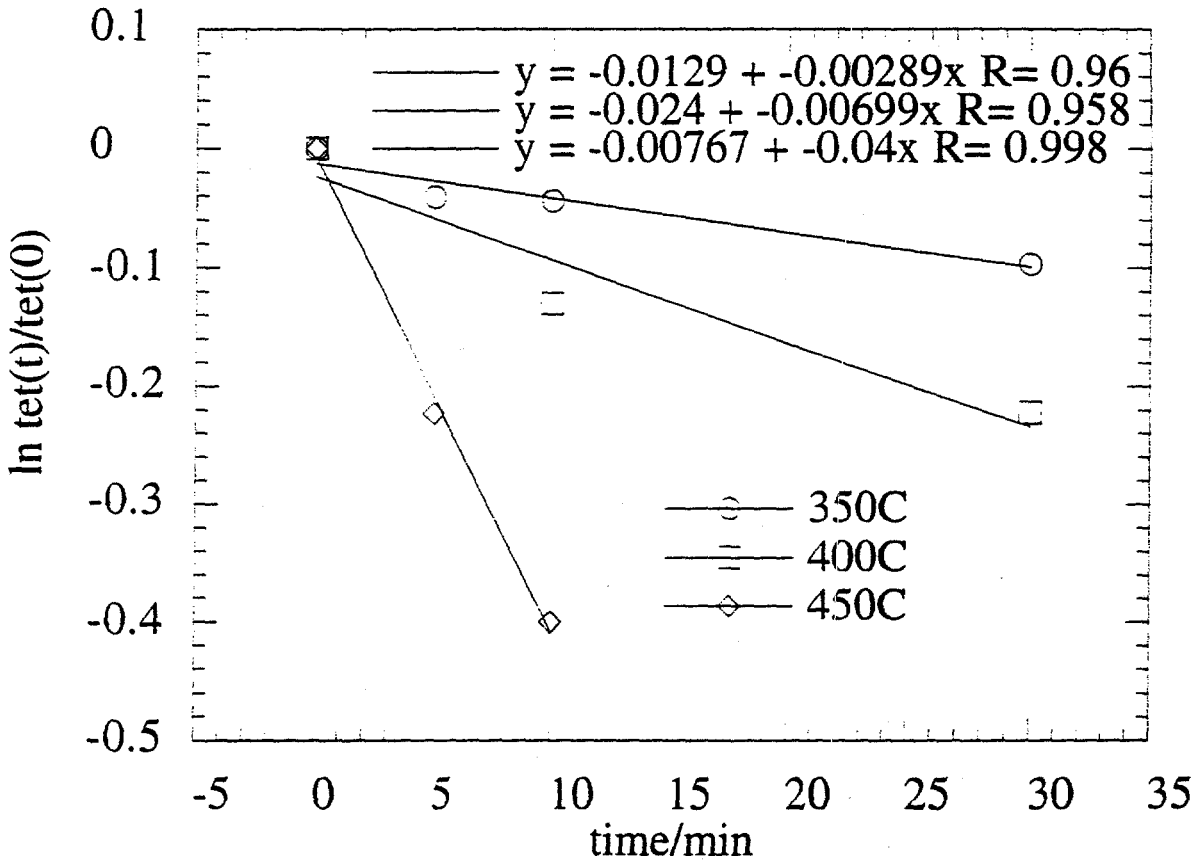

Figure 65. Kinetic plot of tetralin dehydrogenation.

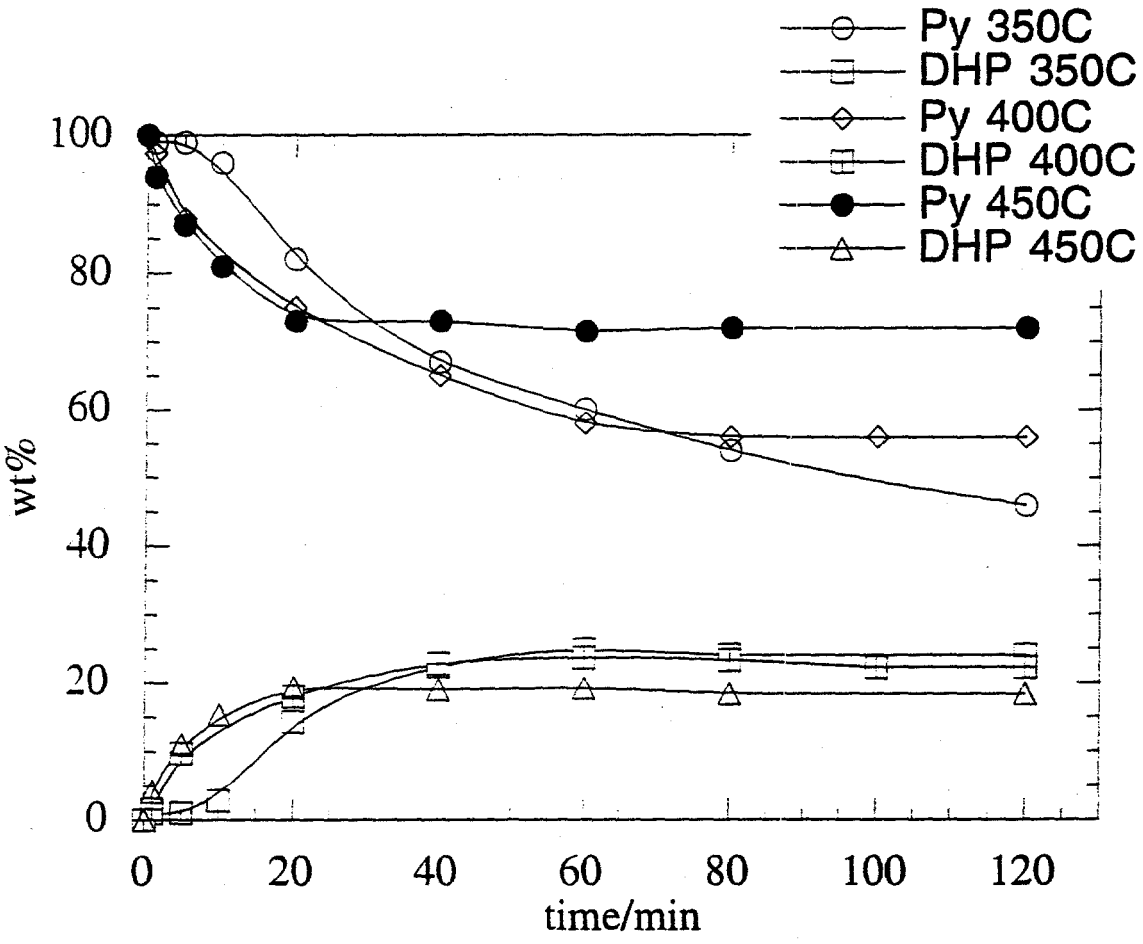

Figure 66. Hydrogenation product distribution - pyrene/dihydropyrene

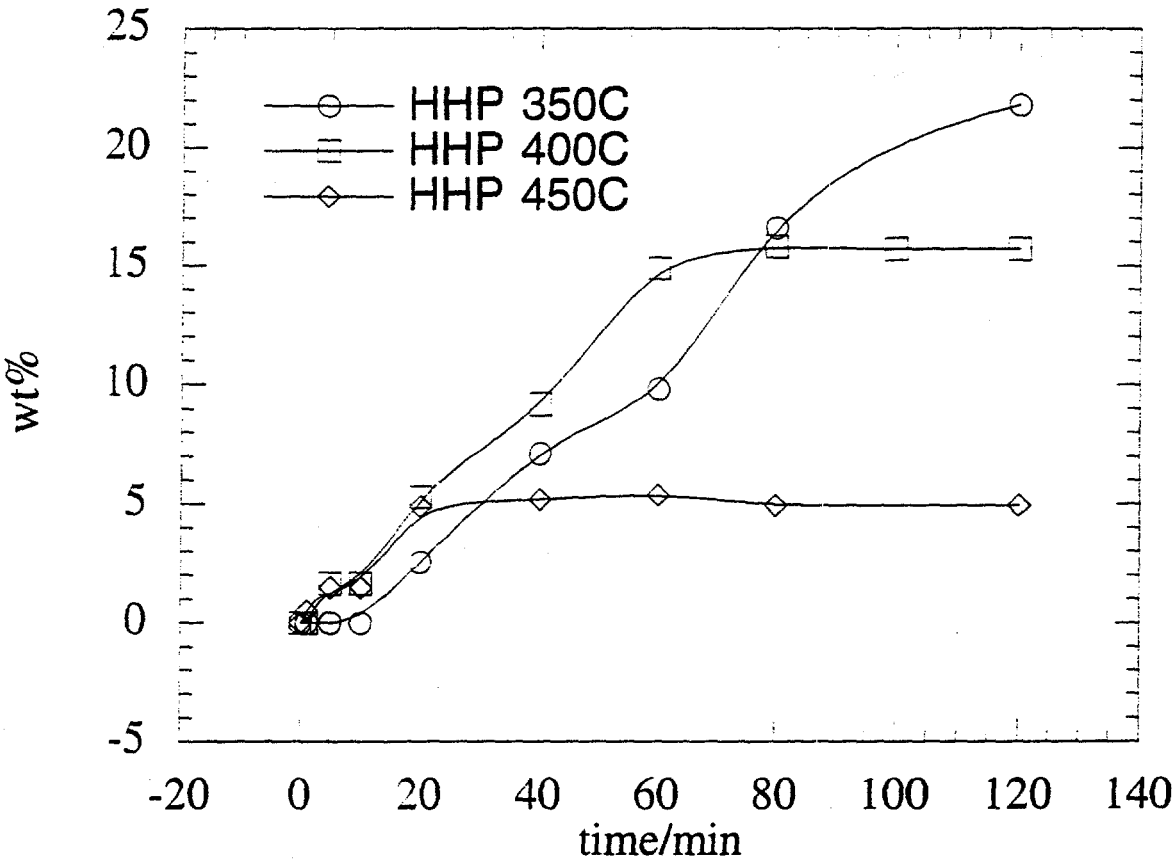

Figure 67. Hydrogenation product distribution - hexahydropyrene.

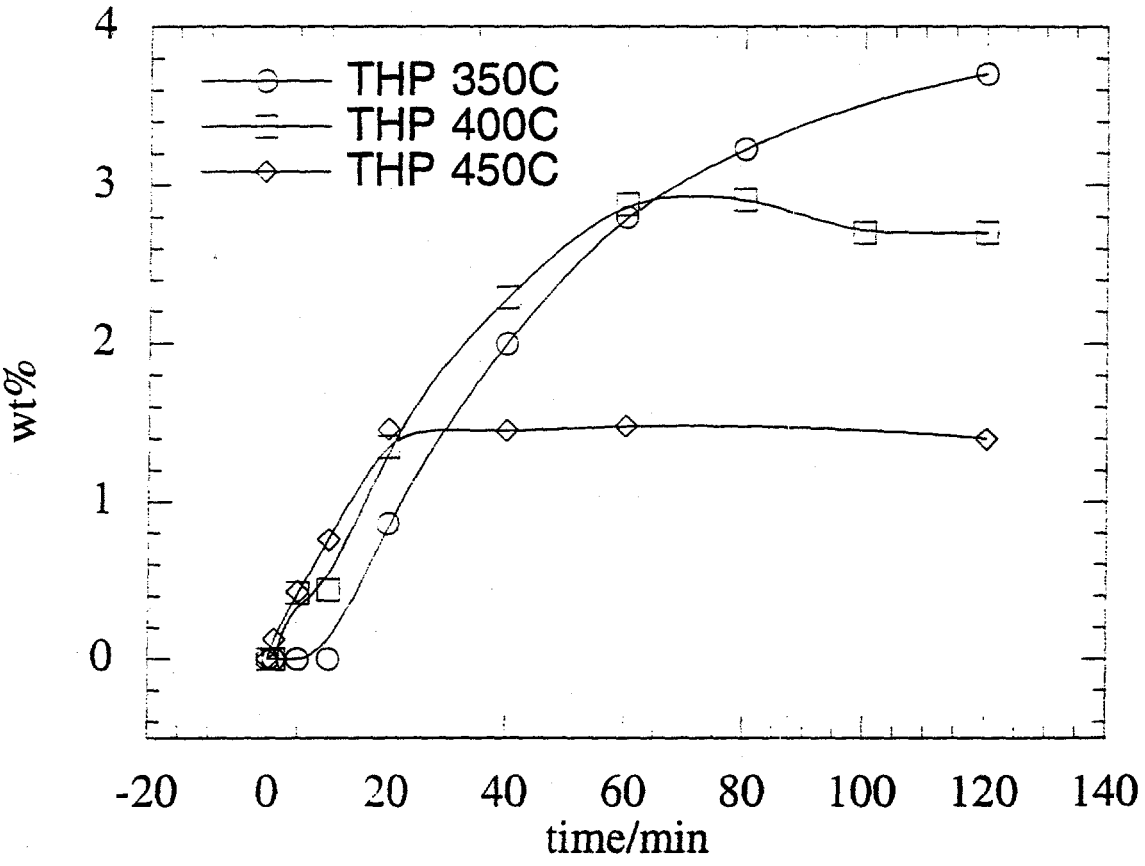

Figure 68. Hydrogenation product distribution - tetrahydropyrene.

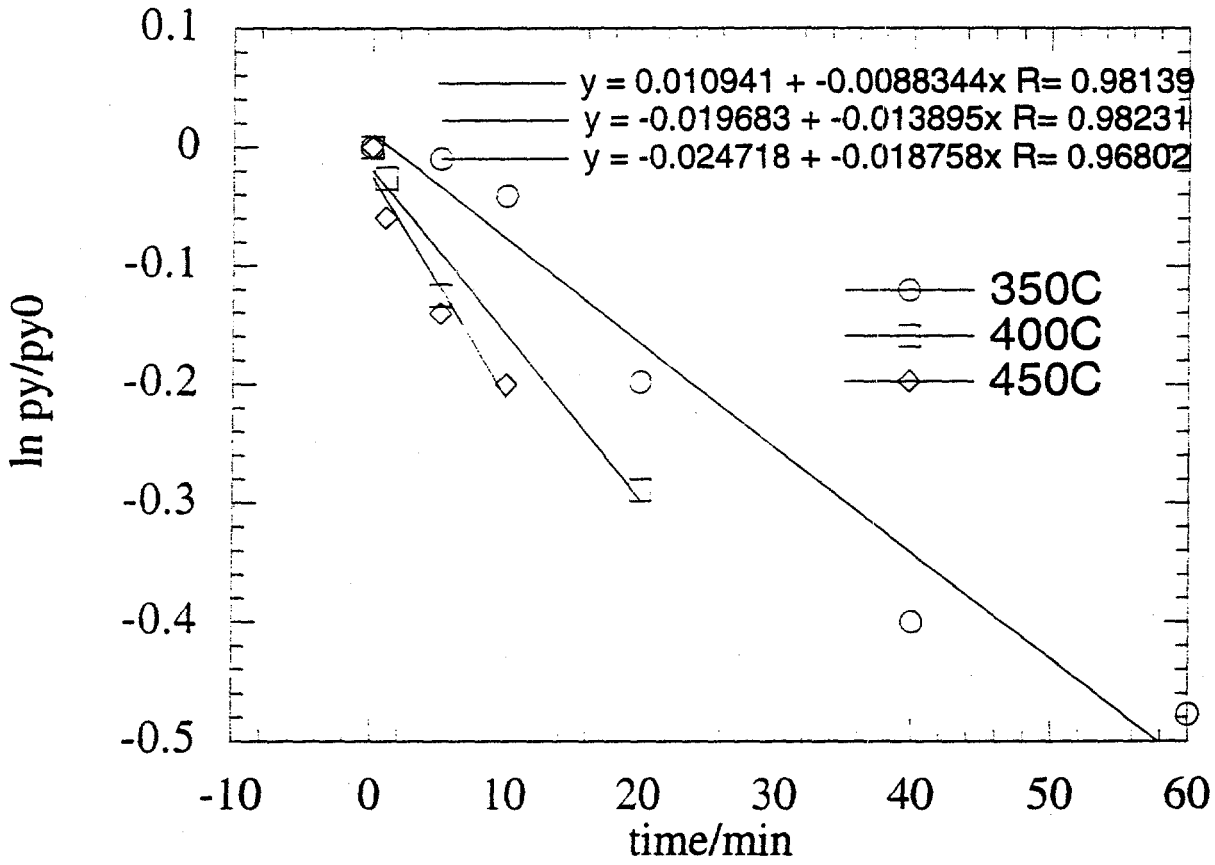

Figure 69. Van't Hoff plot - pyrene hydrogenation.

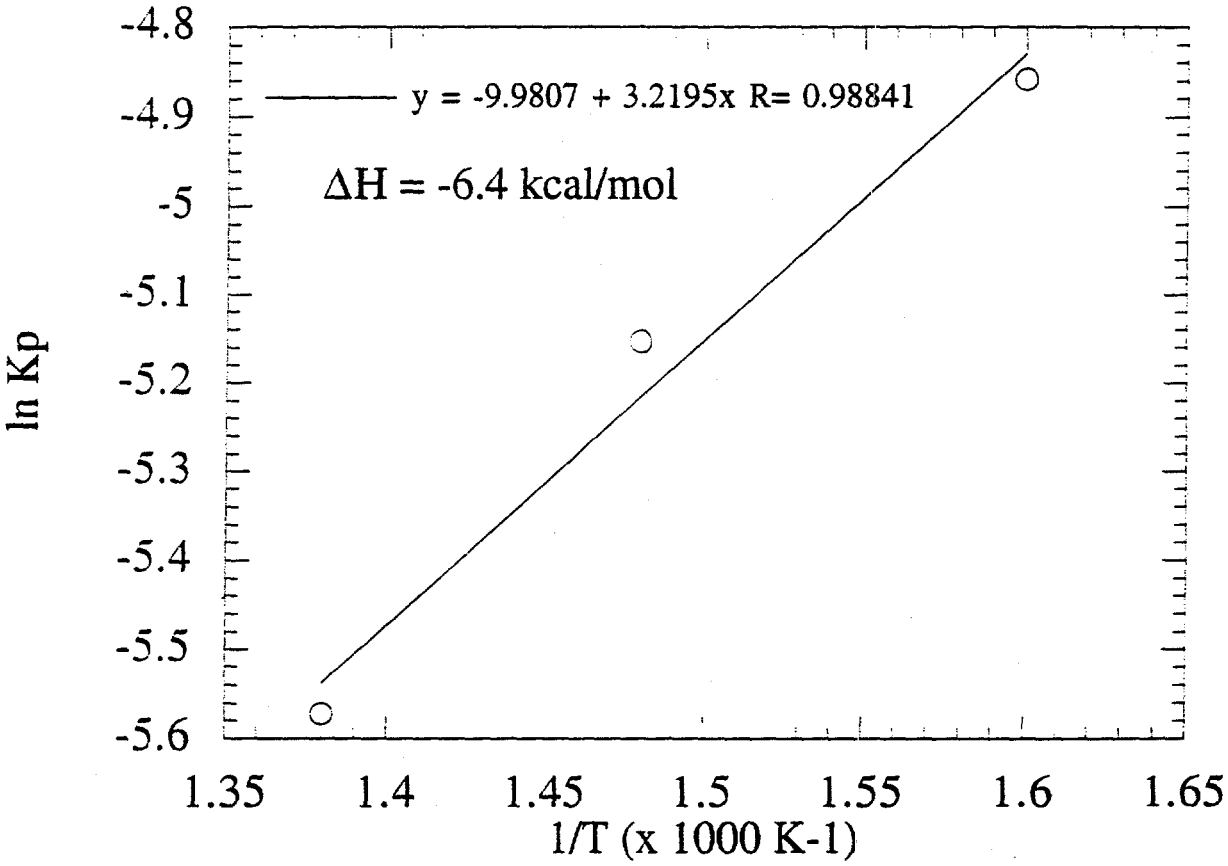

Figure 70. Pseudo first order kinetic plot - pyrene hydrogenation.

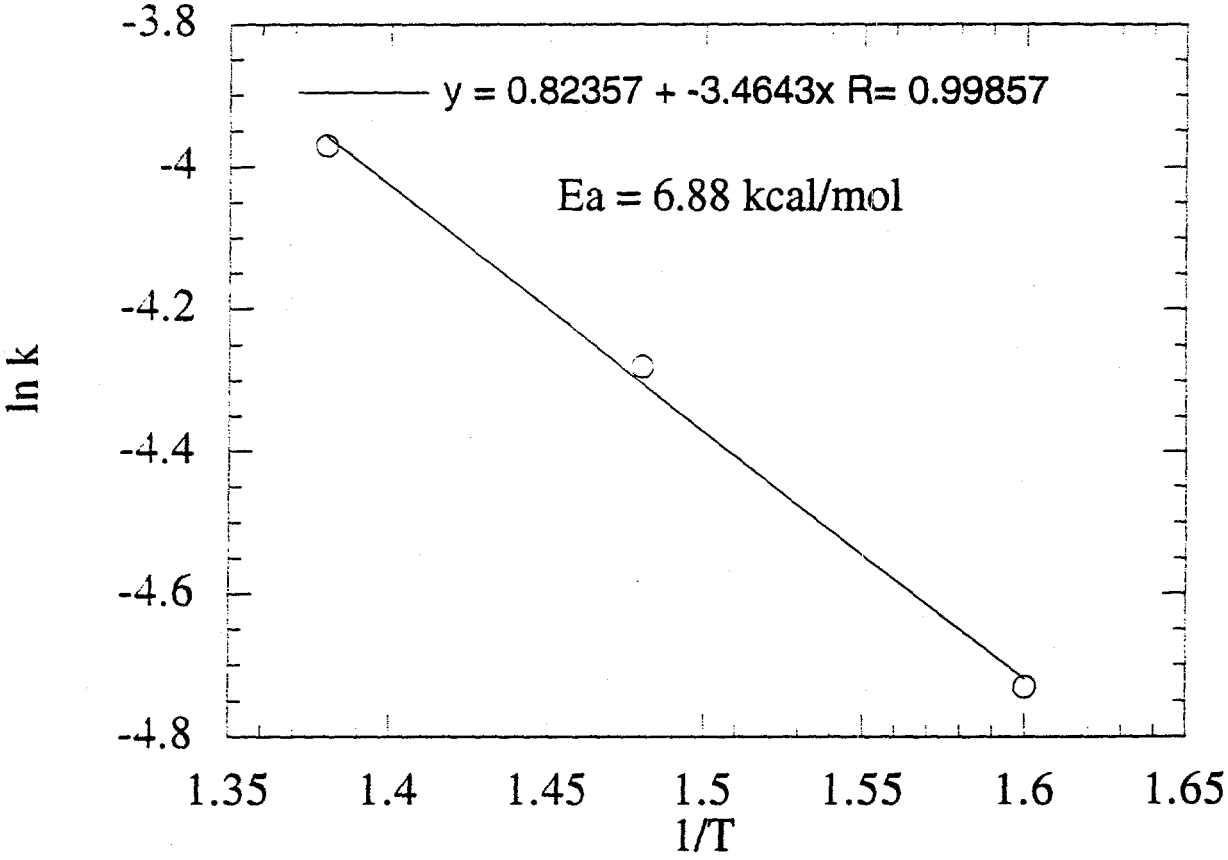

Figure 71. Arrhenius plot - pyrene hydrogenation.

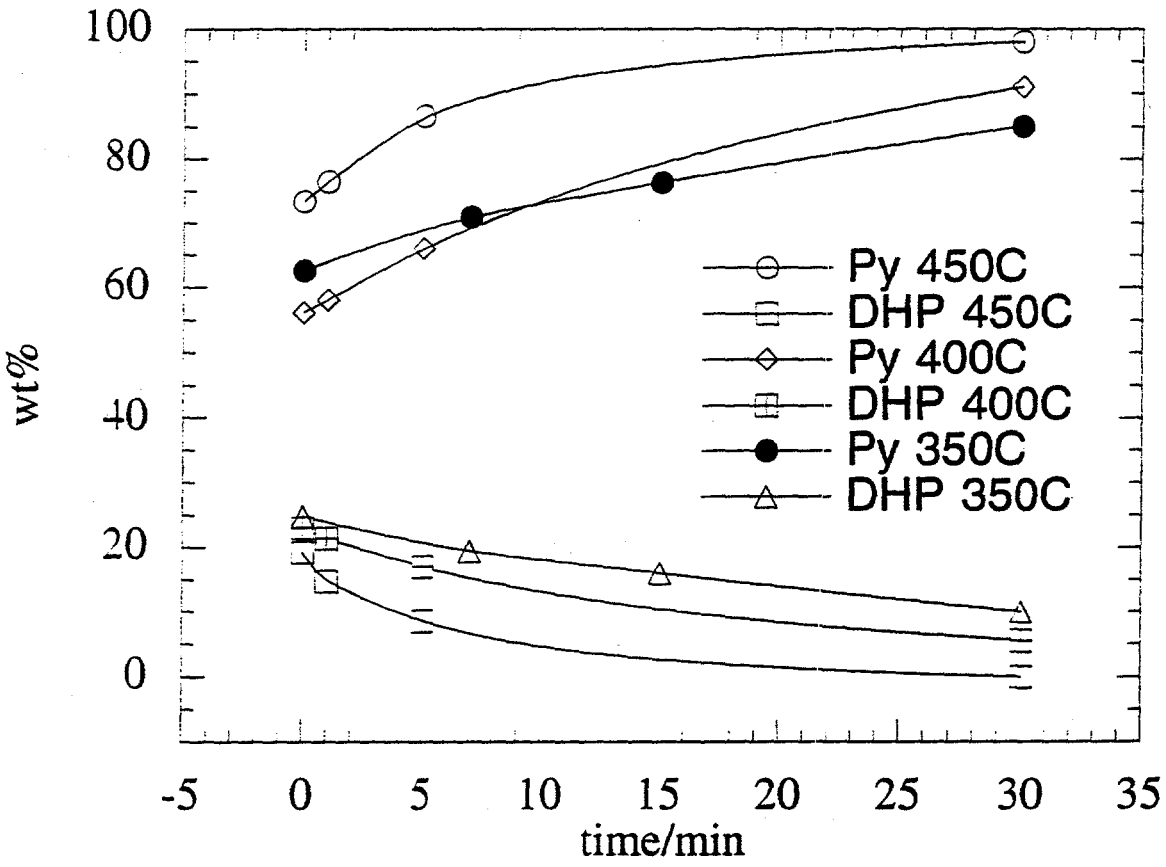

Figure 72. Dehydrogenation product distribution - dihydropyrene/pyrene.

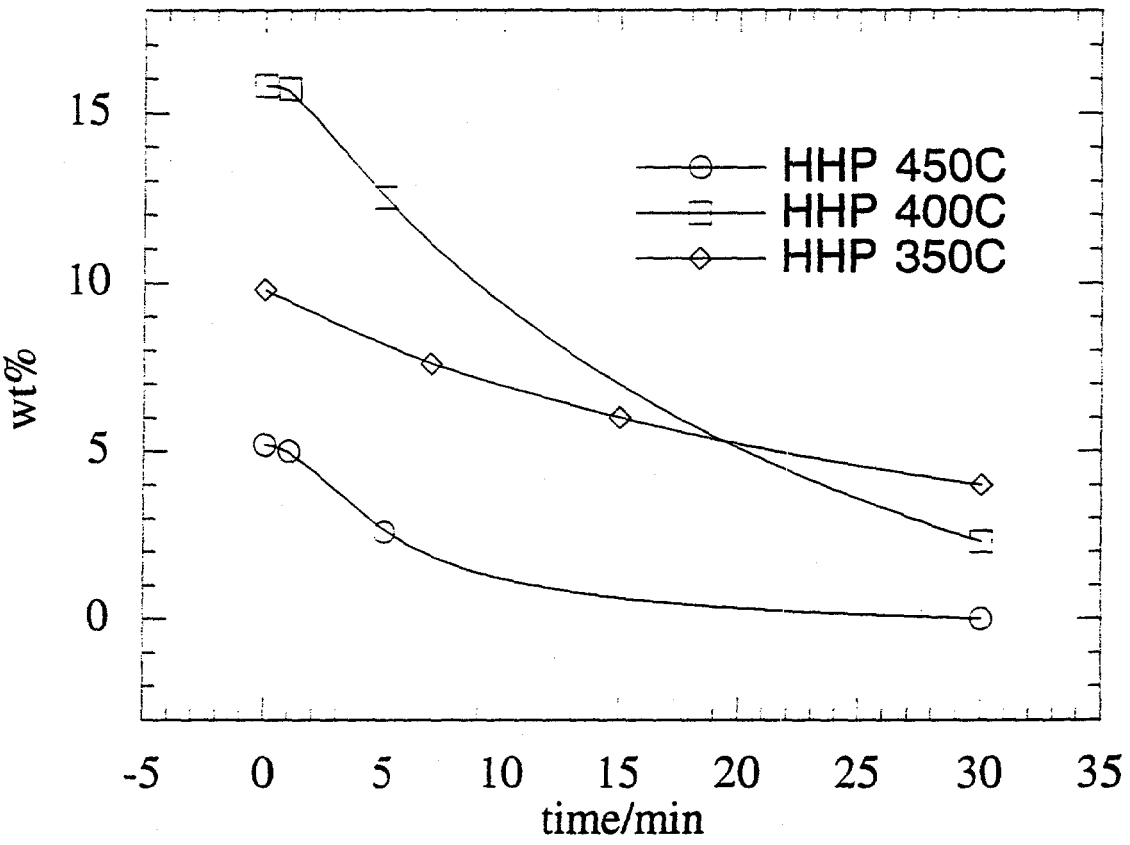

Figure 73. Dehydrogenation product distribution - hexahydropyrene.

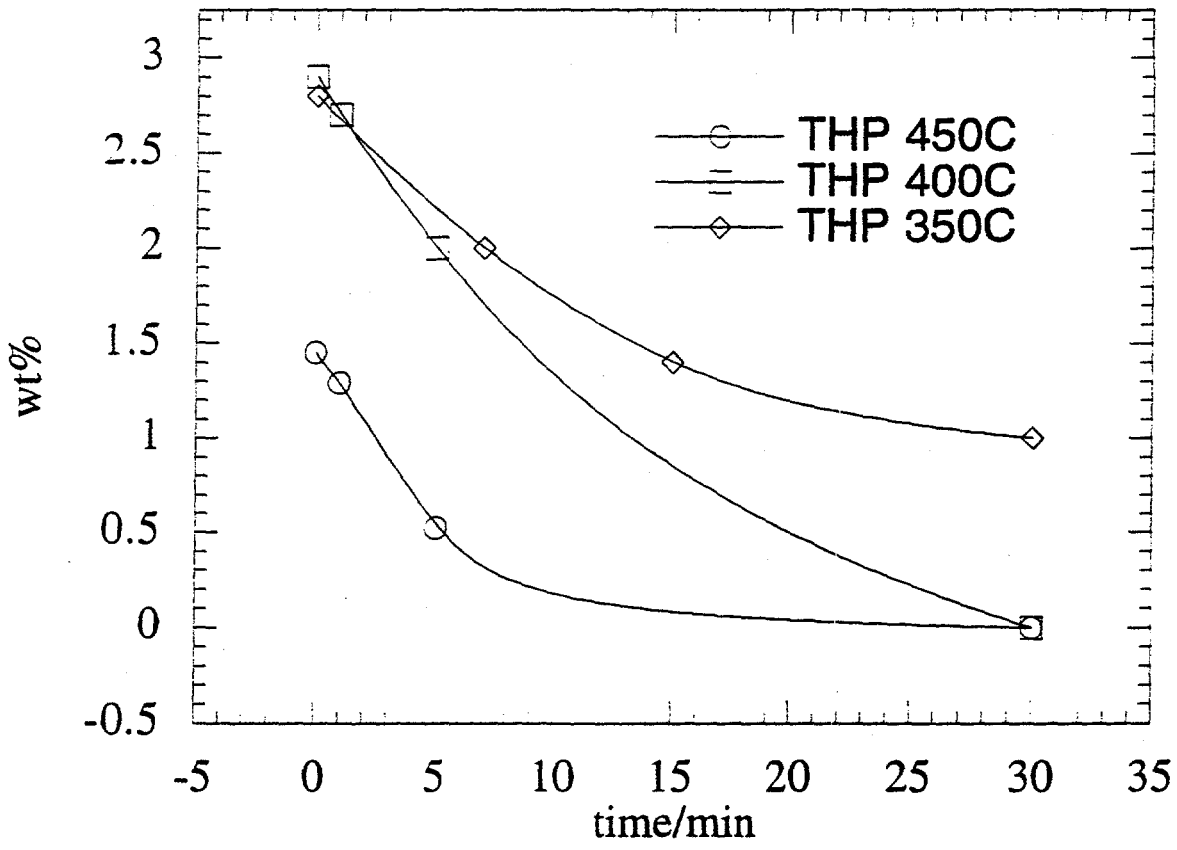

Figure 74. Dehydrogenation product distribution - tetrahydropyrene.

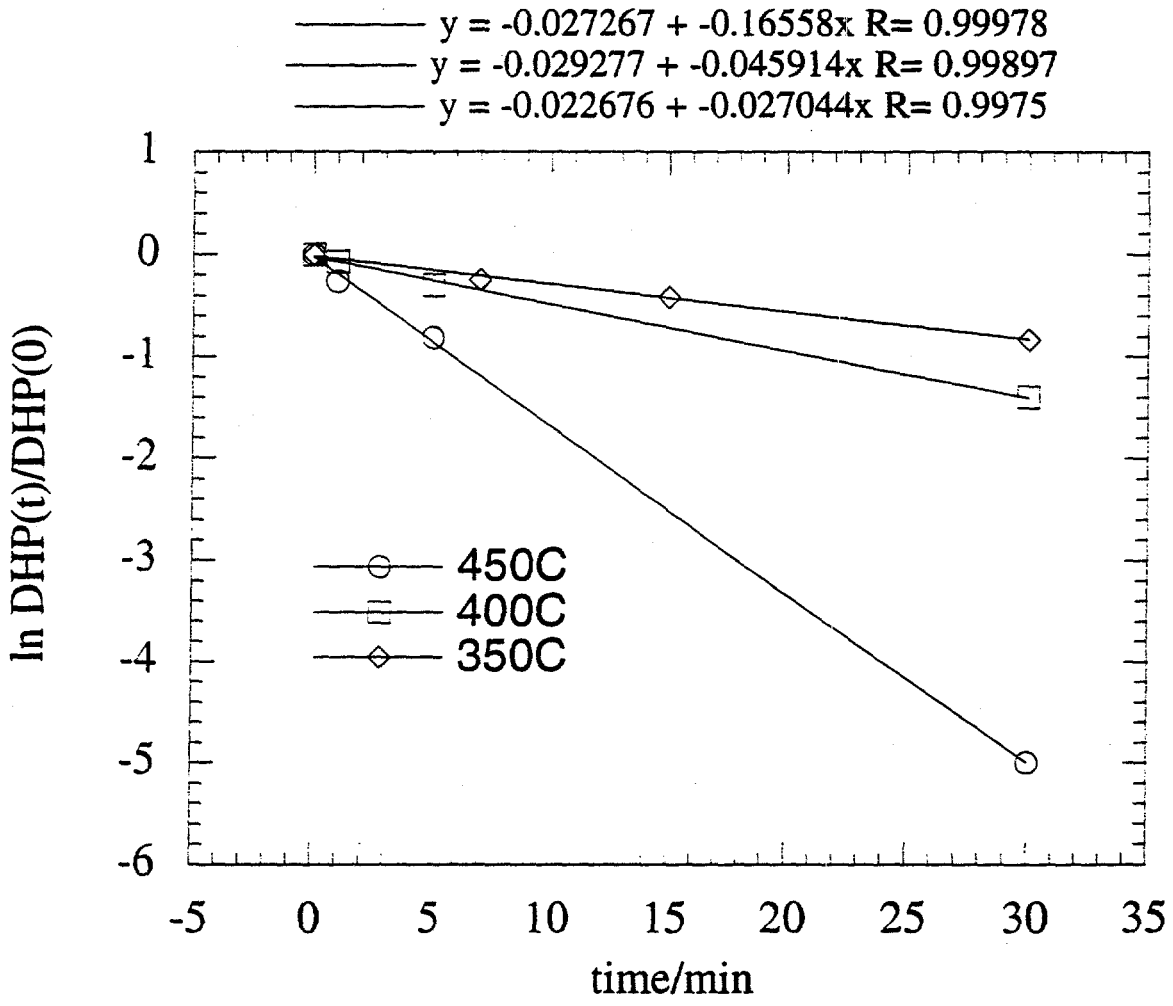

Figure 75. Dehydrogenation kinetic plot - dihydropyrene.

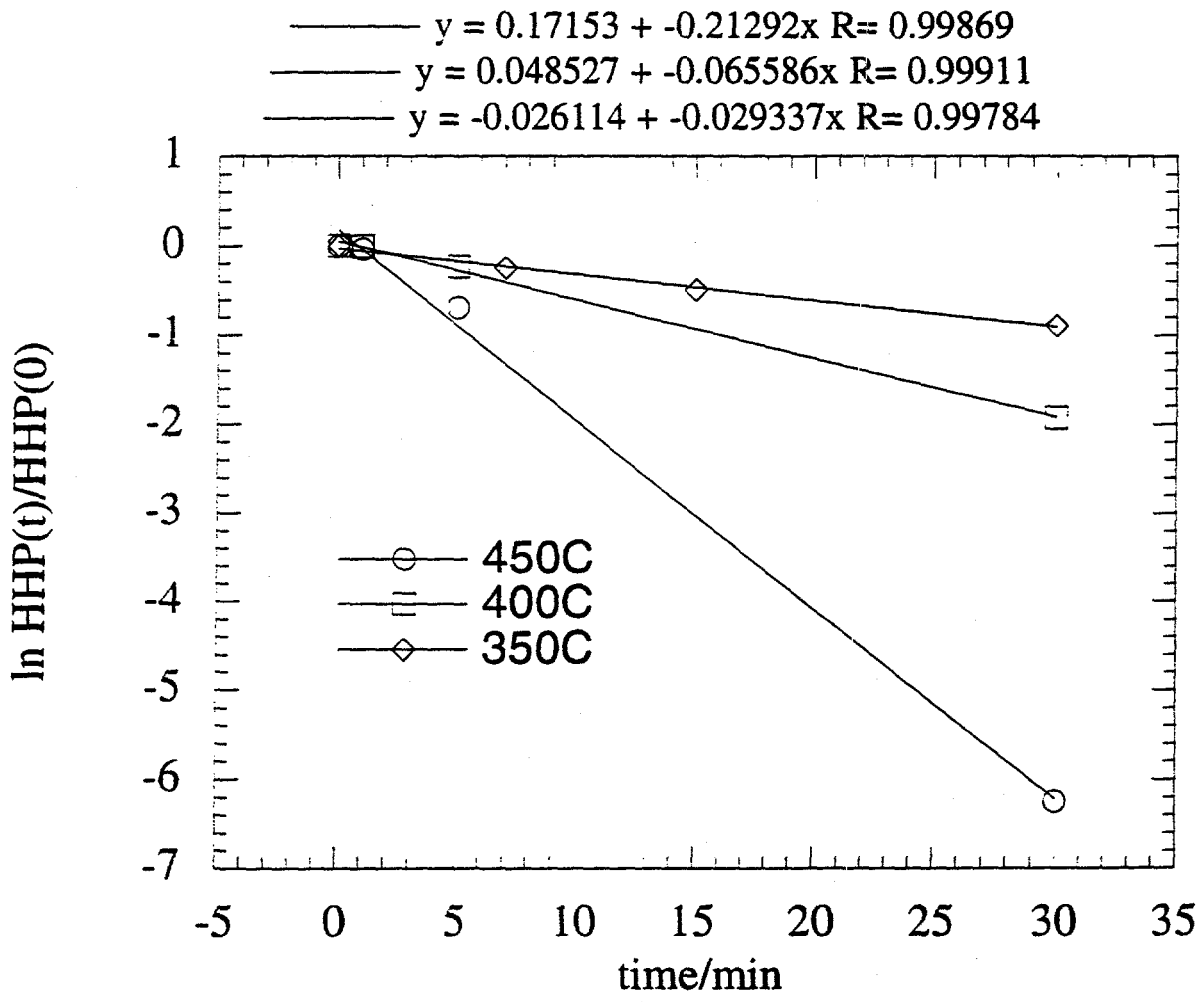

Figure 76. Dehydrogenation kinetic plot - hexahydropyrene.

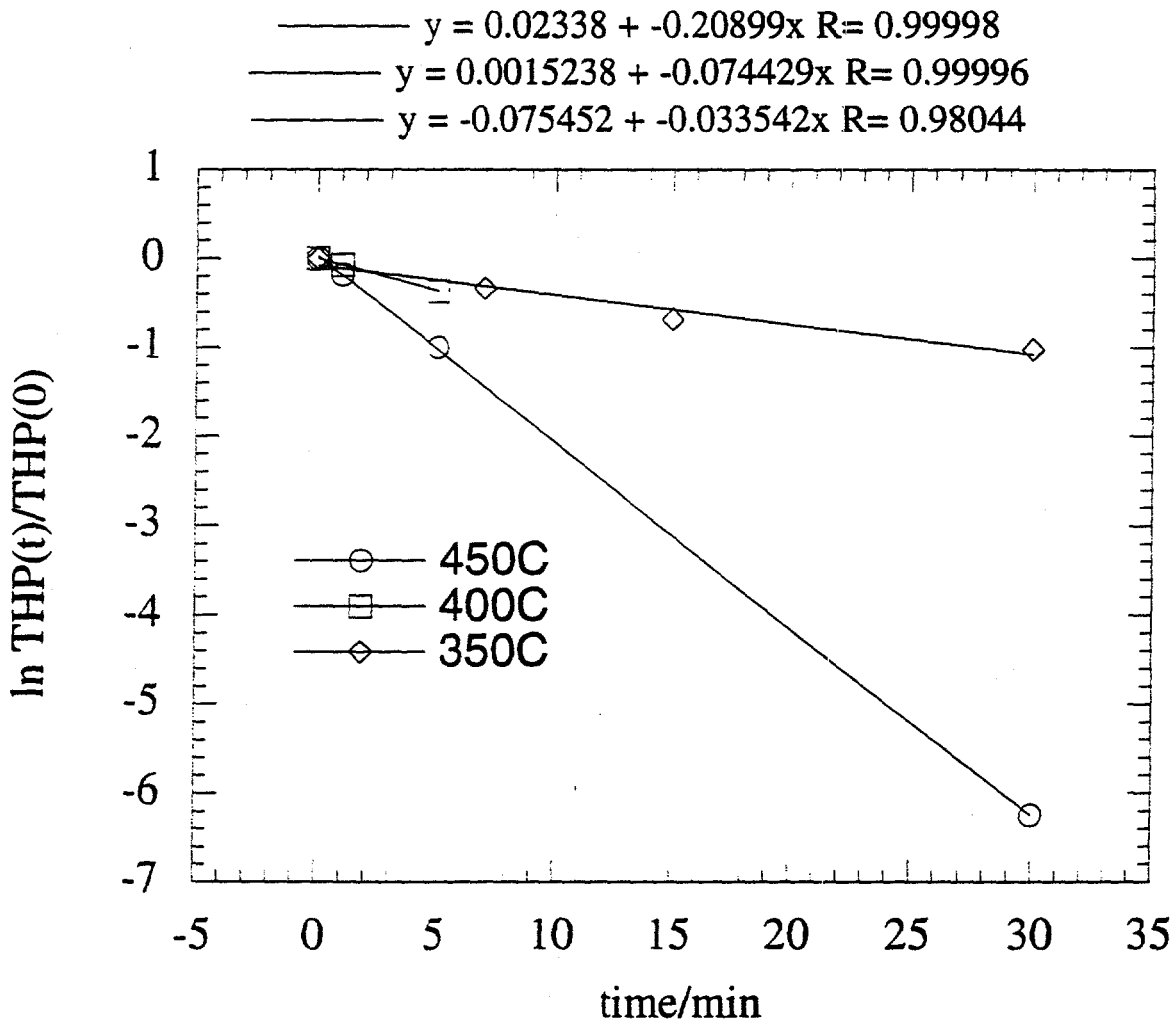

Figure 77. Dehydrogenation kinetic plot - tetrahydropyrene.

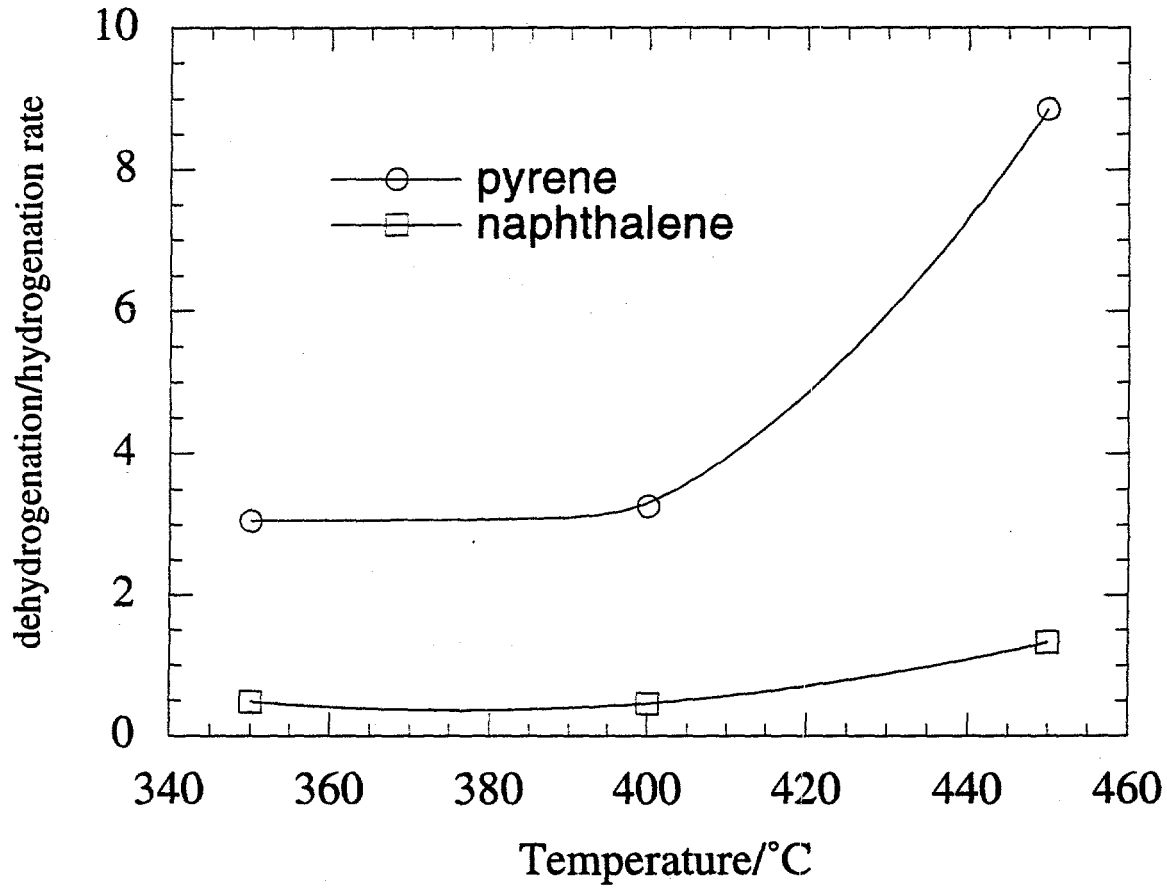

Figure 78. Dehydrogenation / hydrogenation rate vs temperature for naphthalene and pyrene

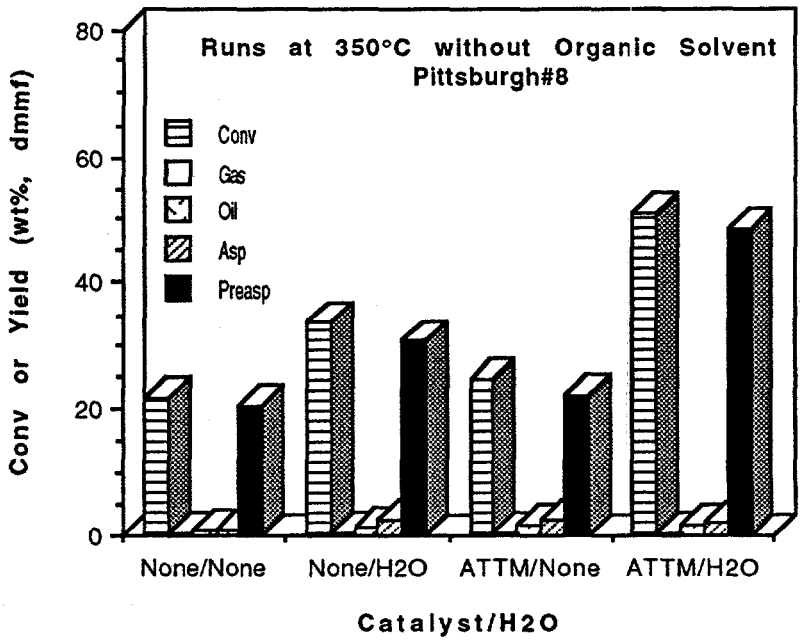

Figure 79 Effect of water on catalytic liquefaction of Pittsburgh #8 coal at 350°C for 30 min.

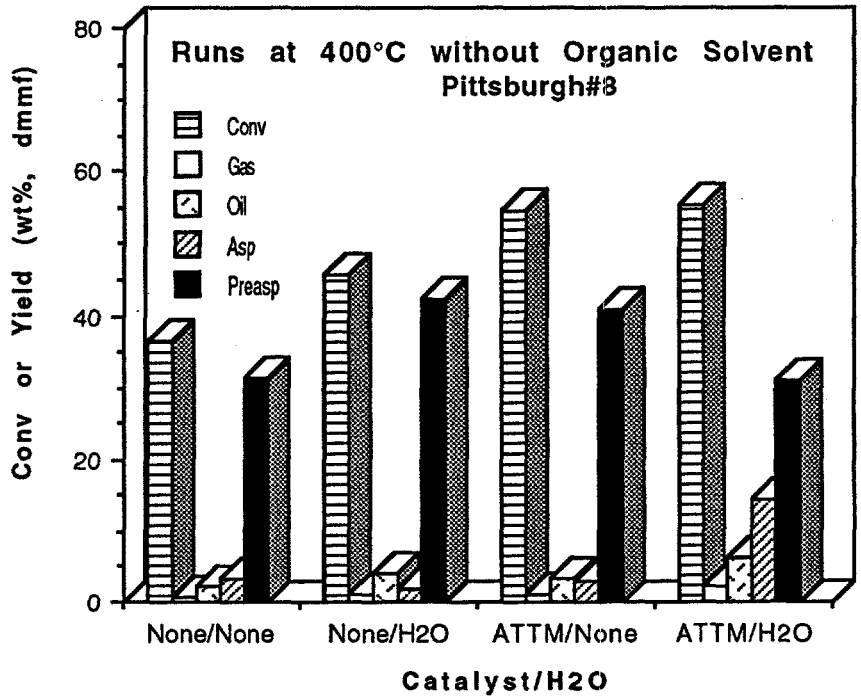

Figure 80. Effect of water on catalytic liquefaction of Pittsburgh #8 coal at 400°C for 30 min.

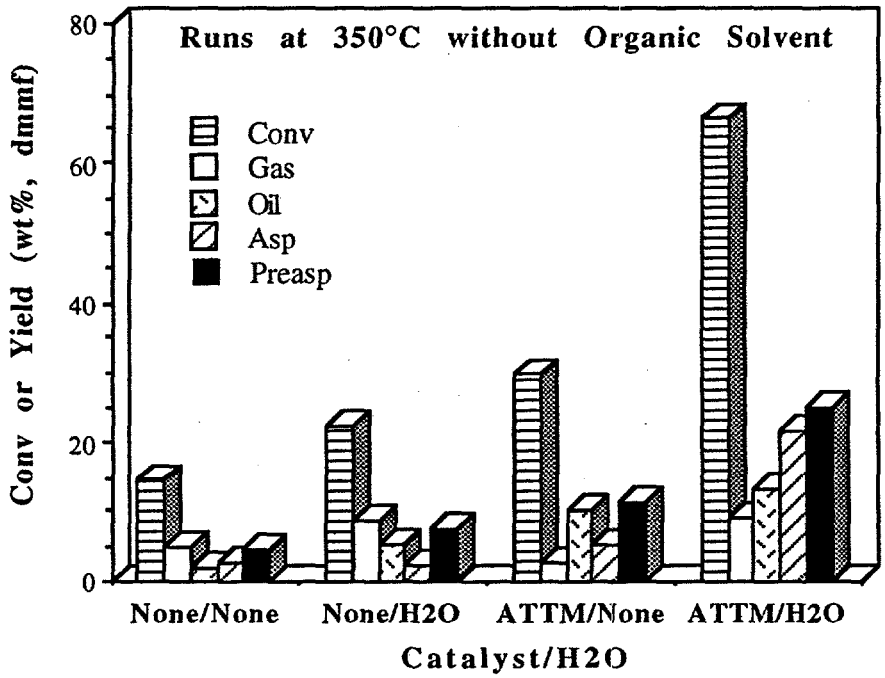

Figure 81. Effect of water on catalytic liquefaction of Wyodak coal at 350°C for 30 min.

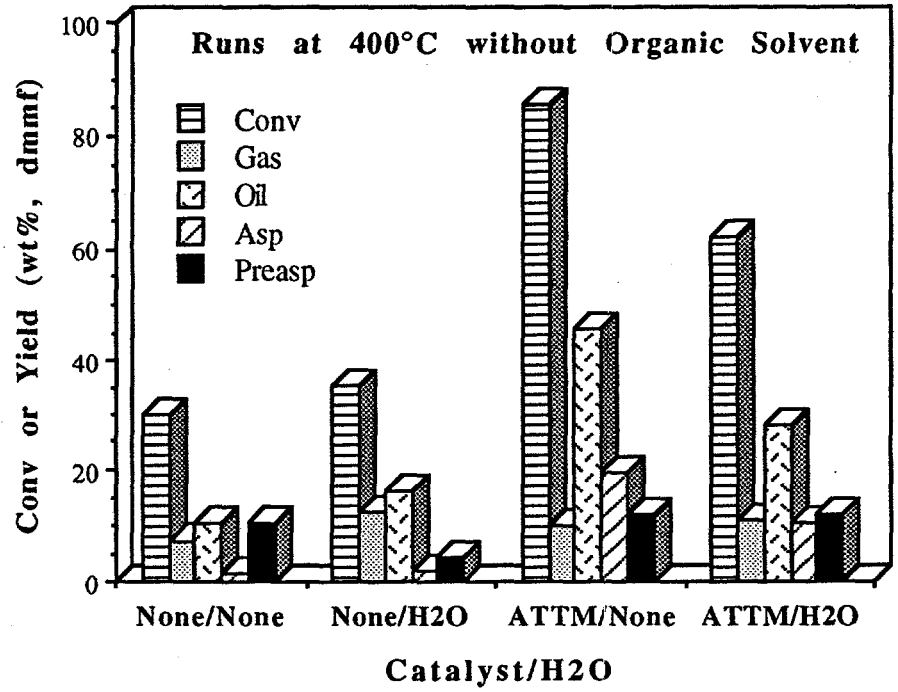

Figure 82. Effect of water on catalytic liquefaction of Wyodak coal at 400°C for 30 min.

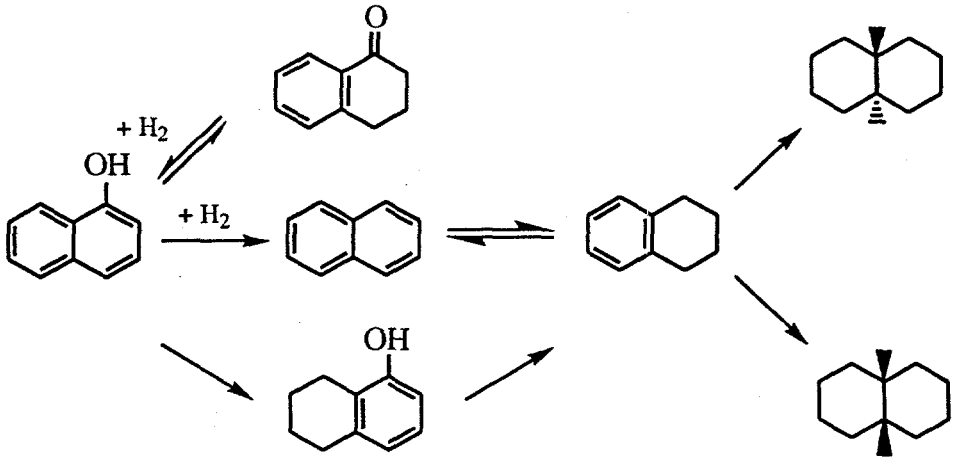

Figure 83. Proposed Reaction Network of 1-naphthol and Hydrogen in the Presence of Ni-Mo/γ-Al_2O_3 catalyst at 200 °C and 35 atm.

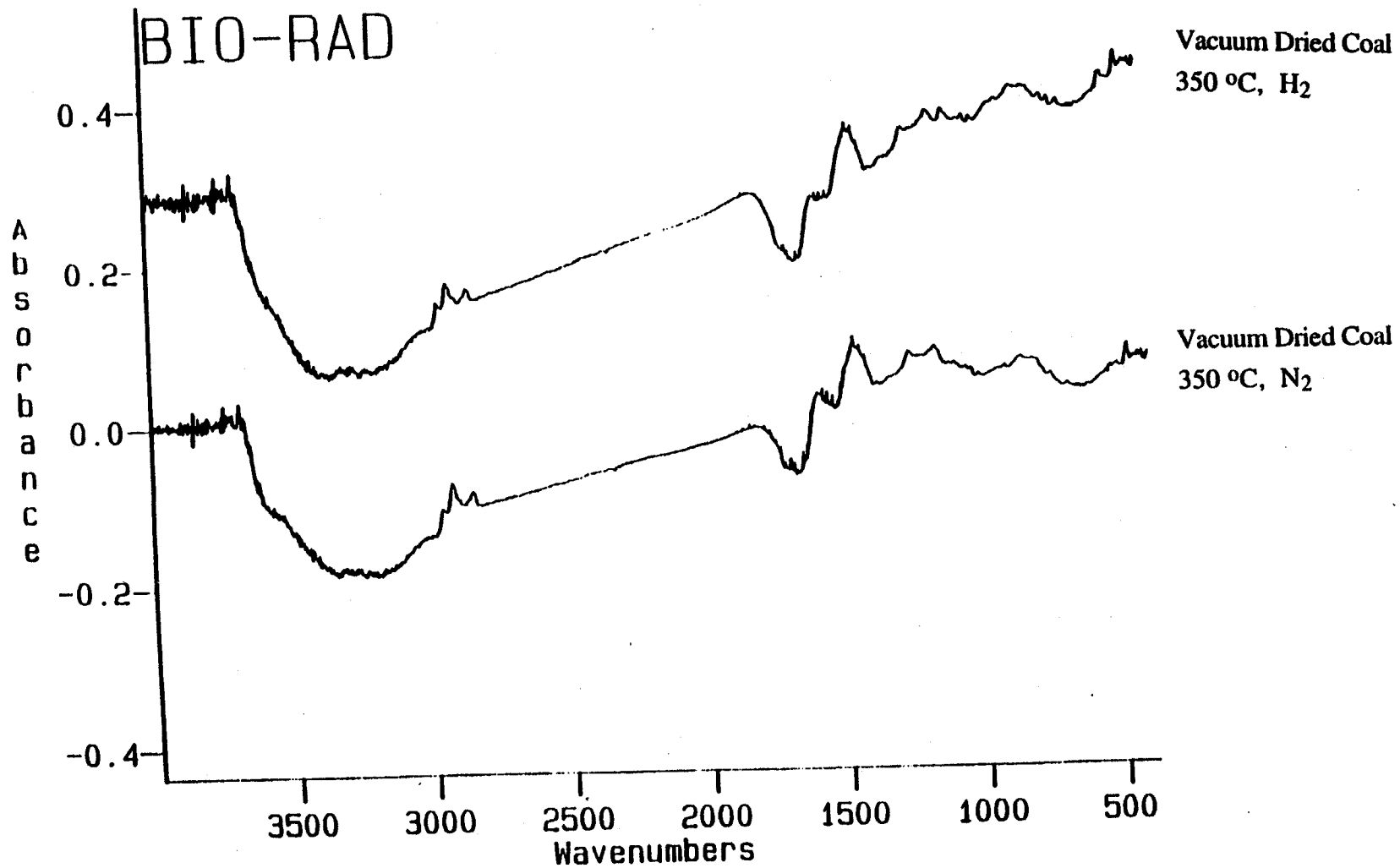

Figure 84. Comparison of FT-IR Spectrum for Products of Non-Catalytic Coal Reactions at 350 °C under H_2 and N_2 Atmospheres.

APPENDIX III

Schemes

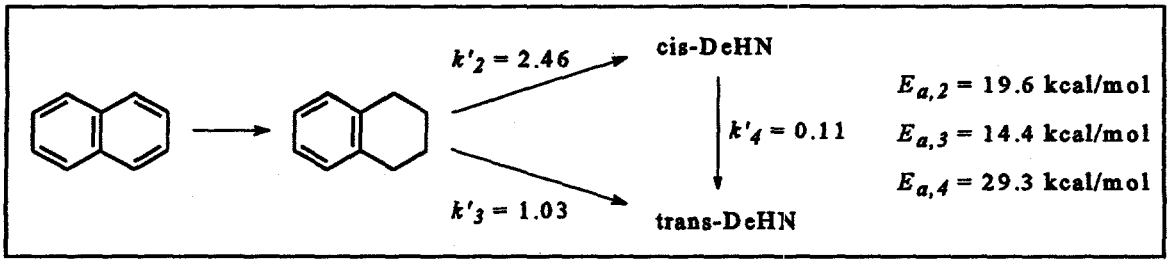

Scheme 1. Naphthalene hydrogenation pathway over Pt/Al_2O_3 from ref. 3. Rate constants are for reaction at 200 °C in units h^{-1}.

$$\frac{\left(k_3'/k_4'\right)_{T\,=\,373\ \mathrm{K}}}{\left(k_3'/k_4'\right)_{T\,=\,473\ \mathrm{K}}} = \frac{\left(A_3/A_4\right)e^{(E_{a,4}-E_{a,3})/(R\,\cdot\,373\ \mathrm{K})}}{\left(A_3/A_4\right)e^{(E_{a,4}-E_{a,3})/(R\,\cdot\,473\ \mathrm{K})}}$$

$$\ln\left\{\frac{\left(k_3'/k_4'\right)_{T\,=\,373\ \mathrm{K}}}{\left(k_3'/k_4'\right)_{T\,=\,473\ \mathrm{K}}}\right\} = \frac{E_{a,4}-E_{a,3}}{R}\left(\frac{1}{373\ \mathrm{K}}-\frac{1}{473\ \mathrm{K}}\right)$$

Scheme 2. Comparison of rate constant ratios at 100 and 200 °C using the Arrhenius equation.

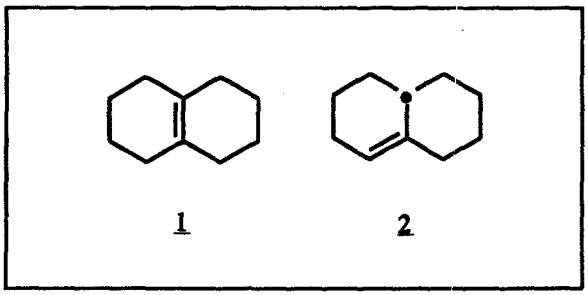

Scheme 3. Olefin stuctures involving the bridgehead carbons.

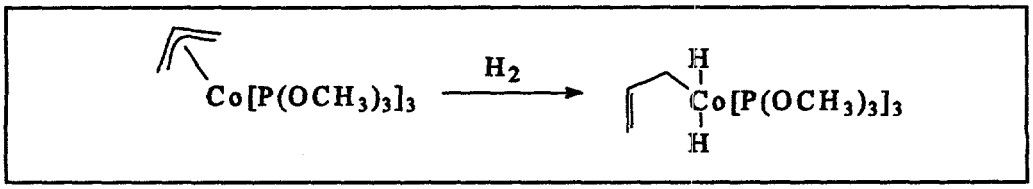

Scheme 4. Oxidative addition of hydrogen with π-allyl $\eta^3 \rightarrow \eta^1$ conversion.

Scheme 5. Dissociative hydrogen chemisorption on heterogeneous metal particles.

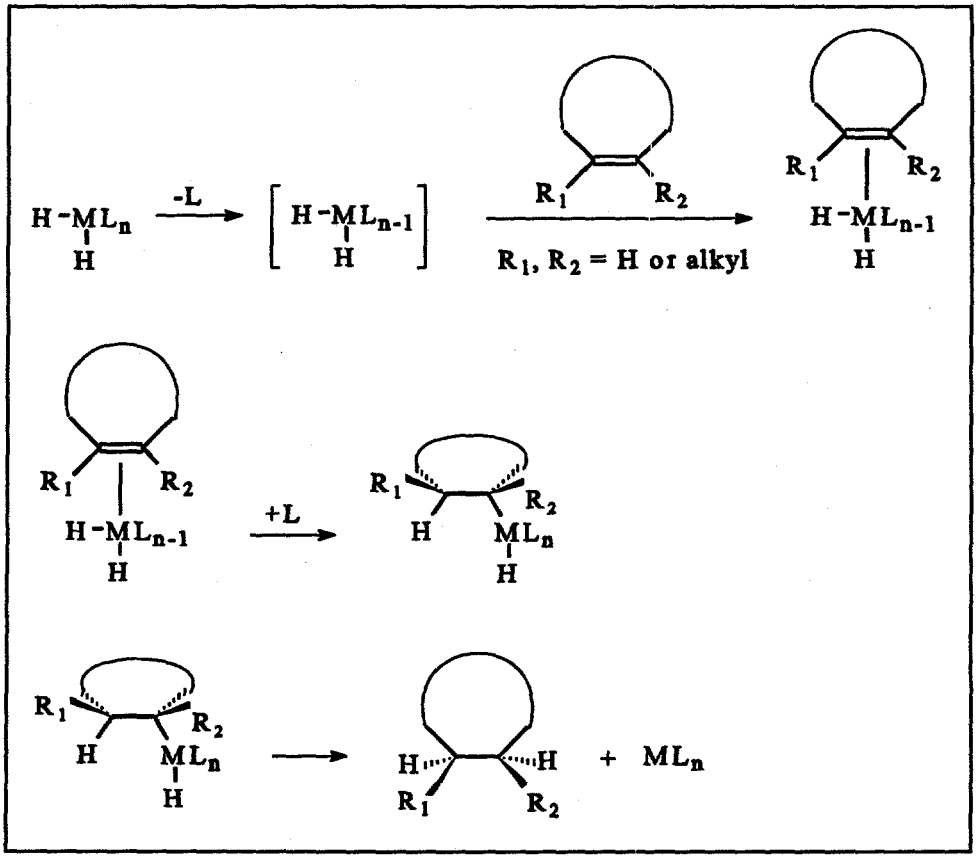

Scheme 6. Mechanism of olefin hydrogenation on a metal complex with prior olefin coordination.

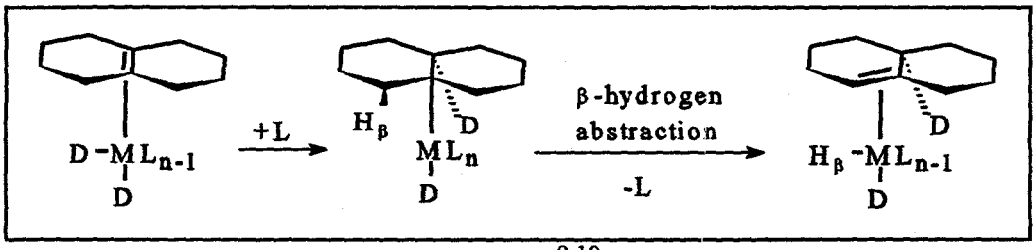

Scheme 7. Proposed mechanism for $\Delta^{9,10}$-octalin isomerization on a metal complex.

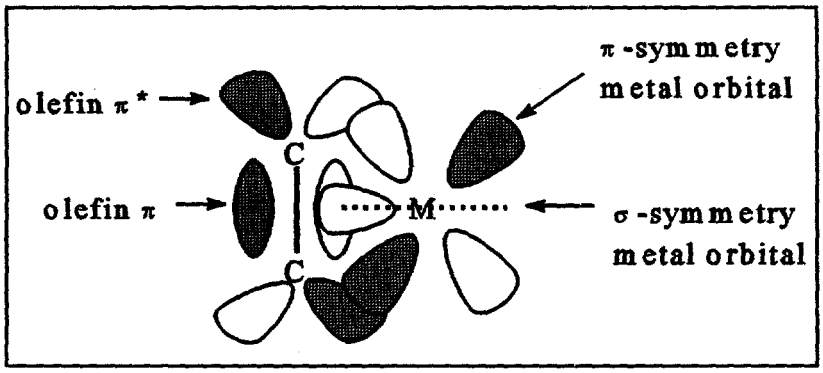

Scheme 8. Orbitals involved in metal-olefin bonding.